

Politecnico di Milano

Department of Chemistry, Materials and Chemical Engineering "Giulio Natta"



PhD thesis in Materials Engineering

Smart Materials and Additive Manufacturing

Author

Giovanni Postiglione

Supervisor

Prof. Stefano Turri

Tutor

Prof. Marinella Levi

Coordinator

Prof. Chiara Castiglioni

2017 - Cycle XXIX

>>

Abstract

The interest of the scientific community in smart materials is constantly growing mainly because of their huge potential in several technological applications, including coatings, structural components and electrical sensors. The strategy for the designing of such systems is correlated to the observation of the natural world where countless examples of stimuli-responsive behaviour can be found. In recent years, the development of novel polymeric smart formulations was encouraged by concurrent advances in the field of additive manufacturing. Additive technologies, initially adopted for rapid prototyping of digital product renderings, have become an established method for manufacturing objects suitable for end use. Their continuous development, especially in term of processable materials, is now allowing the fabrication of cutting-edge devices with unconventional performances.

In the work presented in this PhD thesis, new polymeric smart materials and additive manufacturing technologies were examined independently, at first, and then focusing on the relationship between innovative processing and advanced functionality. The final aim of the research project was developing new smart polymers and composites suitable to be realized by additive manufacturing technologies.

The first part dealt with the study of smart systems designed to give an intelligent response to damage events. One approach consisted in providing a material with the ability to display a visual change as a result of a local deformation due to impacts or scratches. To this end a polymeric coating was functionalized with microcapsules containing an UV-fluorescent dye so that the resulting composite was capable of showing a visual signal upon capsules breakage. This damage sensing material allows to easily detect external damages and its implementation facilitates maintenance operations. The analysis of smart systems was extended to self-healing materials, that, in terms of material functionality, represent the logical evolution of damage sensing. Their ability to counteract degradation and damages with automatic reparation mechanisms was assessed by formulating a polymeric coating based on the Diels-Alder reaction. The resulting polymer, upon application of a simple thermal treatment, reduced or eliminated small defects or microcracks, potential points of weakness that could otherwise lead to structural failure.

The second part focused on the development of polymeric nanocomposites for different extrusion-based additive manufacturing technologies. The proposed processes, termed liquid deposition modeling (LDM) and UV-assisted 3D printing (UV-3DP), consisted in the layer-by-layer deposition of fluid material that solidified after flowing out of a computer-controlled moving nozzle. Using LDM it was possible to fabricate conductive microstructures with resolution down to 100 μm from a solvent based formulation containing carbon nanotubes. Conversely, through UV-3DP, nanocomposites composed by different combinations of photocurable matrix and inorganic fillers were successfully processed. A systematic investigation on the rheological properties of different formulations allowed to achieve a deeper understanding of the processes related criticalities, and hence the best printability conditions. In the attempt to expand the use of UV-3DP to the fabrication of reinforced composites, a sequential interpenetrated polymer

network, loaded with short carbon fibers, was especially devised. The outstanding mechanical properties showed by the resulting prints have significant implications for the future manufacturing techniques of composites.

Finally, self-healing materials based on microvascular networks were designed exploiting the additive process ability in generating controlled geometric patterns. In practice a specific procedure allowed to convert a 3D printed microarchitecture into a system of microchannels. The healing function, comparable to that of human skin, could be performed upon release of liquid healing agents accurately stored into the microchannels embedded within the matrix. This ability favorably affected the durability and mechanical performance of the tested polymeric materials.

The innovative approaches based on additive manufacturing, such as those proposed in this work, will open the way towards the implementation of smart functions, commonly associated with the biological world, into novel polymeric and composite materials.

>>

Table of contents

1	AIMS AND STRUCTURE OF THE WORK	11
1.1	AIMS OF THE WORK	12
1.2	STRUCTURE OF THE WORK	13
2	NEW APPROACHES IN MATERIALS DESIGN AND PROCESSING	17
2.1	FROM BIOMIMETICS TO SMART MATERIALS	18
	2.1.1 DAMAGE SENSING MATERIALS	26
2.2	SELF-HEALING MATERIALS	30
	2.2.1 INTRINSIC SELF-HEALING MATERIALS	32
	2.2.2 EXTRINSIC SELF-HEALING MATERIALS	37
2.3	ADDITIVE MANUFACTURING	46
	2.3.1 3D-PRINTING TECHNIQUES	48
	2.3.2 CURRENT RESEARCH TRENDS AND APPLICATIONS	55
2.4	REFERENCES	64
3	MATERIALS AND EXPERIMENTAL TECHNIQUES	69
3.1	MATERIALS	70
3.2	EXPERIMENTAL TECHNIQUES	76
4	FLUORESCENT SENSORS BASED ON CHEMICALLY-STABLE CORE/SHELL MICROCAPSULES FOR VISUAL MICROCRACK DETECTION	79
4.1	INTRODUCTION	80
4.2	EXPERIMENTAL SECTION	82
	4.2.1 MATERIALS	82
	4.2.2 SYNTHESIS OF THE UV-SCREENING MICROCAPSULES	82
	4.2.3 SYNTHESIS OF THE FLUORESCENT DYE (VPY)	83
	4.2.4 CHARACTERIZATION OF MICROCAPSULES	83
	4.2.5 DETERMINATION OF THE CORE FRACTION OF MICROCAPSULES	84
	4.2.6 CHEMICAL RESISTANCE OF MICROCAPSULES	84

Table of contents

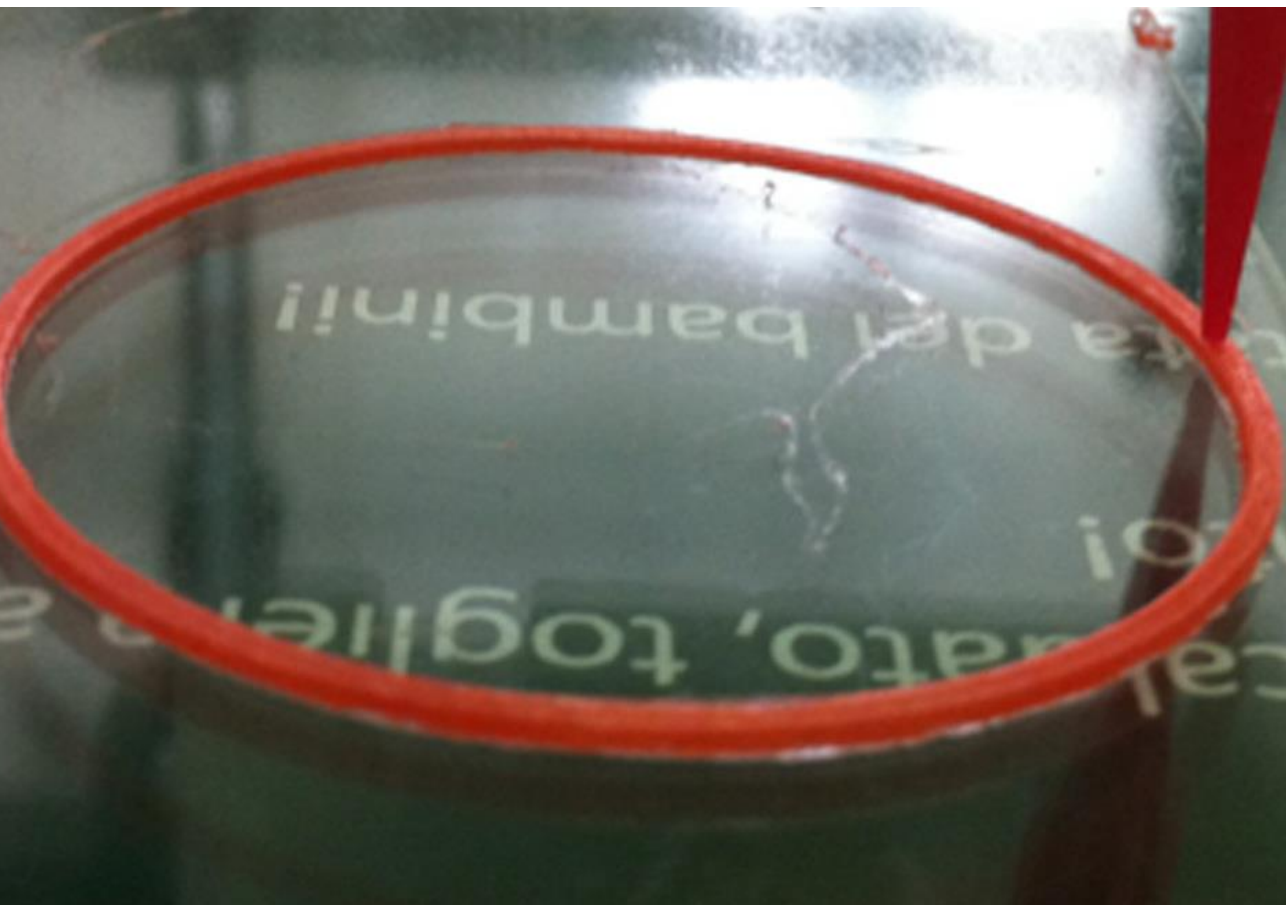
	4.2.7 PREPARATION OF THE CRACK DETECTION COATING SYSTEM CONTAINING MICROCAPSULES_____	86
4.3	RESULTS AND DISCUSSION_____	87
	4.3.1 SYNTHESIS AND CHARACTERIZATION OF MICROCAPSULES_____	87
	4.3.2 CHEMICAL STABILITY OF MICROCAPSULES_____	91
	4.3.3 SMART COATING FUNCTIONAL DEMONSTRATION_____	92
4.4	CONCLUSIONS_____	95
4.5	REFERENCES_____	96
5	SELF-HEALING PROPERTIES OF A POLYMER COATING BASED ON THE THERMOREVERSIBLE DIELS-ALDER REACTION_____	99
5.1	INTRODUCTION_____	100
5.2	EXPERIMENTAL SECTION_____	102
	5.2.1 SYNTHESIS OF 3F AND 2F COMPOUNDS_____	102
	5.2.2 SYNTHESIS OF 2M-3F2F POLYMER_____	103
5.3	RESULTS AND DISCUSSION_____	104
	5.3.1 SYNTHESIS AND CHARACTERIZATION OF 2M-3F2F POLYMER_____	104
	5.3.2 HEALING PROPERTIES_____	108
5.4	CONCLUSIONS_____	111
5.5	REFERENCES_____	112
6	CONDUCTIVE 3D MICROSTRUCTURES BY DIRECT 3D-PRINTING OF POLYMER/CARBON NANOTUBE NANOCOMPOSITES_____	115
6.1	INTRODUCTION_____	116
6.2	EXPERIMENTAL SECTION_____	118
6.3	RESULTS AND DISCUSSION_____	120
	6.3.1 ELECTRICAL CONDUCTIVITY_____	120
	6.3.2 RHEOLOGICAL CHARACTERIZATION_____	121
	6.3.3 3D PRINTED MICROSTRUCTURES_____	124

6.4	CONCLUSIONS	126
6.5	REFERENCES	127
7	UV-ASSISTED 3D-PRINTING OF POLYMER NANOCOMPOSITES BASED ON INORGANIC FILLERS	129
7.1	INTRODUCTION	130
7.2	EXPERIMENTAL SECTION	132
	7.2.1 MATERIALS	132
	7.2.2 NANOCOMPOSITE DISPERSIONS	132
	7.2.3 CHARACTERIZATION TECHNIQUES	133
7.3	RESULTS AND DISCUSSION	135
7.4	CONCLUSIONS	148
7.5	REFERENCES	149
8	3D-PRINTABLE CARBON FIBER REINFORCED POLYMER COMPOSITES WITH DUAL-CURE SEQUENTIAL INTERPENETRATED POLYMER NETWORKS	151
8.1	INTRODUCTION	152
8.2	EXPERIMENTAL SECTION	154
	8.2.1 MATERIALS	154
	8.2.2 RESIN AND COMPOSITE FORMULATION AND CURING	154
	8.2.3 CHARACTERIZATION TECHNIQUES	155
	8.2.4 3D-PRINTING EXPERIMENTS	156
8.3	RESULTS AND DISCUSSION	157
8.4	CONCLUSIONS	162
8.5	REFERENCES	163
9	SELF-HEALING MATERIALS BASED ON MICROVASCULAR NETWORKS VIA ADDITIVE MANUFACTURING	165
9.1	INTRODUCTION	166
9.2	EXPERIMENTAL SECTION	168

Table of contents

9.2.1	MATERIALS AND METHODS	168
9.2.2	SAMPLES DESIGN AND FABRICATION	168
9.2.2	COMPUTERIZED X-RAY MICROTOMOGRAPHY	170
9.3	RESULTS AND DISCUSSION	171
9.3.1	SAMPLE FABRICATION AND MICRO-CT CHARACTERIZATION	171
9.3.2	HEALING TESTS AND MECHANICAL CHARACTERIZATION	174
9.4	CONCLUSIONS	178
9.5	REFERENCES	179
10	TOWARDS 4D PRINTING	181
10.1	CONCLUSIVE REMARKS	182
10.2	FUTURE DEVELOPMENTS	185
10.3	REFERENCES	194
	APPENDIX A: LIST OF SYMBOLS AND ABBREVIATIONS	197
	APPENDIX B: LIST OF PUBLICATIONS AND COMMUNICATIONS	201

1.
Aims and
structure of the work



1.1 AIMS OF THE WORK

The relationship between microstructure and properties is one of the key concepts in material science. A fine control over the material microarchitecture is fundamental in order to design a physical object able to perform a generic function. In recent years, the observation of the natural world to the microscopic scale has led to the conception of a new class of materials with the built-in ability of interacting with the surrounding environment in a way similar to those of the biological species. These materials are generally called *smart* and their stimuli-responsive functionality is strictly dependent upon the combination of material properties and microstructure. Smart materials represent at the same time a great scientific challenge for their design complexity and an enormous resource for their high technological interest in several application fields.

In this PhD work, materials with different smart functionalities are proposed and a throughout study of how new additive manufacturing processes can be exploited in smart materials development is presented. At first (chapters 4 and 5), following a new paradigm in material design based on the concept of damage management, materials able to sense or self-heal after the formation of defects, microcracks or large damages were implemented. With application in structural engineering, these materials were developed with the aim of improving the mechanical behaviour and the aesthetical appearance over the products lifetime. In the second part (chapters 6, 7 and 8) the processability of non-conventional composite polymers using proper additive manufacturing technologies was explored. Beyond widening the available range of materials for additive manufacturing, the results achieved were fundamental to have an exhaustive vision of the critical aspects associated with the manufacturing process and the materials used. Finally (chapter 9), taking inspiration from the circulatory system found in plants or in the human skin, a different type of self-healing material embedding microvascular pathways, was fully designed to be realized through additive manufacturing. The current research strategies having as the main focus the intersection between smart materials and additive manufacturing were discussed in the conclusive chapter (chapter 10).

1.2 STRUCTURE OF THE WORK

This PhD thesis is composed by 10 chapters. The introductory chapter (chapter 2) contains an overview on the current state of art on smart materials and additive manufacturing. It intends to guide the reader through the several topics touched in this PhD thesis and to point out the relationship between the research themes embraced by the various chapters. Each of the chapters, however, has its own introductory and conclusive sections with a more specific focus on the subject addressed and more closely related references. The conclusive chapter (chapter 10) gathers the main research findings of this work and offers some last remarks on the deep correlation between smart materials and additive manufacturing. A brief description of the content of each of the chapters is listed below.

Chapter 1 highlights the aims and the structure of this PhD work.

Chapter 2 presents a discussion on current trends concerning material design and material processing. Firstly an overview on the discipline of biomimetics and on the general principles driving the scientists towards the creation of new bioinspired materials is offered. The innovative field of smart materials is also briefly introduced, with particular emphasis on damage sensing and self-healing materials, these two being the types of smart materials studied in this PhD thesis. Self-healing materials are described more extensively showing the variety of strategy used in their design and fabrication. Finally the technological achievements in the field of additive manufacturing are discussed in full detail with a critical analysis on how the specific processing technologies intersect the world of smart materials.

Chapter 3 contains the lists of chemical substances used in this thesis work and a brief description of all experimental techniques adopted in the synthesis, processing and characterization of materials.

Chapter 4 presents a study on a smart coating able to display microcracks resulting from impact damage upon UV-light exposure. The functionality of this innovative damage sensing system for structural material is extensively illustrated. Being based on microcapsules consisting of a UV-screening polyurea shell and a fluorescent liquid core, their characterization together with the microencapsulation process are examined in detail. Finally the microcapsules chemical stability in different solvents is analyzed to demonstrate their superior solvent resistance over dwell time originating from the highly crosslinked shell structure that prevents undesired core extraction from the microcapsules.

Chapter 5 describes the results obtained from a study on a self-healing polymer based on the Diels-Alder (DA) and *retro*-DA reactions. The polymer network is formed by reacting a mixture of trifunctional and difunctional furanized resins with a bismaleimide. A significant improvement of both the mechanical properties and the self-healing behaviour is achieved by introducing a small amount of benzyl alcohol as a plasticizer. The resulting plasticized polymer is shown to completely recover from surface scratches after *retro*-DA and DA reaction, whilst tensile testing reveals a partial restoring of the pristine mechanical strength.

Chapter 6 presents a study on a new three-dimensional printing system based on liquid deposition modeling (LDM) developed for the fabrication of conductive 3D nanocomposite-based microstructures. The 3D-printed polymer consists of a liquid dispersion of multi-walled carbon nanotubes (MWCNTs) in a poly(lactic acid) (PLA) matrix. Electrical and rheological measurements on the nanocomposite at increasing MWCNTs and PLA concentrations are used to find the optimal processing conditions and the printability windows for these systems. In addition, examples of conductive 3D microstructures directly formed upon 3D printing of such PLA/MWCNT-based nanocomposite dispersions are presented.

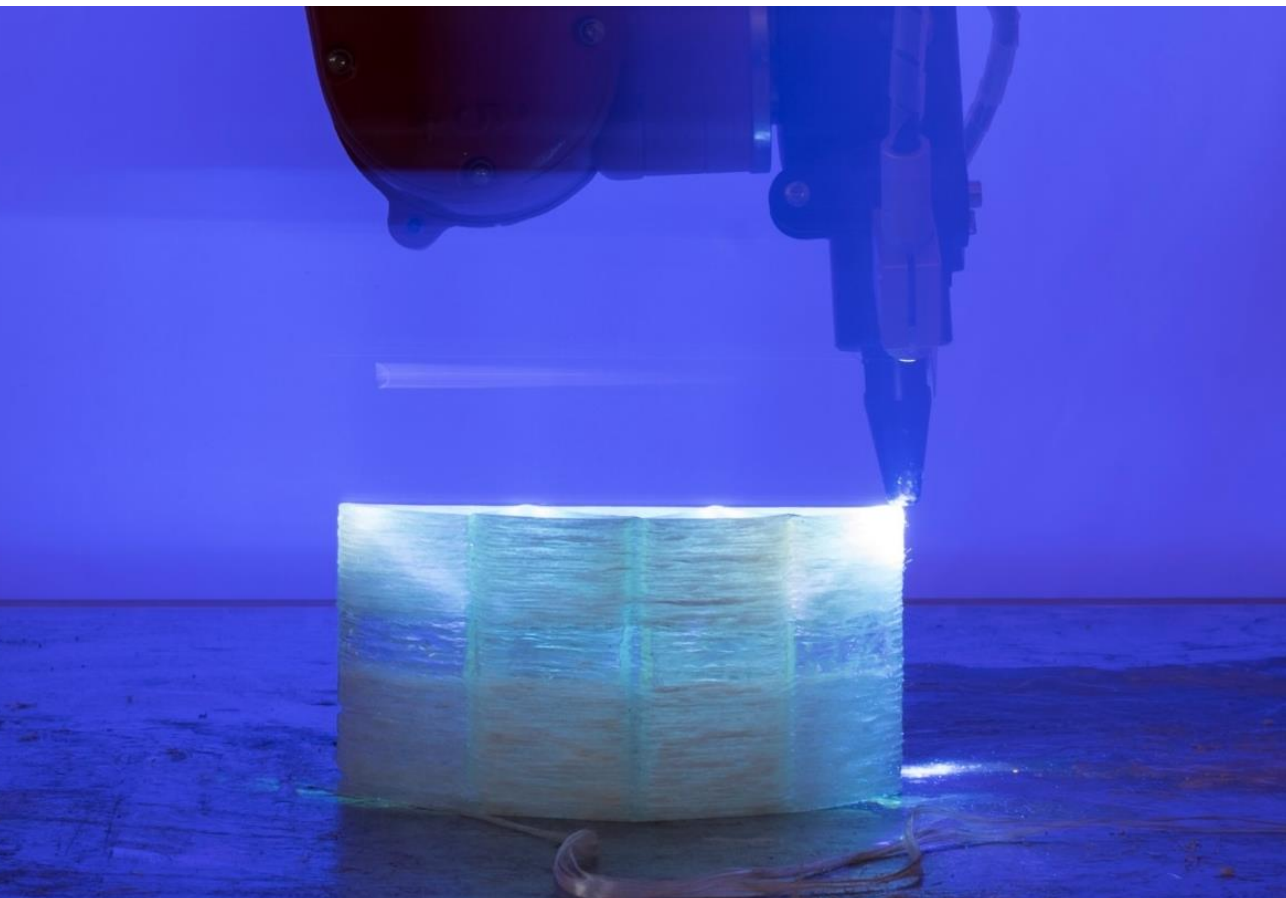
Chapter 7 illustrates how nanocomposites based on a UV-curable polymeric resin and different inorganic fillers were developed for use in UV-assisted three-dimensional (UV-3D) printing. A systematic investigation on the effect of filler concentration on the rheological properties of the polymer nanocomposites is presented. In addition, photocalorimetric measurements used to assess the effect of the inorganic fillers on the thermodynamics and kinetics of the resin photocuring process are shown. Furthermore, the effect of UV-3D printing direction, fill density, and fill pattern on the mechanical properties of UV-3D printed specimens is investigated. Finally, examples of 3D macro- and microarchitectures, spanning features, and planar transparent structures directly formed upon UV-3D printing of such nanocomposite dispersions are illustrated.

Chapter 8 reports on a study on a sequential interpenetrating polymer network (IPN) obtained by co-formulation of a photocurable acrylic resin with a thermocurable epoxy resin. Such IPN is proposed as matrix for the fabrication of carbon-fiber reinforced (CFR) composite structures by means of 3D-printing technology. The photo-crosslinking reaction, the thermal transitions and the mechanical behavior of the developed dual-cure material are examined by means of DSC and DMA analyses. Combining the advantages of the easy free-form fabrication typical of 3D-printing with the purposely customized features of the newly developed IPN material, the possibility of fabricating CFR composite materials in 3D with excellent mechanical properties is demonstrated.

Chapter 9 describes the manufacturing procedure, characterization and application of self-healing polymer resin samples based on embedded microvascular networks. The approach proposed allows to exploit the 3D printers peculiar ability in generating controlled geometric patterns for the creation of microchannels networks. Liquid reacting components are stored within the microstructure enabling the material to self-heal from severe damages. The microchannels microstructures are examined using X-ray computerized microtomography whilst the mechanical properties of healed samples are measured by means of uniaxial tensile tests and compared to those of undamaged samples to determine the mechanical healing efficiency.

Chapter 10 summarizes the main findings of the work and gives an outlook on possible future research lines.

2.
New approaches
in
materials design & processing



2.1 FROM BIOMIMETICS TO SMART MATERIALS

“THOUGH HUMAN INGENUITY MAY MAKE VARIOUS INVENTIONS, [...] IT WILL NEVER DEVISE ANY INVENTION MORE BEAUTIFUL, NOR MORE SIMPLE, NOR MORE TO THE PURPOSE THAN NATURE DOES.” LEONARDO DA VINCI

Nature, in its extraordinary variety, has always fascinated the human being and has represented an enormous source of inspiration for the scientific world. Leonardo da Vinci was one of the first scientists that scrupulously explored the relationship between anatomy and function of living systems for the creation of working apparatus. With his brilliant designs of flying machines inspired by the birds flight, he has pioneered the discipline of modern biometrics, which is today a thriving research field. Biomimetics, according to one of its first definition dated back to the fifties, is the study of the formation, structure or function of biological substances, materials and processes especially for the purpose of synthesizing similar products by artificial mechanisms which mimic natural ones. It intrinsically involves several fields of study, as it combines the comprehension of biological principles investigated in biology, physics and chemistry with the ability to design and manufacture functional device, a prerogative commonly allocated to engineers. The high degree of sophistication often found in natural materials is one of the main obstacles to overcome when tackling the challenge of reproducing a biological material or process. Centuries of evolution allowed living organisms to refine their mechanisms and derive new ones in adapting to the changing habitat even though their access to available resources in term of chemicals was limited and that processing conditions other than at ambient temperature and in aqueous environment were not possible. Given this preconditions, it is clear that the preparation of bioinspired functional materials is a promising and highly complex task at the same time. Over the second half of the twentieth century, however, the field of bioinspired materials exploded as numerous innovative solutions have been proposed by the scientific community. Curiously it has also been found true the contrary, meaning that mechanisms though to be entirely the outcome of the human mind are actually present in nature too. A surprising example of that are the mechanical gears, recently seen in the biological structure of the flightless planthopper insect *Issus coleoptratus* for the first time¹. The nymphs of this insect presents a row of cuticular gear teeth in the proximity of the hindleg joints, as clearly shown in figure 2.1. Due to the close relationship between structure and functions, fruitful results in biomimetics were obtained, in first place, by replicating the natural occurring hierarchical architecture at different scales ranging from nanometers to millimeters. At the mono-dimensional level, biomimetic structures such as the spider silk and the polar bear hairs were deeply investigated with the aim of replicating their excellent mechanical properties and thermal insulation respectively. Going from two- to three-dimensional levels, it is also possible to find electrochromic color shifting coatings for camouflage, bioinspired antifouling or antireflective

surfaces, multi-composites porous damping materials and self-healing materials. It is worth enlighten that a relevant advantage of synthetic materials over natural ones in performing a specific task resides in the superior properties of their building molecules. For this reason, it is not entirely surprising that bioinspired manmade components have sometimes even better properties than the natural counterpart. Unfortunately some problems arise when analyzing the durability of manmade systems. In particular any perturbation of the material structural features generally results in the loss of the function for which they were originally designed. This undesirable perspective is turned into a point of strength when talking about biological species. In fact, most of the biomaterials are stimuli responsive, meaning that the interaction with the environment not only has a negligible effect on their functionality but it is exploited to perform operations at an higher level of complexity. These processes, evolved to enhance the survivability of living organisms, are always more frequently taken as reference mechanisms for the synthesis of new substances. It is fundamental to recognize the molecular mechanisms of natural systems dominating their peculiar functions to the nanoscale in order to be able to possibly replicate them on artificial entities. The next frontier in materials design is thus represented by the creation of materials able to autonomously control their response to the surrounding conditions fully optimizing their self-adapting properties²⁻⁵.

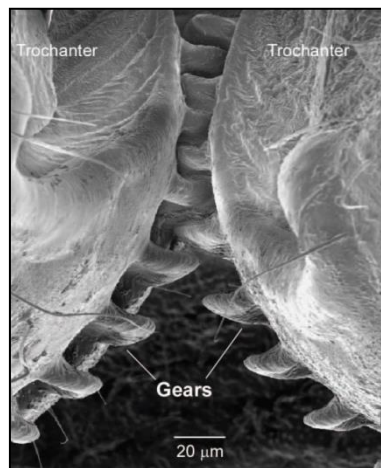


FIGURE 2.1 - HIGHLY MAGNIFIED SCANNING ELECTRON MICROGRAPH OF THE INTERDIGITATION OF THE GEARS FOUND IN THE *ISSUS COLEOPTRATUS*. THE GEARS TEETH MOVEMENT OCCURS DURING THE PREPARATORY COCKING AND THE PROPULSIVE PHASES OF JUMPING ENSURING THAT BOTH HINDLEGS MOVED AT THE SAME ANGULAR VELOCITIES TO PROPEL THE BODY WITHOUT YAW ROTATION¹.

Some examples of bioinspired materials recently proposed by the scientific community are examined to give a first insight of the potential of the biomimetic approach in engineering new materials. An interesting case of bioinspired material is a carbon fiber-epoxy composite fabricated following the design strategy found in the stomatopod club. This crustacean (shown in

figure 2.2a) uses its heavily mineralized club as an hammer-like weapon to strike the shells of its preys. Although the energy of the high-speed impact is considerable, the club is able to resist several repeated smashes without being significantly damaged. This remarkable behaviour attracted the attention of scientists who have carefully examined its microstructure. The stomatopod club is a multiregional biological composite with a heavily mineralized outer layer and the inner endocuticle, in which the periodic region plays a key role in energy dissipation. The microstructure of this region is the result of a helicoidal stacking of aligned fiber layers as illustrated by the SEM image in figure 2.2b).

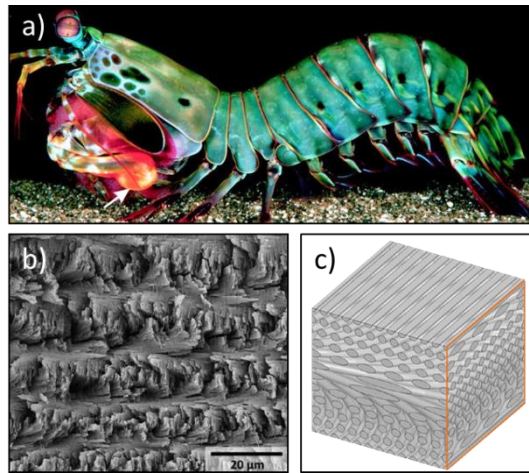


FIGURE 2.2 - A) PHOTOGRAPH OF THE STOMATOPOD ODONTODACTYLUS SCYLLARUS. B) SEM IMAGE OF THE FRACTURED DACTYL CLUB SURFACE REVEALING A HELICOIDAL ORGANIZATION OF FIBERS. C) SCHEMATIC OF THE HELICOIDAL ARRANGEMENT OF ALIGNED FIBER LAYERS⁶.

This convoluted geometry is further clarified by the schematic representation presented in figure 2.2c. The degree of mineralization as well as the density of the helicoidal stacking layers have an influence over the stiffness, strength and hardness of the composite structure. The helicoidal pattern has shown to be beneficial to the mechanical properties of composites in several ways. This peculiar design displays an isotropic response to in-plane loading at the macroscale when there is a small rotation angle between consecutive layers. When loaded in tension, the structure reorientation induced by the loading conditions allows to better resist deformation. In addition an increase in the fracture toughness of helicoidal composites compared to that of a unidirectional control has been demonstrated together with a reduction in through-thickness impact damage and an increase in residual strength following impact damage. Advanced composites materials redesigned taking into account the microarchitecture of these crustaceans can certainly find applications in important industrial fields such as aerospace and automotive⁶.

Impressive results have recently been achieved in the likewise relevant industrial field of adhesives using an analogous imitation strategy. This time the notorious ability of geckos to remain stuck even upside-down to different kind of surfaces was transferred to synthetic materials by finely reproducing the gecko foot microstructure. Figure 2.3a shows a picture of a gecko foot from underneath with its millimetric lamellae also visible to the naked eye. Provided with numerous differently sized and shaped tips every gecko foot hair (setae, averagely 110 μm height and 5 μm diameter) possesses approximately 10 N/cm^2 of shear adhesion strength regardless of the surface roughness thanks to the Van der Waals forces generated. This highly sophisticated design, only examinable using a scanning electron microscope, is presented in figure 2.3b-c. Several studies have been carried out trying to emulate its attachment and detachment mechanisms using various manufacturing strategies.

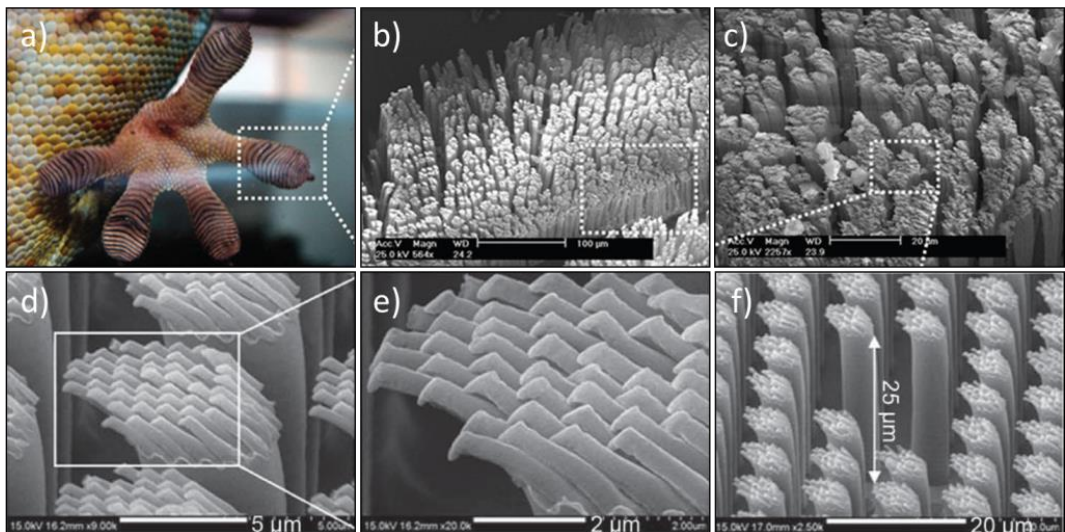


FIGURE 2.3 - A) PICTURE OF THE GECKO FOOT MILLIMETER SCALE LAMELLAE. B-C) SEM IMAGES OF MULTISCALE STRUCTURAL HIERARCHY IN GECKO FOOT-HAIR FROM MICROSCOPIC SETAE TO NANOSCOPIC SPATULAE. D-E) SEM IMAGES OF UV-CURABLE PUA RESIN ANGLED STRUCTURES AT DIFFERENT MAGNIFICATIONS. F) HIGHER MAGNIFICATION SEM IMAGE OF ANGLED NANOHAIRS FORMED ON TOP OF MICROHAIRS (5 MICRONS DIAMETER AND 25 MICRONS IN HEIGHT)⁷.

The realization of organized hierarchical structure with sufficient adhesion force requires adequate control of advanced fabrication techniques such as standard replica molding, angled etching and UV-assisted capillary force lithography. SEM images taken at different magnification of high-aspect ratio and angled nanohairs made of a UV-curable polyurethane acrylate resin are reported in figure 2.3d-e. The astonishing resemblance of the synthetic material with the real gecko foot hair is not limited to the physical appearance but also results in a similar control of the adhesion mechanisms. Micro- and nanopillars are both used because nanopillars provide better adhesion having an elevated number of contacts per unit area but micropillar are generally more

stable over repeated adhesion cycles. Durability, together with problems related to large area fabrication and material properties are the main issues needed to be addressed before bioinspired dry adhesives will be fully developed and ready to be commercialized in a variety of different applications⁷.

Finally, an example of biomimetic solution in the marine technology field is reported. Looking for more environmentally friendly and effective ways of reducing biofouling on the hull structure of marine vessels, scientists have intensely studied the impressive characteristics of many natural surfaces. Physical features, wettability and chemical defenses are some of the factors determining the antifouling performances of biological species. Among the numerous designs explored, shark skin has attracted worldwide interest thanks to the outstanding drag reduction and antifouling properties. Again the skin surface morphology composed by regularly positioned ridged platelet (shown in figure 2.4a) confers to the animal the ability to repel fouling organisms³. The feature size of the shark skin denticles and the resulting hydrodynamic variation induced are thought to be crucial factors in reducing the attachment points and the adhesive contact area preventing the potential accumulation of microorganisms. One possible strategy to reproduce the exceptional surface functions of the shark skin consists in using its real structure as a template replica for the fabrication of coating device with a UV curable paint. Firstly a pre-treatment is performed to preserve the surface micro-morphology, in second place a soft negative mold is prepared by pouring PDMS upon the template ensuring that the micro-cavities are properly filled.

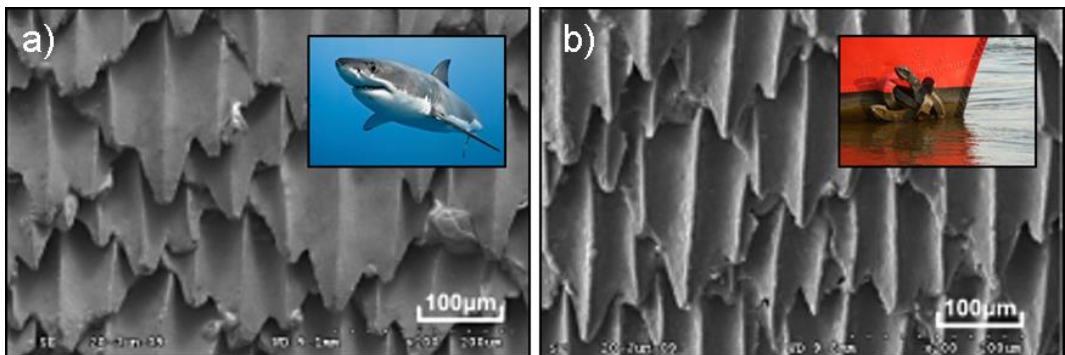


FIGURE 2.4 - A) SEM IMAGE OF THE SHARK SKIN COMPOSED BY ALIGNED DENTICLES (PICTURE OF A WHITE SHARK IN THE INLET). B) SEM IMAGE OF THE BIO-REPLICATED COATING SURFACE (PICTURE OF A PAINTED VESSEL HULL IN THE INLET)⁸.

At the end of the soft lithographic process the soft negative mold is filled with UV curable paint to finally obtain the functional coating surface. The accuracy of the process is high enough to achieve a satisfactory replica of skin denticles as evident from figure 2.4b. Anti-fouling static and dynamic test demonstrated that microorganisms colonization on bio-replicated vivid shark skin is negligible compared to smooth or micro-grooved surfaces. Similarly drag reduction efficiency is

consistently higher than other surfaces. Furthermore, in order to address the issue of large-area fabrication of antifouling coatings this bio-replication approach is being implemented on large scale instruments equipped with rotating wheels and UV lamps. These advances provide important guidelines for the design and development of bioinspired antifouling coating to be installed in marine environment⁸.

Shifting away from the mere concept of replicating a biological organism microstructure, the creation of materials able to interact in a controlled manner with the surrounding environment represents, as previously mentioned, a step forward in advanced material design. Such materials are generally referred to as *smart* and have known a widespread diffusion in academic research due to their potentially revolutionary impact on various technological fields ranging from automotive and aerospace industry to civil engineering or from biomedical applications to smart machines. Although a complete description of the current state of art on smart material developments is out of the scope of this PhD work, they deserve an at least brief overview to enlighten the diverse range of chemico-physical principles exploited to express their functionality. Opposed to the representative examples of bioinspired materials already examined, smart materials are not necessarily the exact replication of a biological mechanism. Their functionality, however, is produced by a change in a specific property as a result of an applied external signal just as some biomolecules provide specific chemical functions when properly stimulated. Temperature, moisture, electric or magnetic fields, pH, and stress are some of the parameters that can somehow be sensed by smart materials thus provoking a response in terms of shape or color changing and mechanical or electromagnetic properties alteration. The physical or chemical event that causes these responses is linked to the formation or destruction of secondary forces, simple reactions of moieties pendant to the polymer backbone, or more significant alterations in the polymeric structure. Responsive polymers can be realized in several different forms: solutions, gels, self-assembled nanoparticles, films or bulk solids. In recent years the research is focusing its attention on stimuli-responsive macromolecular structures, because of their rapid response upon stimulation which is a key feature in many applications. For this reason highly efficient smart materials are mainly being developed as two-dimensional polymeric thin films or three-dimensional systems based on particulates and their assemblies. Figure 2.5 reports the wide range of nanostructured stimuli-responsive polymer materials. Two-dimensional structures exist under the form of thin film, membranes, polymer brushes and layer-by-layer film whilst three-dimensional nanostructures are found in the form of colloids, nanogels, capsules, core-shell particles, Pickering emulsions and aggregates. Hybrid polymers are also created combining different structures. These systems, when receiving an external signal, are capable of conformational and chemical changes depending on their different architectures. Within the two-dimensional structures, reconstructable surfaces are emerging as promising materials in applications where a specific property such as adhesion, transparency, wettability or permeability can rapidly be switched from one extreme to the other.

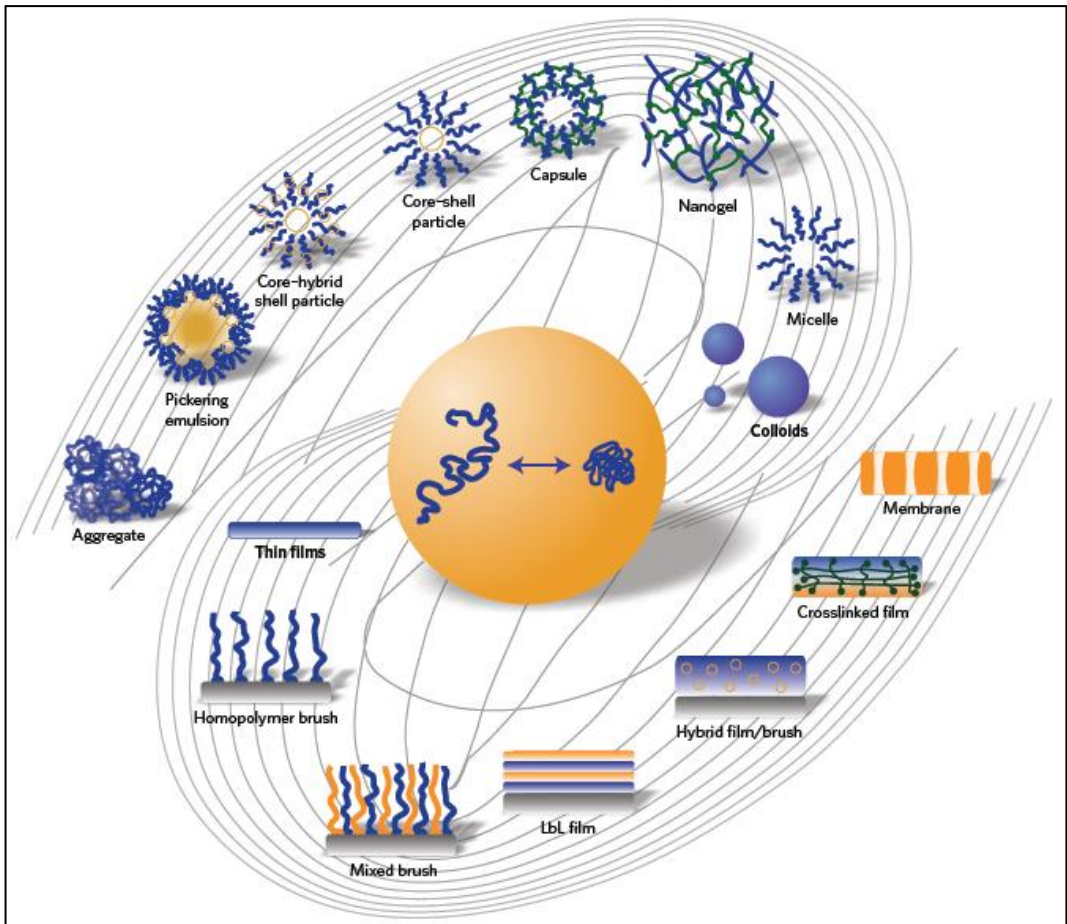


FIGURE 2.5 - SCHEMATIC REPRESENTATION OF NANOSTRUCTURED STIMULI-RESPONSIVE POLYMER MATERIALS⁹.

Reversible switching is a peculiar property in polymer brushes, which are thin polymeric films provided with macromolecules chemically grafted to the surface. The material stimuli-responsiveness is dictated by the change in conformation adopted by the polymeric chains. This is found, for example, in polyelectrolyte brushes where variations in ionic strength and pH modify the molecule conformational state. Zwitterionic brushes, on the other hand, present a temperature dependent wetting behaviour due to their upper critical solution temperature. As shown in figure 2.6a, increasing the temperature from 22 °C to 52 °C reduces significantly the water contact angle. The reversibility of these properties allows the material to sustain several transitions backwards and forwards. Another interesting smart functionality is found in the peculiar swelling behaviour of porous thin gel films.

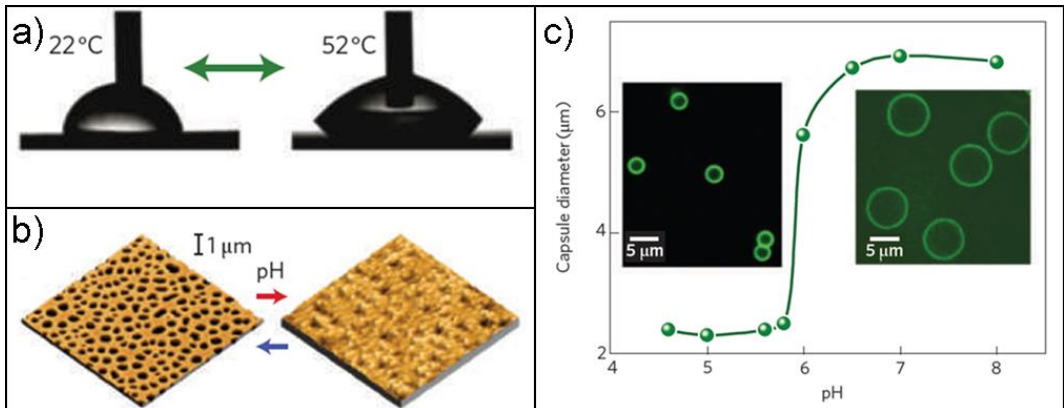


FIGURE 2.6 - A) IMAGES OF WATER CONTACT ANGLE TESTS ON A ZWITTERIONIC POLYMER SHOWING A TEMPERATURE DEPENDENT BEHAVIOUR⁹. B) AFM TOPOGRAPHIC IMAGES OF A P2VP NETWORK THIN FILM AT DIFFERENT PH VALUES⁹. C) CURVE SHOWING POLY(METHACRYLIC ACID) MICROCAPSULES DIAMETER VARIATION AS A FUNCTION OF PH¹⁰.

Being their network attached to a surface, the swelling response of these films result in a reduction of the pore size. The porosity of the film can be fine-tuned by simply shrinking or swelling the polymer. As a consequence this behaviour can be exploited in applications where particle transport through the film is a crucial element. An example is offered by the porous poly(2-vinyl pyridine) (P2VP) thin gel film attached to a solid substrate. Figure 2.6b displays atomic force microscopy (AFM) topographic images of a P2VP network thin film at different pH values. The thin film switches from open to closed pores as the pH decrease from 5.5 to 2. It is thus possible to place the gel film on an electrode and control its permeability to regulate the transport of electrochemically active ions⁹. Stimuli-responsive particles represent a rapidly developing class of stimuli-responsive materials that can be used in numerous ways such as sensors by facilitating efficient transduction mechanisms and drug delivery or diagnostic systems for *in vivo* applications¹¹. Chemical industry, coatings, cosmetic, detergent and food industries are areas where smart particles could be used for the creation of new advanced technologies and products. However biomedical engineering is probably the field of study that is employing smart polymer the most as many natural polymers already possess the intrinsic ability to sense the presence of specific chemical species in their surroundings. As a consequence, the functionalization of synthetic polymers with proper functional groups able to respond when exposed to specific biomolecules is becoming an increasingly important achievement¹². A concrete case of smart polymers based on nanostructures are drug delivery nanocapsules used to protect various drugs until the release mechanism is activated by a specific stimulus. In order to conveniently deliver the cargo, the kinetics of drug release also needs to be controlled. In the most sophisticated materials, the transport across the capsules wall can be regulated together with the mechanical and chemical stability of the caspules shell. Capsules systems can furtherly be manipulated in order to convert them into responsive particles. An example is given by hollow

poly(methacrylic acid) microcapsules whose colloidal content is removed by dissolution. Figure 2.6c shows the microcapsules responsiveness in term of capsules diameter induced by pH variation¹⁰. The microcapsules change significantly their size having diameters shifting rapidly from 2-3 μm for pH less than 6 to 6 μm for higher pH values.

Representing a versatile tool for materials smart functionalization, microcapsules are rapidly spreading out in advanced polymeric and composite systems for structural applications. Due to the high level of reliability always required by these kind of materials, research is focusing the attention on how smart materials can help reducing the risk of material failure. Catastrophic rupture of structural components is preceded in most cases by formation of microcracks and small damages that represent weak points in the material. The reduction of risks related to the formation of such small damages in structural elements is the aim of damage sensing and self-healing materials. Damage sensing materials are designed to allow detection of otherwise invisible cracks in order to facilitate maintenance operation and to reduce their cost. Self-healing materials have the built-in ability to repair or reduce occurring damages extending, as a consequence, their service lifetime and minimizing the external human intervention.

Damage sensing and self-healing materials are the two types of smart materials investigated in this PhD work. A description of the current state of art on microcapsules based systems developed for the realization of damage sensing materials is presented below (section 2.1.1) whilst self-healing materials will be discussed more extensively in section 2.2.

2.1.1 DAMAGE SENSING MATERIALS

Monitoring technologies of engineering structures are an important tool for inspection and early detection of damages. The health assessment is a crucial step in order to define the right characterization and operative strategies. Development in this sector may have relevant implications in industrial areas such as aeronautics and aerospace, where the components reliability is a major issue. The material integrity may be compromised, in fact, by the presence of defects or deteriorations induced by corrosion and by any microstructural change occurring during its service lifetime. Measurement of subsurface residual stresses and computational methods for life prediction are some of the tools that contribute to enhance safety without affecting the high performance required. Instruments based on X-ray or infrared radiation and ultrasounds are other prominent technologies in the fields of nondestructive testing but they often represent, on the other hand, expensive and unpractical solutions in many applications. An emerging research trend in structural health monitoring with possible influence over the aforementioned industrial fields is represented by the implementation of tools for visual detection of damages. These consist in smart materials with the built-in ability of displaying a color change or visible light emission at a specific location when a damage occurs. The main advantage of this approach is that inspection procedures are significantly simplified and that there is no need for

removal of the element. As a result, critical information on the material integrity can be acquired, drastically reducing the evaluation analysis expenses.

One possible strategy to realize devices with color changing ability lies in the incorporation of photochromic or fluorescent macromolecules within polymer matrices. When attached to the polymer backbone, their conformational changes and the structural rearrangements of the surrounding network segments are influenced reciprocally. In this way, external stresses imposed on the network can be sensed by the light emitting group resulting in a photochromic or fluorescent response. Among all possible molecules with a luminescent response, the fluorophores are fairly attractive as it is also possible to measure the induced stress in materials. Pyrene, anthracene, naphthalene, perylene and their derivatives are common systems used. Although some studies indicate that simple dispersing of photochromic moieties may result in mechanochromic responses, this behavior is not always observed¹³. Crosslinking covalently the responsive molecule to the polymer resolves this problem and, in addition, generates more mechanically stable networks. An illustrative material based on this concept was realized using azobenzene crosslinked brominated vinyl ester polymer networks in which azobenzene entities are used as sensors of deformations, stresses and nano-cracks¹⁴. Microcapsules based system are a concrete alternative for the functionalization of polymer matrices and composites. They are often integrated in functional coatings already used for the protection of structural elements. Their working principle consist in the following: when a material provided with the smart coating is affected by a mechanical damage, the rupture of the embedded microcapsules in that area provokes the release of a signaling agent within the polymer matrix. The versatility of these systems lies in the possibility to tune the composition of both shell and core of the microcapsule thus enabling the coating with the desired damage visualization mode. Other differences reside in the diverse activation sources of the mechanisms, varying from UV-light to local chemical reactions. An interesting case is given by the functionalization of an acrylic paint with microcapsules containing crystal violet lactone dye. This molecule is halochromic as it can be transformed into his colored form in acidic environment. For this reason the coating was provided with color developers: silica gel in the polymeric matrix and liquid methyl 4-hydroxybenzoate, which was also encapsulated. The color change is thus related to the reaction occurring between dye and color developer. Indentation testing on the smart coatings upon duralumin substrates demonstrated the visual indication of the damage in the form of a bruise spot¹⁵. A schematic representation of this mechanism is illustrated in figure 2.7a.

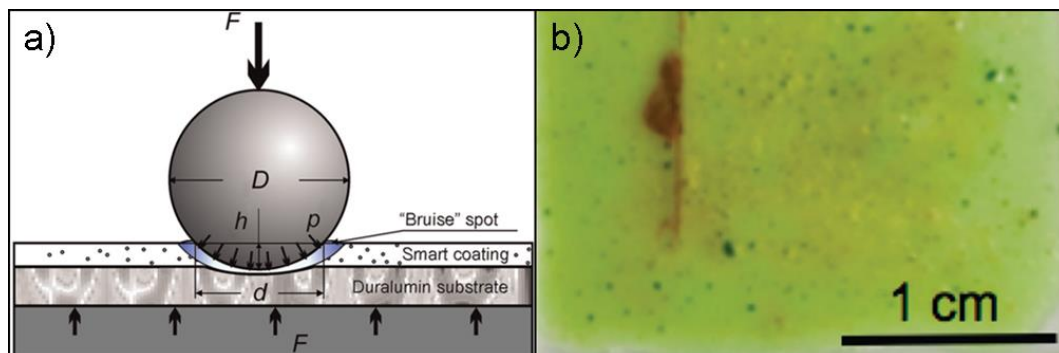


FIGURE 2.7 - A) SCHEMATIC OF AN INDENTATION TEST ON THE DAMAGE-SENSING COATING PROVIDED WITH CRYSTAL VIOLET LACTONE DYE¹⁵. B) PICTURE SHOWING THE DAMAGE-SENSING ABILITY OF A POLYMERIC FILM WITH EMBEDDED MICROCAPSULES. A SCRATCH BECAME EASILY DETECTABLE AS THE RED POLYACETYLENE DIFFUSES¹⁶.

Similarly, the cyclic monomer 1,3,5,7- cyclooctatetraene was encapsulated to exploit its capability to change color being a precursor to the intensely colored polyacetylene. The key reaction of the process is the ring-opening metathesis polymerization for which the presence of the Grubbs-Love ruthenium catalyst was needed. The catalyst was dispersed together with the microcapsules in a 500 μm thick poly(acrylic acid) film. Within one minute after scratching the film with a razor blade, the reaction was triggered and thus the color shift of the signaling agent. Being lime green, the catalyst offered a good color contrast to the red color of polyacetylene as shown in figure 2.7b¹⁶.

Another interesting strategy for the fabrication of smart polymeric coatings consists in the encapsulation of 2',7'-dichlorofluorescein (DCF) as indicating agent due to its high reactivity with a variety of amines followed by a lively color transformation. In contrast to the cases previously reported, the molecule needed to trigger the reaction is no longer encapsulated or dispersed in the polymeric matrix but it is the unreacted amine of the cured epoxy matrix. The presence of the amine causes DCF molecules to evolve into a base form passing from light yellow to bright red. A schematic representation of this autonomous damage indication concept is reported in figure 2.8a. Figures 2.8b-c show the response difference between a control coating with no damage sensing functionality and the smart coating described so far where the cracked region presents a highly localized red color¹⁷. This system is reported to be extremely stable and to provide in situ visual indication of microscopic damages. In such a type of application, microcapsules thermal and chemical stability are fundamental parameters to control as they may undergo severe environmental and processing conditions. Their mechanical properties are obviously crucial as they need to be robust enough to prevent capsules core from leaching causing undesired color change in the coating but they must break when a certain load is applied to the structural element so as to execute their function.

As seen in the cases reported, there are different options available in term of chemicals and mechanisms able to give a satisfactory visual outcome. When using indicators which relate their color change to a chemical transformation, the presence of catalyst or the coexistence of the reactive components is the crucial factor that ensures the successful result. In opposition to these systems, in this PhD work a smart coating based on microcapsules containing a fluorescent signaling agent has been studied. Even though its functionality relies upon the application of an external source of energy, the UV-light, the system proposed presents appealing characteristics such as the possibility to functionalize chemically different coatings. Precisely, one of the problem addressed in this work is enhancing the chemical resistance of microcapsules to distinct solvents. In chapter 4 the fabrication methods, the microcapsules characterization and the system functionality are thoroughly illustrated.

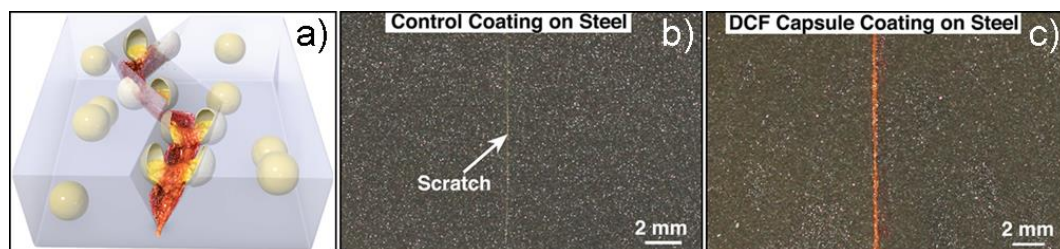


FIGURE 2.8 - A) SCHEMATIC REPRESENTATION OF A COATING EMBEDDING MICROCAPSULES WHICH RELEASE DCF VISUAL INDICATOR UPON MECHANICAL DAMAGE. THE CORE MATERIALS REACT WITH THE FREE AMINE OF THE COATING TO LOCALLY CHANGE COLOR. B) IMAGE OF A SCRATCHED CONTROL COATING SAMPLE. C) IMAGE OF THE EFFECTIVE DAMAGE VISUALIZATION IN THE SMART COATING¹⁷.

2.2 SELF-HEALING MATERIALS

In facing the problem of material ageing, the most common approach in material design consists in preventing the occurrence of degradation phenomena by improving the material intrinsic resistance. Apart from the damage early detection methods mentioned in the section 2.1.1, an innovative solution to extend materials duration is given by self-healing materials. A self-healing material has the built-in ability to activate repair mechanisms in opposition to mechanical damages occurring during its operational life.

The introduction of this innovative concept into polymers and polymer composites allows to obtain more sustainable, and safer materials for applications such as electronics, energy, transportation and coatings. The ability to self-heal is already present in many biological species and some artificial systems are directly inspired from them. Biological repair mechanisms are often long-lasting processes characterized by an immediate inflammatory response and by a slow proliferation of cells in the injured area. Synthetic systems, on the other hand, generally have a faster response because healing agents are either rapidly delivered to the damage area or even readily available. The chemical repair process may occur at a different timescale depending on the type of healing mechanism employed. Damages in polymers and composites can appear as a consequence of environmental conditions, fatigue, impacts or other unpredictable causes. A range of possible damage modes is presented in figure 2.9. Damages can be either superficial as impact cracking, scratches, cuts and ablation, or internal as delamination, crazing and microcracking. A self-healing material is designed according to the type of damage that is most likely to occur in a given application. The detrimental effect of the listed damages can be reduced or recovered either automatically or supported by energy, supplied in form of UV-light, heat, electromagnetic radiation and others. Such category is referred to as heteronomous healing systems opposed to the fully autonomous healing system. Nevertheless in most cases the amount of energy required to activate the healing mechanisms is moderate.

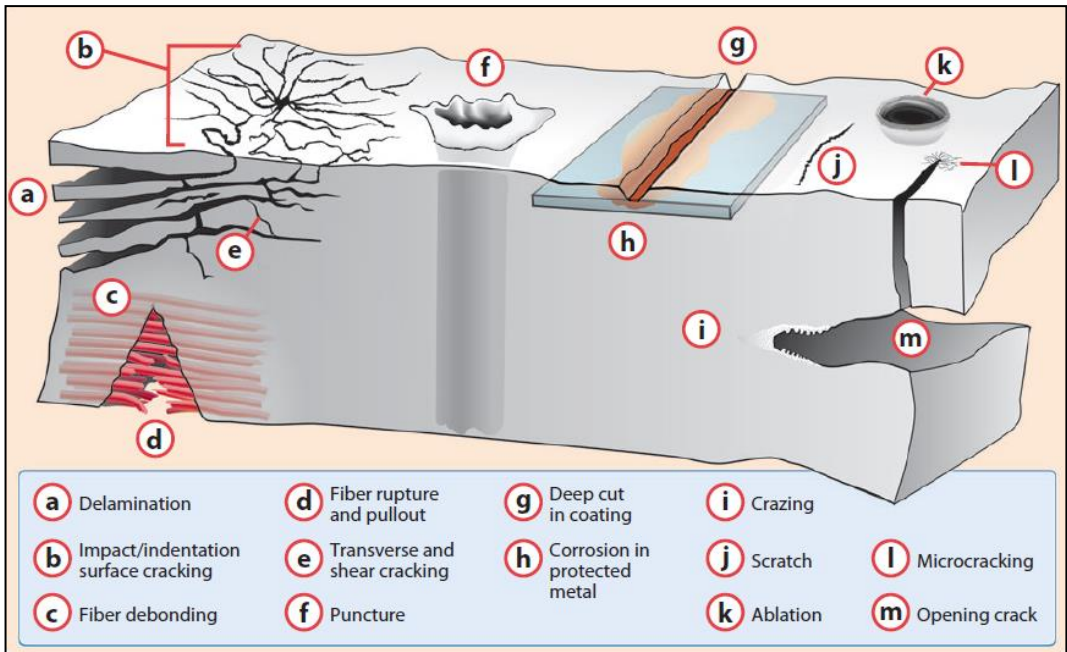


FIGURE 2.9 - OVERVIEW OF THE DAMAGE MODES OCCURRING IN POLYMER COMPOSITES¹⁶.

Heteronomous healing systems still represent a promising option because they might achieve the 100 % healing efficiency target more easily. Apart from the original mechanical strength, healing can concern many other functionalities such as hardness, adhesion, corrosion protection, brightness, hydrophobicity, wear resistance, reflectivity, electrical or thermal conductivity, ion selection, and liquid or gas barrier. Electrical self-healing properties are particularly appealing because, coupled with the mechanical healing, form the basis of the artificial skin. A flexible, pressure-sensitive composite with restorable conductivity has been reported using an healable polymeric matrix and nickel nanostructured microparticles¹⁸. This example demonstrates that natural skin self-healing capability can be mimicked with interesting implications in soft robotics and biomimetic prostheses. Another natural skin fashionable properties is multiple healing. In the ideal self-healing material an infinite number of healing events with no loss of initial properties would be possible. Some polymers with multiple healing ability have been synthesized but their initial mechanical characteristics are often below those required in practical applications. However, the field of self-healing polymer and composites is rapidly growing and a large number of mechanisms based on local polymerization, entanglements and reversible cross-linking have been reported. Among the many classification proposed the easiest one identifies two main types of self-healing materials: intrinsic and extrinsic. In intrinsic self-healing materials the reparation mechanism is associated to the their particular chemical formulation. They are often soft polymers in which the chemical bonds rearrangement upon breaking is either energetically favorable or induced by an external stimulus. Extrinsic self-healing materials base their function

on the presence of physical microscopic reservoirs, such as capsules or channels, delivering specific healing agents to the damaged zone. The healing agents are liquid monomers ready to fill the crack and polymerize, ideally restoring the material original characteristics. The effective polymerization, and thus the healing efficiency, sometimes depends on the presence of specific catalysts or hardeners. Figures 2.10a-c offer a schematic representation of these types of materials.

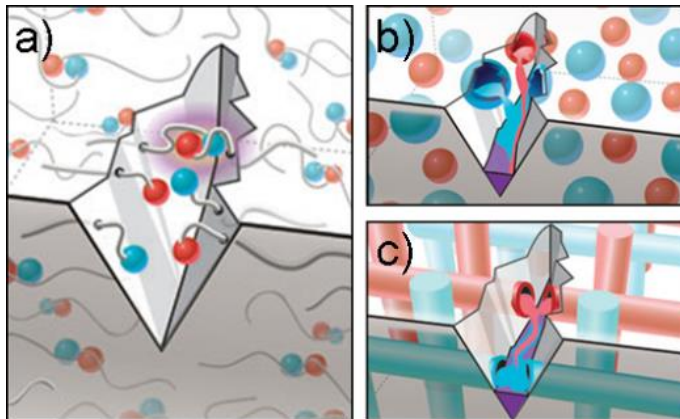


FIGURE 2.10 - SCHEMATIC REPRESENTATION OF MOST COMMON SELF-HEALING SYSTEMS. A) INTRINSIC MECHANISM B) BASED ON MICROCAPSULES. C) BASED ON MICROVASCULAR NETWORKS¹⁶.

In most intrinsic systems the damaged surfaces must be in close contact to efficiently heal themselves as the molecular mobility is limited. But they often offer ideal aesthetic recover of scratches or surface damages. In materials with embedded microcapsules, healing agents can fill small damage volumes due to their inherent limited capacity. Finally, vascular systems are the most suitable to heal larger fractures even though they have the opposite limitation because damages too small to intersect the vascular network cannot be healed^{19,20}. In sections 2.2.1 the diverse chemistries used for intrinsic self-healing materials are discussed whereas extrinsic ones are presented in section 2.2.2.

2.2.1 INTRINSIC SELF-HEALING MATERIALS

Macroscopic reparation in intrinsic self-healing materials results from the local molecular rearrangement induced by temporary mobility of the polymeric chains. Only specific molecular structures allows such inter-chain mobility spontaneously whereas in many examples this behaviour is triggered by temperature, UV-light or by the application of a static load. After the stimulus removal, the material regains its original physical strength. The healing process consists in the execution of three different functions: detecting the damage area, reorganizing the polymeric chains and keeping the polymer integrity during healing. The greatest advantages of

intrinsic healing compared to the extrinsic one is the possibility to perform in principle multiple healing cycle on the same exact damage spot. Extrinsic self-healing systems rely, in fact, on reservoirs which will inevitably run out of chemicals to deliver to damaged areas. In addition, in most cases they do not require additional ingredients such as a catalyst, monomers, or special surface treatment of the fractured interface. The existing intrinsic self-healing polymers can be divided into the following categories according to their main molecular principle: self-healing polymers based on reversible reactions, self-healing via molecular diffusion, supramolecular self-healing materials and ionomeric self-healing materials. Moreover, to improve the healing efficiency, intrinsic polymer systems combining more than one chemical healing principle have also been developed²¹.

Self-healing polymers based on reversible reactions

This category includes chemistries with reversible forming and breaking of covalent bonds. The healing action in response to damages is due to the rapid conformational changes related to the dynamic dissociation and re-association of stress-bearing bonds. The characteristics of the association, the overall flexibility of the molecule, its architecture and environmental conditions all play a role in the healing process. Current dynamic covalent systems comprise a wide range of well-known reaction types, the most remarkable being exchange reactions, heterocyclic compounds bonds reformation and reversible cycloaddition reactions²².

Self-healing polymers based on dynamic exchange reactions between reversible covalent bonds rely on modest activation temperatures. In this context, disulfide bonds are among the most versatile being relatively easy to implement in existing networks. They can undergo metathesis exchange reactions in which two neighboring S-S bonds are disrupted and reformed through free radical or ionic intermediates. The disulfide-promoted healing has been applied to different polymers: from conventional epoxy based thermosets to elastomers and hybrid sol-gel based coatings²³. Polyureas and urea-containing polymers, widely used materials in coating, fibre, adhesive and plastics industries, have also been enabled with self-healing ability exploiting dynamic covalent chemistry. The key factor consists in modifying urea nitrogen with bulky groups thus lowering the dissociation energy of urea C-N bond. The resulting amine/isocyanate reactive groups are reasonably stable under ambient conditions but also ready to react at the same time. The desired dynamic equilibrium between urea and the reactive groups, presented in figure 2.11a, is achieved. Polyurethane-ureas carrying hindered urea bonds have sub-ambient glass transition temperature and are able to self-repair after being cut under ambient conditions, as shown in figure 2.11b²⁴.

Self-healing in heterocyclic compounds, instead, depends not on only one type of bond reformation but on reconnecting multiple free radical intermediates. Self-repairable polyurethane networks were developed using chitosan and a four member heterocyclic compound, oxetanes, forming a heterogeneous crosslinked polyurethane network. Upon mechanical damage, the free radicals generated by chain cleavages, remain stable and can

recouple by exposure to UV radiation²⁵. Among reversible cycloaddition reactions, the Diels-Alder (DA) reaction is the best known and the most commonly used in intrinsic self-healing formulations. The DA reaction, a [4+2] cycloaddition between a diene and a dienophile typically bearing an alkenyl moiety, occurs through a concerted mechanism and is one of the most attractive members of the click chemistry family for polymer design and synthesis.

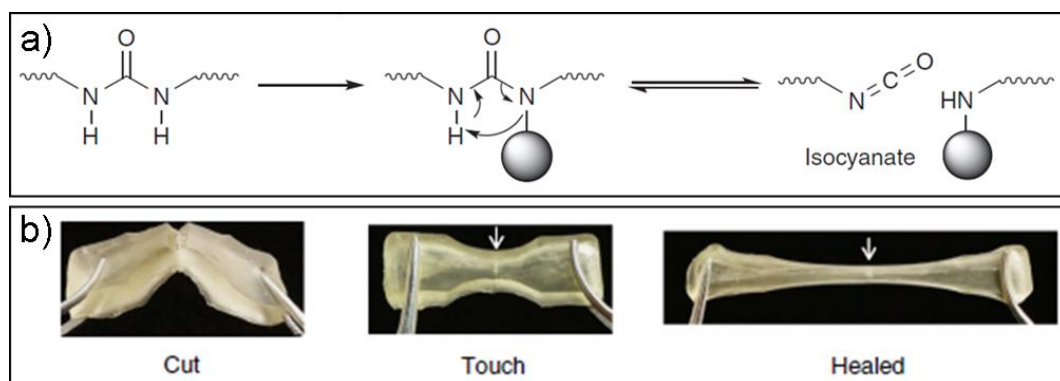


FIGURE 2.11 - A) UREA NITROGEN SUBSTITUTED WITH A BULKY GROUP DISSOCIATES TO ISOCYANATE, WHICH IS STABLE AT LOW TEMPERATURE BUT REACTIVE TO AMINE TO REFORM THE ORIGINAL BOND. B) PICTURES SHOWING THE SELF-REPAIRING ABILITY OF A POLY(URETHANE-UREA) BASED ON DYNAMIC COVALENT BONDS²⁴.

The product of the reaction, named DA adduct, is thermally unstable and could undergo a reverse reaction (retro-DA reaction) at certain temperatures to regenerate the diene and dienophile from which it was originated. The temperature ranges at which the retro-DA takes place depend on the actual diene/dienophile combination. In recent years research pushed towards the application of the Diels-Alder (DA) reaction in the synthesis of thermoreversible polymers incorporating furan (diene) and maleimide (dienophile) moieties²⁶. Figure 2.12a displays how the maleimide group and the furan group react forming the DA adduct. The choice of these particular systems depends on the fact that the furan/maleimide DA adduct displays a relatively low temperature of decoupling through the retro-DA reaction, therefore making them particularly suitable for self-healing materials. For the realization of thermally reversible crosslinked polymers at least one of the reacting groups of the DA reaction has to be attached to polymer chains. This introduces, however, the problem of polymer chains reduced mobility which can be detrimental for an effective healing. This obstacle has been bypassed using multi-functional small molecules as monomers for the construction of crosslinked polymers. Particularly, a macromolecular network formed entirely by thermally reversible DA adducts of furan and maleimide using precursors with 4 furan groups and 3 maleimide groups has been reported²⁷. At temperatures above 120 °C, some linkages disconnect allowing furan and maleimide moieties to have enough mobility to heal the cracks. Upon cooling, new DA bonds are

formed and the chains are crosslinked again. The healing phenomenon is commonly visualized by preparing a thin film of polymer, cutting it with a razor blade, and then heating the damaged film to promote a reverse DA reaction. In figure 2.12b the evolution of an incision during the healing process of a damaged polymer film carried at 120 °C as viewed through optical microscope is shown. After 2 hours of thermal treatment the incision virtually disappears²⁸.

In chapter 5 the synthesis of a Diels-Alder polymer based on furan and maleimide precursors is reported. Particularly, the introduction of a plasticizer into DA crosslinked materials was proposed as an effective solution for increasing the local molecular mobility of the polymeric network thus enabling the reformation of DA-adducts after the retro-DA reaction. The self-healing recovery was assessed in terms of mechanical and aesthetical properties for adhesive and coating applications.

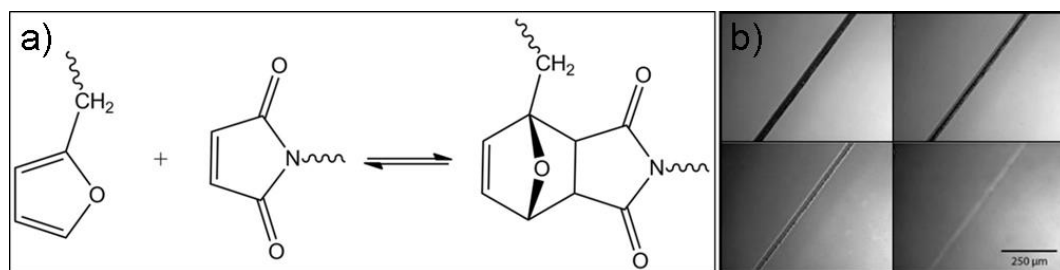


FIGURE 2.12 - A) REVERSIBLE CHEMICAL REACTION BETWEEN A MALEIMIDE GROUP AND A FURAN GROUP FORMING THE DA ADDUCT. B) MICROSCOPY OPTICAL IMAGES SHOWING THE HEALABLE EFFECT OF A THERMAL TREATMENT ON AN A DAMAGED DIELS-ALDER POLYMER COATING²⁸.

Self-healing via molecular diffusion

Self-healing can be promoted in some materials via molecular interdiffusion of polymeric chains occurring at temperatures above the bulk polymer glass transition temperature. This concept can be applied to materials showing at ambient temperature a physical behaviour at the boundary between solid and liquid. Crosslinking in rubbery polymers, for instance, can be carried out so that the structure displays numerous dangling chains, defined as the chain segments whose one end is not connected to the network. The permanent network allows for keeping the material shape whilst the dangling chains, at the transition from glassy state to liquid state, exhibit segmental interdiffusion to heal cracks²⁹. Polymer healing in thermoplastics takes place in a similar way given that, above the melting point, the intermolecular diffusion across the interfaces in intimate contact is highly favorable. A possible strategy to induce self-healing in thermoset materials consists in the incorporation of a thermoplastic additive. The resulting formulation would then be composed by the thermoset phase having superior stiffness and strength to perform the structural function, and a thermoplastic healing phase to repair occurring damages reinstating the mechanical integrity. The introduction of healing properties inevitably reduces part of the thermoset mechanical strength to an extent dependent on the degree of

interpenetration of the two phases. In literature this was obtained using a well-studied process to produce phase-separated polymer blends, the polymerization-induced phase separation. Poly(ϵ -caprolactone) and an epoxy resin were cured with 4,4'-diaminodiphenylsulfone generating a polymer with a unique morphology and surprisingly good thermal-mending performance due to the heating-induced flow and diffusion of the thermoplastic component³⁰.

Supramolecular self-healing materials

Supramolecular self-healing materials are polymers that use noncovalent, transient bonds to generate networks with dynamic behavior. The supramolecular interactions give stimuli-responsive properties to polymers making them ideal candidates for expressing the self-healing ability. Reversible hydrogen bond is the most frequently used chemical interaction in the design of such soft polymers. The general process of self-healing for these materials consists in the following steps. First, when the material is cut in two parts the weak supramolecular bonds are broken preferentially. After the rupture, the generated new interface contains a multitude of now unbound supramolecular bonds. Bringing the interfaces in contact again, the supramolecular bonding motifs can rearrange again eventually healing the crack³¹. The self-healing effect has been found to be higher when the polymer molecular weight decreases as this directly raises the supramolecular bond density and the polymer chain mobility at the expenses, however, of the overall mechanical properties³².

Hydrogen bonding and other relatively weak supramolecular interactions are also the basis of self-healing supramolecular hydrogels. The problem in formulating self-healing hydrogels is to control the difficultly tunable crosslinking force in the network. This can be overcome by introducing a mixture of relatively strong and relatively weak hydrogen bonds. For instance, the addition of polyethylene polyamine into an aqueous solution of oxidized carbon nanotubes generates relatively weak hydrogen bonds coming from intermolecular interactions of the polymer molecules, whereas relatively strong hydrogen bonds are due to the interactions between oxidized carbon nanotubes and the polyethylene polyamine molecules. Thanks to the coexistence of hydrogen bonds with different bonding strength, a hydrogel with multiple responsiveness, autonomous self-healing property and reversible adhesion behavior can be obtained³³.

Ionomeric self-healing materials

Another group of self-healing materials are the novel self-healing ionomeric copolymers. In general, organic ionomers comprise a fraction, no more than 15 mole percent, of ionized units covalently bonded to the polymer backbone as pendant group moieties. Due to their charged nature, the polar ionic groups tends to form ionic-rich domains thus separating from the non-polar backbone segment. Such peculiar morphology confers unique structural, mechanical and dynamic properties. The ionic network is thermally reversible as it can be deactivated at certain temperatures. In addition to conventional heat, UV and IR irradiations are other possible sources

of energy to induce the self-healing effect. Furthermore, by incorporating suitable antenna particles into the material, it is possible to generate heat at the damaged area only. For instance, an acrylate-based elastic ionomer has been functionalized with magnetic nanoparticles to exploit the energy dissipation induced by electromagnetic fields.



FIGURE 2.13 - ACRYLATE-BASED ELASTIC IONOMER SHOWING SELF-HEALING ABILITY AFTER A 30' THERMAL TREATMENT AT 70°C³⁴.

The irradiated regions were locally heated causing a rearrangement of the ionic structure. Pictures of such elastomeric material in its native form, after a cut and after thermal healing are shown in figure 2.13. The mechanical flexibility could be recovered likewise by the application of an oscillating electro-magnetic field for 15 minutes. This last option was found to promote a faster response. On the top of that it allowed a contactless and remote-controlled triggering of the sample properties with interesting implications in devices composed of different materials, including thermosensitive constituents³⁴.

2.2.2 EXTRINSIC SELF-HEALING MATERIALS

Extrinsic self-healing systems are based on the incorporation and delivery of proper healing agents at the liquid state to the damaged area. This concept can be compared to the healing mechanisms of natural systems such as animals and plants. They activate, to repair extended damages, a healing process consisting of two steps: first a liquid spreads out in the zone of interest, and then the same liquid becomes solid to repair the wound. In order to implement the same mechanism into a synthetic material, discrete entities, such as capsules and microchannels, need to be integrated to the designed material. This enhances the degree of complexity in material preparation. In fact, whilst intrinsic materials preparation is limited in most cases to a chemical synthesis, the realization of an extrinsic material relies either on capsules which need to be synthesized separately or on microchannels for which specific fabrication methods have been developed.

Microcapsules based self-healing materials

The first step for the realization of a microcapsules based self-healing material is the encapsulation of the reactive material, acting as healing agent. Microencapsulation is the process of enclosing a substance into a micron-sized polymeric shell, which isolates and protects it from the external environment. Microcapsules consist of two parts, the core material and the outer shell. Core material in self-healing application is often a reactive monomer able to polymerize upon interaction with the surrounding matrix or the environment. The shell wall is in most cases a crosslinked polymer with enough strength and chemical resistant to protect the capsule content from moderate shocks and solvents. The numerous available techniques for encapsulation are used in application fields such as food science, medicine, industry, and agriculture. There is a classification of these techniques according to the type of method used: chemical, physico-chemical and physico-mechanical. For self-healing materials, the most common encapsulation techniques are based on chemical methods, specifically in situ and interfacial polymerization. Physico-chemical and physico-mechanical methods include techniques such as coacervation, phase separation, rapid expansions of supercritical fluids, spray drying, congealing and solvent evaporation but have not been used to date for self-healing materials³⁵. In order to be suitable for self-healing applications, microcapsules need to satisfy certain conditions: first they need to contain sufficient amount of chemicals, secondly they need to exhibit good adhesion with the polymeric matrix so that the material mechanical properties are not compromised and finally they have to break readily upon damages. The first pioneering work on a microcapsules based self-healing material investigated some of these parameters. The chosen reaction for the healing mechanism was the ring-opening metathesis polymerization of dicyclopentadiene because this functional system displayed long shelf life, low monomer viscosity and volatility, rapid polymerization at ambient conditions, and low shrinkage upon polymerization.

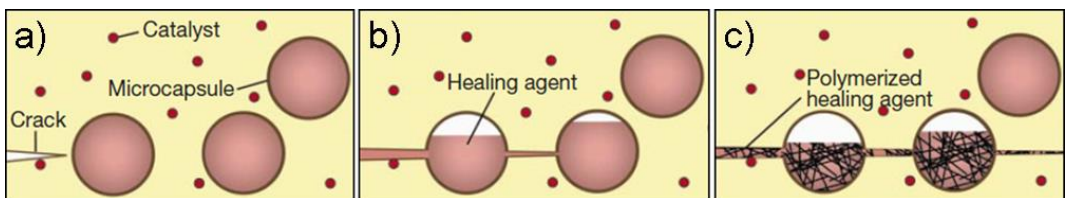


FIGURE 2.14 - A) CRACK FORMATION IN A POLYMERIC MATRIX WITH EMBEDDED MICROCAPSULES AND CATALYST. B) THE LIQUID HEALING AGENT FLOWS OUT FROM THE BROKEN MICROCAPSULES FILLING THE CRACK. C) HEALING AGENT POLYMERIZATION INDUCED BY THE DISPERSED CATALYST³⁶.

Polymerization of the healing agent needed, however, to be triggered by contact with an embedded catalyst, namely Grubbs catalysts, to bond the crack faces. In figure 2.14a-c a schematic representation of the crack formation, the liquid release and the catalyst induced polymerization is reported. The fracture experiments demonstrated a 75% recovery in

toughness³⁶. Microcapsules with the same chemical composition was also used to recover impact damages in composite materials. Their presence not only allowed to reduce the total crack length after self-healing but were found to not affect significantly the impact damage resistance³⁷. The outer shell used in these systems was a urea-formaldehyde polymer. In most self-healing materials the microcapsule polymeric shell is composed by urea-formaldehyde, melamine-formaldehyde, melamine-ureaformaldehyde, polyurethane, or acrylates originated from the reaction at the interface of droplets in an oil-in-water emulsion. Microcapsules with polyurethane shell, for instance, are prepared by reacting toluene diisocyanate prepolymer with 1,4-butanediol via interfacial polymerization carried out under vigorous agitation of a bladed propeller in an aqueous environment³⁸. The core material is hydrophobic and forms an oil-in-water-emulsion; the shell material monomers are hydrophilic and dissolved in the continuous aqueous phase. To obtain a stable emulsion, the reaction is often executed above room temperature carefully dosing the amount of surfactants and solvents in which the reactants are dissolved. Spherical microcapsules of 40-400 μm in diameter can be produced by keeping the agitation rate in the range 500-1500 rpm considering that increasing the agitation rate lead to microcapsules of smaller size. The shell wall thickness also varies with capsules diameter. During the synthesis, parameters such as microcapsules size and morphology, reaction yield and encapsulation efficiency are analyzed to optimize the process. Many factors including the solubility of the polymer in the organic solvent and that of the organic solvent in water, the rate of solvent removal, and the interaction between encapsulated agent and polymer were found to influence to encapsulation process³⁵. As already mentioned in section 2.1.1 in reference to the incorporation of microcapsules within polymeric matrices, their stability and integrity under different processing conditions is a relevant issue. Generally microcapsules for self-healing are fabricated using a wider range of chemicals compared to those used for damage sensing application because encapsulated agents for self-healing are required to perform an intrinsically more complex task. In fact, investigating the critical aspects associated with the synthesis of stable microcapsules, the nature of the core material has been found to strongly affects the microcapsule stability and performance. Obtaining at the end of the synthesis a free-flowing powder of robust microcapsules avoiding problems such as excessive agglomeration and formation of nano-particles is not easily achievable with every core molecules. For instance, encapsulation of viscous liquids such as bisphenol A or bisphenol F epoxidized resins was found to be difficult³⁹. Since epoxy monomers are widely used in composite materials their encapsulation is therefore highly desirable for self-healing. This problem was addressed by adding reactive diluents to decrease the viscosity of epoxy resins. In this way they could be successfully encapsulated and used as self-healing agent by keeping almost unaltered the mechanical properties of the cured product⁴⁰.

An alternative method to synthesize strong and stable microcapsules during their service lifetime consists in adopt a modified procedure that combines the interfacial polymerization and the in situ polymerization.

The final result is a double-wall microcapsule with improved thermal stability. Adding a commercial polyurethane prepolymer to the liquid core provokes the formation of the inner wall by interfacial polymerization in addition to the outer urea-formaldehyde layer. Such structure confers to the shell both higher thermal stability and higher compressive strength compared to single walled microcapsules⁴¹. In term of thermal properties recent interesting advancements have been proposed for processing healing system at elevated temperature. By encapsulating the highly active and chemically stable trifluoromethanesulfonic acid and an epoxy monomer in hollow silica, ultrafast re-bonding at room temperature without manual intervention was achieved. These microcapsules can resist high temperature processing conditions as those found in the fabrication of composites keeping unaltered the healing efficiency. Unfortunately the small amount of healing agent released limits, like in most microcapsule based system, the material self-healing ability to microcracks⁴². The relationship between microcapsule size, microcapsules weight fraction, and crack volume has been explored to be able to rationally design self-healing systems according to the specific type of damage. The optimization of the healing efficiency mainly depends on the quantity of healing agent delivered to the crack. It has been found that, unless the crack volume is larger than the available healing agent, self-healing of 3 μm cracks can be achieved with a microcapsules weight fraction as little as 1.25 % or with microcapsules having diameters inferior to 30 μm ⁴³. From this consideration emerges the possibility to also functionalize thin coatings and composites with high fiber volume fraction.

One of the most interesting application of microcapsule systems is coating protection. The production of intelligent protective coatings where defects arising in the course of service are removed automatically has been extensively studied⁴⁴. Various coating self-healing concepts exists: from mechanisms based on the incorporation of corrosion inhibitors to swelling of macromolecular compounds or the oxidation and passivation of the protected substrate. Compared to these methods, encapsulation have the major advantage of the controlled release of the capsules content and the widely adjustable self-repair properties. For instance microcapsules containing hexamethylene diisocyanate were incorporated into an epoxy coating covering a steel substrate. Hexamethylene diisocyanate was enclosed via an interfacial polymerization reaction of the more reactive methylene diphenyl diisocyanate prepolymer with 1,4-butanediol in the conventional oil-in-water emulsion. The coating system showed excellent protection under an accelerated corrosion process consisting in the immersion of the previously engraved specimens in 10 wt% NaCl solution for 48 hours. Figure 2.15 shows the test outcome for two different specimens: only in one of them the metallic substrate has the microcapsules embedded within the polymeric coating.

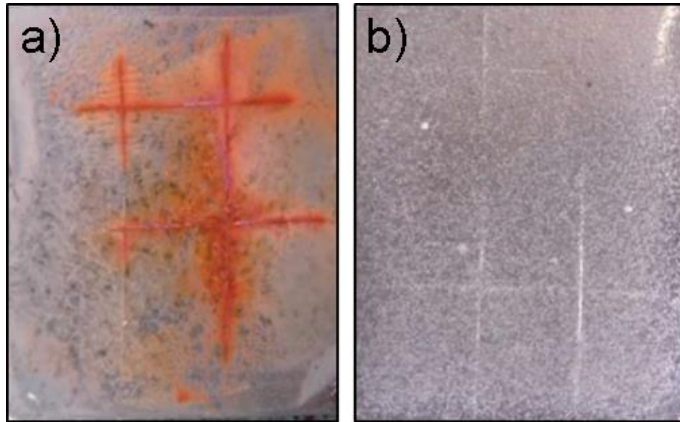


FIGURE 2.15 - A) ACCELERATED CORROSION TEST ON A DAMAGED EPOXY COATING COVERING A STEEL SUBSTRATE. B) THE SAME TEST CARRIED OUT ON A EPOXY COATING EQUIPPED WITH MICROCAPSULES⁴⁵.

The images demonstrate that in the control specimen (figure 2.15a) rust diffusing from the scratched region is clearly visible. The opposite occurred to the smart coating (figure 2.15b) where the encapsulated agent reacted with the surrounding water preventing the saline solution to corrode the metal thus revealing the great potential of this catalyst-free, one-part self-healing system⁴⁵.

Beyond mechanical recovery and corrosion protection, self-healing systems have also been developed to efficiently maintain, after cracking, the optical properties of a polymer film. To achieve a satisfying optical transparency, minimization of light scatter from the capsules in the polymer matrix and minimization of light scatter from the healed polymer are both required. An approach based on a plasticizer agent allowed for obtain such result together with a fair recover of the film barrier properties. Dibutylphthalate was encapsulated and dispersed in a polymethylmethacrylate matrix so that upon a damage event, it could fill the crack, locally plasticize and swell the thermoplastic polymer, enabling it to remend. If the refractive index of the healed part matches that of the polymer matrix it regains the original light transmission properties⁴⁶.

Finally the use of microcapsules for electronic application was reported. The lifetime of an electronic device is limited by disruption of electrical conductivity as a result of fracture or debonding. The investigation of methods for conductivity restoration of mechanically damaged electronic materials without external intervention is particularly appealing in this field. Using core-shell microcapsules it is possible to deliver encapsulated conductive materials to damage sites in an autonomic fashion. For instance, suspensions of polymer-stabilized carbon nanotubes and graphene flakes were enclosed into a urea-formaldehyde shell. This system provides autonomic restoration of conductivity in fractured gold lines paving way to their incorporation in integrated circuits⁴⁷.

Microvascular systems

Self-healing materials based on the presence of a microvascular system are designed taking inspiration from biological species provided with a network of microchannels. The cardiovascular system of a human being, for instance, consists of the heart, blood, and blood vessels (arteries, veins, and capillaries). The diverse number of functions executed by this system includes: transportation of blood, proteins, nutrients, O₂, CO₂, and other molecules, regenerating tissues, thermoregulation, immune response and wound healing. Both small and large vessels are needed in the vascular network to control the different levels of blood flow and pressure according to the location within the body. The complexity of this system is furtherly enhanced by the composition of the vascular tissue, in terms of cell types, that determines its permeability for passive and active transport across the vessel wall. The combination of these features makes such systems so much sophisticated that mimicking their functions in a synthetic materials is an extremely difficult task. The main obstacle to overcome consists in reproducing the metabolic capability of biological systems⁴⁸. Synthetic materials, at present, are not able to replace outdated components as living organisms do. However, recent advances in microfabrication technologies have led to the creation of synthetic system embedding microvascular networks that imitate many of the key responses of biological vascular systems. These systems differ from capsule-based materials with respect to fabrication and integration within a matrix material. The interactions between the matrix materials and the healing agents vary according to the fabrication method employed. Every manufacturing technique for the creation of microchannels in a composite structure has its own limitations in terms of network design. One of the most relevant parameters influenced by the manufacturing technique is the network connectivity. The channels can be discrete (1D connectivity) or interconnected (2D and 3D connectivity). If on one hand 1D connectivity offers some advantages in terms of manufacturing practicality, additional connectivity gives numerous performance advantages such as multiple connection points, reduced risk of channel blockages and a larger accessible reservoir for the healing agents. Refilling the network is also easier for networks with multiple connections between channels. Irrespective of the manufacturing technique used, the channel diameter, orientation, degree and location of branching are other fundamental parameters affecting the overall functionality and healing performance of a microchanneled structure.

Polymer composites can be vascularized with isolated or interconnected networks by either incorporating pre-fabricated channels or removing pre-loaded solid performs from the cured laminates. The most common 1D connectivity system employs hollow glass fibers as channels, filled with the appropriate healing agent. Hollow glass fibers can be easily integrated within polymer matrices using existing glass fiber drawing techniques. They have, in fact, no problem of compatibility with many standard polymer, and are inert to the most frequently used self-healing agents. Furthermore these fibers can be integrated into glass and carbon fiber plies for use in composites due to their similar size and shape.

Alternatively, the fabrication of higher-connectivity vascular networks is mostly based on additive manufacturing technologies such as direct-ink writing. In direct-ink writing, generically referred to as 3D printing in a less rigorous manner, a computer controlled fine nozzle moves and creates a three dimensional pattern by depositing a viscous ink in a controlled architecture. Through this method, a fugitive ink scaffold can be 3D printed and subsequently infiltrated with an uncured polymeric precursor. The scaffold is subsequently removed after solidification, leaving a hollow channel network embedded within the polymer matrix. This technique provides control over network shape and connectivity but requires an accurate choice of materials to use for the fugitive scaffold and the matrix. The importance of such approach resides in the fact that some of the crucial parameters influencing the healing response can be finely adjusted when designing the fugitive scaffold. Self-healing materials represent only one example of the possible applications interested by additive manufacturing technologies. An overview of the impact of additive manufacturing on the development of advanced and smart material is reported in section 2.3.2.

Below, a full list of the manufacturing strategies available for producing microvascular polymeric composites is proposed. Despite being designed for self-healing materials the following techniques can also be suitable for self-cooling, and damage sensing applications.

- Non-removable hollow cores

The basic principle behind non-removable hollow cores based techniques has been mentioned when referring to 1D connectivity systems. Basically, an array of straight, non-removable hollow tubes made of glass, metal or polymer is placed between the fabric layers during composite manufacturing. Upon curing, these embedded hollow tubes serve as microchannels for various applications.

- Removable solid cores/preforms

The procedure for creating microchannels by removable solid preforms resembles that of non-removable hollow cores. After positioning removable solid preforms that may be polymer or metallic between the dry fabric layers, some resin is infiltrated and cured thus obtaining a composite laminate. Finally, hollow channels are revealed by removing preforms from the cured laminate.

- Micromachining/laser processing

Opposed to additive manufacturing, subtracting manufacturing methods such as micromachining have conventionally been used to create vasculature in metals for cooling applications. Precision machining, computer numerical controlled machining, electric discharge machining (EDM) and laser machining are valuable techniques to create microchannels of few hundred microns. Unfortunately these manufacturing techniques, similarly to those based on non-removable or removable cores, restrict their usefulness to the creation of simple and straight microchannels within polymeric matrices.

- Electric discharge

In this process, a high level of electric charge is first implanted inside a dielectric polymer using electron beam irradiation. The accumulated energy is then discharged in a controlled manner to locally vaporize and fracture the material, leaving behind a network of branched microchannels arranged in a tree-like architecture with diameters ranging from 10 μm to 1 mm.

- Vaporization of sacrificial components

This technique consists in mechanically weaving a combination of glass or carbon fibers and catalyst impregnated polylactic acid sacrificial fibers. Microchannels are produced by first replacing a fiber tow with sacrificial fibers, and then infiltrating the structure with a low viscosity resin, like epoxy. After curing, sacrificial fibers are vaporized at 200 °C and removed from the composite structure by application of modest vacuum. The resulting composite structure contains, as a consequence, a three-dimensional interconnected microchannel network⁴⁹.

In terms of microchannel architecture, the main difference among the various techniques lies in the network connectivity. The techniques based on non-removable hollow cores, removable solid cores and laser processing allow to produce basic straight, unidirectional channels. On the other hand, direct-ink writing, electric discharge and vaporization of sacrificial components generate 2D and 3D multidirectional channels. Electric discharge and vaporization, however, allow to obtain more complex 3D structure than direct-ink writing. With electric discharge irregular branched tree like structures are produced while vaporization manufactured ordered, orthogonal structures. With almost all approaches channel sizes can be controlled within the interval 20 μm - 1.5 mm, except with non-removable metallic tubes which only produces channels larger than 1 mm in size. Finally, it is important to highlight that the presence of cavities (microchannels), resin-rich areas and absence of fibers cause a reduction of mechanical strength in the material, irrespective of the manufacturing strategy applied for the vascularization of the composite. The mechanical properties of microvascular systems can be fine-tuned by acting on the network wall stiffness, the network volume fraction, and channel distribution and uniformity.

The use of microvascular networks for autonomic healing of structural damage has been demonstrated in a coating–substrate architecture that mimics human skin. Figure 2.16a shows a schematic image of the outer epidermal layer of human skin and the underlying dermal layer supplying the epidermis with nutrient-laden blood. Just as a cut in the skin triggers blood flow from the capillary network in the dermal layer to the wound site rapidly forming a clot, so a vascular self-healing materials deliver the healing agent from the microchannel network to the damaged area through capillary action. Owing to the vascular nature of this coating-substrate system, minor damage to the same area can be healed repeatedly. An optical image of a self-healing structure after cracks are formed in a brittle epoxy coating is shown in figure 2.16b.

The self-healing process requires a suitable chemistry to heal cracks and microcracks efficiently. Although the microvascular approach opens up a broad range of potential monomers and compounds, healing of the coating was first demonstrated via ring-opening metathesis polymerization of dicyclopentadiene monomer by Grubbs' catalyst, which had already used

successfully in previous microencapsulated composites⁵⁰. The healing efficiency of these systems can be assessed by the recovery of coating fracture toughness in a four-point beam bending experiment⁵¹. The healing of a single crack achieved by systems provided with microvascular network is repeatable many times, a significant advantage over coating containing microencapsulated healing agents for which only one healing cycle is possible.

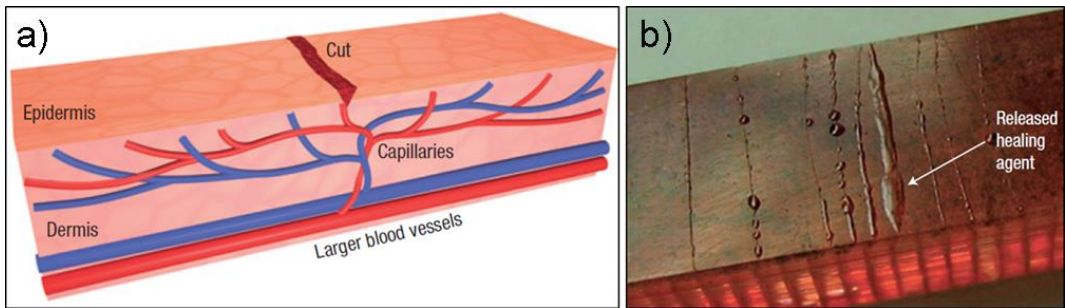


FIGURE 2.16 - A) SCHAMATIC DIAGRAM OF THE HUMAN SKIN WITH BLOOD VESSELS AND CAPILLARIES DELIVERING BLOOD TO HEAL A SUPERFICIAL CUT. B) OPTICAL IMAGE OF A SELF-HEALING COATING-SUBSTRATE SYSTEM AFTER RELEASE OF THE HEALING AGENT ALONG THE CRACK PLANE⁵⁰.

The number of healing cycles of a single crack achievable by microvascular materials depends on the chemistry used for the healing agents. Going beyond the dicyclopentadiene and Grubbs' catalyst option, epoxy and amine-based curing agents have demonstrated to be a valid alternative for this task. Given that they need to remain separated and stable in the vascular networks until crack formation occurs in the coating, two independent vascular networks have to be employed within the substrate to prevent unwanted reaction. Similarly to the mechanism described for the dicyclopentadiene, both healing components are transported by capillary forces into the crack plane, where they react and effectively repair the crack. The 16 intermittent healing cycles of a single crack reported in literature⁵² represent a remarkable achievement in term of material performance.

Vascular materials differ from capsule-based systems in another fundamental aspect: the healing agents are introduced after the network has been integrated into the matrix. This determines the chance to replenish the healing agent reservoir when needed, enabling repeated healing cycles. The properties determining the choice of healing agents are surface wettability, chemical reactivity, and viscosity. Too highly viscous liquids or chemically incompatible substances need to be avoided. The network design, especially the channel diameter, must take into account such properties as they affect the transport of the healing agents to the damaged zone and thus the healing performance.

2.3 ADDITIVE MANUFACTURING

In terms of material transformation, the production of an object can be realized in three possible ways: reshaping an existing part without reducing or adding material, subtracting materials from a bigger rough part using cutting tools or, finally, adding material to form the finished item. All the fabrication processes that consist in the addition of material go under the name of additive manufacturing. More precisely, additive manufacturing, also referred to as 3D printing by the general public, is the set of technologies that allow to fabricate finished products by deposition of material, generally in a layer by layer fashion. It represents the logic evolution of two-dimensional printing, because the object final three-dimensional shape results from the superimposition of virtually two-dimensional layers. In fact, early additive manufacturing processes descend from historical technologies such as photo-sculpture, topography and photolithography recording developed between mid-nineteenth and mid-twentieth century. It was only in 1986 that, thanks to the advancements in computing, lasers, and photopolymers, modern stereolithography (SLA) was patented opening the way to the current mass diffusion of additive manufacturing machines. Advances in digital technologies, the variety of processable materials, both polymeric and non-polymeric ones, and their reduced cost, allowed to the development of a wide range of additive manufacturing techniques. At the same time the interest of industry towards additive manufacturing, driven by its extremely diverse applications, has continuously grown. In this perspective additive manufacturing is seen as a technology with a revolutionary impact on traditional production models. If in the recent past it was thought to be limited to rapid prototyping application, now both small corporation and big companies are using additive manufacturing process to realize finished products. Its remarkable proliferation in industry is related to some crucial aspects that make it more advantageous compared to traditional fabrication systems. The distinctive characteristic of the additive processes is the possibility to create complex geometric shapes. Such feature gives an enormous flexibility in term of design and modeling. Techniques based on subtracting processes or casting and forming impose design constraints including difficulties in creating undercuts and internal cavities. In conventional productions, in facts, such features require assembly of multiple parts. Additive manufacturing, on the other hand, allows to build hollow objects in one process having the possibility to place the material exactly where it is needed, thus reaching the best trade-off between amount of material used and final product performances. The use of removable support material gives further freedom during the modeling operation. On the top of that, contorted shapes achievable with 3D printing do not require additional costs neither in term of designing neither in term of fabrication time. With technologies such as injection molding, instead, geometric complexity is generally proportional to the cost due to additional value of the mold; as a consequence only large scale productions justify the realization of a complex part. Even though additive manufacturing is not the ideal technology for mass production, the possibility to fabricate on

demand can lower significantly inventory costs and potentially reduce the expenses associated with supply chain and delivery. This aspect together with the very limited amount of wasted material when fabricating components considerably help to reduce the impact of additive manufacturing technologies on the environment. The combination of improved object designs, reduction of costs and decreased environmental impact explains the revolutionary effect that additive manufacturing is expected to bring to modern society⁵³. In fact, the significant amount of recent interest and investment towards additive manufacturing technologies have attracted individual consumers and academic laboratories which also contribute to spread the knowledge on product design and material properties in a sort of positive loop. The effect of such phenomena is the birth of several startup companies that are creating 3D printers with innovative hardware and software features, thus making complex shapes fabrication more and more accessible.

In terms of additive manufacturing fundamental attributes, the fabrication can be divided into the following steps: the conception of the model, the slicing operation and the actual printing process (possibly followed by post-processing operations). A schematic representation of the three fabrications steps is offered in figure 2.17. The process begins with a three-dimensional solid model, which is initially modeled or scanned as a digital computer-aided design (CAD) file. The preliminary object design phase is performed using a modeling software that generates three-dimensional shapes exploiting the construction of solids or surfaces. Once the virtual model is ready, it is converted in a different format, often the .stl format, compatible with the software that controls the machine. Such operation transform the original shape into a solid with a meshed surface. After that, the object can be reoriented in space to optimize the fabrication process, supporting parts are generated to prevent the structure collapse and finally the object is sliced.



FIGURE 2.17 - SCHEMATIC REPRESENTATION OF THE MAIN PHASES NEEDED TO FABRICATE AN OBJECT.

The slicing operation consists in the separation of the part in several slices. The slices are oriented horizontally to the machine printing bed. Their relative position determines the path followed by the machine. In fact the output of the slicing operation, is a file (.gcode) containing the machine path and all the relevant information needed to guide the moving parts for the fabrication of the object: printing speed, layer height, temperature, etc. Once the object is printed, the supports, if present, are removed. Supports generally have shapes and dimensions

that facilitate their removal. According to the type of 3D printer they can be in powder form and thus sucked away or they can be made of hydrosoluble material such as polyvinyl alcohol and simply dissolved. Since the object is the result of multiple layers overlapping, its lateral surface shows the so called staircase effect. The staircase effect is accentuated by the offset needed between two layers in order to create a slope. Such undesired effect is more or less noticeable depending on the layer height resolution and on the printing technology used. The higher the machine layer height resolution the smoother the surface of the printed object. Finishing operation such as sanding or polishing are sometimes executed to improve the aesthetical appearance of the object or to modify specific properties: adhesion, wettability, chemical resistance, hardness, etc. Post printing treatments also depends on the technique used. For instance, stereolithographic printers allows to fabricate parts using photopolymeric material which always need to be post cured to terminate the polymerization reaction. In section 2.3.1 the main additive manufacturing techniques are briefly illustrated.

2.3.1 3D PRINTING TECHNIQUES

Material extrusion

The most common 3D printing method based on extrusion is known as Fused Deposition Modeling (FDM). As shown in figure 2.18, it consists in the extrusion of a filament of thermoplastic material such as ABS or PLA onto a substrate at the correspondent melting temperature. Although the resulting prints are partially porous, this system is quite inexpensive, reliable and easy to use. These characteristics make FDM one of the most popular 3D printing technique. However, extrusion methods are not limited to polymeric material. Ceramic and metal pastes can also be extruded not necessarily at high temperature.

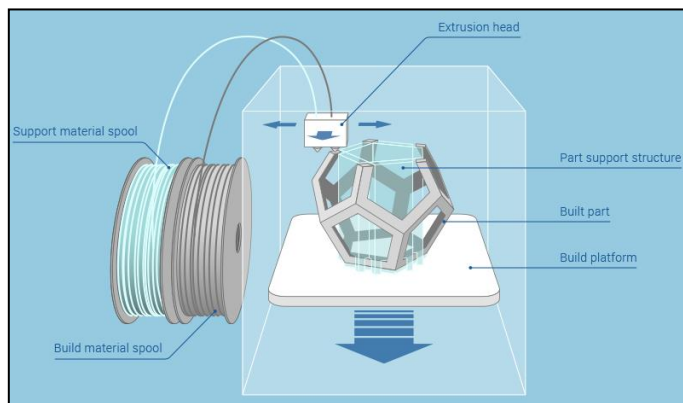


FIGURE 2.18 - SCHEMATIC REPRESENTATION OF THE MATERIAL EXTRUSION PROCESS.

Powder bed fusion

Powder bed fusion techniques use a source of energy (generally a laser or an electron beam) to locally melt or sinter powder particles. The process consists in the spreading of the powder material over previously scanned layers with either a rolling mechanism or a blade. A reservoir placed below or aside the bed powder provides new fresh material that is subsequently fused to the previous layer. A schematic representation of the full mechanism is reported in figure 2.19. Polymer powder bed fusion typically processes polyamides and polymer composites but the process can also be used to create ceramic and metal parts. Direct metal laser sintering (DMLS), Selective heat sintering (SHS), Selective laser melting (SLM) and Selective laser sintering (SLS) are the main type of 3D printing process based on powder bed fusion.

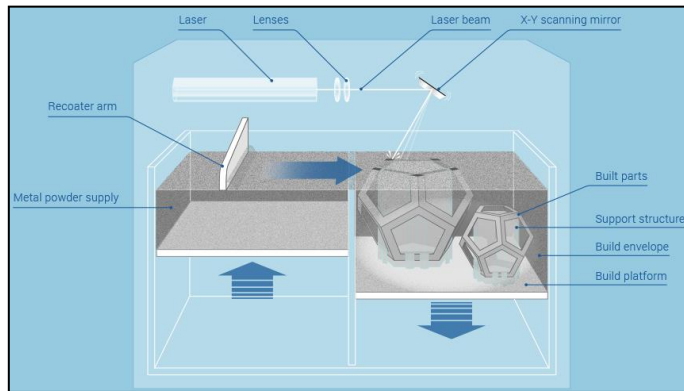


FIGURE 2.19 - SCHEMATIC REPRESENTATION OF THE POWDER BED FUSION PROCESS.

Vat photopolymerization

The 3D printing processes based on vat photopolymerization, the most known being the aforementioned stereolithographic method (SLA), use a vat of liquid resin to create a layer of solidified material. The model is fabricated layer by layer using a source of ultraviolet light to cure the resin at a specific location, whilst a platform moves the object downwards after each new layer is cured (see figure 2.20). Unlike powder based methods, there is no structural support from the material during the build phase and therefore support structures are often modeled with dedicated software. Considerably high printing speed and layer resolution can be achieved by regulating the UV power intensity according to the material absorbance. The downside of this technology, in term of material processability, is its intrinsic limitation to photopolymers. However, developing innovative formulation based on nanoparticles, materials with non-conventional functionalities have also been processed. Finishing treatments involving sealants, primers, paints or metallic coatings are also possible.

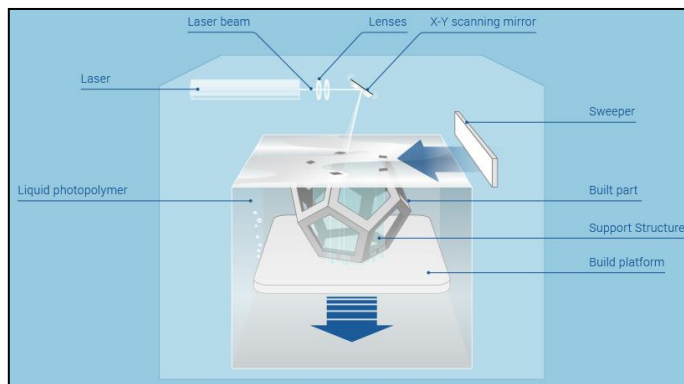


FIGURE 2.20 - SCHEMATIC REPRESENTATION OF THE VAT POLYMERIZATION PROCESS.

Material jetting

As the name suggests, the working principle of material jetting technology resembles that of a two dimensional ink jet printer. The material, often wax or photopolymer droplets, are flown from a reservoir to the printing head and then jetted onto a substrate using either a continuous or a drop on demand approach. Once deposited from the moving nozzle the material solidify via heating or photocuring allowing the object fabrication (figure 2.21). Polymers are the class of material most suitable for this process because they can easily be modified into printable inks. Researchers have developed numerous formulation, including suspensions of ceramics and metals in order to create final parts with added functionality.

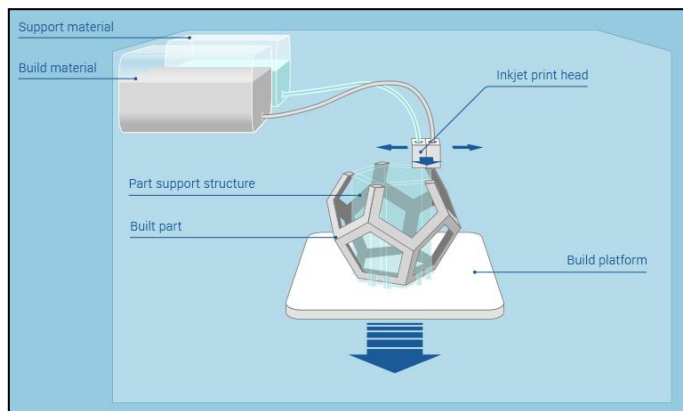


FIGURE 2.21 - SCHEMATIC REPRESENTATION OF THE MATERIAL JETTING PROCESS.

Binder jetting

Similarly to material jetting, the binder jetting process delivers in a controlled manner a liquid polymer from a reservoir onto a bed of powder. The liquid polymer is the binder that infiltrates the powder surface and unifies the overlapping layers. New fresh powder is provided after each layer has been completed, as in powder bed fusion techniques. Figure 2.22 offers a schematic representation of the process. The resulting object is mainly composed by the powder material and can require further liquid infiltration to improve its mechanical strength. Ceramic, metal and polymeric powders can all be 3D printed with this technique as long as they can efficiently be bound by the liquid binder.

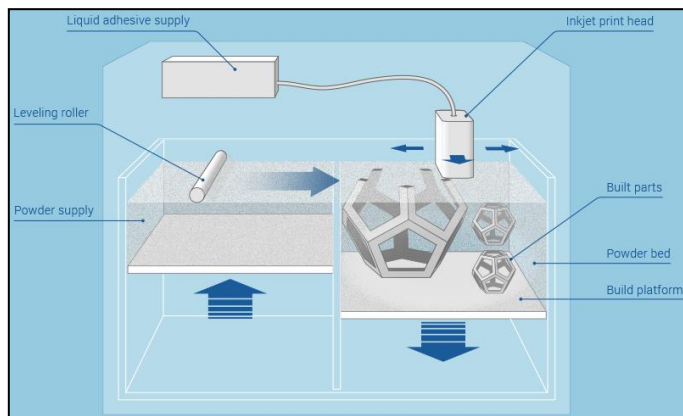


FIGURE 2.22 - SCHEMATIC REPRESENTATION OF THE BINDER JETTING PROCESS.

Sheet lamination

In the sheet lamination process, schematically represented in figure 2.23, the input material are thin sheets made of paper, metals or polymers. They are shaped and bound one over the other until the desired three-dimensional object is obtained.

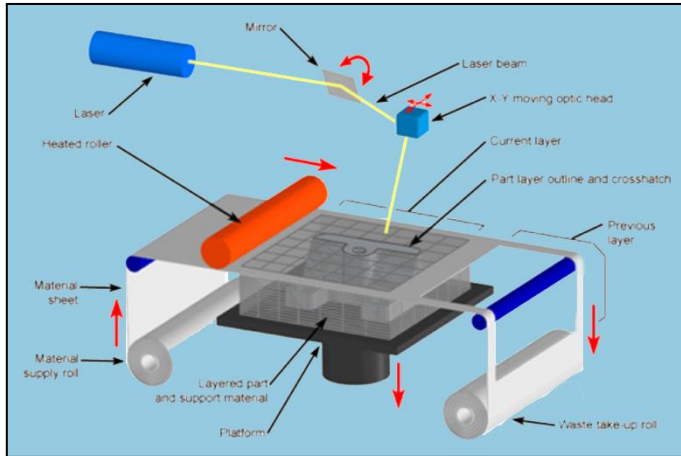


FIGURE 2.23 - SCHEMATIC REPRESENTATION OF THE SHEET LAMINATION PROCESS.

The first sheet is positioned onto the working platform where it is cut by a laser according to the model. After that, the printing platform is lowered by an amount equal to the sheets thickness so that a second sheet can be shaped and glued onto the previous one. Layers are bound together by a heated roller exploiting the double effect of pressure and temperature. Sheet lamination processes also include ultrasonic additive manufacturing, technology that uses ultrasonic welding to attach metal sheets. Sheet lamination is a process suitable for different materials and requires relatively little energy, as the metal is not melted.

Directed energy deposition

Direct energy deposition refers to a group of processes in which the material is directly deposited on the final location in the product. It does so by jetting the build material into the heated zone, created by a laser, electron beam or an ionized gas (see figure 2.24). Parts fabricated with this process can achieve up to 99.9% theoretical density of the material. Layers of material powder are supplied under vacuum during the process to avoid undesired reaction with the oxygen. The finished products have no residual stress and no need for post processing treatments. The most common metals used with this technique are steel, titanium alloys and aluminum alloys. Using directed energy deposition it is possible to change the product material easily, thus allowing for the graded functional materials.

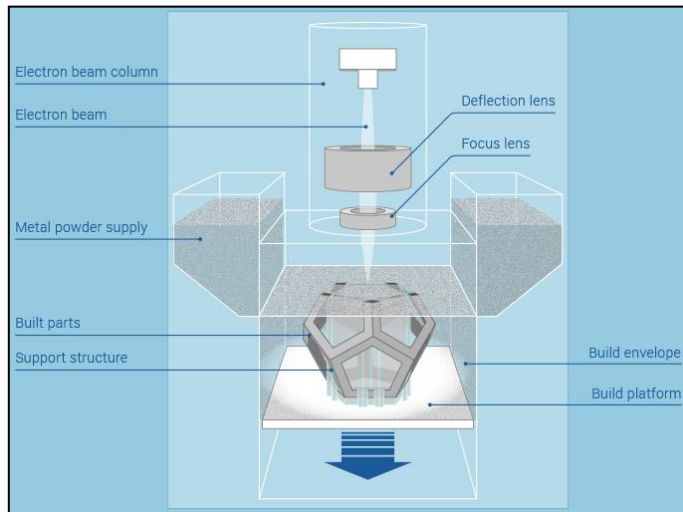


FIGURE 2.24 - SCHEMATIC REPRESENTATION OF THE DIRECT ENERGY DEPOSITION PROCESS.

2.3.2 CURRENT RESEARCH TRENDS AND APPLICATIONS

Academic and industrial researchers working with additive manufacturing technologies are focused on two main objectives: improving the existent technologies in terms of costs, process speed, printing resolution and developing innovative materials with added functionality for a broader applicability. Generally speaking, the build time for a large size model can take several hours especially if a good resolution is required, thus implying low values of layer thickness and printing speed. The only parameter that can speed up the process is the build orientation. Regardless of the printing processes, in fact, given the print speed and object size, to reduce the build time it is convenient to orient the object so that the its height is minimized. The additive manufacturing methods described in the previous section (section 2.3.1) are intrinsically slow because they rely on layer-by-layer printing processes. A recent development of the SLA process has been proposed to drastically reducing printing time without losing resolution. Such method, named continuous liquid interface production (CLIP), exploits the inhibition effect of the oxygen onto the radical polymerization of common photopolymers used in stereolithography⁵⁴. The process differs from traditional SLA because it is conducted above an oxygen-permeable build window that creates an oxygen-containing dead zone, a thin uncured liquid layer between the window and the cured part surface. Such layer, of approximately 20-30 μm , avoids attachment of the 3D part to the oxygen-permeable window, which is a thin, amorphous Teflon film with excellent optical clarity and gas transport potential. The photo-active resin viscosity and reactivity are crucial since the oxygen diffusion within the resin can easily be perturbed. The combination of rate of resin replenishment in this dead-zone, the initiation efficiency and the resin reactivity allows the process to advance in continuous rather than in a layer-by-layer fashion. In other words, in CLIP the UV exposure, resin renewal, and part movement are no longer conducted in separate and discrete steps as in traditional SLA, and therefore the vertical print speed can achieve values greater than 1000 mm/hour, easily exceeding the SLA limit of a few millimeters per hour. Furthermore the choice of the model layer thickness, which is related to the aforementioned staircase effect, does not influence print speed, as shown in the ramp test patterns in figure 2.25. Smooth 3D objects with no model slicing artifacts can be fabricated thanks to the continuity of the process.

The advances promoted by technologies such as CLIP helps to extend the utility of additive manufacturing to many areas of science and technology. Thus far the great potential of additive manufacturing was limited to rapid prototyping, a technique conceived as to allow engineers to rapidly convert virtual concepts from computer-aided design to physical models. Despite being still driven by the rapid production of prototypes the 3D printing market is living a transition towards full functional end-use parts. This fact is intimately related to the intense research on novel materials and applications for additive manufacturing. Such transition has already allowed many companies to switch from mass production to the manufacturing of short series of customized products with added value.

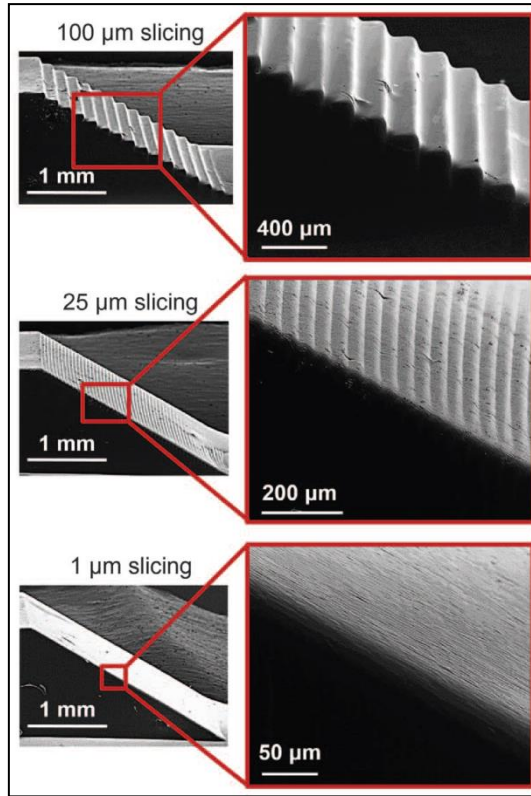


FIGURE 2.25 - RAMP TEST PATTERNS OF 100, 25, AND 1 MICRON PRODUCED AT THE SAME PRINT SPEED⁵⁴.

This phenomenon encompasses several application fields. Figure 2.26 shows the main sectors where additive manufacturing technologies are already a valuable recourse; interestingly the processes are highly scalable going from nanometric samples in bio-fabrication to large-scale productions in architecture and aerospace.

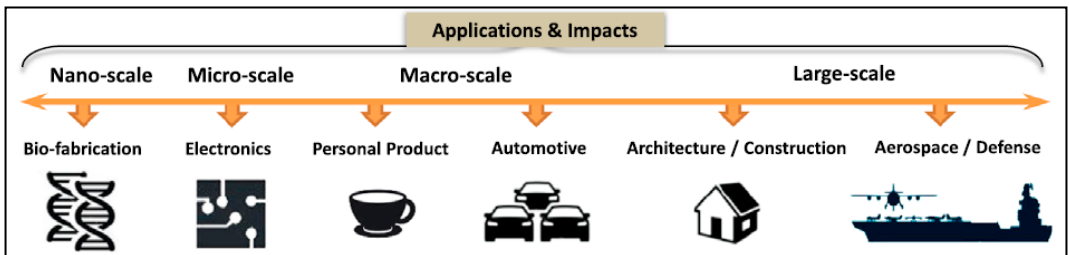


FIGURE 2.26 - APPLICATION FIELDS INTERESTED BY ADDITIVE MANUFACTURING⁵³.

The main reason why the aerospace industry has targeted additive manufacturing is to increase the strength-to-weight ratio of important components. The weight reduction is particularly beneficial because it has a great influence on fuel consumption. Furthermore conventional processes themselves are more wasteful, and thus more expensive, than additive manufacturing ones. The direct fabrication of structures with a controlled apparent density also reduces the use of raw materials. Comparing traditional manufacturing processes for aerospace and automotive parts with selective laser melting showed that the same part, redesigned for selective laser melting, had the same mechanical properties and 40% less material. In other words, the cost reduction combines both the lower price of raw materials needed and the lower energy consumption during products operational life⁵⁵. The development of large-scale additive manufacturing has not been limited to metals but has also interested, in the last decade, cementitious materials. Cement-based 3D printing aims at producing multifunctional structural elements with increased performance for construction and architecture. In developing a large-scale additive manufacturing technology the crucial requirement must be the optimization of the structural stability. For this reason the traditional layer-by-layer deposition is set aside in favor of the tangential continuity method, that exploits the geometrical potentialities of 3D printing technologies by overlapping layers of materials in a non-planar fashion.

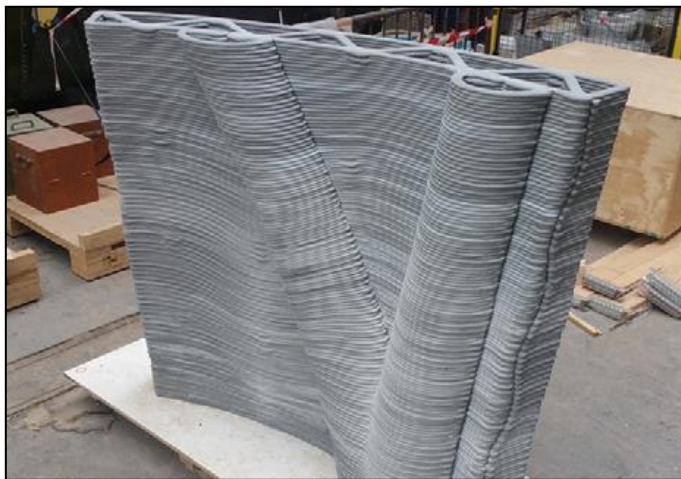


FIGURE 2.27 - 3D PRINTED HIGH-PERFORMANCE CONCRETE WALL (DIMENSIONS: 1360 MM × 1500 MM × 170 MM, WITH A WEIGHT CA. 450 KG)⁵⁶.

Through this method the parts are built by keeping contact surfaces constant between two layers, hence avoiding the geometrical gaps between two layers which are often a negligible problem in smaller scale processes, such as FDM and powder-bed-based processes. The obvious advantage of such strategy is that the layered structures obtained can be mechanically loaded in pure compression, perpendicularly to the layer interface plane. From a structural mechanics

viewpoint, the tangential continuity method yields more efficient and resistant constructions. Figure 2.27 presents one of the largest example of 3D printed concrete part ever produced⁵⁶. Such element could have hardly been produced using any other way, at least with any traditional or economically feasible processing route, hence emphasizing the interest of 3D printing for large-scale applications.

Shifting towards small-scale applications, biomedical engineering and electronics are two of the areas in which scientific research is currently more active. In biomedicine additive manufacturing has found widespread use as a tool to bioengineer different tissues⁵⁷. Since the main concerns when introducing a foreign element to the body are the degradation products of the material (bioresorption) and whether or not it will be rejected by the body (biocompatibility), research has been focused on the development of biocompatible materials that are resorbable. It has been possible to customize 3D printed scaffold for the regeneration of tissues with varying composition: from bone and teeth to vascular system and organs. A further area of health care that has been considerably impacted by 3D printing is that of surgical interventions. Starting from the three-dimensional information enclosed within MRI or CT scans, it is now possible to 3D print tangible models of the patient's anatomy. Being relatively easy to manufacture they offer to the surgeon a priceless advantage when planning the specific treatment to execute. Furthermore, having an exact replica of the anatomy allows for medical procedures to be simulated beforehand⁵⁸.

With the development of new materials with added functionalities, electronics devices also begun to benefit from 3D printing. Thus far inkjet printing has used conductive glues or paints to generate interface boards which have an intrinsically reduced versatility as the output of such technology is two-dimensional.

Opposed to this approach, 3D printing allows to create electronic components totally integrated within the macroscopic structural element. Interactive devices based on sensors, actuators, capacitors are illustrative examples of the potential that 3D printing can bring in term of innovative applications. In 3D printing the conductive character of the deposited material is very often due to the presence of nanoparticles within the matrix and the resulting composite is processed with extrusion-based methods. Although some conductive materials have been made available for the FDM technology, the predominant method for processing formulations based on nanocomposites has been direct ink writing. Extrusion-based direct-write technique, consists in the deposition of a continuous ink filaments flowing out from a moving nozzle according to the computer instructions. Being half-way between the material extrusion and the material jetting technologies, direct ink writing offers numerous benefits, such as the ease of use, reliability and cost-effectiveness. The possibility to process different classes of materials make it highly versatile and particularly suitable for microelectronics and microsystems⁵⁹. The competitive advantage of this technologies is that it can be combined with nanomaterials without the need for expensive accessories and tooling. If, on one hand, nanomaterials expand the multifunctionality of printed devices thus able to accomplish more complex tasks, their incorporation also affects the material

printability. Despite the many benefits offered by the union of nanotechnology and 3DP, in fact, challenges related to nanocomposite processing and reliability have to be addressed in order to exploit the full potential of 3DP in practical applications. For instance, the rheological properties of generic formulations often need to be adapted to the process by the addition of reactive diluents or particles that convert them into shear-thinning fluid. The extrusion-based 3DP technique may also encounter problems such as aggregation of the nanomaterials, the increase of viscosity after addition of the nanoparticles to the printing materials, and nozzle clogging. Therefore, proper mixing strategies, solidification methods and correspondent printing parameters need to be identified and optimized in order to achieve the desired process performance. Part of the work of this thesis is focused on the improvement of the current understanding of the various types of nanomaterials and nanocomposites and their processing. In chapters 6 to 8, 3DP of nanocomposite materials using extrusion-based direct-write techniques are deeply investigated with an emphasis on the printing capability and material requirements. Two different extrusion-based 3DP methods are discussed, both based on an increase of material rigidity straight after being flown out of the nozzle. Particularly chapter 6 shows a solvent-assisted 3DP method that have been used for the fabrication of nanocomposite microstructures for potential applications in microelectronics and sensors. The great advantages of the simple method proposed are the room-temperature processing and the low viscosity of the materials. The extruded material solidifies in seconds upon the fast evaporation of low-boiling-point solvent and retains its filamentary shape. In the effort to find proper printing techniques to build 3D engineered microstructures with freeform and supported features, chapter 7 deals with another emerging extrusion-based direct-write technique: UV assisted 3D printing (UV-3DP). The UV-3DP technique consists of the common computer-controlled print head depositing an ink filament under UV exposure. The ink material must, therefore, be an uncured viscous liquid photopolymer that crosslinks as soon as it is irradiated. A systematic study on the effect of nanofiller loading on the material printability and tensile mechanical properties of UV-3D printed nanocomposite materials is proposed. UV-3DP is also used in the fabrication of reinforced composites based on carbon fibers. In chapter 8 a system composed by a photocurable resin and a thermally reactive one to form a interpenetrated polymer network is presented. Such dual-cure formulation was characterized to investigate the potential of 3D printing in the production of high performance composite. In chapter 9, finally, the possibilities offered by additive manufacturing for the development of self-healing materials are explored. As already mentioned in section 2.2.2, substances generally used as support materials, such as wax or soluble polymers, can serve as sacrificial material for the fabrication of microvascular networks. 3D printing techniques such as direct ink writing and fused deposition modeling enable the construction of complex microstructures typically associated with microfluidic applications. For instance, direct ink writing of a fugitive organic ink was the strategy used in the fabrication of square-spiral towers to promote fluid mixing through chaotic advection⁶⁰. The control over fluid flow and mixing is a common problem in microfluidic devices. To ensure the complete mixing of two liquids with

laminar flow and diffusion being the dominant phenomena, long mono-dimensional path length would be required. An alternative solution consists in forcing the two liquids to flow within a three-dimensional non-linear path that causes stretching and folding of fluid interfaces. It has been proved that the geometric complexity of square-spiral towers give rise to dramatic improvements in mixing compared to mono-dimensional simple straight channels and bi-dimensional square-wave channels. Figures 2.28a-c show microfluidic device experiments through which the mixing effect of two differently colored (red and green) fluid streams were evaluated. Using fluorescent microscopy, the intensity of the resulting yellow fluid could be measured thus clearly indicating the superior mixing efficiency of the 3D square-spiral towers.

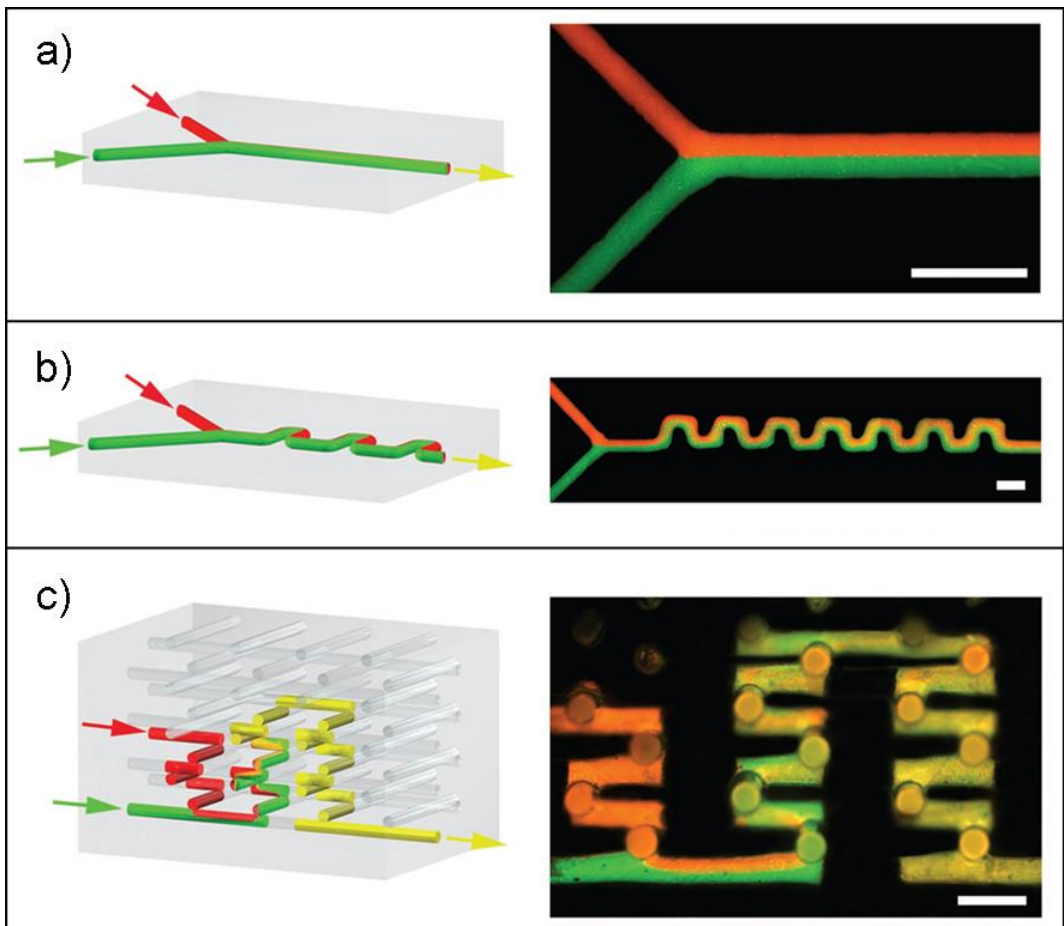


FIGURE 2.28 - SCHEMATIC REPRESENTATIONS AND FLUORESCENT MICROSCOPE IMAGES OF MICROFLUIDIC DEVICE MIXING EXPERIMENTS, WHERE TWO FLUIDS (RED AND GREEN) ARE MIXED TO PRODUCE THE YELLOW (MIXED) OUTPUT. A) 1D STRAIGHT MICROCHANNEL. B) 2D SQUARE-WAVE MICROCHANNELS. C) 3D SPIRAL TOWERS. ALL SCALE BARS = 0.5 MILLIMETERS⁶⁰.

The realization of such a valuable device is only possible if the scaffold structure is fabricated using 3D printing. The following step consists in the infiltration of the scaffold with an epoxy resin followed by curing and fugitive ink extraction. Finally the infiltration of a photocurable resin and its selective photopolymerization led to the patterned features. 3D structures of varying architecture can thus rapidly be transformed from computer-aided design to physical devices. The potential of this approach is not limited to microfluidics but can be beneficial for a wide array of potential technological applications including self-healing microvascular networks.

The last example of advanced material based on a peculiar additive manufacturing strategy bring us back to the opening section of this chapter (section 2.1), where the microstructures of some biological species were described. Having illustrated the working principles of additive processes, it is now possible to enlighten more clearly the manufacturing procedures to synthesize bioinspired materials that exhibit exceptional mechanical properties. Nature evolution through centuries originated materials with outstanding performances: devising what strategies nature employs and combining them with the necessary knowledge of additive manufacturing tools is the path followed by scientists to imitate biological materials as accurately as possible. Natural composites utilize reinforcing particles ingeniously organized into complex architectures as seen in the dactyl clubs of mantis shrimp. To develop these reinforcement architectures, biological systems rely on complex cellular and molecular processes. Such ordered, yet heterogeneous, reinforcement architectures has always been hardly replicable because of two main reasons: firstly, the diversity of reinforcement architectures in natural materials far exceeds the composite design currently available in synthetic materials and secondly, a full control over the local orientation of the stiff elements that comprise the reinforcement architecture is not easily achievable. Despite the complexity of natural manufacturing processes, this last obstacle is now finding unexpected solutions thanks to the extremely high level of sophistication reached by additive manufacturing techniques. An elegant approach consist in orienting anisotropic reinforcing particles during the printing of composites. This can be done through the application of a magnetic field that allows to control in real-time the microparticles disposition within the structure. This technology, termed as 3D magnetic printing, allows to recreate complex bioinspired reinforcement architectures that deliver enhanced material performance compared with monolithic structures⁶¹. 3D magnetic printing process incorporates additional steps to orient the reinforcing microparticles during the print.

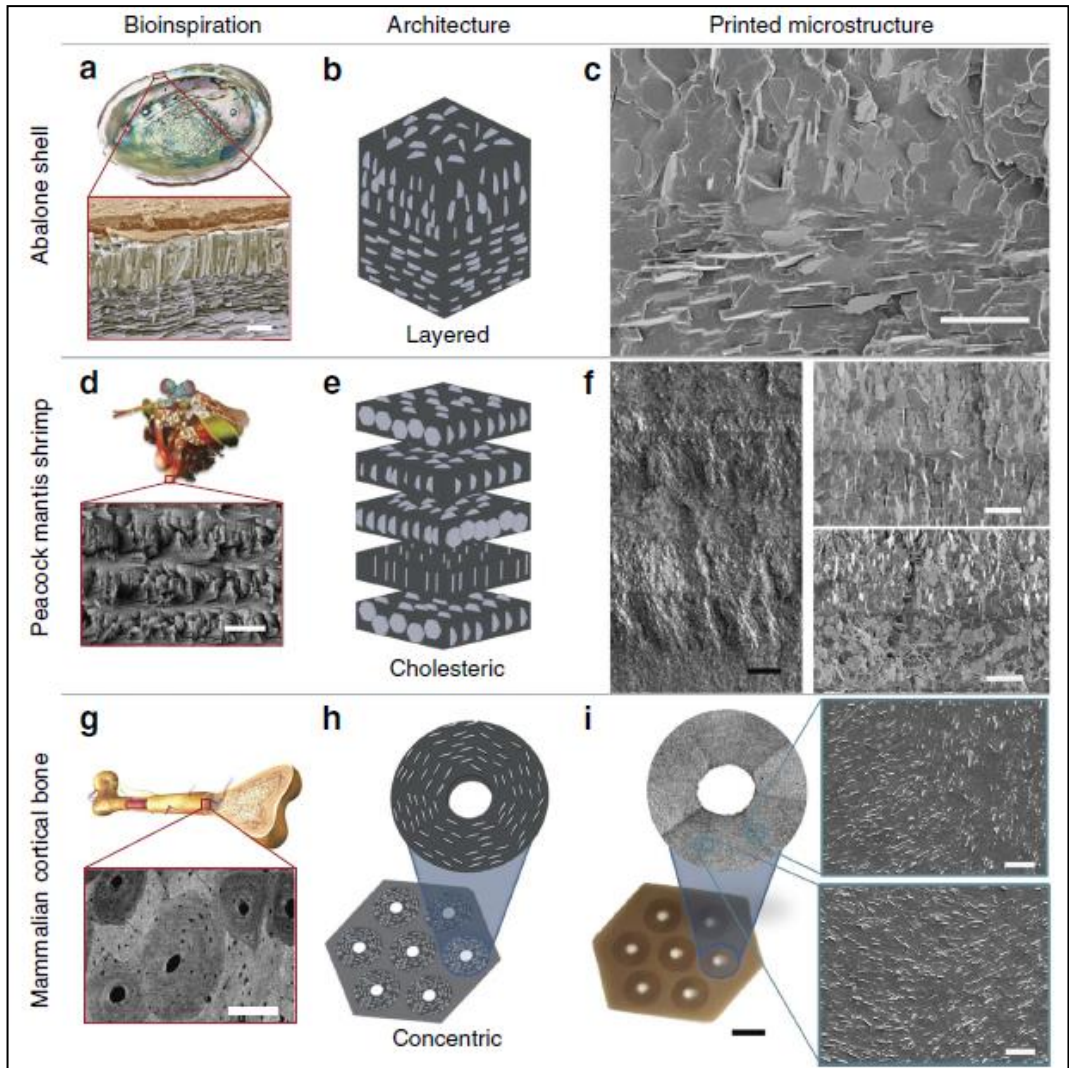


FIGURE 2.29 - BIOINSPIRED COMPOSITES WITH MICROSTRUCTURED ARCHITECTURES CAN BE RECREATED WITH 3D MAGNETIC PRINTING. (A) THE ABALONE SHELL EXHIBITS A LAYERED STRUCTURE OF CALCITE PRISMS TOPPING IN-PLANE ARAGONITE PLATELETS (NACRE). THIS ARCHITECTURE IS (B) SIMPLIFIED AND (C) 3D MAGNETIC PRINTED. (D) THE DACTYL CLUB OF THE PEACOCK MANTIS SHRIMP EXHIBITS A CHOLESTERIC ARCHITECTURE OF MINERALIZED CHITIN FIBRES. THIS ARCHITECTURE IS (E) SIMPLIFIED AND (F) 3D MAGNETIC PRINTED. (G) THE MAMMALIAN CORTICAL BONE EXHIBITS CONCENTRIC PLYWOOD STRUCTURES OF LAMELLAE-REINFORCED OSTEONS. THIS ARCHITECTURE IS (H) SIMPLIFIED AND (I) 3D MAGNETIC PRINTED. SCALE BAR, 5 MM IN A; 25 MM IN C; 15 MM IN D; 50 MM (BLACK) AND 20 MM (WHITE) IN F; 200 MM IN G; AND 5MM (BLACK) AND 25 MM (WHITE) IN I⁵⁷.

Figures 2.29a-i show some structures that demonstrate the capability of this technique to recreate reinforcement architectures exhibited by biological discontinuous fibre composite systems including the osteon structures within mammalian cortical bone, the layered nacreous shell of abalones and the cholesteric reinforced dactyl club of the peacock mantis shrimp. The impressive composite properties are a direct consequence of the specific orientation of the reinforcing elements. It is also possible to customize the discontinuous fibre orientation according to geometric patterns not necessarily found in nature. Thanks to its robustness and scalability, 3D magnetic printing represent the first step towards the realization of composite materials with added functionality. Further advances of novel assembly techniques will give rise to an entire new class of smart composite with tunable properties.

2.4 REFERENCES

1. Burrows, M. & Sutton, G. Interacting gears synchronize propulsive leg movements in a jumping insect. *Science* **341**, 1254–6 (2013).
2. Sanchez, C., Arribart, H. & Guille, M. M. G. Biomimetism and bioinspiration as tools for the design of innovative materials and systems. *Nat. Mater.* **4**, 277–288 (2005).
3. Zhao, N. *et al.* Bioinspired materials: From low to high dimensional structure. *Adv. Mater.* **26**, 6994–7017 (2014).
4. Wang, D., Jin, Y., Zhu, X. & Yan, D. Progress in Polymer Science Synthesis and applications of stimuli-responsive hyperbranched polymers. *Prog. Polym. Sci.* **64**, 114–153 (2017).
5. Wei, M., Gao, Y., Li, X. & Serpe, M. J. Stimuli-responsive polymers and their applications. *Polym. Chem.* 127–143 (2017). doi:10.1039/c6py01585a
6. Grunenfelder, L. K. *et al.* Bio-inspired impact-resistant composites. *Acta Biomater.* **10**, 3997–4008 (2014).
7. Kwak, M. K. *et al.* Towards the next level of bioinspired dry adhesives: New designs and applications. *Adv. Funct. Mater.* **21**, 3606–3616 (2011).
8. Chen, H. *et al.* Investigation on large-area fabrication of vivid shark skin with superior surface functions. *Appl. Surf. Sci.* **316**, 124–131 (2014).
9. Tokarev, I. *et al.* Stimuli-responsive hydrogel membranes coupled with biocatalytic processes. *ACS Appl. Mater. Interfaces* **1**, 532–536 (2009).
10. Vladimir, V. & Winnik, F. Emerging applications of stimuli-responsive polymer materials. *Nat. Mater.* **9**, 101–113 (2010).
11. Constantin, M., Bucatariu, S., Doroftei, F. & Fundueanu, G. Smart composite materials based on chitosan microspheres embedded in thermosensitive hydrogel for controlled delivery of drugs. *Carbohydr. Polym.* **157**, 493–502 (2017).
12. Aguilar, M. R., Elvira, C., Gallardo, A., Vázquez, B. & Román, J. S. Smart polymers and their applications as biomaterials. *J. Polym. Mater.* **23**, 225–248 (2006).
13. Roberts, D. R. T. & Holder, S. J. Mechanochromic systems for the detection of stress, strain and deformation in polymeric materials. *J. Mater. Chem.* **21**, 8256 (2011).
14. Ramachandran, D. & Urban, M. W. Sensing macromolecular rearrangements in polymer networks by stimuli-responsive crosslinkers. *J. Mater. Chem.* **21**, 8300 (2011).

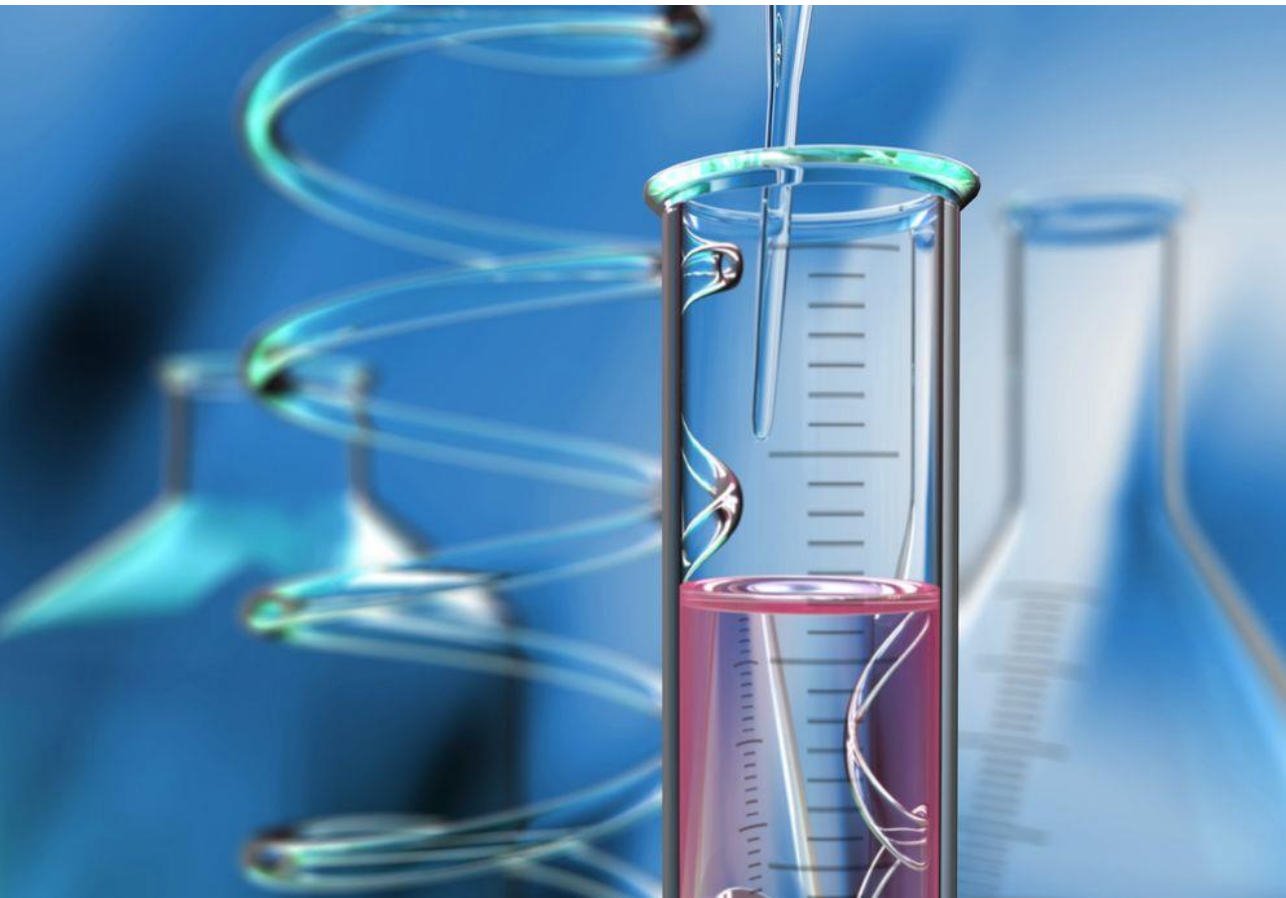
15. Vidinejevs, S., Aniskevich, A. N., Gregor, A., Sjoberg, M. & Alvarez, G. Smart polymeric coatings for damage visualization in substrate materials. *J. Intell. Mater. Syst. Struct.* **23**, 1371–1377 (2012).
16. Odom, S. a *et al.* Visual Indication of Mechanical Damage Using Core – Shell Microcapsules. *Appl. Mater. Interfaces* **3**, 4547–4551 (2011).
17. Li, W. *et al.* Autonomous Indication of Mechanical Damage in Polymeric Coatings. *Adv. Mater.* **28**, 2189–2194 (2016).
18. Tee, B. C.-K., Wang, C., Allen, R. & Bao, Z. An electrically and mechanically self-healing composite with pressure- and flexion-sensitive properties for electronic skin applications. *Nat. Nanotechnol.* **7**, 825–32 (2012).
19. White, S. R. *et al.* Self-healing polymers and composites. *Am. Sci.* **99**, 392–399 (2011).
20. Thakur, V. K. & Kessler, M. R. Self-healing polymer nanocomposite materials: A review. *Polymer (Guildf)*. **69**, 369–383 (2015).
21. Garcia, S. J. Effect of polymer architecture on the intrinsic self-healing character of polymers. *Eur. Polym. J.* **53**, 118–125 (2014).
22. Yang, Y., Ding, X. & Urban, M. W. Chemical and physical aspects of self-healing materials. *Prog. Polym. Sci.* **49–50**, 34–59 (2015).
23. Canadell, J., Goossens, H. & Klumperman, B. Self-healing materials based on disulfide links. *Macromolecules* **44**, 2536–2541 (2011).
24. Ying, H., Zhang, Y. & Cheng, J. Dynamic urea bond for the design of reversible and self-healing polymers. *Nat. Commun.* **5**, 3218 (2014).
25. Ghosh, B. & Urban, M. W. Self-Repairing Oxetane-Substituted Chitosan Polyurethane Networks. *Science* **323**, 1458–1460 (2009).
26. Gandini, A. The furan/maleimide Diels-Alder reaction: A versatile click-unclick tool in macromolecular synthesis. *Prog. Polym. Sci.* **38**, 1–29 (2013).
27. Chen, X. *et al.* A thermally re-mendable cross-linked polymeric material. *Science (80-.)*. **295**, 1698–1702 (2002).
28. Weizman, H., Nielsen, C., Weizman, O. S. & Nemat-Nasser, S. Synthesis of a self-healing polymer based on reversible Diels-Alder reaction: An advanced undergraduate laboratory at the interface of organic chemistry and materials science. *J. Chem. Educ.* **88**, 1137–1140 (2011).

29. Yamaguchi, M., Ono, S. & Okamoto, K. Interdiffusion of dangling chains in weak gel and its application to self-repairing material. *Mater. Sci. Eng. B Solid-State Mater. Adv. Technol.* **162**, 189–194 (2009).
30. Luo, X. *et al.* A thermoplastic/thermoset blend exhibiting thermal mending and reversible adhesion. *ACS Appl. Mater. Interfaces* **1**, 612–620 (2009).
31. Herbst, F., Döhler, D., Michael, P. & Binder, W. H. Self-healing polymers via supramolecular forces. *Macromol. Rapid Commun.* **34**, 203–220 (2013).
32. Kim, Y. J., Huh, P. H. & Kim, B. K. Synthesis of self-healing polyurethane urea-based supramolecular materials. *J. Polym. Sci. Part B Polym. Phys.* **53**, 468–474 (2015).
33. Du, R. *et al.* Hierarchical hydrogen bonds directed multi-functional carbon nanotube-based supramolecular hydrogels. *Small* **10**, 1387–1393 (2014).
34. Hohlbein, N., Shaaban, A. & Schmidt, A. M. Remote-controlled activation of self-healing behavior in magneto-responsive ionomeric composites. *Polym. (United Kingdom)* **69**, 301–309 (2015).
35. Venkata Naga Jyothi, N. *et al.* Microencapsulation techniques, factors influencing encapsulation efficiency. *J. Microencapsul.* **27**, 187–197 (2010).
36. White, S. R. *et al.* Autonomic healing of polymer composites. *Nature* **409**, 794–797 (2001).
37. Patel, A. J., Sottos, N. R., Wetzel, E. D. & White, S. R. Autonomic healing of low-velocity impact damage in fiber-reinforced composites. *Compos. Part A Appl. Sci. Manuf.* **41**, 360–368 (2010).
38. Yang, J. *et al.* Microencapsulation of Isocyanates for Self-Healing Polymers. *Microencapsulation of Isocyanates for Self-Healing Polymers.* **41**, 9650–9655 (2008).
39. Nesterova, T., Dam-Johansen, K. & Kiil, S. Synthesis of durable microcapsules for self-healing anticorrosive coatings: A comparison of selected methods. *Prog. Org. Coatings* **70**, 342–352 (2011).
40. Yuan, L., Gu, A. & Liang, G. Preparation and properties of poly(urea-formaldehyde) microcapsules filled with epoxy resins. *Mater. Chem. Phys.* **110**, 417–425 (2008).
41. Caruso, M. M. *et al.* Robust, double-walled microcapsules for self-healing polymeric materials. *ACS Appl. Mater. Interfaces* **2**, 1195–1199 (2010).
42. Ye, X. J. *et al.* Self-healing epoxy with ultrafast and heat-resistant healing system processable at elevated temperature. *Compos. Sci. Technol.* **104**, 40–46 (2014).

43. Rule, J. D., Sottos, N. R. & White, S. R. Effect of microcapsule size on the performance of self-healing polymers. *Polymer (Guildf)*. **48**, 3520–3529 (2007).
44. Stankiewicz, A., Szczygieł, I. & Szczygieł, B. Self-healing coatings in anti-corrosion applications. *J. Mater. Sci.* **48**, 8041–8051 (2013).
45. Huang, M. & Yang, J. Facile microencapsulation of HDI for self-healing anticorrosion coatings. *J. Mater. Chem.* **21**, 11123 (2011).
46. Jackson, A. C., Bartelt, J. A. & Braun, P. V. Transparent self-healing polymers based on encapsulated plasticizers in a thermoplastic matrix. *Adv. Funct. Mater.* **21**, 4705–4711 (2011).
47. Odom, S. A. *et al.* Autonomic restoration of electrical conductivity using polymer-stabilized carbon nanotube and graphene microcapsules. *Appl. Phys. Lett.* **101**, (2012).
48. Urban, M. W. The chemistry of self-healing. *Nat. Chem.* **4**, 80–82 (2012).
49. Saeed, M. U., Chen, Z. & Li, B. Manufacturing strategies for microvascular polymeric composites: A review. *Compos. Part A Appl. Sci. Manuf.* **78**, 327–340 (2015).
50. Toohey, K. S., Sottos, N. R., Lewis, J. A., Moore, J. S. & White, S. R. Self-healing materials with microvascular networks. *Nat. Mater.* **6**, 581–585 (2007).
51. Toohey, K. S., Sottos, N. R. & White, S. R. Characterization of microvascular-based self-healing coatings. *Exp. Mech.* **49**, 707–717 (2009).
52. Toohey, K. S., Hansen, C. J., Lewis, J. A., White, S. R. & Sottos, N. R. Delivery of two-part self-healing chemistry via microvascular networks. *Adv. Funct. Mater.* **19**, 1399–1405 (2009).
53. Gao, W. *et al.* The status, challenges, and future of additive manufacturing in engineering. *Comput. Des.* **69**, 65–89 (2015).
54. Tumbleston, J. R. *et al.* Continuous liquid interface production of 3D objects. *Science (80-.)*. **347**, 1349–1352 (2015).
55. Petrovic, V. *et al.* Additive layered manufacturing: sectors of industrial application shown through case studies. *Int. J. Prod. Res.* **49**, 1061–1079 (2011).
56. Gosselin, C. *et al.* Large-scale 3D printing of ultra-high performance concrete - a new processing route for architects and builders. *Mater. Des.* **100**, 102–109 (2016).
57. Bulysheva, A. A., Burcus, N. & Lundberg, C. 3D bioprinting of functional human skin : production and in vivo analysis. *Biofabrication* **9**, 15006 (2017).

58. Gross, B. C., Erkal, J. L., Lockwood, S. Y., Chen, C. & Spence, D. M. Evaluation of 3D printing and its potential impact on biotechnology and the chemical sciences. *Anal. Chem.* **86**, 3240–3253 (2014).
59. Farahani, R. D., Dubé, M. & Therriault, D. Three-Dimensional Printing of Multifunctional Nanocomposites: Manufacturing Techniques and Applications. *Adv. Mater.* (2016). doi:10.1002/adma.201506215
60. Therriault, D., White, S. R. & Lewis, J. A. Chaotic mixing in three-dimensional microvascular networks fabricated by direct-write assembly. *Nat. Mater.* **2**, 265–271 (2003).
61. Martin, J. J., Fiore, B. E. & Erb, R. M. Designing bioinspired composite reinforcement architectures via 3D magnetic printing. *Nat. Commun.* **6**, 8641 (2015).

3. Materials and experimental techniques



In this chapter a quick look at all materials and experimental techniques encountered in the following chapters is given in a schematic manner in order to provide a collection of crucial information accessible at any moment during the reading.

3.1 MATERIALS

In this section all raw materials used in this thesis, from monomers and initiators to solvents and powders, are listed. The acronym, the molecule, the function of each material and their physical state at ambient temperature are also reported. The materials are grouped according to the chapters (4 - 9) they are encountered. A more detailed description of the experimental activity is given in each chapter.

Chapter 4

The main experimental activity consisted in the synthesis of polymeric microcapsules of suitable composition and dimensions, containing a photochromic or a fluorescent dye. The materials used for the synthesis and characterizations are found in table 3.1.

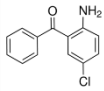
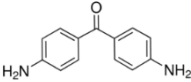
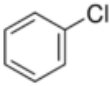
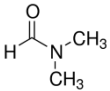
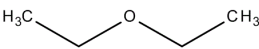
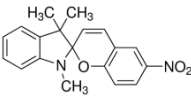

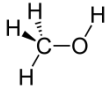
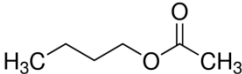
Material	Acronym	Molecule/Description	Use
Gum arabic	GA	-	surfactant agent, powder
2-amino-5-chlorobenzophenone	ACBP		synthesis reactant, powder
4,4'-Diaminobenzophenone	DABP		synthesis reactant, powder
Chlorobenzene	CB		reaction solvent, liquid
Dimethylformamide	DMF		reaction solvent, liquid
Petroleum ether	PE		washing solvent, liquid
1',3'-dihydro-1',3'-trimethyl-6-nitrospiro[2H-1-benzopyran-2,2'-(2H)-indole]	SP		photochromic dye, powder
1-Vinyl-Pyrene	VPy		fluorescent dye, powder
Sunflower oil	-	-	dye carrier
Desmodur L-75	-	aromatic polyisocyanate prepolymer	synthesis reactant, powder
N-Hexane	-	-	washing solvent, liquid
Fluorolink® P56	-	-	polymeric coating, liquid
Methanol	MeOH		dye extraction solvent, liquid
Butyl acetate	BuOAc		dye extraction solvent, liquid

TABLE 3.1 - LIST OF MATERIALS FOUND IN CHAPTER 4

Chapter 5

The main experimental activity of this chapter consisted in the synthesis of a self-healing polymer starting from epoxide precursors. The materials used for the synthesis are found in table 3.2.

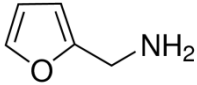
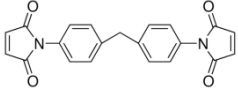
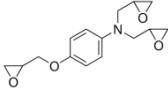
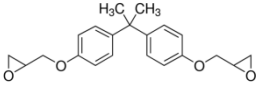
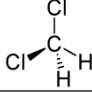
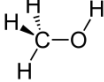
Material	Acronym	Molecule/Description	Use
Furfurylamine	FA		synthesis reactant, powder
1,1'-(methylenedi-4,1-phenylene)bismaleimide	2M		synthesis reactant, powder
N,N-diglycidyl-4-glycidyoxyaniline	DGGO		synthesis reactant, liquid
Bisphenol A diglycidyl ether	DGEBA		synthesis reactant, liquid
Dichloromethane	DCM		solvent, liquid
Methanol	MeOH		solvent, liquid

TABLE 3.2 - LIST OF MATERIALS FOUND IN CHAPTER 5

Chapter 6

The main experimental activity of this chapter consisted in the production of a conductive polymer with suitable processing and electrically conductive properties. Table 3.3 reports the list of materials used.

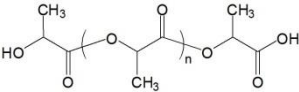
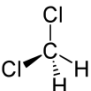
Material	Acronym	Molecule/Description	Use
Multiwall carbon nanotubes	MWCNTs	Nanocyl NC 3100 purity >95 % 9.5 nm average diameter 1.5 μ m average length	additive, powder
Poly(lactic acid)	PLA		polymer matrix, solid
Dichloromethane	DCM		solvent, liquid

TABLE 3.3 - LIST OF MATERIALS FOUND IN CHAPTER 6

Chapter 7

The main experimental activity of this chapter consisted in the production of photocurable formulations with different inorganic fillers. The materials used for their fabrication are found in table 3.4.

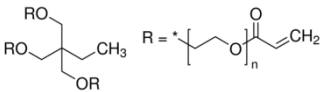
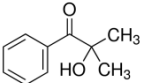
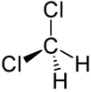
Material	Acronym	Molecule/Description	Use
Trimethylolpropane ethoxylate triacrylate	TMPETA		photopolymer matrix, Mn ≈ 560, liquid
2-hydroxy-2-methyl-1-phenyl-propan-1-one Darocur VR 1173	DAR		photoinitiator, liquid
Fumed silica AerosilVROX50	OX50	specific surface area 50 m ² /g, primary particle size distribution range 10-100 nm	additive, powder
Fumed silica	OX200	specific surface area 200 m ² /g, primary particle size distribution range 8-20 nm	additive, powder
Nanoclay Dellite VR 43B	D43B	6-8 μm characteristic length	additive, powder
Dichloromethane	DCM		solvent, liquid

TABLE 3.4 - LIST OF MATERIALS FOUND IN CHAPTER 7

Chapter 8

The main experimental activity of this chapter consisted in the production of an interpenetrated polymer network UV-3D printable loaded with carbon fibers. In table 3.5 the materials of chapter 8 are indicated.

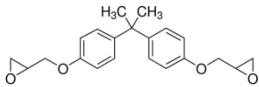
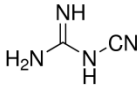
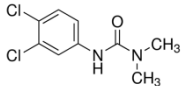
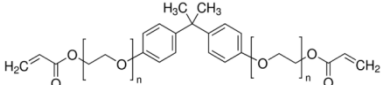
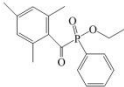
Material	Acronym	Molecule/Description	Use
Bisphenol A diglycidyl ether	DGEBA		polymer matrix, liquid
Dicyandiamide	DICY		hardener, powder
1,1-dimethyl, 3-(3', 4'-dichlorophenyl) urea	Diuron™		accelerator, powder
Bisphenol A ethoxylate diacrylate	SR349		photopolymer matrix, liquid
2,4,6-trimethylbenzoylphenyl phosphinate Irgacure TPO-L	TPO-L		photoinitiator, liquid
Fumed silica	OX200	specific surface area 200 m ² /g, primary particle size distribution range 8-20 nm	additive, powder
Carbon fibers	CF	99% carbon, density 1.8 g/mL, fiber diameter 7.2 μm, fiber length 100-150 mm	additive, powder

TABLE 3.5 - LIST OF MATERIALS FOUND IN CHAPTER 8

Chapter 9

The main experimental activity consisted in the production of a polymeric thermosetting samples with self-healing ability. The materials used for their fabrication are found in table 3.6.

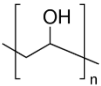
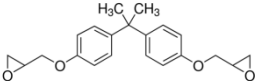
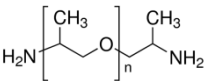
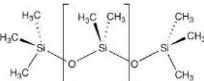
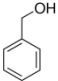
Material	Acronym	Molecule/Description	Use
Poly vinyl alcohol	PVA		3D printing filament, diameter 1.75, solid
Bisphenol A diglycidyl ether	DGEBA		polymer, liquid
Hexamethylene diamine	HMDA	$\text{H}_2\text{N}-\text{CH}_2-\text{CH}_2-\text{CH}_2-\text{CH}_2-\text{CH}_2-\text{CH}_2-\text{NH}_2$	hardener, solid
O,O'-bis(2-aminopropyl)polypropylene glycol	JD400		hardener, liquid
Polydimethylsiloxane Sylgard® 184	PDMS		polymer, liquid
Benzyl alcohol	BA		diluent, liquid

TABLE 3.6 - LIST OF MATERIALS FOUND IN CHAPTER 9

3.2 EXPERIMENTAL TECHNIQUES

Morphological characterization

In order to observe the structures of produced samples at the microscopic scale optical microscopy, scanning electron microscopy and computerized X-ray microtomography were used. Optical microscopy were employed to evaluate the microstructural features using an Olympus BX-60 reflected-light optical microscope with bright-field (BF) and dark-field (DF) imaging equipped with an Infinity 2 digital camera. A SZ-CTV Olympus stereoscopic microscope equipped with the same Infinity 2 digital camera was used to obtain images with lower magnification.

A Carl Zeiss EVO 50 Extended Pressure scanning electron microscope with an acceleration voltage of 15.00–17.50 kV was employed to perform more detailed analyses allowing the detection of nanoscopic features. Furthermore SEM analysis with energy-dispersive X-ray spectroscopy (EDS) on cryo-fractured samples was performed to evaluate the quality of filler dispersions.

Finally certain samples were analyzed with computerized X-ray microtomography. Samples internal structure could be reconstructed and analyzed using the Compact X-ray micro-CT SkyScan 1174v2 manufactured by Bruker microCT. The instrument relies on the use of high quality X-ray microfocus source operating at 20-50kV / 0-800 μ A, combined with high-resolution CCD-camera based on a 1.3 Megapixel CCD-sensor. The object manipulator rotated scanned samples to acquire angular shadow projections for tomographic reconstruction. After reconstruction, it was possible to display the sample cross sections on-screen and calculate the internal three-dimensional morphometric parameters based on binary segmentation of the given cross section images. Furthermore realistic 3D-images of scanned samples were constructed with the possibility to rotate the object model.

Infrared and ultraviolet spectroscopy

The absorption of chemical species within liquid or solid samples was performed via FTIR and UV-vis spectroscopic analyses. Fourier-transform infrared (FTIR) spectra of samples were collected using a Nicolet 760-FTIR spectrophotometer at room temperature in air in the 4000–400 cm^{-1} wavenumber range, with 64 accumulated scans and a resolution of 2 cm^{-1} . FTIR spectra were acquired in transmission mode on films cast on KBr disks (for liquid samples) or on solid pellets obtained by dispersing the sample in dry KBr powder (for solid samples).

UV-vis spectra were collected at room temperature in the 250-700 nm wavelength range, using an Evolution 600 UV-vis spectrophotometer (Thermo Scientific). A liquid cell of 1 cm path length with quartz windows was used.

Thermo-mechanical characterization

Differential scanning calorimetry (DSC), thermogravimetric analysis (TGA), dynamic mechanical analysis (DMA) and uniaxial tensile tests were the techniques used to explore the thermal and mechanical properties of the materials synthesized in this work.

Differential scanning calorimetry was carried out with a Mettler-Toledo TA3000 instrument, indium and n-hexane calibrated. The heating was performed in a N₂ environment at various temperatures intervals and rates (typically 10 °C/min or 20 °C/min) according to the type of sample analyzed.

The same instrument could be coupled to a fiber-guided UV light source generated by a medium-pressure mercury lamp (Lightningcure LC8, Hamamatsu) in the 300–450 nm wavelength range at an intensity of 15 mW/cm² to perform photocalorimetric measurements. Samples (5 mg, 500 mm thickness) were placed into an open aluminum crucible and exposed to such UV light at 25 °C under nitrogen flow (50 mL/min). This technique allowed to measure the heat of reaction of a photopolymer by integrating the resulting exotherms.

TGA were performed by means of a Q500 TGA system (TA Instruments) by testing the samples from 0 to 600 °C at a rate variable from 3 °C/min to 20 °C/min in nitrogen or in air.

DMA was conducted on a Mettler Toledo DMA/SDTA861 instrument in both shear mode and three-point bending mode at ambient temperature or in dynamic scans.

Uniaxial tensile tests were performed at room temperature on a Zwick-Roell Z010 with a 10 kN load cell and a longstroke extensometer following the American Society for Testing and Materials (ASTM) D638 standard. A constant crosshead rate (variable within the range 5 - 25 mm/min) was used. Tested samples had different dimensions and were either obtained by resin casting or by 3D-printing.

Other characterization techniques

Gloss measurements were made on 100 μm thick coatings deposited on a white cementitious substrate at a reflective angle of 60 °.

As ultrasonic treatments an ultrasonic bath (Starsonic 90) at room temperature and a Sonic & Materials VCX130 sonicator tip (frequency 20 kHz, power 130 W, oscillation amplitude 80 %) were employed to finely disperse fillers in suspension.

Electrical measurements were necessary to obtain the electrical conductivity of a polymeric matrix loaded with carbon nanotubes. The electrical conductivity of the nanocomposite films was measured using a four-point probe apparatus connected to a Keithley 2612 digital source-measure unit. A current scan between 0.01 and 0.1 A was applied on each sample with 50 steps and a settling time of 1 s for each measured step. The electrical conductivity of the nanocomposites was then calculated from resistance measurements.

Rheological measurements were performed using a Rheometrics DSR200 rheometer with a 25 mm plate-cone configuration at 25 °C. Steady shear tests on fluid dispersions were carried out for 3 min in the 0–4500 Pa range.

Post-printing treatments were sometimes necessary in order to fully polymerize the printed parts. Thermal curing cycles were carried out in a ventilated oven whilst photopolymers were UV treated under nitrogen using a bromograph (MF 1030, Nuova Delta Elettronica, Italy) with 4 UV-A tubes ($\lambda_{\text{emission}} = 350 \text{ nm}$) with a power of 15 W.

3D printers

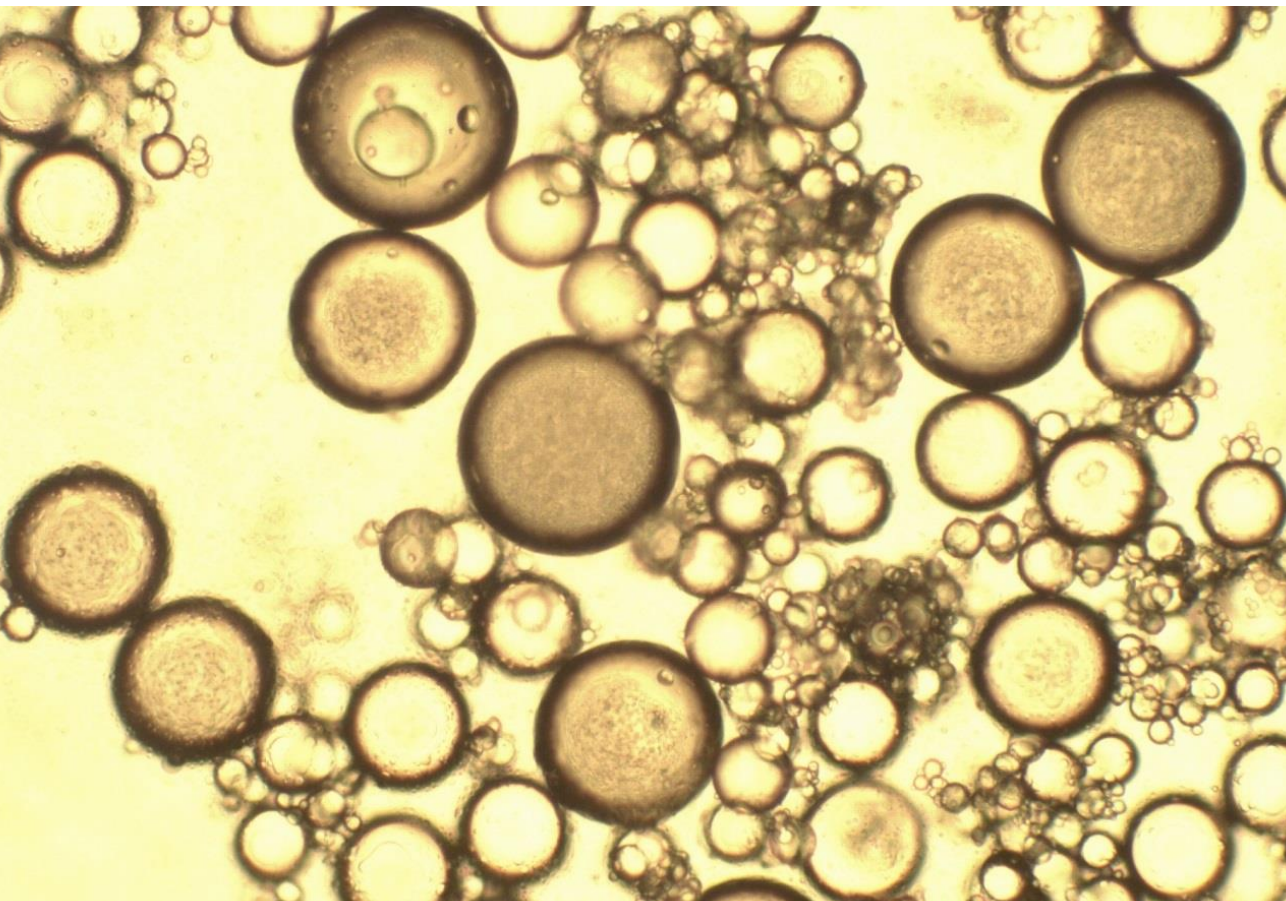
A low-cost home-assembled 3Drag 1.2 benchtop printer (Futura Elettronica, Italy) incorporating a syringe dispenser was used for 3D printing different polymeric formulations (chapters 6 - 8)

The machine was composed of a printing plate moving along the x and y axes and of an extrusion nozzle moving along the z axis. In the present PhD thesis standard thermally controllable extruder of the commercial version of such 3D printer was replaced by a syringe extruder for fluid deposition that was fabricated in house using a conventional FDM 3D printer (PowerWASP EVO 3D printer, Centro Sviluppo Progetti srl, Italy). Thanks to its particular design, such syringe slot may accommodate syringes with capacity ranging from 10 ml to 100 ml. When using liquid photopolymers the 3D printer was equipped with five low-power UV light emitting diodes (LEDs) with light emission peaked at 365 nm and a viewing angle of 20–25° (Aftertech SAS, Italy). LEDs were placed at about 30 mm distance from the extruding nozzle.

The pressure on the syringe piston was controlled by a computer-activated NEMA17 stepper motor. For the experiments described in this work, 10 ml INJ-LIGHT syringes were employed (from RAYS S.p.A., Italy) coupled with polypropylene nozzles supplied by E.O.I. Tecne srl, Italy. Print speed and nozzle diameter ranged between 0.1-30 mm/s and 0.2-1.5 mm, respectively. The printing apparatus was computer-controlled by means of *.Gcode* language, obtained from CAD-generated *.stl* files using a slicing open-source software (Cura, Ultimaker, from <http://software.ultimaker.com/>) or custom-made in the case of 3D models with dynamic variation along the z axis.

The other 3D printer used in this work to process PVA in form of filament was a Dual Extrusion Flashforge Dreamer produced by FlashforgeUSA.

4.
Fluorescent sensors based on
chemically-stable core/shell
microcapsules for visual microcrack
detection



Based on the manuscript submitted to: *Sensors & Actuators: B. Chemical*.

"Fluorescent sensors based on chemically-stable core/shell microcapsules for visual microcrack detection".

Authors: Giovanni Postiglione, Alessia Colombo, Claudia Dragonetti, Marinella Levi, Stefano Turri, Gianmarco Griffini.

4.1 INTRODUCTION

The lifetime of structural materials strongly depends on their mechanical integrity at the microscopic scale. For this reason, detection of microcrack-induced damages represents a key topic in a variety of engineering and industrial fields. At present, several nondestructive techniques are employed for sensing or probing the presence and propagation of microcracks in materials, including acoustic and ultrasonic methods, magnetic fields and radiographic testing¹⁻³. However, all these approaches often require the use of expensive instrumentation and they cannot be easily applied *in situ*. As opposed to these damage sensing techniques, visual inspection methods represent an alternative approach that is characterized by high versatility and ease of use also by non-specialized personnel⁴. Most visual inspection methods currently rely on the use of appropriately developed mechanochromic smart materials, which are able to convert a mechanical stimulus into a definite and measurable chromatic response that can be monitored non-invasively also at a distance from the material⁵⁻⁷. Among the several examples of mechanoresponsive polymeric materials appeared in the literature in the past decades⁸⁻¹⁰, those based on core/shell microcapsules are the nearest to commercialization as they can in principle be easily embedded into any type of coating formulation without significantly altering their functional properties¹¹⁻¹³.

Recently, crack detection by the use of microcapsules containing fluorescent dyes has been proposed as an effective strategy to inspect structural damages at the microscopic scale on a variety of engineering materials. In this context, one interesting approach made use of a fluorescent species (4,4'-diamino-2,2'-stilbenedisulfonic acid) microencapsulated in a melamine-urea-formaldehyde shell containing a healing agent (endo-dicyclopentadiene or 5-ethylidene-2-norbornene)¹⁴. The resulting multifunctional system was shown to be effective in both damage visualization and mending when dispersed in an epoxy resin serving as the carrier matrix. Very recently, polyurea-formaldehyde microcapsules containing a fluorescent fluid based on perylene and naphthalimide dyes have been also developed and tested as sensors for the detection of microcracks in cementitious materials¹⁵. While promising, these very preliminary approaches are still fundamentally limited by the transparency of the shell material to UV light, which determines that both broken and intact microcapsules (though with different emission intensities) are detected upon UV exposure. This behavior is clearly disadvantageous in terms of technological applicability of this system due to the relatively poor visibility contrast in the proximity of the localized crack. Therefore, these systems typically need to be combined with dark topcoats that prevent UV photons from penetrating the shell of intact microcapsules and exciting the encapsulated UV-sensitive fluorescent dye.

In addition to the optical properties of the shell, another key aspect for the successful incorporation of any type of core/shell microcapsule into coating materials is represented by the need of ensuring a sufficiently high chemical stability of the shell so as to prevent undesired release of the core material upon diffusion through the shell wall. Indeed, in several practical applications (e.g., solution-processing of polymer-based composites in the coating field) microcapsules are often exposed to harsh environments such as the presence of strong solvents (often combined with high processing temperatures). In particular, for damage sensing applications, the preparation and final use of microcapsules may entail their prolonged interaction with solvent media that typically act as diluting agents in several coating systems. In these circumstances, the shell wall can undergo partial chemical dissolution, and diffusion of the core material towards the dispersing medium can be significantly accelerated. This behavior causes a substantial loss of the functionality of the microcapsules prior to their actual use and results in a significant worsening of the damage visualization capabilities of the microcapsule-based composite system. Notwithstanding the importance of preserving the prolonged chemical integrity of microcapsules in such conditions, only a relatively small number of reports has tackled this fundamental technological issue¹⁶⁻¹⁹. In particular, these works have focused on the application of additional layers to the microcapsule outer shell in the form of extra-wall material¹⁶⁻¹⁷ or protective coating¹⁸⁻¹⁹, thus relying on the need of additional synthetic steps after microcapsule preparation to impart improved stability to the microcapsule system. On the contrary, the straightforward preparation of intrinsically robust microcapsules with superior chemical resistance to solvent attacks would be highly desirable, in view of their direct use as multifunctional damage sensing platform for coating applications.

In this work, core/shell microcapsule-based fluorescent probes are presented for potential use as early visual detection tool of damages in structural materials. Based on previous studies by our group²⁰, a new microcapsule system is developed here consisting of a UV-screening polyurea shell containing a fluorescent liquid core. The UV-screening functionality allows to prevent unwanted fluorescence emission from intact microcapsules upon UV-light exposure and yields excellent visibility contrast of the locally damaged region where fluorescent liquid core released from ruptured microcapsules is present. By carefully tuning the chemical composition of the shell material, significantly improved chemical stability of the newly prepared microcapsules can be achieved compared to previous systems, as demonstrated by their excellent solvent resistance over dwell time. A thorough chemical, thermal, morphological and optical characterization combined with a functional demonstration of the damage visualization capabilities of this new microcapsule based system highlights its potential as a highly chemically-stable damage sensor for smart coating applications.

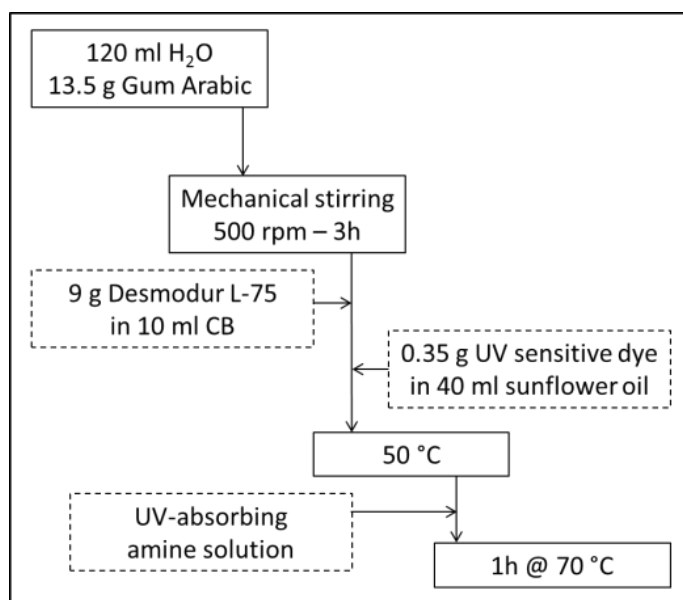
4.2 EXPERIMENTAL SECTION

4.2.1 MATERIALS

Gum arabic (GA), 2-amino-5-chlorobenzophenone (ACBP), 4,4'-Diaminobenzophenone (DABP), chlorobenzene (CB), dimethylformamide (DMF), petroleum ether, 1',3'-dihydro-1',3',3'-trimethyl-6-nitrospiro[2H-1-benzopyran-2,2'-(2H)-indole] (SP) and all reagents and solvents for the synthesis of the fluorescent dye were all purchased from Sigma–Aldrich (Italy) and used without further purification. Sunflower oil was kindly provided by Benasedo S.p.A. (Italy), Desmodur L-75 (aromatic polyisocyanate prepolymer) by Bayer Materials Science (Germany) and Fluorolink® P56 was obtained from Solvay Specialty Polymers (Italy).

4.2.2 SYNTHESIS OF THE UV-SCREENING MICROCAPSULES

The synthetic procedure used in this work to produce UV-screening polyurea-based microcapsules, partly based on a previous work carried out in our group¹¹, is reported in scheme 4.1.



SCHEME 4.1 - SYNTHETIC PROCEDURE FOR THE PRODUCTION OF UV-SCREENING POLYUREA-BASED MICROCAPSULES

Briefly, 120 mL of deionized water and 13.5 g of GA were mixed in a flanged glass reactor equipped with a jacketed external thermal recirculation system and allowed to mechanically stir

at 500 rpm for 3 h. During this time, the shell and core precursor solutions were prepared. To investigate the effect of shell composition on the chemical stability of the synthesized microcapsules, two different shell types were examined, namely ACBP-based and DABP-based microcapsules. To this end, 1.52 g of DABP (3.53 g of ACBP) were dissolved in 5 mL of DMF (15 mL of CB) under magnetic stirring. Similarly, Desmodur L-75 (9.0 g) was dissolved into 10 mL of dry CB and maintained in a nitrogen atmosphere to avoid moisture uptake. For the preparation of the core precursor solutions, the chosen chromophore was added to sunflower oil (0.35 g/40 mL) and magnetically stirred until a homogeneous mixture was achieved. The previously prepared Desmodur L-75 and core material solutions were gently poured into the stirring GA solution, and the mixture was heated up to 50 °C. Successively, the amine solution (ACBP or DABP) was slowly added to the stirring emulsion, the temperature was raised to 70 °C and the reaction was allowed to proceed for 1 h. After completion, the emulsion was cooled down to ambient temperature and the microcapsule suspension was separated from the mother liquor and left to settle overnight. Finally, the recovered microcapsules were washed repeatedly with deionized water and then with n-hexane before being vacuum-dried for 24 h prior to use. The average yield was ~70 wt %.

4.2.3 SYNTHESIS OF THE FLUORESCENT DYE (VPY)

1-Vinyl-Pyrene (VPy) was synthesized by standard Wittig reaction between the commercially available 1-Pyrene-carboxaldehyde and methyltriphenylphosphonium iodide (this salt was prepared as reported in literature²¹). In a 100 mL round bottom flask, methyltriphenylphosphonium iodide (1.23 g, 3.06 mmol) was dissolved in 15 mL of dry THF (tetrahydrofuran) then the mixture was cooled to 0 °C and potassium t-butyl oxide (0.43 g, 3.80 mmol) was added; the mixture was stirred for 30 min at this temperature. Then, 1-Pyrenecarboxaldehyde (0.59 g, 2.55 mmol) was added and the mixture was stirred at room temperature for 4 h. The mixture was quenched with water and then extracted with ethylacetate. The organic layer was dried on Na₂SO₄ and the solvent was removed at reduced pressure. The crude product was purified by flash chromatography on silica gel eluting with hexane/dichloromethane 4:1. A yellow solid was obtained in 70% yield. ¹H NMR (400 MHz, CDCl₃): δ (ppm) 8.41 (d, J = 9.3 Hz, 1H), 8.26–8.16 (m, 5H), 8.13 (d, J = 9.3 Hz, 1H), 8.034–8.00 (m, 2H), 7.82 (dd, J₁ = 10.99 Hz, J₂ = 17.31 Hz, 1H), 6.02 (d, J = 17.31 Hz, 1H), 5.64 (d, J = 10.99 Hz, 1H).

4.2.4 CHARACTERIZATION OF MICROCAPSULES

Optical microscopy (Olympus BX-60 reflected-light optical microscope equipped with an Infinity 2 digital camera) was used to investigate the morphology and the surface features and to determine the average diameter of the synthesized microcapsules, the latter obtained from datasets of at least 300 measurements. To evaluate the internal and external morphology of the synthesized microcapsules and to measure the shell wall thickness, scanning electron microscopy

(SEM) was employed (Carl Zeiss EVO 50 Extended Pressure, with an accelerating voltage of 15.00–17.50 kV). Fourier-transform infrared (FTIR) spectra of the microcapsules and their components were collected using a Nicolet 760-FTIR spectrophotometer at room temperature in air in the 4000–400 cm^{-1} wavenumber range, with 64 accumulated scans and a resolution of 2 cm^{-1} . FTIR spectra were acquired in transmission mode on films cast on KBr disks (for liquid samples) or on solid pellets obtained by dispersing the sample in dry KBr powder (for solid samples). Thermogravimetric analysis (TGA) on the microcapsules was performed by means of a Q50 TGA system (TA Instruments) by testing the samples from 0 to 600 °C at a rate of 20 °C/min in air.

4.2.5 DETERMINATION OF THE CORE FRACTION OF MICROCAPSULES

A given amount of synthesized microcapsules was thoroughly crushed with a pestle in a mortar and subsequently transferred to a glass container filled with petroleum ether. After resting for 24 h at room temperature, the mixture was carefully filtered on filter paper and the container was completely rinsed with additional petroleum ether to collect all the residual solid material. Upon complete evaporation of the solvent (petroleum ether), the final mass of the extracted core material (i.e., sunflower oil) could be measured and the microcapsule core fraction X_c could be calculated as $X_c = m_c/m_i$, with m_c and m_i being the final mass of the extracted core and the initial mass of microcapsules, respectively. It was concluded that the type of amine used in the synthesis (ACBP vs. DABP) did not affect the final core weight fraction which was found to be 70% for all microcapsule types.

4.2.6 CHEMICAL RESISTANCE OF MICROCAPSULES

The chemical resistance of the synthesized polyurea microcapsules was evaluated by prolonged immersion in different solvents, namely methanol (MeOH) and butyl acetate (BuOAc). 1.5 mg of microcapsules (ACBP-based and DABP-based systems, separately) were immersed in 10 mL of solvent, then the UV-vis spectra of the solvent medium were recorded at fixed time intervals up to 60 min. For ease of visualization, the model SP-chromophore was used as the encapsulated dye, because of its favorable optical properties. In figure 4.1 the UV-vis spectrum of SP-chromophore is illustrated, in comparison with those of ACBP and DABP. In particular, two distinct peaks can be observed in the UV-vis spectrum of SP at 266 nm and 345 nm.

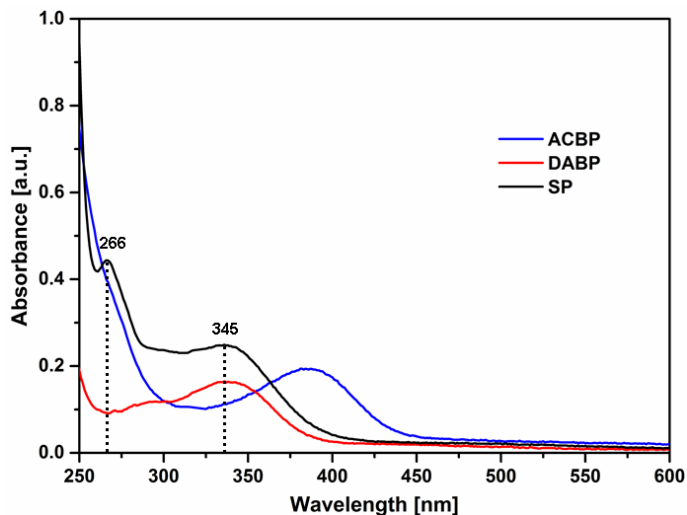


FIGURE 4.1 - UV-VIS ABSORPTION SPECTRA OF ACBP- AND DABP-BASED POLYUREA FILMS AND OF SP-DYE

In this study, the peak at 266 nm was used for monitoring the core release rate upon solvent extraction, as this peak can be directly related to the absorbance of the spiropyran species. Following what reported in the section 4.2.4, the core weight fraction was assumed to be 70% for all samples. This value gives an indication of the maximum amount of core material that can be released from the microcapsules upon immersion in the solvent. By knowing the amount of encapsulated core material, the theoretical maximum concentration of chromophore in the selected solvent could be evaluated, corresponding to its complete leakage from the microcapsules into the solvent. To this end, a 1 wt.% SP dye solution in sunflower oil (the same concentration of SP-dye in oil used for microcapsules synthesis) was prepared and dissolved in the selected solvents so as to obtain a reference solution characterized by a final concentration of dye in solvent equal to the maximum theoretical concentration achievable in case of complete core release from the microcapsules under test. As a result, the relative amount of chromophore released from the microcapsules at a given time could be evaluated based on the relative absorbance value of the solvent medium at increasing microcapsule immersion times. UV-vis spectra were collected at room temperature in the 250-700 nm wavelength range, using an Evolution 600 UV-vis spectrophotometer (Thermo Scientific). A liquid cell of 1 cm path length with quartz windows was used.

4.2.7 PREPARATION OF THE CRACK DETECTION COATING SYSTEM CONTAINING MICROCAPSULES

For crack detection experiments, a polyurethane-based coating formulation (Fluorolink P56) was used as the carrier matrix to prepare the microcapsule-containing smart coating system. DABP (ACBP) microcapsules filled with VPy were poured into a beaker containing the polyurethane formulation and magnetically stirred until a homogenous dispersion was obtained (microcapsule concentration was 20 wt.% with respect to the dry polyurethane). The liquid formulation was cast onto a carbon fiber reinforced polymer substrate and allowed to dry in air. The thickness of the resulting coating was approximately 200 μm .

4.3 RESULTS AND DISCUSSION

4.3.1 SYNTHESIS AND CHARACTERIZATION OF MICROCAPSULES

The synthetic procedure used to prepare the new UV-screening microcapsules containing fluorescent core is schematically depicted in figure 4.2. The microencapsulation process took place in an oil-in-water emulsion where the liquid core (sunflower oil containing the fluorescent molecule) was encapsulated within a polyurea-based shell resulting from the interfacial reaction between a polyisocyanate prepolymer (Desmodur L-75) based on toluene-diisocyanate (TDI) and a benzophenone-based diamine (DABP).

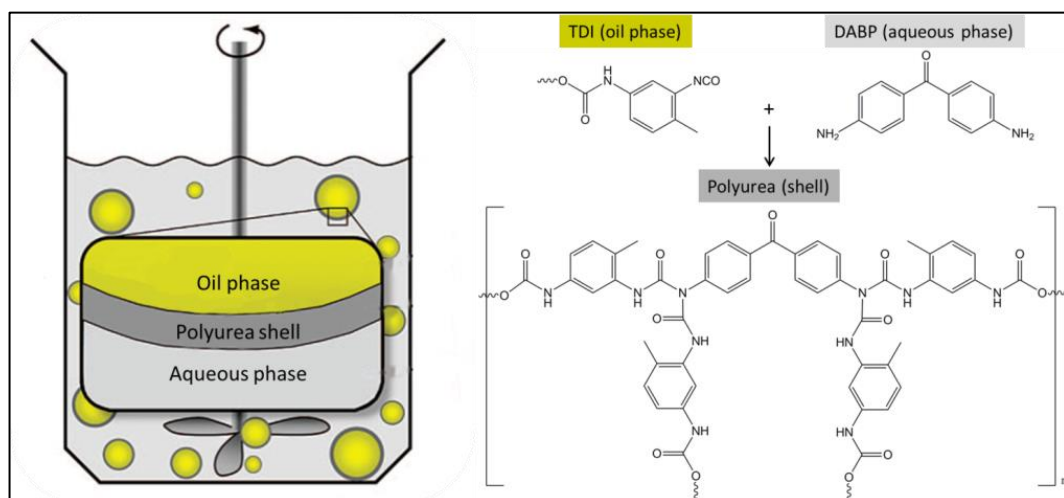


FIGURE 4.2 - SCHEMATIC REPRESENTATION OF THE MICROENCAPSULATION REACTION, IN WHICH THE LIQUID CORE IS ENCAPSULATED WITHIN A POLYUREA-BASED SHELL RESULTING FROM THE REACTION BETWEEN A TDI-BASED POLYISOCYANATE PREPOLYMER (DESMODUR L-75) AND AN AROMATIC DIAMINE (DABP). THE REACTION TAKES PLACE AT THE INTERFACE BETWEEN THE OIL AND THE WATER PHASES.

A preliminary characterization of the obtained microcapsules was performed to evaluate their dimensions, size distribution and morphological properties. The determination of the mean diameter of the synthesized microcapsules was carried out making use of optical microscopy (figure 4.3a) from datasets of at least 300 measurements. As reported in figure 4.3b, diameters falling within the 50-400 μm range were found after the microencapsulation process, with a size distribution centered in the 50-100 μm interval. These dimensions are compatible with the use of such microcapsules in functional coatings²². SEM analysis was employed to evaluate the morphological and surface features of the microcapsules. As shown in figure 4.3c, the microcapsules are typically characterized by a spherical shape. In addition, the outer shell surface appears rather smooth and uniform, irrespective of the microcapsule diameter. As evident from

figure 4.3d, the average wall thickness was found to uniformly fall within the 3-5 μm range, while no particular correlation between the wall thickness and microcapsule diameter was observed.

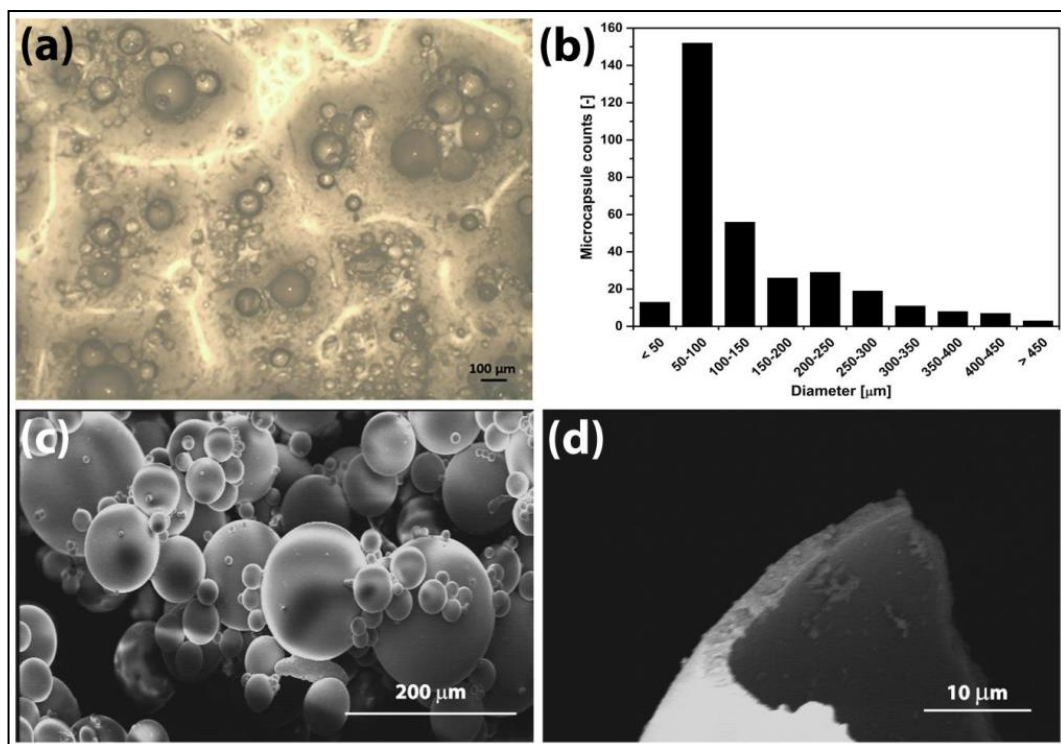


FIGURE 4.3 - A) OPTICAL MICROGRAPH OF THE DABP-BASED MICROCAPSULES SYNTHESIZED IN THIS WORK. B) THEIR SIZE DISTRIBUTION. C) SEM IMAGE OF THE SAME MICROCAPSULES. D) ZOOM ON THE SHELL WALL THICKNESS.

Both inner and outer shell surface appeared relatively rough, likely due to the presence of accumulated core material released from the microcapsules upon rupture prior to SEM analysis. The microencapsulation process was chemically characterized by collecting FTIR spectra of the as-formed microcapsules and by comparing them with the FTIR spectra of the main microcapsule constituents. As shown in figure 4.4, complete disappearance of the $\text{N}=\text{C}=\text{O}$ stretching signal (2270 cm^{-1}) attributable to the polyisocyanate prepolymer was observed in the microcapsule shell material, giving a first clear evidence of successful reaction between the NH_2 groups present in DABP and the NCO group in Desmodur L-75 with subsequent formation of the urea bond. In addition, the characteristic peaks of polyurea-urethane could also be easily identified in the FTIR spectrum of the microcapsule shell. In particular, the typical signals attributed to N-H stretching vibrations in the urea/urethane bond were found at 3318 cm^{-1} . In addition, a broad band centered at 1724 cm^{-1} was observed in the carbonyl region accompanied by a shoulder at 1622

cm^{-1} . These two signals are characteristic of stretching vibrations of C=O bonds in urethane and urea moieties, respectively. Finally, distinctive peaks were found at 1597 cm^{-1} , 1536 cm^{-1} , 1300 cm^{-1} and 1222 cm^{-1} that can be assigned to C-N (urethane, secondary amide), C=O (urea, secondary amide), C-N (urea, aromatic ring) and C-O-C (urethane) stretching vibrations, respectively. All these signals provide a strong evidence of the successful formation of a polyurea shell at the oil-water interface during the microencapsulation process²³. As to the encapsulated material, excellent matching was found between the FTIR spectra of sunflower oil and the extracted liquid core. In particular, all notable peaks observed in the FTIR spectrum of sunflower oil ($3100\text{-}2700 \text{ cm}^{-1}$, $1850\text{-}1650 \text{ cm}^{-1}$, $1500\text{-}1000 \text{ cm}^{-1}$) were also found in the FTIR spectrum of the extracted core material. These observations clearly demonstrate effective encapsulation of sunflower oil as core material in the polyurea-based shell.

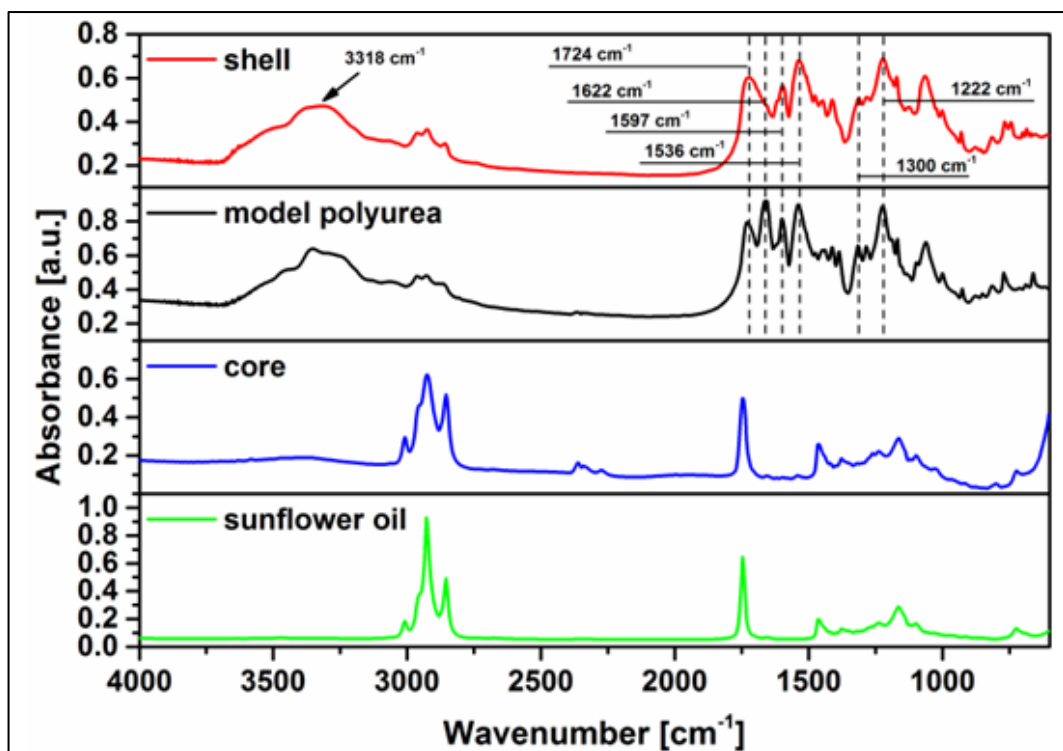


FIGURE 4.4 - FTIR SPECTRA OF EXTRACTED SHELL MATERIAL, MODEL POLYUREA FILM OBTAINED FROM REACTION BETWEEN DESMODUR L-75 AND DABP, EXTRACTED CORE MATERIAL AND SUNFLOWER OIL. FOR THESE ANALYSES, MICROCAPSULES WERE PREPARED WITHOUT THE ADDITION OF FLUORESCENT SPECIES IN THE SUNFLOWER OIL PHASE.

The thermal stability of the synthesized microcapsules was investigated by means of TGA. As shown in figure 4.5, no significant weight losses are observed up to $150 \text{ }^{\circ}\text{C}$, thus indicating relatively high thermal stability of the prepared microcapsules (a negligible $< 5\%$ mass loss

contribution is observed in the 100-150 °C temperature range, correlated with the evaporation of solvent (DMF) trapped in the system during microcapsule synthesis). At higher temperatures, three major mass loss events can be distinguished. In particular, a first ~15% mass loss is observed in the 160-250 °C range, followed by another significant weight loss (~30%) between 250 °C and 400 °C and a final major thermal degradation (~45% weight loss) for higher temperatures. As observed on previous works^{11,24}, such three-step mass loss profile may be partly associated with thermal degradation of sunflower oil, thus providing evidence of successful encapsulation of the core material. Additionally, thermal decomposition of the shell material may also contribute to the weight loss experienced for temperatures higher than 300 °C. It is known that polyureas are characterized by a microphase-separated morphology that consists of hard-segment domains covalently bonded to a soft segment matrix into a block copolymer architecture^{25,26}. In particular, the hard domains are extensively hydrogen-bonded and serve as reversible physical cross-links, thus providing the material with good mechanical properties, especially toughness²⁷. Based on these considerations, the second mass loss peak observed in figure 4.5 may include a contribution given by the thermal degradation of the polyurea shell hard segments, as a result of the relatively low thermal stability of the urea group²⁶. Analogously, thermal degradation of the soft segments may be partly associated with the major mass loss event observed for temperatures above 400 °C.

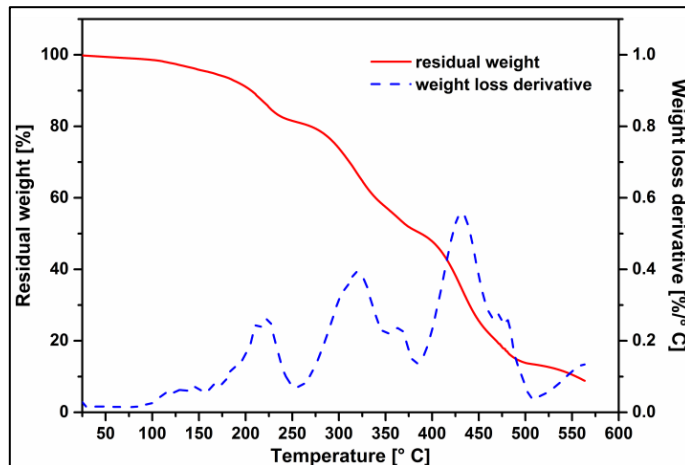


FIGURE 4.5 - TGA SCAN IN AIR OF THE UV-SCREENING DABP-BASED MICROCAPSULES SYNTHESIZED IN THIS WORK.

4.3.2 CHEMICAL STABILITY OF MICROCAPSULES

In practical applications, microcapsules have to be robust enough to survive under severe processing or application conditions, where the presence of aggressive solvents is typically encountered. Therefore their long-term chemical stability represents a key technological aspect for their successful use. Accordingly, the chemical resistance to solvent attacks of the new UV-screening microcapsules synthesized in this work was investigated by prolonged immersion in methanol (MeOH) and butyl acetate (BuOAc), separately. These two solvents were selected because they belong to two distinct chemical classes, namely alcohols and esters. In particular, BuOAc is one of the most commonly used solvents for application in the field of industrial coatings²⁸. On the other hand, MeOH was selected because of its different polarity and low molecular weight that may favor core diffusion through the porous microcapsule shell and subsequent core extraction. The capability of microcapsules to retain the encapsulated material and consequently their chemical resistance in solvents was evaluated using UV-vis spectroscopy. More specifically, a given amount of microcapsules loaded with a model chromophore (SP) was immersed in the solvent (MeOH or BuOAc), then UV-vis spectra of the solvent medium were systematically recorded at increasing dwell times. By comparing the absorption intensity of the chromophore solution recovered at a given time t with the absorption intensity of a reference solution in which the chromophore is present at a concentration corresponding to complete core leakage from the microcapsules under test (maximum theoretical concentration), release curves could be obtained. To allow swift visualization of the core release process in the extracting solvents, SP-dye dissolved in sunflower oil was the encapsulated core material used as model optical probe, due to its favorable optical properties (see section 4.2.6). In addition, the absorption spectrum of SP-dye does not overlay with the optical response of the two selected solvents, thus making it easily detectable by UV-vis spectroscopy.

The release profiles of the synthesized microcapsules in BuOAc and MeOH are presented in figure 4.6. For comparison, the release profiles of another microcapsule system based on UV-screening shell obtained by reaction of a polyisocyanate with a monofunctional amine (ACBP) are also reported¹¹. Clearly, DABP-based microcapsules possess a significantly improved resistance in solvents compared to the previously reported ACBP-based microcapsules. Core release of the ACBP-based system in MeOH appeared to be significant (around 50%) already after 10 min of immersion. For longer immersion times, core release was found to gradually increase up to a value of 70% after 60 min. In BuOAc, an even faster release rate was observed for the same ACBP-based microcapsules. Approximately 60% of core material was extracted within the first minute of immersion, with complete release after 60 min. Conversely, the release rate of DABP-based microcapsules was found to be significantly reduced, maintaining a constant value during the entire duration of the leakage test. This behavior was found to be independent of the immersion solvent, clearly demonstrating the excellent chemical stability of the system proposed

in this work, which can therefore be reliably employed in combination with commercial solvent-based coatings.

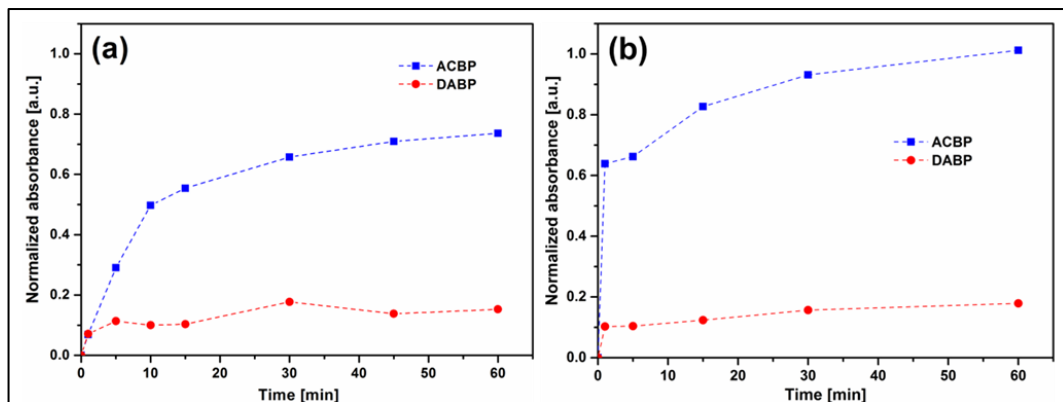


FIGURE 4.6 - CORE RELEASE RATE PROFILES OF DABP- AND ACBP-BASED MICROCAPSULES IN A) MEOH AND B) BUOAC (DASHED LINES WERE DRAWN TO GUIDE THE EYE).

To further broaden the applicability of this newly proposed system, DABP-based microcapsules were also immersed in water and a UV-vis analysis of the resulting solvent after one day of immersion was performed. As expected, no absorption signals ascribable to the encapsulated chromophore were detected, indicating the suitability of these systems also for use in waterborne coatings. The better chemical resistance of DABP- compared to ACBP-based microcapsules may be ascribed to the higher crosslinking density of the DABP-based shell material, which results from its tetrafunctional character. In this case, more amine groups can be made available for reaction with the isocyanate groups to yield urea bonds, thus leading to a denser three-dimensional crosslinked structure that may better withstand solvent attacks compared to the bifunctional ACBP-based counterpart.

4.3.3 SMART COATING FUNCTIONAL DEMONSTRATION

Ascertained the improved chemical stability of the UV-screening shells developed in this work, their functional response was assessed by synthesizing UV-screening microcapsules encapsulating a model pyrene-based fluorescent dye (VPy) whose optical properties well match the UV-absorption response of the new microcapsules (figure 4.7a-b). In particular, the absorption spectrum of VPy fully overlaps with that reported for the synthesized microcapsules, thus prospecting effective screening of the incoming UV light that is prevented from interacting with the encapsulated fluorescent molecule. Such VPy-containing UV-screening microcapsules were placed over a microscope slide and irradiated with UV-light ($\lambda = 366$ nm). As presented in figure 4.7c, no evidence of fluorescence emission was observed on intact microcapsules, clearly indicating the effective UV-screening action performed by the polyurea based shell. The same

microcapsules were then crushed between two glass slides and the liquid core was allowed to be released by diffusion. As shown in figure 4.7d, a strong fluorescence emission was observed after exposing the broken microcapsules to UV-light, coherently with the fluorescence emission properties of the encapsulated VPY dye.

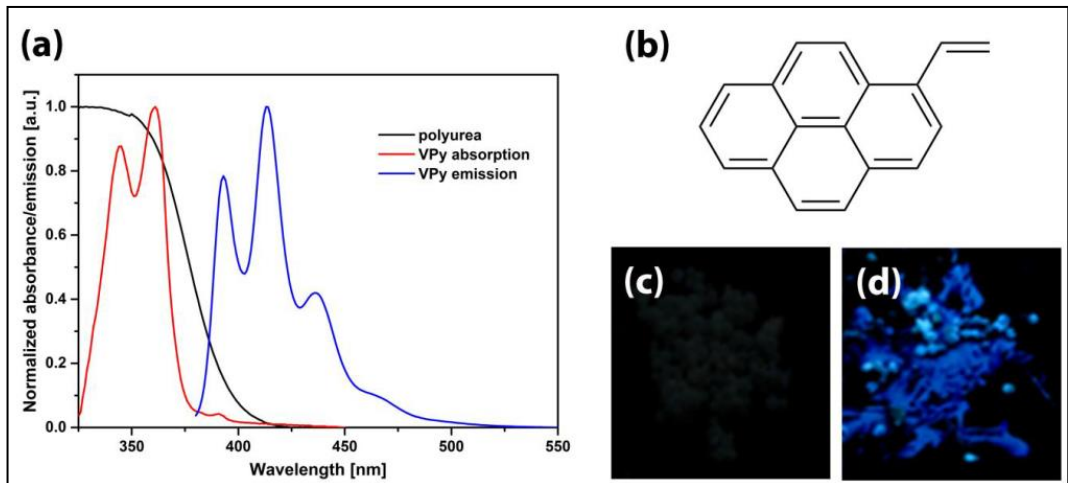


FIGURE 4.7 - A) ABSORPTION SPECTRUM OF THE POLYUREA-BASED SHELL MATERIAL COMPARED WITH THE ABSORPTION/EMISSION RESPONSE OF THE VPY FLUOROPHORE, WHOSE CHEMICAL STRUCTURE IS REPORTED IN B). DIGITAL PHOTOGRAPHS OF THE UV-SCREENING SHELL/FLUORESCENT CORE DABP-BASED MICROCAPSULES SYNTHESIZED IN THIS WORK: C) AS PREPARED INTACT MICROCAPSULES UNDER UV-LIGHT, D) BROKEN MICROCAPSULES UNDER UV-LIGHT.

To further highlight the potential of the proposed fluorescent core/UV-screening shell microcapsule system, a smart damage-sensing polymer coating was prepared. To this end, the as-synthesized microcapsules were dispersed into a polyurethane based matrix formulation and subsequently deposited onto a carbon-fiber reinforced polymer (CFRP) substrate and allowed to dry out in air (figure 4.8a). Being CFRPs widely employed as structural materials in several engineering fields, evidence of the feasibility of the approach presented in this work on this type of substrates would give a clear demonstration of its potential as damage visualization tool in real life applications. As shown in figure 4.8b, no fluorescence emission was observed on the undamaged composite coating upon UV-light exposure, which appears uniformly dark. This is a further confirmation of the excellent UV-screening ability of the newly synthesized microcapsules, which are also found to be sufficiently stable to withstand the mechanical stresses arisen during the dispersion process. To evaluate the capability of the new microcapsule-based system to serve as fluorescent probe for damage visualization, the composite coating was mechanically damaged with a hammer shot to induce rupture of the microcapsules and release of the fluorescent core material within the polymer matrix (figure 4.8c). Under visible light, no evidence of the mechanical damage could be detected. However, after exposure to UV-light, a

sharp fluorescence emission was clearly observed on the cracked portion of the coating, resulting from the direct excitation of the released VPy-loaded fluorescent core from the ruptured microcapsules (figure 4.8d). This behavior is a further clear demonstration of the potential of our newly proposed microcapsule system as fluorescent probe for in situ microcrack detection.

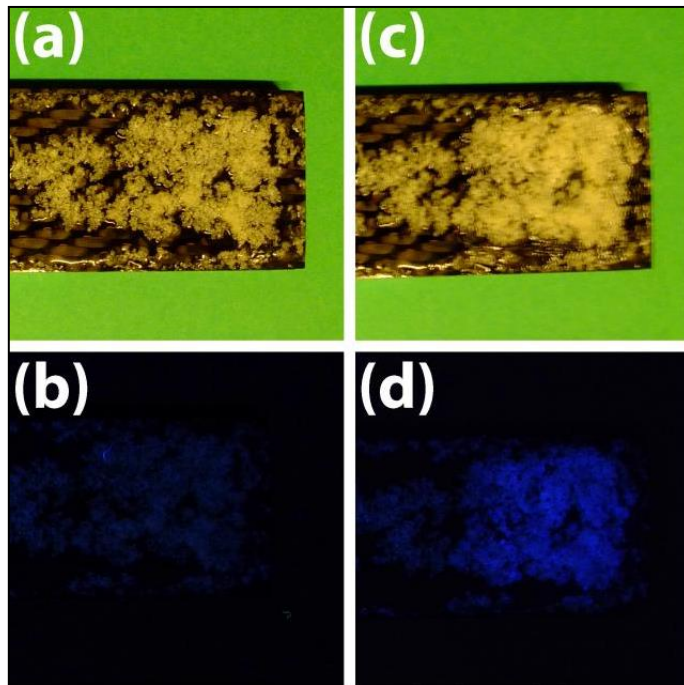


FIGURE 4.8 - DIGITAL PHOTOGRAPHS OF THE FUNCTIONAL DAMAGE-SENSING SMART COATING SYSTEM DEVELOPED IN THIS WORK DEPOSITED ONTO A CFRP SUBSTRATE: A) COATING BEFORE DAMAGE. B) COATING BEFORE DAMAGE UNDER UV-LIGHT. C) COATING AFTER A DAMAGE WAS APPLIED ON PART OF THE SAMPLE. D) DAMAGED COATING UNDER UV-LIGHT (A CLEAR FLUORESCENCE EMISSION IS OBSERVED ON THE DAMAGED AREA).

4.4 CONCLUSIONS

In this work, new high-chemical-stability microcapsules consisting of a UV-screening shell and a fluorescent core were obtained via interfacial polymerization between an isocyanate prepolymer and a difunctional benzophenone amine. A thorough morphological, chemical and thermal characterization of the synthesized microcapsules evidenced successful encapsulation of the core material and excellent thermal stability of the proposed microcapsule system. In addition, the chemical resistance of these new UV-screening microcapsules was assessed by leakage tests conducted in different solvent media, which highlighted the excellent chemical stability of this system likely originating from the highly crosslinked shell structure that prevents core extraction and subsequent diffusion outwards. This behavior was found to significantly overcome the limited chemical stability previously observed on analogous UV-screening microcapsule systems. Finally, the damage visualization ability of this new fluorescent sensor was demonstrated by embedding the newly synthesized fluorescent-core/UV-screening microcapsules into a polymer matrix to form a smart functional coating system able to visually detect (by fluorescence emission) the presence of local microcracks forming upon mechanical damage to the coating. The excellent UV-screening ability of this new microcapsule-based sensor system combined with its exceptional resistance to common organic solvents paves the way for the development of reliable core/shell microcapsule-based smart systems for damage detection and visualization in structural materials.

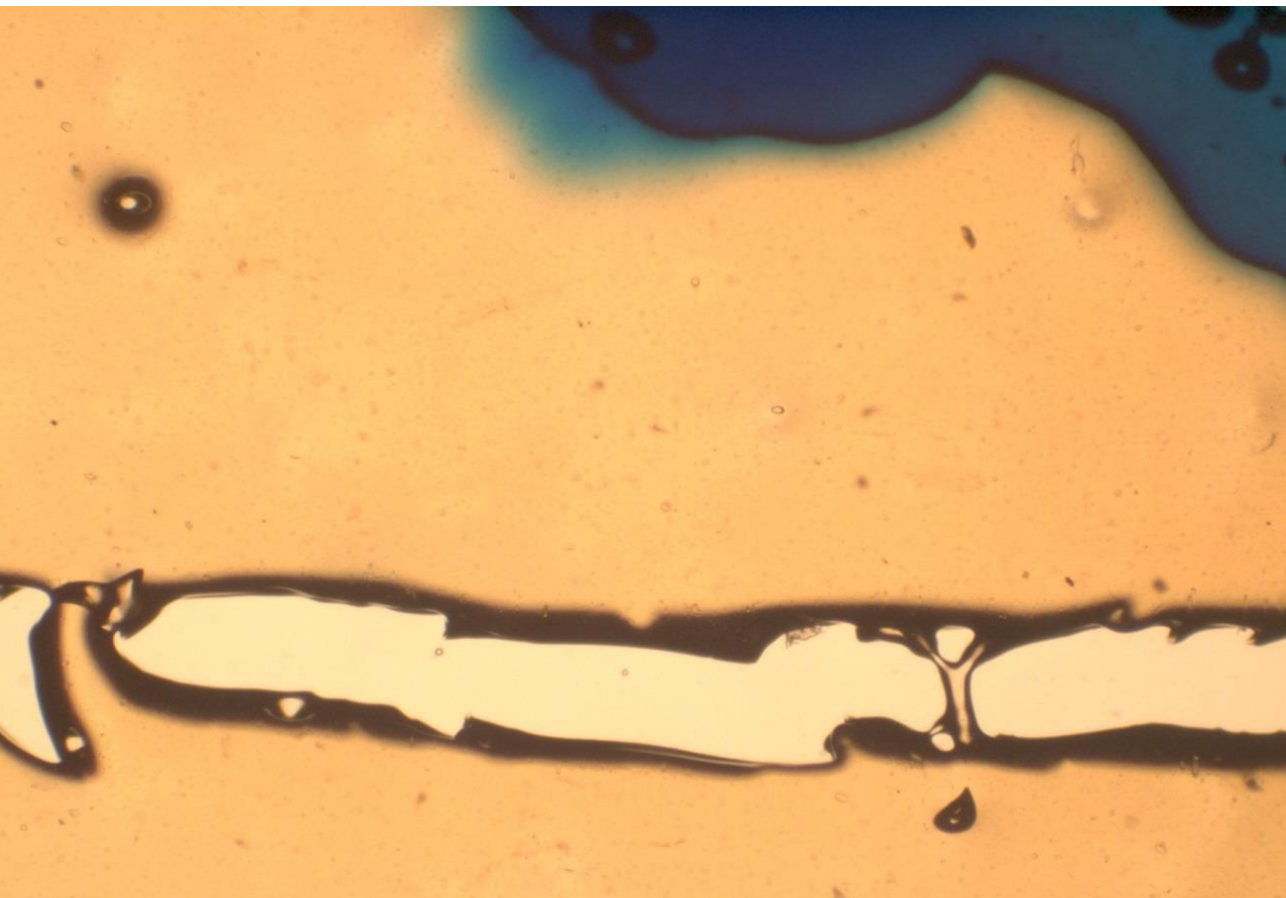
4.5 REFERENCES

1. J. Kerouedan, P. Quéffélec, P. Talbot, C. Quendo, S. De Blasi & A. Le Brun, Detection of micro-cracks on metal surfaces using near-field microwave dual-behavior resonator filters, *Meas. Sci. Technol.* **19**, 105701 (2008).
2. S. Gholizadeh, A review of non-destructive testing methods of composite materials, *Procedia Structural Integrity*, **1**, 50-57 (2016).
3. Chuck Hellier, Handbook of Nondestructive Evaluation, Second Edition, McGraw-Hill Education, 2012.
4. J.W.C. Pang & I.P. Bond, A hollow fibre reinforced polymer composite encompassing self-healing and enhanced damage visibility, *Compos. Sci. Technol.* **65**, 1791-1799 (2005).
5. David R.T. Roberts & Simon J. Holder, Mechanochromic systems for the detection of stress, strain and deformation in polymeric materials, *J. Mater. Chem.* **21**, 8256-8268 (2011).
6. D. Ramachandran & M.W. Urban, Sensing macromolecular rearrangements in polymer networks by stimuli-responsive crosslinkers, *J. Mater. Chem.* **21**, 8300-8308 (2011).
7. G.I. Peterson, M.B. Larsen, M.A. Ganter, D.W. Storti & A.J. Boydston, 3D-Printed Mechanochromic Materials, *ACS Appl. Mater. Interfaces* **7**, 577-583 (2015).
8. J.W.C. Pang & I.P. Bond, 'Bleeding composites'—damage detection and self-repair using a biomimetic approach, *Compos. Part A-Appl. S.* **36**, 183-188 (2005).
9. D. Ramachandran, F. Liu & M.W. Urban, Self-repairable copolymers that change color, *RSC Adv.* **2**, 135-143 (2012).
10. F. Maia, J. Tedim, A.C. Bastos, M.G.S. Ferreira & M.L. Zheludkevich, Active sensing coating for early detection of corrosion processes, *RSC Adv.* **4**, 17780-17786 (2014).
11. B. Di Credico, G. Griffini, M. Levi & S. Turri, Microencapsulation of a UV-responsive photochromic dye by means of novel UV-screening polyurea-based shells for smart coating applications, *ACS Appl. Mater. Interfaces* **5**, 6628-6634 (2013).
12. W. Li, C.C. Matthews, K. Yang, M.T. Odarczenko, S.R. White & N.R. Sottos, Autonomous indication of mechanical damage in polymeric coatings, *Adv. Mater.* **28**, 2189-2194 (2016).
13. S. Vidinejevs, A.N. Aniskevich, A. Gregor, M. Sjoberg & G. Alvarez, Smart polymeric coatings for damage visualization in substrate materials, *J. Intell. Mater. Syst. Struct.* **22**, 1371-1377 (2012).

14. H.H. Noh & J.K. Lee, Microencapsulation of self-healing agents containing a fluorescent dye, *eXPRESS Polym. Lett.* **7**, 88-94 (2013).
15. Young-Kyu Song, Kwang-Hun Lee, Dong-Min Kim & Chan-Moon Chung, A microcapsule-type fluorescent probe for the detection of microcracks in cementitious materials, *Sens. Actuators, B* **222**, 1159-1165 (2016).
16. G. Li, Y. Feng, P. Gao & X. Li, Preparation of Mono-Dispersed Polyurea-Urea Formaldehyde Double Layered Microcapsules, *Polym. Bull.* **60**, 725-731 (2008).
17. Y. Yang, Z. Wei, C. Wang & Z. Tong, Versatile Fabrication of Nanocomposite Microcapsules with Controlled Shell Thickness and Low Permeability, *ACS Appl. Mater. Interfaces* **5**, 2495-2502 (2013).
18. A.C. Jackson, J.A. Bartelt, K. Marczewski, N.R. Sottos & P.V. Braun, Silica-Protected Micron and Sub-Micron Capsules and Particles for Self-Healing at the Microscale, *Macromol. Rapid Commun.* **32**, 82-87 (2011).
19. S. Kang, M. Baginska, S.R. White & N.R. Sottos, Core-Shell Polymeric Microcapsules with Superior Thermal and Solvent Stability, *ACS Appl. Mater. Interfaces* **7**, 10952-10956 (2015).
20. B. Di Credico, M. Levi & S. Turri, An efficient method for the output of new self-repairing materials through a reactive isocyanate encapsulation, *Eur. Polym. J.* **49**, 2467-2476 (2013).
21. B. Saikia, T. J. Devi & N. C. Barua, Stereoselective total synthesis of both (6R,9R,10S,7E)- and (6S,9R,10S,7E)-epimers of oxylipin (9R,10S,7E)-6,9,10- trihydroxyoctadec-7-enoic acid, *Tetrahedron* **69**, 2157-2166 (2013).
22. S. A. Odom, A.C. Jackson, A.M. Prokup, S. Chayanupatkul, N.R. Sottos, S.R. White & J.S. Moore, Visual Indication of Mechanical Damage Using Core-Shell Microcapsules, *ACS Appl. Mater. Interfaces* **3**, 4547-4551 (2011).
23. K. Sahre, M. H. Abd Elrehim, K.-J. Eichhorn & B. Voit, Monitoring of the synthesis of hyperbranched poly(urea-urethane)s by real-time attenuated total reflection (ATR)-FT-IR, *Macromol. Mater. Eng.* **291**, 470-476 (2006).
24. A. Gouveia de Souza, J.C. Oliveira Santos, M.M. Concei o, M.C. Dantas Silva & S. Prasad, A thermoanalytic and kinetic study of sunflower oil, *Brazilian J. Chem. Eng.* **21**, 265-273 (2004).
25. D. Fragiadakis, R. Gamache, R.B. Bogoslovov & C.M. Roland, Segmental dynamics of polyurea: Effect of stoichiometry, *Polymer* **51**, 178-184 (2010).

26. W.H. Awad & C.A. Wilkie, Investigation of the thermal degradation of polyurea: The effect of ammonium polyphosphate and expandable graphite, *Polymer* **51**, 2277-2285 (2010).
27. J.A. Pathak, J.N. Twigg, K.E. Nugent, D.L. Ho, E.K. Lin, P.H. Mott, C.G. Robertson, M.K. Vukmir, T.H. Epps III & C.M. Roland, Structure Evolution in a Polyurea Segmented Block Copolymer Because of Mechanical Deformation, *Macromolecules* **41**, 7543-7548 (2008).
28. W. Freitag & D. Stoye (Editors), *Paints, Coatings and Solvents*, 2nd Edition, Wiley-VCH Verlag GmbH, Weinheim, 1998.

5.
Self-healing properties
of a polymer coating
based on the
thermoreversible
Diels-Alder reaction



Published in: *Progress in Organic Coatings* 78 (2015) 526-531.

"Effect of the plasticizer on the self-healing properties of a polymer coating based on the thermoreversible Diels-Alder reaction".

Authors: Giovanni Postiglione, Stefano Turri, Marinella Levi.

5.1 INTRODUCTION

Smart polymers are materials able to respond to changes in external environments by developing readable signals and/or corrective actuation mechanisms; among them, self-healing polymers are gaining an increasing interest for their ability to heal cracks or mechanical damages thus extending their lifetime¹. Different approaches have been followed to design and realize a self-healing mechanism: namely autonomous and heteronomous healing. The first approach is achieved introducing microcapsules²⁻⁵, hollow fibers⁶ or microvascular networks⁷ inside the material, so that, in response to a mechanical damage, a healing agent can be released, and repairs the structure by spontaneous polymerization. With this approach the healing efficiency is granted only once, thus limiting their applications. Externally stimulated or heteronomous healing systems, on the contrary, exploit physical or chemical changes occurring in the material in response to stimuli such as heat, light, electricity or magnetic field⁸. In Urban et al. works some examples of polymers self-repairing in response to UV-light radiation and magnetic field oscillation are reported⁹⁻¹¹. The well-known Diels–Alder (DA) reaction, which is thermally reversible, can be used for designing thermosetting self-healing polymers¹²⁻¹⁴. In that case, multiple cycles of heating treatment for activating the healing reaction are possible. Frequently used Diels–Alder functional groups are furans and maleimides as dienes and dienophiles, respectively, allowing the material to healing a narrow temperature range¹⁵⁻²². In Tian et al. work^{23,24}, a new molecule with both epoxide and furan groups was synthesized and crosslinked with maleimides, and the final material showed both mending ability and high mechanical strength. In these polymer networks at temperature above 120 °C the chemical linkages disconnect (through retro-DA reaction) and then reconnect upon cooling. It was also possible to graft furan and maleimide pendant groups to polymeric chains; crosslinking, via DA reaction, gave the polymer self-repairing properties. This approach has been followed for polyamides, polyketones and copolymers²⁵⁻²⁸. In another study, a reversible crosslinked healing gel totally based on DA bonds was synthesized in dimethylformamide (DMF) as solvent. Subsequently, it was included as a secondary phase within the structure of a conventional epoxy-amine thermoset polymer²⁹. Our study combines the idea of creating a network totally based on DA crosslinks with the use of thermosetting polymers for adhesives and coating application. Using an epoxy resins as precursors, a new thermosetting polymer network completely based on DA crosslinks has been realized. Benzyl alcohol was used as a plasticizer in order to improve the healing efficiency.

During the curing process, DA adducts formation has been monitored by means of infrared spectroscopy. Thermal and mechanical characterization, together with optical microscopy observations and gloss measurements, demonstrated the ability to heal scratches and cracks several times with controlled thermal treatments and quantified the healing efficiency.

5.2 EXPERIMENTAL SECTION

Furfurylamine (FA), 1,1'-(methylenedi-4,1-phenylene)bismaleimide (2M), N,N-diglycidyl-4-glycidyl-4-oxyaniline (DGGO), bisphenol A diglycidyl ether (DGEBA), dichloromethane and methanol were all purchased by Sigma Aldrich and used as received. Fourier transform infrared spectra (FTIR) were acquired using a Thermo Nicolet Nexus FTIR spectrometer. Spectra were collected from 400 to 4000 cm^{-1} . Thermo gravimetric analyses (TGA) were performed on a TA Instrument Q500 in nitrogen and air at a heating rate of 3 $^{\circ}\text{C}/\text{min}$. Differential scanning calorimetry (DSC) was carried out with a Mettler-Toledo TA3000 instrument, indium and n-hexane calibrated, heating from 20 $^{\circ}\text{C}$ to 140 $^{\circ}\text{C}$ with a rate of 10 $^{\circ}\text{C}/\text{min}$ in a N_2 environment. Dynamic mechanical analysis (DMA) was conducted on a Mettler Toledo DMA/SDTA861 instrument from 20 $^{\circ}\text{C}$ to 180 $^{\circ}\text{C}$ at a 3 $^{\circ}\text{C}/\text{min}$ heating rate. Tensile properties were tested at room temperature by a Zwick/Roell Z010 under a constant crosshead rate of 25 mm/min (5 specimens, 18 mm gauge length, 5 mm width, 3 mm thickness). Gloss measurements were made on 100 μm thick coatings deposited on a white cementitious substrate at a reflective angle of 60 $^{\circ}$.

5.2.1 SYNTHESIS OF 3F AND 2F COMPOUNDS

First, 12 g of viscous resin DGGO were mixed with 12.6 g of liquid FA (in the stoichiometric ratio 1:3 molar) under stirring and left to react in methanol at 85 $^{\circ}\text{C}$ for 3 h. At the end of the reaction, the product (trifuran, 3F) was obtained by drying the sample under vacuum until constant weight was reached. Similarly, 10 g of DGEBA were mixed and heated with 5.7 g of furfurylamine (in the stoichiometric ratio 1:2 molar) leading to the formation of bifuran, 2F following the same procedure. Yields were >95 % in both cases. Chemical characterization of furan adducts was performed with FTIR spectroscopy, monitoring the progressive disappearance of peak of oxirane ring at 910 cm^{-1} .

5.2.2 SYNTHESIS OF 2M-3F2F POLYMER

The Diels-Alder based polymer was prepared by reacting a mixture of the two furan adducts (3F:2F = 1:1 molar ratio, $3F + 2F = 0.0106$ mol), pre-heated at 70 °C for lowering their viscosity, with the bismaleimide powder (2M, 0.0132 mol) dissolved in dichloromethane. The reaction mixture was heated on a hot-plate at 50 °C with a magnetic stirrer until most of the solvent was evaporated. The resultant highly viscous liquid was poured in a mould and cured at 80 °C for 10 h in vacuum to remove the residual solvent. A highly crosslinked network (2M-2F3F) based on DA bonds was achieved as shown in figure 5.1. An identical procedure was followed for plasticized formulations. Benzyl alcohol (10 %, w/w) was added into the solution at the beginning of the crosslinking reaction leading to formation of 2M-3F2F/BA polymer.

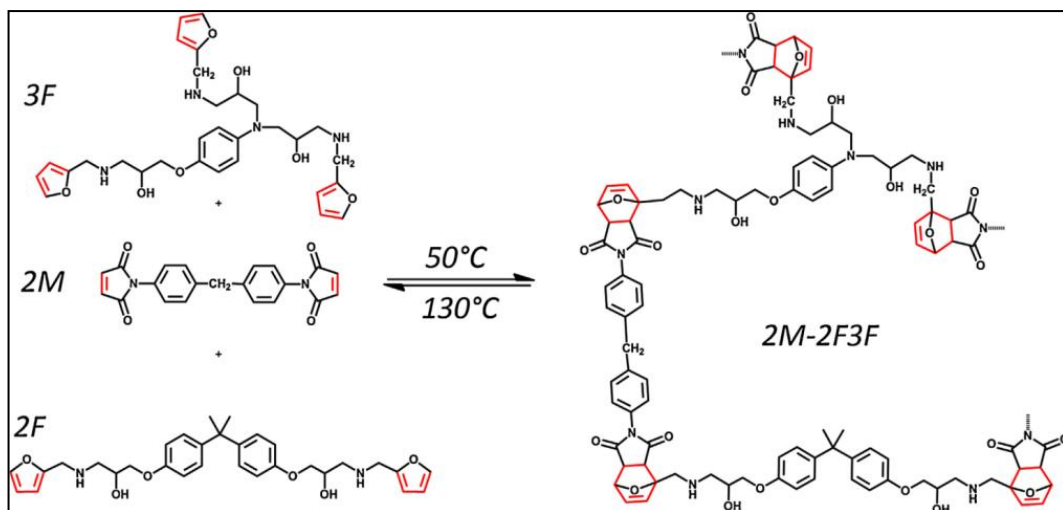


FIGURE 5.1 - DA AND RETRO-DA REACTIONS

5.3 RESULTS AND DISCUSSION

5.3.1 SYNTHESIS AND CHARACTERIZATION OF 2M-3F2F POLYMER

The monitoring of the 2M-2F3F polymer synthesis and its curing process was carried out by means of FTIR analysis. There are three significant peaks that have been considered: one at 700 cm^{-1} , representing the C-H bonds attached to the C-C in the maleimide ring, which is involved in the DA reaction, the peak at 1774 cm^{-1} typical of the DA adducts of maleimides and the maleimide carbonyl peak at 1712 cm^{-1} (invariant during the reaction). The first two peaks give a measure of the DA adducts formation from maleimide pendant groups; the third has been taken as a reference. In figure 5.2, FTIR spectra of 2M, 2M-2F3F uncured and 2M-2F3F after curing at 80°C are presented.

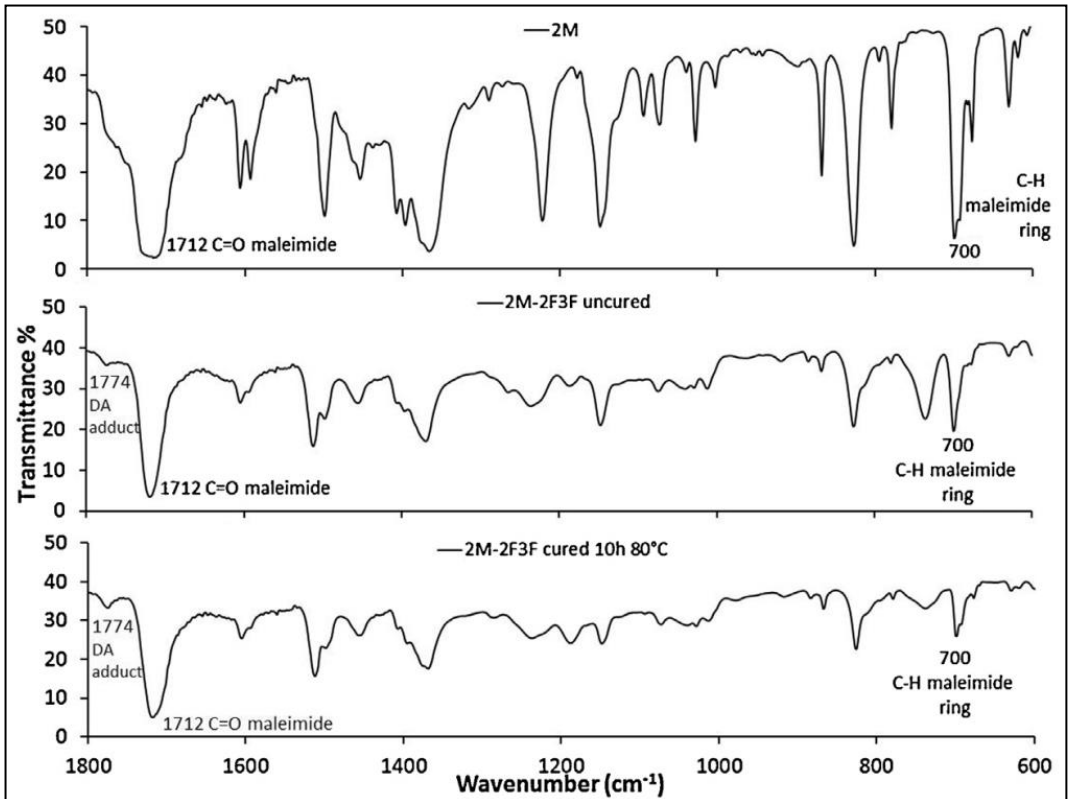


FIGURE 5.2 - FTIR SPECTRA OF 2M, 2M-2F3F NOT CURED AND 2M-2F3F CURED FOR 10 H AT 80°C .

The presence of the peak at 1774 cm^{-1} in the 2M-2F3F polymer reveals the DA adducts generation within their structure after the reaction. As expected the intensity of the peak at 700 cm^{-1} is high in the 2M compound but its signal is reduced in the 2M-2F3F polymers; moreover after the curing process, the peak is even less intense but does not disappear. Although the network is totally composed by DA bonds, not all pendant groups can react generating DA crosslinks. DA adducts conversion in the 2M-2F3F has been estimated by a spectroscopic quantitative analysis of absorbance spectra, comparing the maleimide peak intensity at 700 cm^{-1} (I_m) to the carbonyl peak intensity at 1712 cm^{-1} (I_c) at different curing times. In particular, the fraction of unreacted maleimide groups can be calculated using the following equation:

$$\%DA = \left(1 - \frac{I_m^x/I_c^x}{I_m^{ref}/I_c^{ref}}\right) \times 100 \quad (5.1)$$

in which I_m^x and I_c^x are the maleimide peak intensity and the carbonyl peak intensity of the 2M-2F3F polymer after x hours of curing time, whilst I_m^{ref} and I_c^{ref} refer to the intensity of the 2M. The percentage of DA conversion has been calculated at different curing time. Results are shown in figure 5.3. It seems that after 10 h of curing at $80\text{ }^\circ\text{C}$ about 60 % of the maleimide groups has reacted. The trend shown in figure 5.3, suggests that extending the curing time does not lead to a further progression of the reaction.

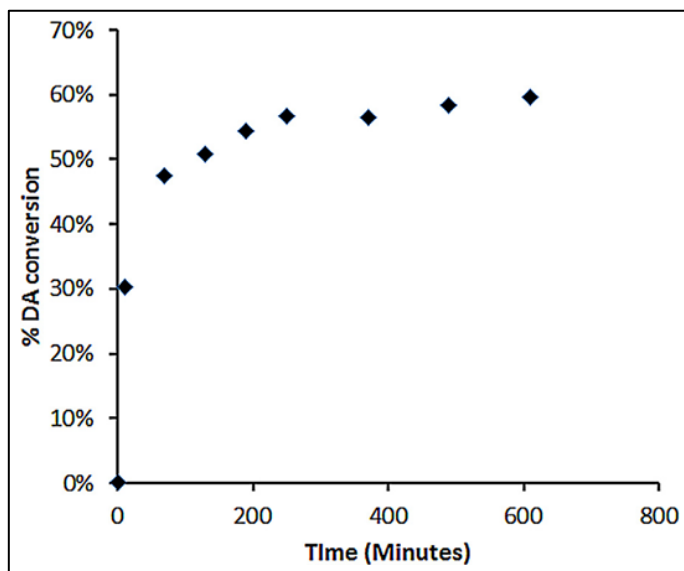


FIGURE 5.3 - ISOTHERMAL ($80\text{ }^\circ\text{C}$) CONVERSION CURVE OF THE DA POLYMER.

This is due to the fact that the crosslinking process proceeds until the T_g of the material meets the cure temperature and vitrification occurs (see also figure 5.4). Being the polymer network

thermoreversible at temperature exceeding 100 °C, it is not possible to further increase the process temperature because such a treatment would result into a partial debonding of DA adducts just formed. This could be therefore an intrinsic limitation of the particular formulation developed in this present work. DSC and DMA analyses help to better interpret the thermal behaviour of the 2M-2F3F polymer. Figure 5.4 shows the heating DSC curve of the cured 2M-2F3F polymer. The curve has a first transition, corresponding to the T_g , at about 80 °C and an evident endothermic peak at 130 °C, the latter indicating the retro-Diels–Alder reaction occurring in the polymer.

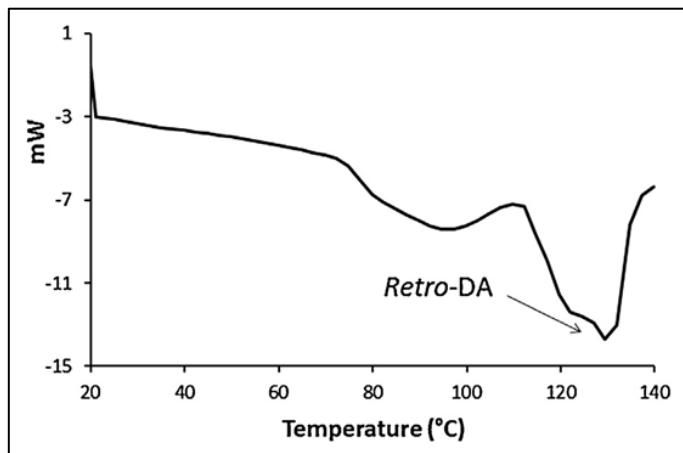


FIGURE 5.4 - DSC SCAN OF 2M-2F3F POLYMER. HEATING RATE AT 10 °C/MIN.

Such behaviour is confirmed by also the DMA analysis in which the $\tan \delta$ curve also shows a peak around +130 °C and a glass transition at +80 °C (figure 5.5).

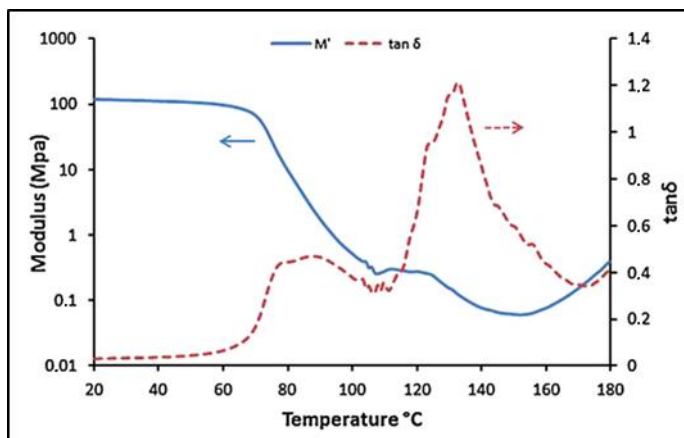


FIGURE 5.5 - DMA CURVES OF 2M-2F3F POLYMER. HEATING RATE AT 3 °C/MIN.

DSC was also used to study the effects of multiple heating cycles on the sampled polymer. Figure 5.6 shows three subsequent DSC scans performed at a rate of 10 °C/min on the same sample, letting it cooling down after every cycle at ambient temperature. A large endothermic peak is evident at about 130 °C in the first heating curve; in following heating cycles the peaks, despite being slightly pushed towards higher temperatures, still confirm the presence of retro-DA reaction.

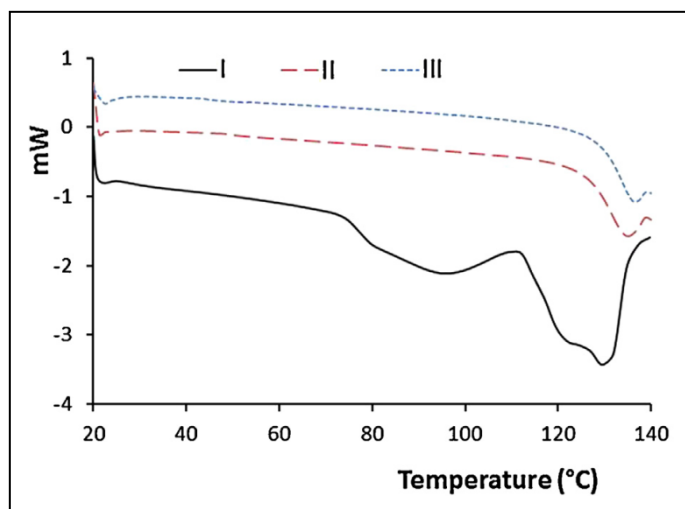


FIGURE 5.6 - DSC CURVES OF 2M-2F3F POLYMER. THREE HEATING CYCLE ON THE SAME SAMPLE AT 10 °C/MIN.

The repeatability of the process of disconnection and reconnection of DA bonds has interesting implication as it is possible to perform multiple healing cycles on a same damaged spot. In spite of the evidences of thermal analysis, the 2M-3F2F neat polymer was very brittle and showed visually a quite poor efficiency in the healing process of scratches and cracks induced on the surface. Brittleness and unsatisfactory healing performances are likely due to the low conversion and early vitrification. Introduction of a plasticizer may increase the free volume and molecular mobility of the polymer network, allowing to obtain a higher conversion of the crosslinking process. Benzyl alcohol has been chosen as a plasticizer for its good compatibility, low toxicity and relatively low volatility. FTIR analyses demonstrated that DA and retro-DA reactions are not affected by the presence of the plasticizer, while a TGA was needed to assess the suitability of BA with the thermal cycles used for the thermally induced self-healing experiments. As shown in figure 5.7, the 2M-3F2F/BA plasticized polymer shows a good thermal stability in the whole temperature range needed to activate DA and retro-DA reactions. At 140 °C it only has <1 % of weight loss. A significant weight loss which can be attributed to BA evaporation starts above 200 °C. The DA polymer network plasticized with 10 % of benzyl alcohol showed macroscopically

much better mechanical and self-healing properties, which are described in detail in section 5.3.2.

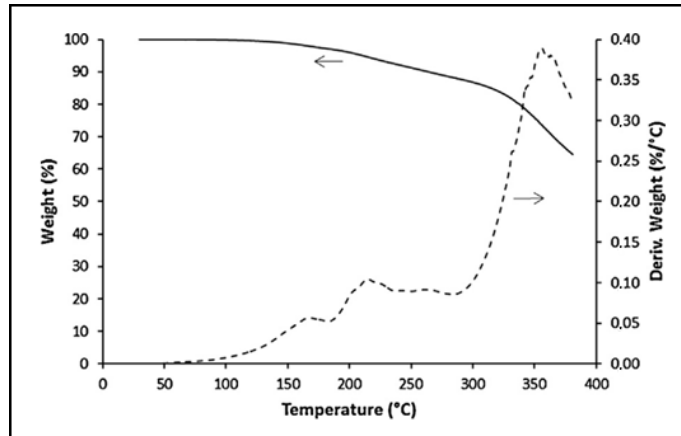


FIGURE 5.7 - TGA CURVE OF 2M-2F3F/BA POLYMER.

5.3.2 HEALING PROPERTIES

The self-healing properties of the neat and plasticized DA polymers were first investigated through optical microscopy. The resulting images are shown in figures 5.8a-d. A razor blade was used to make a scratch on the sample surface. The sample was then heated at 120 °C for 10 min. Figures 5.8a-b show the effect of the heating treatment on the 2M-3F2F neat polymer. The average width of the crack, being 51.3 μm before heating, became 40.6 μm , thus resulting in a minimal healing of the scratch. The low mobility of the high T_g chains does not allow the material to totally recover the damage. Figure 5.8c-d show the same experiment repeated for the 2M-3F2F/BA formulation. The same heating cycles allows for the total recovery of a 100 μm scratch. The same location on the surface has been scratched and re-healed two more times with the same effectiveness demonstrating that multiple healing cycles are feasible.

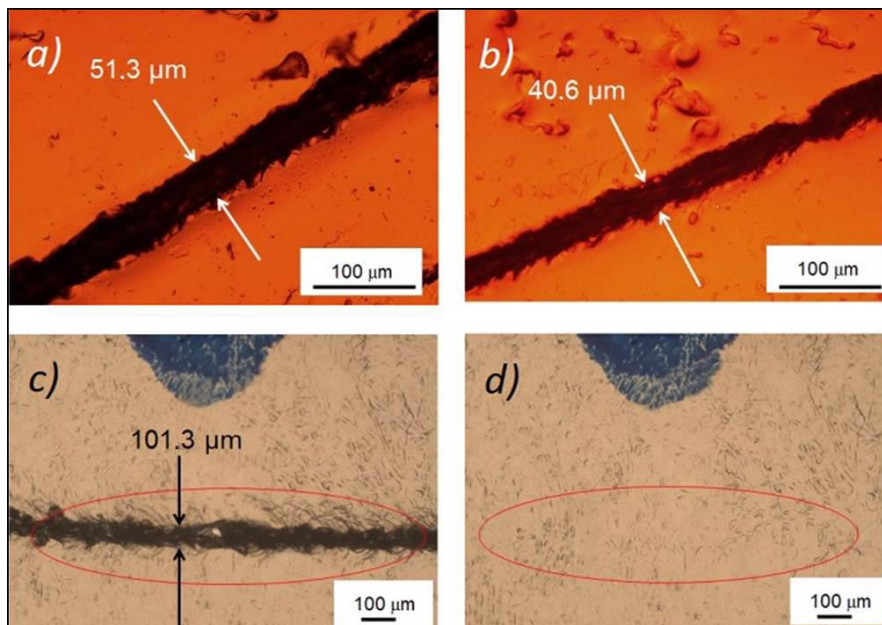


FIGURE 5.8 - OPTICAL MICROSCOPE IMAGES OF (A) 2M-2F3F POLYMER SCRATCHED, (B) 2M-2F3F POLYMER AFTER 10 MIN HEATING TREATMENT AT 120 °C, (C) 2M-2F3F/BA POLYMER SCRATCHED, (D) 2M-2F3F/BA POLYMER AFTER 10 MIN HEATING TREATMENT AT 120 °C.

A more quantitative assessment of the healing performances was done through tensile tests carried out on virgin, mechanically damaged, and thermally healed samples. The results concerning maximum stress values are shown in figure 5.9. The mechanical strength of the 2M-3F2F/BA polymer is about 9 MPa. After causing a 15 mm lengthwise damage on the sample (images of a virgin, an artificially damaged and a healed sample are shown in the inset), the stress values drop significantly to less than 2 MPa. After the 120 °C/10 min healing cycle, the mechanical properties are partially restored leading to a maximum stress of 4.3 MPa. The significant 48 % recovery in maximum stress reached by the 2M-3F2F/BA polymer indicates an efficient thermoreversibility of the DA network. In previous reports, the healing efficiency of DA based formulation has been investigated through different mechanical tests. In compact tension experiments the healing efficiency as a percentage of the load recovered stays within a 37–80 % range^{29,30}. On dumbbell-shaped samples a 55 % tensile strength recovery has been reported³¹, thus confirming the results of our formulation.

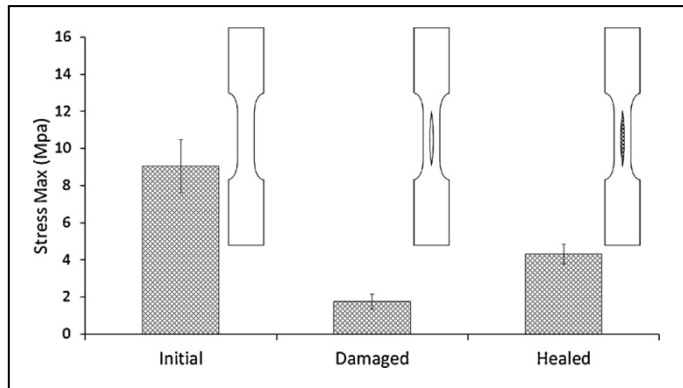


FIGURE 5.9 - MECHANICAL STRENGTH FOR VIRGIN, MECHANICALLY DAMAGED, AND THERMALLY HEALED DA POLYMERS.

The healing behaviour of the 2M-3F2F/BA polymer was also assessed in term of gloss recovery after a mar test. The optical measurements were firstly taken on a virgin sample, then the surface was marred with a steel scrub to obtain a matt finish, and finally the gloss measurements were repeated after the thermal healing cycle. Results are shown in figure 5.10. The virgin DA coating surface is very bright resulting in an average gloss value of 93.5 GU; the same surface, once marred, becomes opaque thus inducing a significant drop of the gloss values down to 19.4 GU. The healing treatment allows the material to almost completely recover its original gloss (88.0 GU), corresponding to an aesthetic healing efficiency of about 95 %. The procedure was repeated three times always observing an excellent gloss recovery.

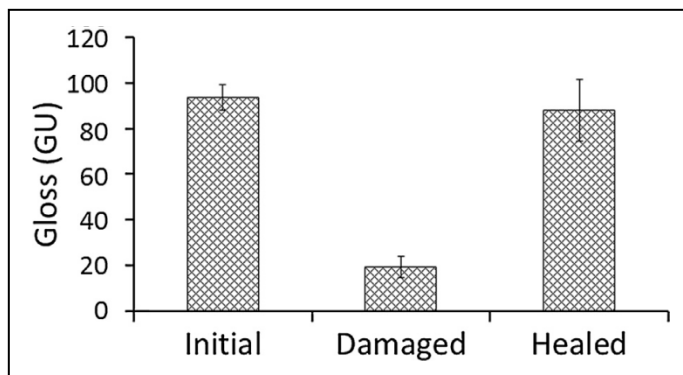


FIGURE 5.10 - GLOSS VALUES FOR VIRGIN, MARRED AND THERMALLY HEALED DA POLYMERS.

5.4 CONCLUSIONS

A new crosslinked polymer based on thermoreversible Diels–Alder reaction was presented. Thermoreversibility was proved by FTIR spectroscopy, DSC and DMA. It was however observed that thermoreversibility alone is not enough to provide an efficient thermally stimulated healing behaviour. The smart behaviour of the polymer was significantly improved by the addition of low amounts (10 % w/w) of a proper plasticizer, benzyl alcohol in the specific instance, which is thermally stable in the temperature range needed to activate the retro Diels–Alder reaction. The plasticized formulation showed an excellent recovery of aesthetic appearance of the scratched surface. The use of benzyl alcohol as a plasticizer is intrinsically a limitation, however a good thermal stability and no exudation in practical use conditions were verified. The thermally stimulated healing behaviour was positively demonstrated more times in the same place. An evaluation of the healing efficiency was done through proper mechanical and gloss tests, showing an efficiency of around 48 % and 95 % respectively. Diels–Alder polymers are promising candidates for the development of heteronomous self-healing coatings with multiple healing efficiency, and excellent aesthetic recovery of the surface appearance.

5.5 REFERENCES

1. S.J. García, H.R. Fischer & S. van der Zwaag, A critical appraisal of the potential of self healing polymeric coatings, *Prog. Org. Coat.* **72**, 211–221 (2011).
2. S.R. White, N.R. Sottos, P.H. Geubelle, J.S. Moore, M.R. Kessler, S.R. Sriram, E.N. Brown & S. Viswanathan, Autonomic healing of polymer composites, *Nature* **409**, 794–797 (2001).
3. B. Di Credico, M. Levi & S. Turri, An efficient method for the output of new self-repairing materials through a reactive isocyanate encapsulation, *Eur. Polym. J.* **49**, 2467–2476 (2013).
4. J.L. Yang, M.W. Keller, J.S. Moore, S.R. White & N.R. Sottos, Microencapsulation of Isocyanates for Self-Healing Polymers, *Macromolecules* **41**, 9650–9655 (2008).
5. M. Kouhi, A. Mohebbi, M. Mirzaei & M. Peikari, Optimization of smart self-healing coatings based on micro/nanocapsules in heavy metals emission inhibition, *Prog. Org. Coat.* **76**, 1006–1015 (2013).
6. J.W.C. Pang & I.P. Bond, A hollow fibre reinforced polymer composite encompassing self-healing and enhanced damage visibility, *Compos. Sci. Technol.* **65**, 1791–1799 (2005).
7. K.S. Toohey, N.R. Sottos, J.A. Lewis, J.S. Moore & S.R. White, Self-healing materials with microvascular networks, *Nat. Mater.* **6**, 581–585 (2007).
8. E.B. Murphy & F. Wudl, The world of smart healable materials, *Prog. Polym. Sci.* **35**, 223–251 (2010).
9. B. Ghosh & M.W. Urban, Self-Repairing Oxetane-Substituted Chitosan Polyurethane Networks, *Science* **323**, 1458–1460 (2009).
10. C.C. Corten & M.W. Urban, Repairing Polymers Using an Oscillating Magnetic Field, *Adv. Mater.* **21**, 5011–5015 (2009).
11. M.W. Urban, Stratification, stimuli-responsiveness, self-healing, and signaling in polymer networks, *Prog. Polym. Sci.* **34**, 679–687 (2009).
12. X.X. Chen, M.A. Dam, K. Ono, A. Mal, H.B. Shen, S.R. Nutt, K. Sheran & F. Wudl, A Thermally Re-mendable Cross-Linked Polymeric Material, *Science* **295**, 1698–1702 (2002).
13. M.A. Tasdelen, Diels-Alder “click” reactions: recent applications in polymer and material science, *Polym. Chem.* **2**, 2133–2145 (2011).
14. A. Gandini, The furan/maleimide Diels–Alder reaction: A versatile click–unclick tool in macromolecular synthesis, *Prog. Polym. Sci.* **38**, 1–29 (2013).

15. Y. Imai, H. Itoh, K. Naka & Y. Chujo, Thermally Reversible IPN Organic-Inorganic Polymer Hybrids Utilizing the Diels-Alder Reaction, *Macromolecules* **33**, 4343–4346 (2000).
16. T.A. Plaisted & S. Nemat-Nasser, Quantitative evaluation of fracture, healing and re-healing of a reversibly cross-linked polymer, *Acta Mater.* **55**, 5684–5696 (2007).
17. Y.L. Liu & C.Y. Hsieh, Crosslinked Epoxy Materials Exhibiting Thermal Remendability and Removability from Multifunctional Maleimide and Furan Compounds, *J. Polym. Sci. A: Polym. Chem.* **44**, 905–913 (2006).
18. C. Zeng, H. Seino, J. Ren, K. Hatanaka & N. Yoshie, Bio-Based Furan Polymers with Self-Healing Ability, *Macromolecules* **46**, 1794–1802 (2013).
19. N. Bai, K. Saito & G.P. Simon, Synthesis of a diamine cross-linker containing Diels-Alder adducts to produce self-healing thermosetting epoxy polymer from a widely used epoxy monomer, *Polym. Chem.* **4**, 724–730 (2013).
20. M. Wouters, E. Craenmehr, K. Tempelaars, H. Fischer, N. Stroeks & J. van Zanten, Preparation and properties of a novel remendable coating concept, *Prog. Org. Coat.* **64**, 156–162 (2009).
21. G. Scheltjens, M.M. Diaz, J. Brancart, G. Van Assche & B. Van Mele, A self-healing polymer network based on reversible covalent bonding, *React. Funct. Polym.* **73**, 413–420 (2013).
22. C. Vilela, L. Cruciani, A.J.D. Silvestre & A. Gandini, Reversible polymerization of novel monomers bearing furan and plant oil moieties: a double click exploitation of renewable resources, *Adv. RSC* **2**, 2966–2974 (2012).
23. Q. Tian, Y.C. Yuan, M.Z. Rong & M.Q. Zhang, A thermally remendable epoxy resin, *J. Mater. Chem.* **19**, 1289–1296 (2009).
24. Q. Tian, M.Z. Rong, M.Q. Zhang & Y.C. Yuan, Synthesis and characterization of epoxy with improved thermal remendability based on Diels-Alder reaction, *Polym. Int.* **59**, 1339–1345 (2010).
25. Y.-L. Liu & Y.-W. Chen, Thermally Reversible Cross-Linked Polyamides with High Toughness and Self-Repairing Ability from Maleimide and Furan-Functionalized Aromatic Polyamides, *Macromol. Chem. Phys.* **208**, 224–232 (2007).
26. C. Toncelli, D.C. De Reus, F. Picchioni & A.A. Broekhuis, Properties of Reversible Diels–Alder Furan/Maleimide Polymer Networks as Function of Crosslink Density, *Macromol. Chem. Phys.* **213**, 157–165 (2012).
27. M.J. Barthel, T. Rudolph, A. Teichler, R.M. Paulus, J. Vitz, S. Hoepfener, M.D.Hager, F.H. Schacher & U.S. Schubert, *Adv. Funct. Mater.* **23**, 4921–4932 (2013).

28. A.A. Kavitha & N.K. Singha, Smart “All Acrylate” ABA Triblock Copolymer Bearing Reactive Functionality via Atom Transfer Radical Polymerization (ATRP): Demonstration of a “Click Reaction” in Thermoreversible Property, *Macromolecules* **43**, 3193–3205 (2010).
29. A.M. Peterson, R.E. Jensen & G.R. Palmese, Reversibly Cross-Linked Polymer Gels as Healing Agents for Epoxy-Amine Thermosets, *ACS Appl. Mater. Interfaces* **1**, 992–995 (2009).
30. X.X. Chen, F. Wudl, A.K. Mal, H.B. Shen & S.R. Nutt, New Thermally Remendable Highly Cross-Linked Polymeric Materials, *Macromolecules* **36**, 1802–1807 (2003).
31. N. Yoshie, S. Saito & N. Oya, A thermally-stable self-mending polymer networked by DielsAlder cycloaddition, *Polymer* **52**, 6074–6079 (2011).

6.
Conductive 3D microstructures
by direct 3D-Printing
of polymer/carbon nanotube
nanocomposites



Published in: Composites: Part A 76 (2015) 110–114.

“Conductive 3D microstructures by direct 3D printing of polymer/carbon nanotube nanocomposites via liquid deposition modeling”.

Authors: Giovanni Postiglione, Gabriele Natale, Gianmarco Griffini, Stefano Turri, Marinella Levi.

6.1 INTRODUCTION

Three-dimensional (3D) printing is a fabrication technology that consists in the creation of a 3D object starting from a digital model. 3D printing technologies have evolved very rapidly in recent years and have shifted apart from their traditional application field, namely rapid prototyping. Indeed, 3D printing is now being used routinely in a variety of manufacturing sectors ranging from aerospace and automotive to bioengineering^{1,2}. At present, stereolithography, selective laser sintering, selective laser melting and fused deposition modeling (FDM) are among the most widely employed and investigated additive manufacturing methods both in academia and in industrial environments³. The various 3D printing technologies differ in terms of cost, maximum spatial resolution and type of materials used. In particular, for the first three methods, 3D features with a very high spatial resolution (in the order of a few μm at most) have been demonstrated but at the expense of relatively high equipment costs and the need of specialized personnel to operate them^{3,4}. On the other hand, FDM has recently become fairly popular especially among non-specialized personnel as it represents a very cost effective approach to produce 3D objects with a relatively good resolution, which can approach $40\ \mu\text{m}$ ⁵. However, being a thermally-driven process that requires melting of a thermoplastic filament prior to the additive deposition of the extruded feature, it exhibits some limitations related to the materials to deposit, as only relatively few polymers possess the right thermal and rheological properties to be easily processable with this technology (with poly(lactic acid) – PLA and acrylonitrile–butadiene–styrene – ABS being among the most widely employed)⁶. Recently, the FDM approach was shown to allow a high degree of orientation of short reinforcing fibers in polymer-based composites during filament extrusion, resulting in 3D printed components with unique structural properties that can significantly exceed those of traditional compression molded samples⁷. In addition, the potential of the FDM technology for the fabrication of electronic sensors was recently demonstrated by 3D-printing solid filaments obtained starting from a dispersion of conductive carbon black into a solution of a commercial formulation of poly(caprolactone) (PCL) in dichloromethane (DCM) followed by evaporation of the solvent to form the solid filament to be extruded in a table-top FDM 3D printer⁸. Even though the approach presented in this work clearly allows the possibility to 3D-print objects with embedded sensors and electronic functionalities in a relatively simple fashion, it still requires the additional step of the production of a solid (nano)composite filament to be heated and melted in order to be processed with a standard FDM 3D printer. Very recently solvent-cast 3D printing has emerged as a versatile and cost-effective strategy to overcome some of the limits imposed by the FDM approach⁹. This

relatively new technology consists in the additive deposition of material layers directly from a solution in a volatile solvent. By means of this technology, the production of freeform structures, scaffolds and other self-standing microstructures was recently demonstrated using a computer-controlled robot moving along the x, y and z axes a dispensing apparatus equipped with a 100 μm inner-diameter extruding nozzle, starting from a concentrated solution of PLA in DCM⁹. In addition, by sputtering a metallic layer a few tens of μm thick onto the 3D printed structure, electrically conducting objects could also be obtained. However, no examples of the fabrication of intrinsically conductive 3D microstructures via direct 3D printing of conductive polymer-based nanocomposite materials from liquid dispersion have so far been reported in the literature, notwithstanding their enormous technological potential for application in fields such as microelectronics and biomedical engineering, where this approach would allow the direct fabrication of conductive microstructures with tailored 3D architectures in a low-cost and highly versatile fashion. In the effort to address this issue, a 3D printing technique is developed in this work for the fabrication of conductive 3D microstructures with arbitrary shapes via the deposition of a new conductive nanocomposite from liquid dispersion by means of a low-cost commercial benchtop 3D printer equipped with a syringe dispenser (see section 6.2). This method, that will be called liquid deposition modeling (LDM) throughout the text in analogy to the FDM approach introduced earlier, is based on the direct deposition of a homogeneous dispersion of multiwall carbon nanotubes (MWCNTs) in PLA using a high volatility solvent (i.e., DCM) as dispersion medium to ensure fast evaporation during wet filament deposition and rapid formation of rigid 3D microstructures. A thorough electrical characterization of the nanocomposite at increasing MWCNT concentrations is performed to evaluate the percolation threshold to achieve electrical conductivity. In addition, the rheological behavior of the nanocomposite dispersion is experimentally investigated at varying solid (PLA) content and a printability window for this system is identified based on the shear-rate of the material at the extrusion nozzle. Finally, examples of conductive 3D microstructures directly formed upon LDM of such MWCNT-based nanocomposite dispersion are presented. Conductive features as small as 100 μm can be reproducibly obtained with this method, indicating the high reliability of our approach. LDM clearly lends itself to the possibility of incorporating different types of structural and functional (nano)fillers in the 3D printed extruded feature without the need of producing a solid (nano)composite filament, thus presenting clear benefits compared to the more common FDM approach.

6.2 EXPERIMENTAL SECTION

MWCNTs were purchased from Nanocyl, Belgium (Nanocyl NC 3100, purity >95 %, 9.5 nm average diameter and 1.5 μm average length). PLA pellets were supplied by Futura Elettronica, Italy. DCM was purchased from Sigma–Aldrich, Italy. All products were used as received. For the preparation of the nanocomposite dispersions at increasing MWCNT concentration, a 3 wt% stock solution of PLA in DCM was prepared under magnetic stirring at room temperature for 3 h. After complete dissolution of PLA, the desired amount of MWCNTs (ranging from 0.5 wt% to 10 wt% in PLA) was dispersed in the PLA/DCM solution using the following procedure¹⁰: addition of the MWCNTs, 30 min magnetic stirring at 950 rpm, 1 h ultrasonic bath (Starsonic 90) at room temperature, 30 min ultrasonication with a Sonic & Materials VCX130 sonicator tip (20 kHz, 130 W, oscillation amplitude 80 %). This last step was carried out in an ice bath in order to prevent DCM evaporation and to minimize undesired exothermic phenomena resulting from the ultrasonication process. A similar procedure was employed for the preparation of nanocomposite dispersions at increasing PLA concentrations in DCM. In this case, a 1 wt% MWCNT concentration in PLA was employed and the PLA content in DCM was progressively varied (25 wt%, 30 wt% and 35 wt%). To perform electrical measurements, 25 mm x 75 mm thin film samples with a thickness ranging between 40 and 100 μm were prepared by drop-casting each nanocomposite dispersion with a given MWCNT concentration on a glass substrate. Upon drying in a ventilated oven, a solid self-standing nanocomposite film was obtained. The electrical conductivity of the nanocomposite films was measured using a four-point probe apparatus connected to a Keithley 2612 digital source-measure unit. A current scan between 0.01 and 0.1 A was applied on each sample with 50 steps and a settling time of 1 s for each measured step. The electrical conductivity of the nanocomposites was then calculated from resistance measurements¹¹. Characterization of the rheological properties of the nanocomposite dispersions at increasing PLA concentrations (1 wt% MWCNT in PLA) was performed using a Rheometrics DSR200 rheometer with a 25 mm plate-cone configuration at 25 °C. Steady shear tests on the MWCNT/PLA/DCM dispersions were performed for 3 min in the 0–4500 Pa range. Optical microscopy was employed to evaluate the microstructural features of the 3D-printed architectures using an Olympus BX-60 reflected-light optical microscope with bright-field (BF) and dark-field (DF) imaging equipped with an Infinity 2 digital camera. Scanning electron microscopy (SEM) was performed on 3D-printed nanocomposite-based microstructures with a Carl Zeiss EVO 50 Extended Pressure scanning electron microscope (acceleration voltage of 15.00–17.50 kV) to evaluate their surface morphology and the 3D architecture (samples were sputtered with a gold coating prior to SEM analysis). A low-cost home-assembled 3Drag 1.2 benchtop printer (Futura Elettronica, Italy) was used for LDM-based 3D printing of the conductive nanocomposite microstructures (figure 6.1). The machine was composed of a printing plate moving along the x and y axes and of an extrusion nozzle moving along the z axis (figure 6.1a). Commercial versions of such 3D printer are equipped

with a standard thermally controllable extruder which is fed with the solid filament to be melted and deposited on the printing plate. In the present work, such standard printing head was replaced by a syringe extruder for fluid deposition that was fabricated in house using a conventional FDM 3D printer (PowerWASP EVO 3D printer, Centro Sviluppo Progetti srl, Italy). Thanks to its particular design, such syringe slot may accommodate syringes with capacity ranging from 10 ml to 100 ml (figure 6.1b-c). The pressure on the syringe piston is controlled by a computer-activated NEMA17 stepper motor. For the experiments described in this work, 10 ml INJ-LIGHT syringes were employed (from RAYS S.p.A., Italy) coupled with 200 μm -diameter polypropylene nozzles supplied by E.O.I. Tecne srl, Italy. The printing apparatus was computer-controlled by means of *.Gcode* language, obtained from CAD-generated *.stl* files using a slicing open-source software (Cura, Ultimaker, from <http://software.ultimaker.com/>) or custom-made in the case of 3D models with dynamic variation along the z axis.

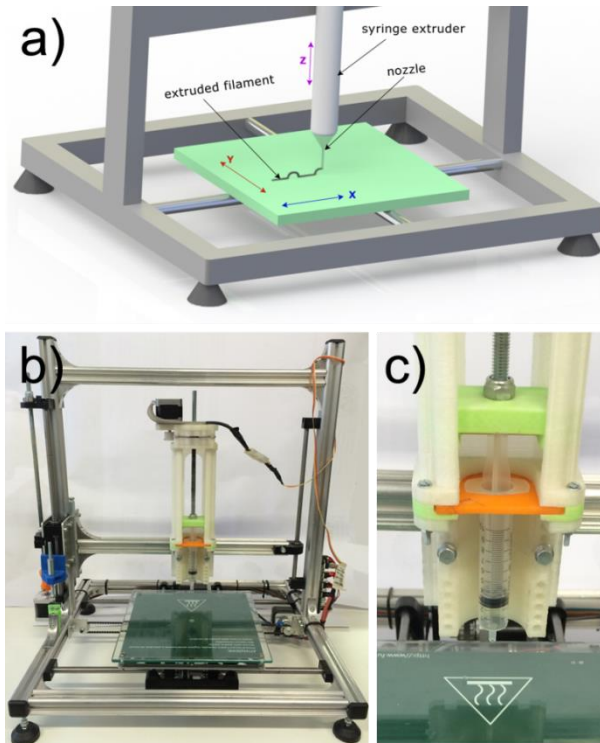


FIGURE 6.1 - A) SCHEMATIC REPRESENTATION OF 3D PRINTING OF A CONDUCTIVE MICROSTRUCTURE BY MEANS OF THE LDM APPROACH: THE SYRINGE (MOVING ALONG THE Z AXIS) EXTRUDES THE WET FILAMENT THROUGH THE NOZZLE ONTO THE PRINTING PLATE THAT MOVES ALONG THE X AND Y AXES; B) PHOTOGRAPH OF THE LDM 3D PRINTING SETUP USED IN THIS STUDY; C) CLOSE-UP ON THE SYRINGE EXTRUDER HOUSING.

6.3 RESULTS AND DISCUSSION

6.3.1 ELECTRICAL CONDUCTIVITY

In this work, the high electrical conductivity of MWCNTs was exploited to impart conductive character to the final MWCNT/PLA nanocomposite. To determine the effect of the addition of MWCNTs to the PLA matrix, the volume electrical conductivity σ of MWCNT/PLA nanocomposites was evaluated from resistance measurements on solvent-cast nanocomposite films with increasing MWCNT content (0.5–10 wt%). As shown in figure 6.2a, conductivity σ is found to increase substantially with respect to pristine PLA already upon addition of 0.5 wt% MWCNTs. Furthermore, a progressive increase in σ is observed for increasing MWCNT concentrations following a typical percolation behavior, until values in the range 10–100 S/m are reached for highly concentrated (5–10 wt%) MWCNT/PLA nanocomposites. Similar values of electrical conductivity were obtained on analogous nanocomposite systems based on MWCNTs and PLA matrix^{12,13}. Achieving a uniform homogeneous dispersion of MWCNTs within a polymeric matrix is a key factor for the development of printable MWCNT-based nanocomposites because of the high tendency of MWCNTs to form bundles and aggregates¹⁴ that may cause clogging of the printing nozzle and flux instability during the printing process. Therefore, an appropriate MWCNT concentration is required to obtain a nanocomposite material that is simultaneously conductive and 3D printable. The fracture surface of cryo-fractured 3D printed MWCNT/PLA nanocomposites containing 10 wt% of MWCNTs obtained from SEM analysis is shown in figure 6.2b.

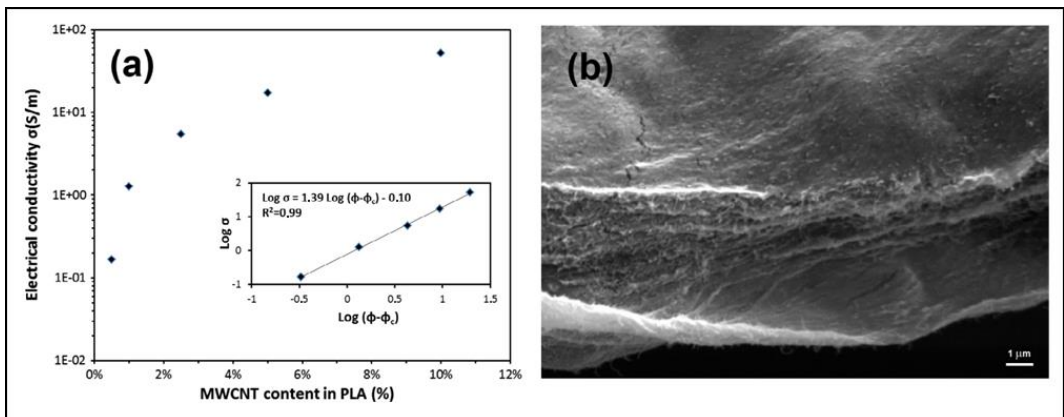


FIGURE 6.2 - A) VOLUME ELECTRICAL CONDUCTIVITY AS A FUNCTION OF MWCNT CONCENTRATION. THE INSET SHOWS THE LOG-LOG PLOT OF THE ELECTRICAL CONDUCTIVITY VERSUS THE VOLUME FRACTION OF MWCNTS. B) SEM MICROGRAPH OF CRYO-FRACTURED 3D-PRINTED MWCNT/PLA NANOCOMPOSITES (10 WT% MWCNT IN PLA).

As evident from the SEM micrograph, a good level of dispersion and distribution of MWCNTs (white dots in the image) is achieved in the PLA matrix without the formation of any noticeable aggregates, even at high MWCNT content. With the aim of determining the minimum theoretical MWCNT concentration to achieve electrical conductivity in the nanocomposite system, the electrical percolation threshold for the MWCNT/PLA nanocomposite system was evaluated using the following power law¹⁵:

$$\sigma \propto (\varphi - \varphi_c)^\alpha \quad (6.1)$$

where σ is the electrical conductivity, φ is the MWCNT volume concentration in the nanocomposite, φ_c is the critical MWCNT volume concentration at electrical percolation and α is a critical exponent. An excellent fit to the experimental values of $\log(\sigma)$ versus $\log(\varphi - \varphi_c)$ was obtained by a MWCNT percolation threshold concentration of 0.67 wt% and $\alpha = 1.39$, as shown in the inset to figure 6.2a. These values are in agreement with recently reviewed data on polymer-based nanocomposites, in which α values between 1.3 and 4 and φ_c well below 1 wt% are commonly found for systems containing MWCNTs¹⁶. Despite electrical measurements in this work were conducted on cast nanocomposite films, it is worth pointing out that the percolation threshold values obtained herein should represent an underestimate of the actual electrical behavior found in 3D printed filaments. Indeed, it was shown that the percolation conductivity of the nanocomposite may also be affected by the shearing at the nozzle tip due to shear-induced alignment of the MWCNT¹⁷.

6.3.2 RHEOLOGICAL CHARACTERIZATION

In addition to optimizing the electrical properties of the MWCNT/PLA nanocomposites, their rheological behavior needs to be thoroughly analyzed. Indeed, in the LDM-based 3D printing process the rheological profile of the nanocomposite dispersion critically determines its ability to flow through the printing nozzle and thus influences its actual printability into stable 3D solid microstructures. To this end, the viscosity of nanocomposite dispersions with varying PLA/DCM weight ratio (25/75, 30/70, 35/65) and fixed MWCNT concentration (1 wt% in PLA) was determined by isothermal cone-plate rheological measurements and the results are presented in figure 6.3.

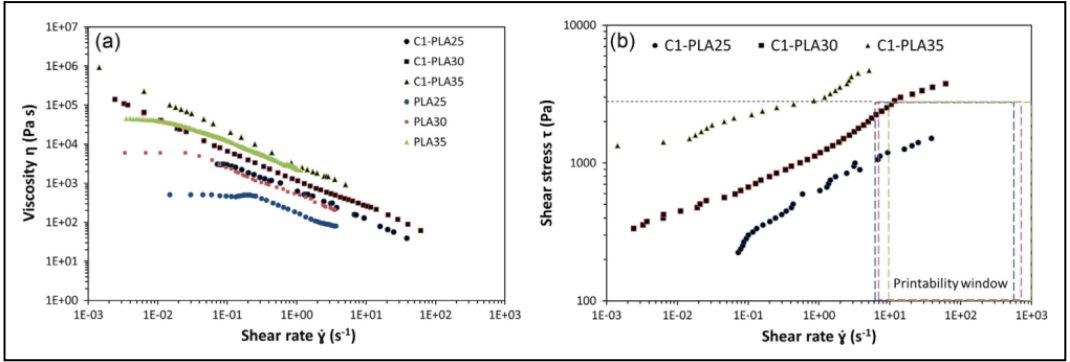


FIGURE 6.3 - A) VISCOSITY AND FLOW CURVES FOR NEAT PLA AND MWCNT/PLA NANOCOMPOSITE DISPERSIONS AT INCREASING PLA CONCENTRATION IN DCM. B) SHEAR-STRESS AS A FUNCTION OF SHEAR RATE FOR THE MWCNT/PLA NANOCOMPOSITE DISPERSIONS AT INCREASING PLA CONCENTRATIONS IN DCM (25 WT% (C1-PLA25), 30 WT% (C1-PLA30) AND 35 WT% (C1-PLA35) – THE CORRESPONDING PRINTABILITY WINDOWS ARE ALSO PRESENTED AS THE AREAS WITHIN THE DASHED LINES).

All nanocomposite dispersions clearly exhibited a typical shear-thinning behavior characterized by decreasing viscosity with increasing shear rate. In addition, an increase in viscosity is found upon addition of MWCNT. This rheological response is highly desirable in the context of LDM-based 3D printing as it allows to enhance nanocomposite processability through the capillary nozzle under the high shear-rates typical of the extrusion process due to the decreased viscosity of the material. In order to determine the correct printability window of the nanocomposite dispersions investigated, the process-related wall shear-rate and wall shear-stress were estimated using the capillary flow model^{18,19}. Particularly, the process-related wall shear-stress τ was calculated using the following relationship²⁰:

$$\tau = \frac{P_{max} - P_a}{2L/R} \quad (6.2)$$

where P_{max} is the maximum applicable pressure, P_a is the atmospheric pressure, L is the length of the capillary, R is its inner radius. Considering a maximum allowable value of working pressure $P_{max} = 0.8$ MPa originating from the maximum pressure attainable by the stepper motor controlling the syringe dispenser, an upper limit of the maximum shear-stress applicable by the printer $\tau_{max} = 2900$ Pa was determined (the Bagley correction could be neglected because the $L/2R$ ratio was larger than 50^{21}). The process-related wall shear-rate $\dot{\gamma}$ was estimated from the volumetric flow rate Q according to the following expression²⁰:

$$\dot{\gamma} = \frac{4Q}{\pi R^3} \left(\frac{3n+1}{4n} \right) \quad (6.3)$$

that takes into account the Rabinowitch-Mooney correction factor for non-Newtonian fluids (term into brackets, with n being the power-law index). The volumetric flow rate Q can be calculated from the machine linear printing speed through the cross-section area of the printing nozzle. In this case the linear printing speed of the machine exhibits its optimal operational interval within the range $0.1 - 10 \text{ mm s}^{-1}$. As a result, an allowable process-related shear-stress interval for a given material can be estimated as a function of the printing-speed (viz., shear-rate) settings and a material-related printability window can also be determined. Accordingly, plots of the process-related shear-stress τ as a function of the process-related shear-rate $\dot{\gamma}$ for the different MWCNT/PLA nanocomposite dispersions investigated in this work were constructed and presented in figure 6.3b, where the corresponding above mentioned printability windows are also shown. As evident from figure 6.3b, the rheological curve of the highly concentrated C1-PLA35 system (35 wt% PLA in DCM, 1 wt% MWCNTs) is completely outside its printability window, indicating that a minimum extruding pressure (minimum applied shear-stress τ) higher than the maximum pressure attainable by the printing machine P_a (maximum allowable shear-stress τ_{\max}) is required to process such system. This means that the viscosity of such nanocomposite dispersion is not compatible with our printing system. On the other hand, C1-PLA30 and C1-PLA25 dispersions (1 wt% MWCNTs – 30 wt% and 25 wt% PLA in DCM, respectively) showed a finite overlap between the process-related shear-stress curve of the material and its printability window, indicating that printing of these nanocomposite systems can be accomplished, provided that the appropriate combination of processing conditions (namely, shear-rate and shear-stress) are employed. In particular, it is evident from figure 6.3b that C1-PLA30 only allows for a very short range of useful shear-rates ($\dot{\gamma} = 5\text{--}11 \text{ s}^{-1}$, low printing speeds) while C1-PLA25 is characterized by a much broader printability range (higher printing speeds). These differences can be attributed to the different rheological response of these two systems at high shear-rates, as also evident from figure 6.3a. These results were confirmed by printing experiments of these nanocomposite systems directly performed with the 3D printing apparatus. Although the C1-PLA25 system offered a wider range of printing speeds, the best results in terms of resolution of 3D printed features at constant printing settings were obtained by processing the C1-PLA30 system at very low printing speeds (i.e., 0.1 mm s^{-1} , $\dot{\gamma} = 10 \text{ s}^{-1}$), likely due to the lower amount of solvent present in this case.

6.3.3 3D PRINTED MICROSTRUCTURES

In order to demonstrate the potential of LDM-based 3D printing of conductive MWCNT-based nanocomposite systems, different microstructures were fabricated using a low-cost benchtop 3D printer appropriately modified to accommodate a pressure-activated syringe (see section 6.2) feeding the extruding nozzle with the MWCNT/PLA nanocomposite dispersions (figure 6.4). First, a woven-like microstructure was obtained by depositing two layers of materials on top of each other. In order to do so, the C1-PLA30 nanocomposite system was employed, at a printing speed of 0.1 mm s^{-1} ($\dot{\gamma} = 7 \text{ s}^{-1}$). As shown in the optical micrograph presented in figure 6.4a, the wet MWCNT/PLA nanocomposite filament extrusion resulted in planar solid features of $100 \text{ }\mu\text{m}$ average width. The same printing process parameters (0.1 mm s^{-1} printing speed) and MWCNT-PLA nanocomposite system (C1-PLA30) were used to fabricate a 3D-printed ten-layer scaffold. As shown in figures 6.4b and c where the SEM images of different regions of a representative 3D-printed scaffold are presented, a comparable feature resolution ($100 \text{ }\mu\text{m}$) as that obtained in the 2D woven-like microstructure presented in figure 6.4a could be achieved. In addition, the stability of the as-formed solid nanocomposite filament allows to fabricate 3D features spanning over a few hundreds μm , as evident from figure 6.4b. Furthermore, the scaffold side-view reveals the characteristic circular cross-section of the extruded filament of approximately $100 \text{ }\mu\text{m}$ (figure 6.4c) of diameter, which is maintained even in the presence of multiple overlying layers. Figure 6.4d presents an example of a freeform 3D microstructure in which a $100 \text{ }\mu\text{m}$ diameter solid filament allows to achieve spanning self-standing features covering a few mm in length repetitively. In this case, C1-PLA25 system was employed at 5 mm s^{-1} ($\dot{\gamma} = 315 \text{ s}^{-1}$), so as to be able to speed-up the 3D printing process, induce rapid solvent evaporation and allow the formation of the spanning features. Such 3D microstructures suggest the possibility of employing these LDM-based 3D-printed architectures to fabricate conductive electronic components at the microscale in a very versatile fashion. To this end, a $75 \text{ mm} \times 25 \text{ mm}$ free-standing and flexible woven structure was fabricated by means of the proposed LDM technology (figure 6.4e) and it was employed to set up a simple electrical circuit to turn on a commercial green LED by means of a 3 V CR2032-type watch battery, thus giving a further practical demonstration of the potential applicability of these fully-functional conductive microstructured systems in the field of microelectronics.

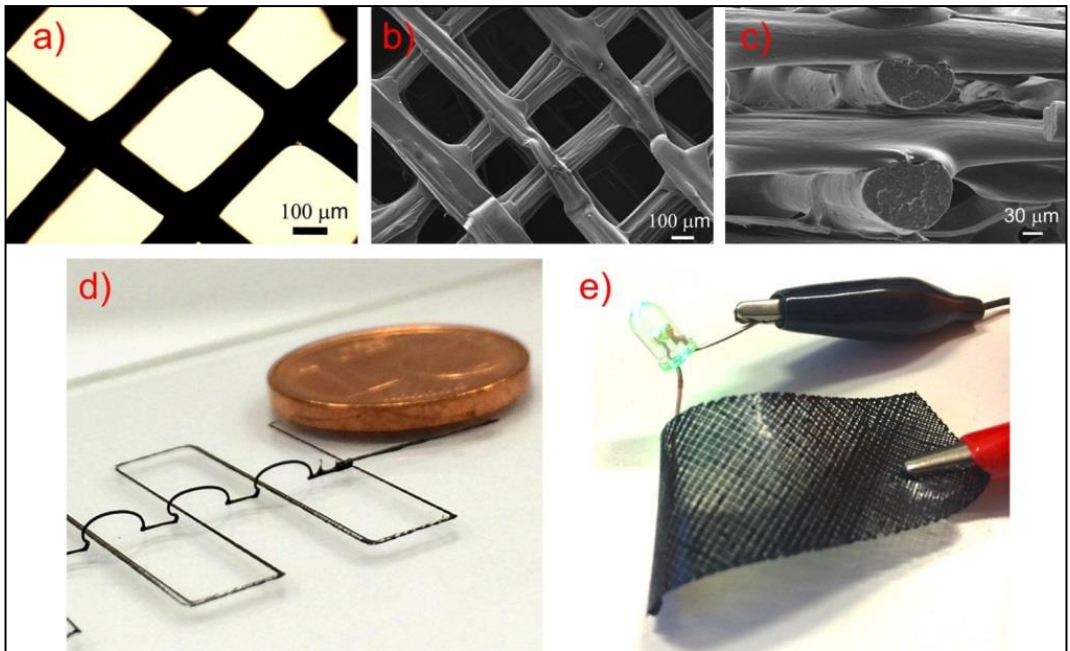


FIGURE 6.4 - A) TOP-VIEW OPTICAL MICROSCOPY IMAGE OF A LDM-BASED 3D PRINTED TWO-LAYER WOVEN-LIKE MICROSTRUCTURE. B-C) SEM TOP AND SIDE VIEW IMAGES OF A REPRESENTATIVE TEN LAYER SCAFFOLD. D) OPTICAL PHOTOGRAPH OF A LDM-BASED 3D PRINTED FILAMENT DEPOSITED IN A FREEFORM MANNER (A 1 CENT EURO COIN IS REPORTED IN THE IMAGE FOR DIMENSIONAL REFERENCE); E) 3D PRINTED MWCNT-BASED NANOCOMPOSITE WOVEN STRUCTURE USED AS CONDUCTIVE ELEMENT IN A SIMPLE ELECTRICAL CIRCUIT.

6.4 CONCLUSIONS

In summary, the fabrication of conductive 3D microstructures with arbitrary shapes is demonstrated by means of a new LDM 3D printing method based on the solvent-assisted additive deposition of a conductive nanocomposite using a modified low-cost benchtop 3D printer. Characterization of the electrical properties of the materials at increasing MWCNT concentrations evidenced a significant increase in the electrical conductivity of the nanocomposite with respect to the pristine PLA matrix material. Values of electrical conductivity in the 10-100 S/m range were obtained for high (>5 wt%) MWCNT concentrations, with a percolation threshold concentration of 0.67 wt%. Characterization of the rheological properties of the nanocomposite dispersions at varying PLA content was performed and printability windows for these systems were identified based on the estimation of the shear-rate of the dispersion at the extrusion nozzle. Finally, examples of spanning and self-supported conductive 3D microstructures directly formed upon LDM-based 3D printing of such MWCNT-based nanocomposite dispersions were presented. Conductive features as small as 100 μm could be reproducibly obtained with our method, demonstrating the high reliability of our approach. To the best of our knowledge, this represents the first demonstration of direct additive layer deposition of intrinsically conductive 3D microstructures from polymeric nanocomposite materials by means of a low-cost 3D printing technique based on the LDM approach. The results of this study clearly demonstrate the technological potential of conductive nanocomposite LDM-based 3D printing that may enable the integration of electronic functionalities into complex 3D objects in a straightforward and versatile fashion.

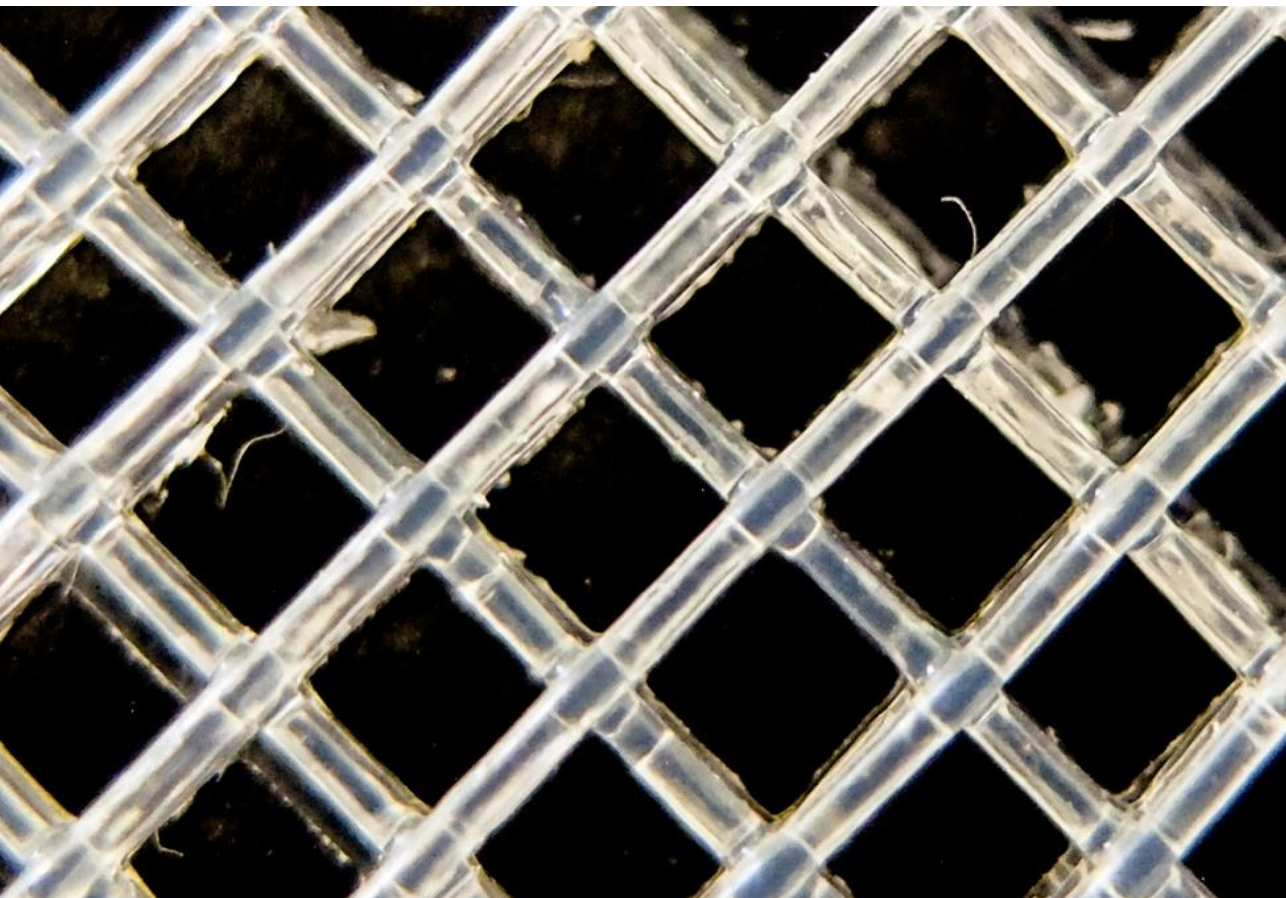
6.5 REFERENCES

1. B. C. Gross, J. L. Erkal, S. Y. Lockwood, C. Chen & D. M. Spence, Evaluation of 3D printing and its potential impact on biotechnology and the chemical sciences, *Anal Chem* **86**, 3240–53 (2014).
2. V. Petrovic, J. V. Haro Gonzalez, O. Jordá Ferrando, J. Delgado Gordillo, J. R. Blasco Puchades & L. Portoles Griñan, Additive layered manufacturing: sectors of industrial application shown through case studies, *Int J Prod Res* **49**, 1061–79 (2011).
3. I. Gibson, D. W. Rosen & B. Stucker, Additive manufacturing technologies – Rapid prototyping to direct digital manufacturing. Springer; 2010.
4. R. D. Farahani, K. Chizari & D. Therriault, Three-dimensional printing of freeform helical microstructures: a review, *Nanoscale* **6**, 10470–85 (2014).
5. A. Yamada, F. Niihara & K. Ikuta, A three-dimensional microfabrication system for biodegradable polymers with high resolution and biocompatibility, *J. Micromech. Microeng.* **18**, 025035 (2008).
6. M. D. Monzón, I. Gibson, A. N. Benítez, L. Lorenzo, P. M. Hernández, & M. D. Marrero, Process and material behavior modeling for a new design of micro-additive fused deposition, *Int J Adv Manuf Technol* **67**, 2717–26 (2013).
7. H. L. Tekinalp, V. Kunc, G. M. Velez-Garcia, C. E. Duty, L. J. Love, A. K. Naskar et al. Highly oriented carbon fiber–polymer composites via additive manufacturing, *Compos Sci Technol* **105**, 144–50 (2014).
8. S. J. Leigh, R. J. Bradley, C. P. Purcell, D. R. Billson & D. A. Hutchins. A Simple, low-cost conductive composite material for 3D printing of electronic sensors, *PLoS ONE* **7**, e49365 (2012).
9. S.-Z. Guo, F. Gosselin, N. Guerin, A.-M. Lanouette, M.-C. Heuzey & D. Therriault, Solvent-cast three-dimensional printing of multifunctional microsystems, *Small* **9**, 4118–22 (2013).
10. D. Molina, G. Griffini, M. Levi & S. Turri, Novel conductive nanocomposites from perfluoropolyether waterborne polyurethanes and carbon nanotubes, *Polym Adv Technol* **25**, 1082–8 (2014).
11. ASTM Designation: F 84–99, Standard test method for measuring resistivity of silicon wafers with an in-line four-point probe.
12. F. Mai, Y. Habibi, J.-M. Raquez, P. Dubois, J.-F. Feller, T. Peijs, et al. Poly(lactic acid)/carbon nanotube nanocomposites with integrated degradation sensing, *Polymer* **54**, 6818–23 (2013).

13. S.-I. Moon, F. Jin, C.-J. Lee, S. Tsutsumi & S.-H. Hyon, Novel carbon nanotube/poly(Llactic acid) nanocomposites: their modulus, thermal stability, and electrical conductivity, *Macromol Symp* **224**, 287–95 (2005).
14. P.-C. Ma, N. A. Siddiqui, G. Marom & J.-K. Kim, Dispersion and functionalization of carbon nanotubes for polymer-based nanocomposites: a review, *Compos A* **41**, 1345–67 (2010).
15. I. Balberg, A comprehensive picture of the electrical phenomena in carbon black polymer composites, *Carbon* **40**, 139–43 (2002).
16. W. Bauhofer & J. Z. Kovacs, A review and analysis of electrical percolation in carbon nanotube polymer composites, *Compos Sci Technol* **69**, 1486–98 (2009).
17. F. Du, J. E. Fischer & K. I. Winey, Effect of nanotube alignment on percolation conductivity in carbon nanotube/polymer composites, *Phys Rev B* **72**, 121404 (2005).
18. H. A. Barnes, J. F. Hutton & K. Walters, *An introduction to rheology*. Elsevier; 1997.
19. G. C. Pidcock & M. in het Panhuis, Extrusion printing of flexible electrically conducting carbon nanotube networks. *Adv Mater* **22**, 4790–800 (2012).
20. J. Bruneaux, D. Therriault & M.-C. Heuzey. Micro-extrusion of organic inks for direct-write assembly. *J Micromech Microeng* **18**, 115020 (2008).
21. S. G. Hatzikiriakos & K. B. Migler (eds) *Polymer processing instabilities: control and understanding*, Boca Raton, FL: CRC Press; 2004.

7.

UV-assisted 3D-Printing
of polymer nanocomposites based on
inorganic fillers



Published in: *Polymer Composites* (2015) DOI: 10.1002/pc.23735.

"UV-Assisted Three-Dimensional Printing of Polymer Nanocomposites Based on Inorganic Fillers".

Authors: Giovanni Postiglione, Gabriele Natale, Gianmarco Griffini, Stefano Turri, Marinella Levi.

7.1 INTRODUCTION

Polymer-based nanocomposites have been studied extensively in the last decades as a means to achieve improved thermal, mechanical, optical, magnetic, and barrier properties in the resulting material via the control of the interactions between the polymeric host and the nanostructured filler¹⁻⁵. Currently, great efforts are being produced in the attempt to develop new nanocomposite processing techniques that may allow the production of highly reliable and precise three-dimensional (3D) microdevices⁶. Stereolithography, two-photon polymerization, multijet modeling, and digital light processing represent some of the most explored techniques used for the fabrication of such microdevices that make use of photopolymerizable resins to achieve spatial resolutions that can approach 100 nm^{7,8}. Besides these relatively consolidated microfabrication technologies, a very promising and potentially cost-effective approach to manufacture such microdevices is represented by 3D printing, which consists in the direct fabrication of a 3D object starting from a digital model. 3D printing is now being used routinely in a variety of manufacturing sectors ranging from aerospace and automotive to bioengineering^{9,10}. An interesting evolution of the 3D printing technology is represented by ultraviolet-assisted 3D (UV-3D) printing, which allows the manufacturing of microdevices with 3D freeform or supported features starting from a photocurable polymeric material¹¹. This technology consists of a computer-controlled microextrusion apparatus to which a source of UV light is applied. Upon UV light exposure, the extruded photocurable material undergoes a crosslinking process which gives instant rigidity to the extruded filament, thereby enabling the creation of multidirectional self-supported shapes along the trajectory of the extrusion point. In the last few years, the use of UV-3D printing has allowed the fabrication of polymer based conductive microstructures, sensors, and electrical components by addition of conductive organic nanofillers such as carbon nanotubes into the polymeric matrix¹²⁻¹⁶. In addition, it has been recently demonstrated that by fine-tuning UV-3D printing processing parameters such as the extrusion nozzle speed, the material flow rate, and the intensity and position of the UV source according to the rheological properties of the photocurable resin, the fabrication of microcoils in a freeform manner can be made possible¹⁷. While most of the works on UV-3D printing have been mainly focused on the fabrication of free-standing or spanning micro-features embedding conductive nanofillers to impart electrical functionalities¹¹⁻¹⁵, very little is known about the effect of the addition of inorganic fillers into the photocurable resin on the rheological and mechanical properties of the resulting UV-3D printed nanocomposite material. Clearly, this information would provide a greater insight into the UV-3D printing process, thus allowing to widen the material selection and potentially improve further the mechanical properties of the 3D printed microstructure.

Moreover, the effect of 3D printing direction, fill density (infill), and fill pattern on the mechanical properties of UV-3D printed microstructures has not been thoroughly investigated in the literature to date, being the vast majority of the studies on this topic mainly focused on more traditional 3D printing techniques such as fused deposition modeling (FDM) based on thermoplastic materials^{18,19}. In particular, the fabrication of cellular nanocomposites via UV-3D printing and the evaluation of their mechanical properties for different printing patterns and different reinforcing fillers have not been demonstrated in the literature to date, notwithstanding the enormous potential of these systems as light-weight highly performing structural materials²⁰. In the effort to address these issues, a systematic investigation on the effect of the addition of different inorganic fillers on the rheological and mechanical properties of polymer-based nanocomposites for UV-3D printing is presented in this work. In particular, the rheological response of nanocomposite dispersions based on a solvent-free UV-curable resin loaded with different types of inorganic fillers is experimentally investigated at varying filler content. The fillers employed in this work are two different types of silica characterized by different specific surface areas and a montmorillonite-based nanoclay. Following such rheological characterization, optimal printability parameters for these systems are identified based on the shear rate of the materials at the extrusion nozzle. In addition, photocalorimetric measurements are used to assess the effect of the presence of the inorganic fillers on the thermodynamics and kinetics of the photocuring process of the resins. Moreover, by direct deposition of homogeneous solvent-free nanocomposite dispersions of filler in the UV-curable matrix, the effect of UV-3D printing direction, infill density, and fill pattern on the mechanical properties of UV-3D printed specimens is investigated by means of uniaxial tensile tests. Finally, examples of 3D macrostructures and microstructures directly formed upon UV-3D printing of such dispersions are reproducibly obtained and demonstrated, with a maximum spatial resolution approaching 200 μm .

7.2 EXPERIMENTAL SECTION

7.2.1 MATERIALS

Fumed silica OX50 (specific surface area 50 m²/g, primary particle size distribution range 10-100 nm) was purchased from Evonik Industries, Germany (AerosilVROX50, OX50). Dichloromethane (DCM), fumed silica OX200 (200 m²/g, primary particle size distribution 8-20 nm), and the photoinitiator 2-hydroxy-2-methyl-1-phenyl-propan-1-one (Darocur VR 1173, DAR) were purchased from Sigma-Aldrich, Italy. Trimethylolpropane ethoxylate triacrylate (TMPETA, average Mn ≈ 560) was kindly provided by Arkema, while the nanoclay (Dellite VR 43B, 6-8 μm characteristic length, D43B) was obtained from Laviosa Chimica Mineraria, Italy. All products were used as received.

7.2.2 NANOCOMPOSITE DISPERSIONS

For the preparation of the nanocomposite dispersions at increasing filler concentration, a 3 wt% stock solution of DAR in TMPETA was prepared under magnetic stirring at room temperature for 30 min. Two different procedures were followed for dispersing fumed silica and dellite into the DAR/TMPETA stock solution. For silica compounds, the desired amount of OX200 or OX50 (ranging from 5 wt% to 15 wt% for OX200 and from 15 wt% to 30 wt% for OX50) was slowly added to the DAR/TMPETA solution, which was manually mixed until homogenization. The nanoclay dispersions were prepared by mixing the desired amount of D43B in DCM so as to obtain a 0.01 w/w dispersion. After 10 min magnetic stirring at 500 rpm, the solution was ultrasonicated for 45 min with a Sonic & Materials VCX130 sonicator tip. This last step was carried out in an ice bath to prevent DCM evaporation and to minimize undesired exothermic phenomena resulting from the ultrasonication process.

Finally, the proper amount of DAR/TMPETA solution was added to the D43B dispersion and the solvent was evaporated under a fume hood. Four dispersions of D43B in DAR/TMPETA at D43B concentrations ranging from 3 wt% to 15 wt% were prepared.

7.2.3 CHARACTERIZATION TECHNIQUES

The rheological characterization of the nanocomposite dispersions at increasing filler concentration was performed using a Rheometrics DSR200 rheometer with a 25 mm plate-cone configuration at 25 °C. Steady shear tests on the DAR/TMPETA dispersions were performed for 3 min in the 0-4500 Pa range. Photocalorimetric measurements were performed on a DSC/823e (Mettler Toledo) coupled to a fiber-guided UV light source generated by a medium-pressure mercury lamp (Lightningcure LC8, Hamamatsu) in the 300-450 nm wavelength range at an intensity of 15 mW/cm². Nanocomposite samples (5 mg, 500 mm thickness) were placed into an open aluminum crucible and exposed to such UV light at 25 °C under nitrogen flow (50 mL/min). The heat of reaction was obtained by integration of the resulting exotherms. Optical microscopy was employed to evaluate the microstructural features of the UV-3D printed architectures using an Olympus BX-60 reflected-light optical microscope with bright-field (BF) and dark-field (DF) imaging and a SZ-CTV Olympus stereoscopic microscope both equipped with an Infinity 2 digital camera. Scanning electron microscopy (SEM) was performed on UV-3D printed nanocomposite-based microstructures with a Carl Zeiss EVO 50 Extended pressure scanning electron microscope (acceleration voltage of 15.00–17.50 kV) to evaluate their surface morphology and the 3D architecture. SEM analysis with energy-dispersive X-ray spectroscopy (EDS) on cryo-fractured samples was performed to evaluate the quality of filler dispersion into the polymer matrix. A low-cost home-assembled 3Drag 1.2 benchtop printer (Futura Elettronica, Italy) incorporating a syringe dispenser (figure 7.1a) equipped with five low-power UV light emitting diodes (LEDs) with light emission peaked at 365 nm and a viewing angle of 20–25° (Aftertech SAS, Italy) was used for UV-3D printing of the nanocomposite microstructures. LEDs were placed at about 30 mm distance from the extruding nozzle, as schematically illustrated in figure 7.1b. Figure 7.1c presents the outline of the system with a schematic representation of the motor driven mechanism that moves the piston pushing the photopolymer out of the nozzle. Print speed and nozzle diameter ranged between 0.1-30 mm/s and 0.2-1.5 mm, respectively. A post-printing UV treatment under nitrogen was carried out using a bromograph (MF 1030, Nuova Delta Elettronica, Italy) with 4 UV-A tubes ($\lambda_{\text{emission}} = 350 \text{ nm}$) with a power of 15 W. Tensile tests were performed on cast and UV-3D printed dumbbell specimens (narrow section 3 mm x 5 mm x 20 mm) at 1 mm/min testing speed on a Zwick- Roell Z010 with a 10 kN load cell and a longstroke extensometer following the American Society for Testing and Materials (ASTM) D638 standard. The specimens with reduced infill density had a 3 mm x 13 mm x 50 mm narrow section. UV-3D printed specimens were obtained by operating the 3D printer at 7 mm/s with a 0.51 mm nozzle. At least three specimens of each type were tested.

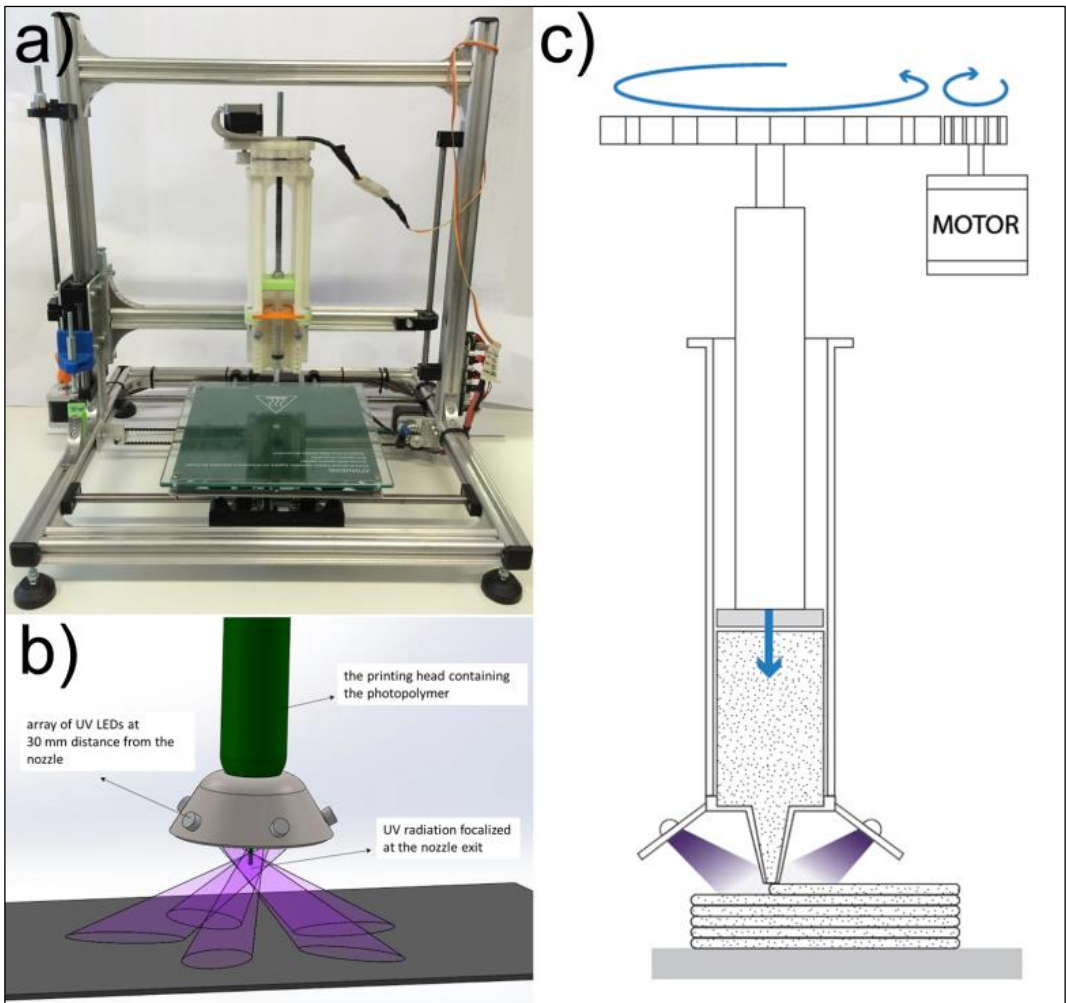


FIGURE 7.1 - A) THE LOW-COST HOME-ASSEMBLED MODIFIED 3D PRINTER EMPLOYED IN THIS WORK. B) RENDERING OF THE PRINTING HEAD EQUIPPED WITH THE ARRAY OF FIVE UV LEDES. C) SCHEMATIC REPRESENTATION OF THE EXTRUSION MECHANISM.

7.3 RESULTS AND DISCUSSION

In order to ensure optimal printability of the liquid nanocomposite dispersions into stable 3D solid structures at the printing nozzle exit, their rheological behavior needs to be comprehensively investigated. To this end, the viscosity of nanocomposite dispersions based on DAR/TMPETA and increasing concentrations of D43B, OX50, and OX200 was determined by isothermal cone-plate rheological measurements. Figures 7.2a-c show the plots of DAR/TMPETA viscosity as a function of shear rate at different filler concentrations (the name of the sample is identified by the acronym indicating the type of filler used, followed by a number indicating the filler concentration as wt%). Four different concentrations were selected for each filler type, so that the viscosity of the resulting polymer composite dispersion was suitable for processing in the UV-3DP apparatus presented in this work. In order to allow for comparisons, the plot of viscosity vs. shear rate for the unloaded DAR/TMPETA resin is also presented.

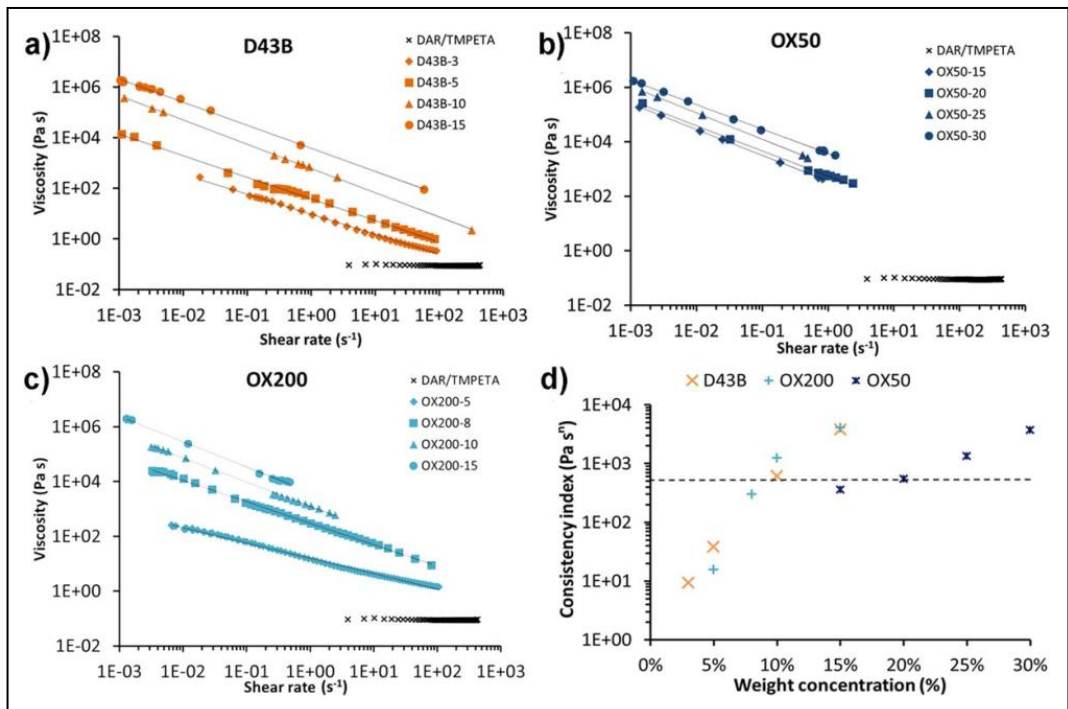


FIGURE 7.2 - VISCOSITY CURVES OF A) D43B, B) OX50, C) OX200 FORMULATIONS AT DIFFERENT FILLER CONCENTRATIONS. D) CORRESPONDING CONSISTENCY INDEXES K AS A FUNCTION OF FILLER CONCENTRATION.

As expected, the pristine resin shows a typical Newtonian behavior, characterized by a constant viscosity for increasing shear-rate values ($\eta \approx 0.09 \text{ Pa s}$ in the $3 - 5 \cdot 10^2 \text{ 1/s}$ shear-rate interval). As opposed to this, all nanocomposite dispersions clearly exhibit a typical shear-thinning response characterized by decreasing viscosity with increasing shear rate, indicating that both fumed silica and dellite strongly interact with the polymer matrix. Such rheological behavior is highly desirable as it allows to enhance the nanocomposite processability through the capillary extrusion nozzle due to the decreased viscosity of the material under the high shear-rate characteristics of the 3D printing process. As shown in the plots, the viscosity curves of all formulations can be very well fitted with a power-law fluid relationship according to the following equation:

$$\eta = K\dot{\gamma}^{n-1} \quad (7.1)$$

The values of the coefficients calculated by means of the power-law equation 7.1 (consistency index K and power-law index n) were used to compare the rheological response of the different nanocomposite formulations. In particular, the power-law index n is related to the slope of the viscosity curve and can therefore provide an indication on the extent of shear-thinning character given to the UV-curable resin by the presence of the inorganic filler. Conversely, the consistency index K gives an indication of the viscosity of the specific formulation at shear rate of 1 1/s. The calculated values of the power-law index n and consistency index K are shown in table 7.1.

	D43B	OX50	OX200
n [-]	3 % n = 0.21	15 % n = 0.05	5 % n = 0.44
	5 % n = 0.15	20 % n = 0.08	8 % n = 0.22
	10 % n = 0.04	25 % n = 0.03	10 % n = 0.12
	15 % n = 0.09	30 % n = 0.10	15 % n = 0.08
K [Pa·s ⁿ]	3 % K = 9.4	15 % K = 360	5 % K = 16
	5 % K = 38	20 % K = 550	8 % K = 300
	10 % K = 610	25 % K = 1300	10 % K = 1200
	15 % K = 3800	30 % K = 3700	15 % K = 4100

TABLE 7.1 - VALUES OF THE POWER-LAW INDEX N AND OF THE CONSISTENCY INDEX K FOR THE FORMULATIONS INVESTIGATED

Due to their shear-thinning behavior, all formulations present power-law indexes $n < 1$ with values slightly higher for the systems with filler concentration below 10 wt% (OX200-5, OX200-8, D43B-3, and D43B-5), likely ascribable to the weaker polymer–filler interactions arising in lightly loaded systems. Conversely, the consistency index K is found to be greatly affected by the concentration and type of inorganic filler. As shown in figure 7.2d where K values calculated for the different nanocomposite formulations by means of Eq. 1 are plotted as a function of filler concentration, a significantly lower increase in filler concentration gives rise to a much sharper increase of consistency index K in the case of OX200 as compared to OX50. In particular, while an over-two-order-of magnitude increase in K is observed for OX200 when its concentration in the

formulation is increased from 5 wt% to 15 wt%, the progressive addition of OX50 to the DAR/TMPETA system in the 15-30 wt% range only results in a tenfold increase in K. These trends can be explained by considering that OX200 fumed silica is characterized by a larger specific surface area than OX50 (200 g/m² vs. 50 g/m², respectively) that is responsible for stronger interactions between the inorganic filler and the polymer host matrix, leading to a more efficient viscosity increase on the UV-curable resin. As also evident from figure 7.2d, the addition of nanoclay filler D43B leads to a similar rheological response as that observed with OX200, likely indicating similar filler–polymer matrix interactions for D43B and OX200.

Based on the values of the consistency index K and the power-law index n for each formulation calculated from Eq. 7.1, it is possible to predict the rheological behavior of the nanocomposite dispersions within the 3D printer extruder using the capillary flow model^{21,22}. First, the apparent shear rate $\dot{\gamma}_{app}$ of the fluid inside a capillary is determined from the Hagen–Poiseuille equation:

$$\dot{\gamma}_{app} = \frac{4Q}{\pi R^3} \quad (7.2)$$

where Q is the volumetric flow rate and R is the radius of the capillary. The actual shear rate $\dot{\gamma}$ be derived using the well-known Mooney-Rabinowitch correction for non-Newtonian fluids (with n being the power-law index calculated from the power-law equation 7.1):

$$\dot{\gamma} = \dot{\gamma}_{app} \frac{3n + 1}{4n} \quad (7.3)$$

Since the volumetric flow rate through the 3D printer nozzle can easily be calculated from the printing speed and nozzle cross section, an allowable process related shear rate interval can be determined for a given material by simply varying the 3D printing speed settings and the nozzle size. Following the theoretical approach presented above, the printability of all dispersions was also practically tested with the 3D printer. Despite the fact that all formulations could be extruded through the various nozzles employed in this work in good agreement with the previous calculations, only some of them showed good printability properties. Indeed, in order to guarantee optimal printing resolution and well defined printed features, the extruded wet filament must retain its integrity right after its deposition onto the printing plate and prior to UV irradiation. As representatively shown in figure 7.3 where an example of UV-3D printed feature is demonstrated (D43B nanocomposite dispersion at increasing filler content – from 3% to 15% – UV-3D printed through a 0.51 mm extrusion nozzle), only nanocomposite formulations with sufficiently high consistency indexes ($K > 550 \text{ Pa}\cdot\text{s}^n$) were found to exhibit optimal printability properties (this printability limit is represented in figure 7.2d as a dotted line).

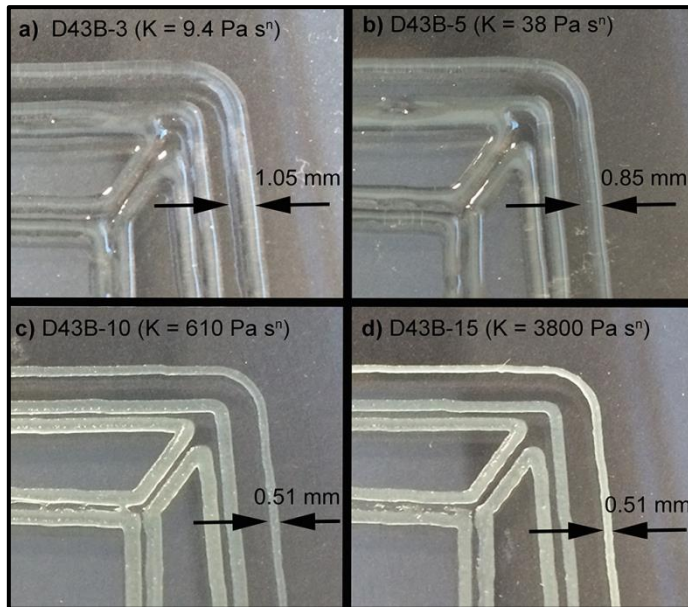


FIGURE 7.3 - A-D) EXAMPLES OF UV-3D PRINTED FEATURES OBTAINED BY UV-3D PRINTING THE D43B NANOCOMPOSITE DISPERSION AT INCREASING FILLER CONTENT – FROM 3 % TO 15 % - UV-3D PRINTED THROUGH A 0.51 MM EXTRUSION NOZZLE. CORRESPONDING CONSISTENCY INDEX VALUES (K) ARE ALSO SHOWN.

In particular, in the case of D43B-3 ($K = 9.4 \text{ Pa}\cdot\text{s}^n$) and D43B-5 ($K = 38 \text{ Pa}\cdot\text{s}^n$) the extruded filament exhibits significant expansion after deposition leading to the formation of printed features with poorly controlled dimensional resolution. The extruded filament size with these systems is found to be 1.05 mm and 0.85 mm for D43B-3 and D43B-5, respectively (see figures 7.3a-b). As opposed to this, in figures 7.3c-d a very well controlled resolution of the printed feature is found for D43B-10 ($K = 610 \text{ Pa}\cdot\text{s}^n$) and D43B-15 ($K = 3800 \text{ Pa}\cdot\text{s}^n$), with a printed filament size equal to the extrusion nozzle size (0.51 mm). Similar trends were observed on all nanocomposite dispersions investigated in this work, irrespective of the type of filler employed, clearly indicating that higher K values are necessary to allow for optimal printability of the nanocomposite dispersions.

In order to characterize the photopolymerization process of the UV-curable resin and the possible effect of the presence of the filler on the thermodynamics and the kinetics of the curing reaction, photocalorimetric measurements were performed on all nanocomposite formulations. The values of enthalpy of polymerization are shown in figure 7.4a as a function of filler type and concentration. In the plot, the measured heat (ΔH) of polymerization has been corrected considering the exact DAR/TMPETA weight fraction present in every formulations during the photocalorimetric scan. Clearly, the presence of the different inorganic fillers has no practical effect on the heat of polymerization of the nanocomposite, as in all cases a ΔH value of approximately 300 J/g is measured, similarly to what observed in unfilled DAR/TMPETA. Slightly lower ΔH values are found in OX200-8, OX200-10, OX200-15, and D43B-15 formulations, likely

ascrivable to the stronger filler-polymer matrix interactions occurring for these high specific surface area fillers at such high concentrations that may partially hinder polymer chain growth during the photopolymerization reaction. However, such counteracting effect is relatively limited, as even for the formulation exhibiting the lowest value of measured heat of polymerization (OX200-15), the conversion of the UV-curing reaction (calculated as the ratio between the enthalpy of reaction for the nanocomposite formulation and the enthalpy of reaction for the unfilled resin) is over 80 %. As opposed to OX200-based and D43B-based nanocomposite systems, no effect on the UV-curing thermodynamics is observed for OX50 nanocomposites, irrespective of filler concentration. In the attempt to investigate the effect of filler type and concentration on the photopolymerization kinetics of the DAR/TMPETA resin, the photocalorimetric scans of resin formulations based on different fillers (D43B, OX200, and OX50) were compared with the photocalorimetric scan of unfilled DAR/TMPETA. Figure 7.4b reports the results for the resin formulations based on the three different fillers at the highest filler concentration examined in this work (D43B-15, OX200-15, and OX50-30). As shown in the plot, all filled systems present similar polymerization kinetics, comparable to what found for the unfilled DAR/TMPETA resin, with the exothermic peak of polymerization found after 4 s from the beginning of the UV exposure.

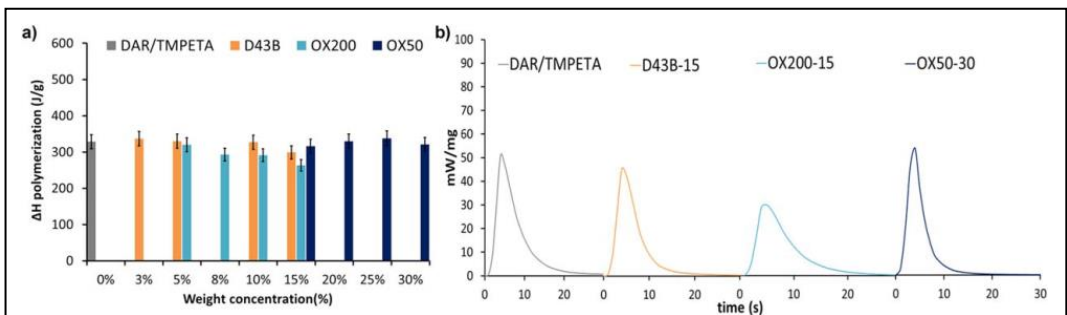


FIGURE 7.4 - A) ENTHALPY OF PHOTOPOLYMERIZATION OF THE UV-CURABLE NANOCOMPOSITES AS A FUNCTION OF FILLER CONCENTRATION. B) PHOTOCALORIMETRIC SCANS OF THE UV-CURABLE RESIN TMPETA/DAR AND OF THE POLYMER-BASED UV-CURABLE NANOCOMPOSITES WITH DIFFERENT FILLER TYPES.

These results clearly indicate that the presence of the filler does not alter significantly the curing speed of the polymer-based nanocomposite at the filler concentrations investigated in this work (which are suitable for 3D printing purposes), thus enabling an effective UV-3D printing process via the rapid UV-induced polymerization of the extruded nanocomposite wet filament. This represents a very favorable feature in view of the UV-3D printing fabrication process of these polymer based nanocomposite formulations. Indeed, the material flowing out from the extrusion nozzle can be polymerized rapidly enough to withstand the subsequent deposition of additional layers of materials without collapsing and to potentially allow for the production of spanning

features. Additionally, the filler concentration in the UV-curable resin may be tuned in such a way that desirable physical characteristics of the system such as the initial nanocomposite fluid viscosity or the mechanical properties of the final 3D printed material may be independently optimized without significantly affecting the UV-curing reaction. On the top of that, the well-known problem of the oxygen inhibition in free radical photopolymers, such as the TMPETA used in this work, was turned into an advantageous feature within our 3D-printing process. As soon as the material was deposited, in fact, the external surface of the filament, that remained unreacted due to the oxygen inhibition, could better adhere to the following layer of photopolymer. Once overlapped, the portions of filament in contact were no longer exposed to oxygen and could then polymerize favoring an optimum interlayer adhesion. This behaviour, irrespective of the formulation tested, led to the realization of multiple layers of material for which delamination would be probably less likely to occur than if a resin not based on free radical photopolymerization was used. Obviously the external surface of the prints remained uncured but a rapid post-printing UV treatment under nitrogen atmosphere fully polymerized the resin. In order to investigate the mechanical response of the nanocomposites with different filler types, dumbbell specimens were UV-3D printed and assessed by means of uniaxial tensile testing. According to the outcomes of the rheological characterization presented in figure 7.2, formulations containing the minimum allowable amount of filler to enable optimal UV-3D printing were selected for the mechanical tests, namely D43B-10, OX50-20, and OX200-10 (i.e., nanocomposite formulations with the lowest filler concentration giving consistency index values K above the printability threshold value represented by the dotted line in figure 7.2d). The conversion of the UV-curing process on samples employed for mechanical testing was evaluated with photocalorimetric experiments by measuring the residual exothermic heat of reaction of the nanocomposite after the UV-3D printing process and by comparing this value with the heat of reaction of the uncured nanocomposite (see figure 7.5). It is worth noting that after UV-3D printing all samples achieved a nearly 100 % crosslinking conversion, as evidenced by the negligible residual exothermic heat of reaction observed on UV-3D printed samples (namely 0 J/g for D43B, 5 J/g for OX200 and 4 J/g for OX50, dotted lines in figure 7.5).

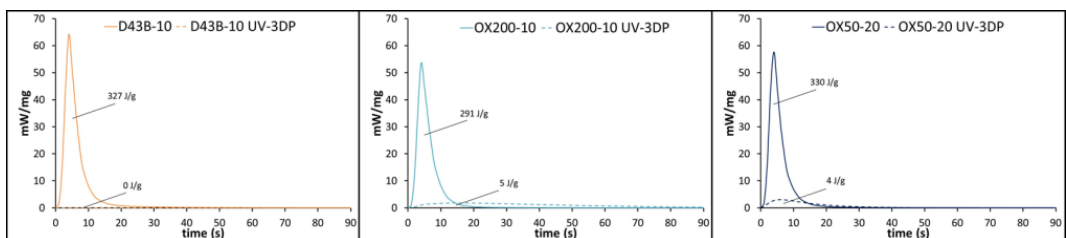


FIGURE 7.5 - PHOTOCALORIMETRIC SCANS OF THE UV-CURABLE NANOCOMPOSITES WITH DIFFERENT FILLER TYPES (LEFT: D43B-10, MIDDLE: OX200, RIGHT: OX50) BEFORE AND AFTER UV-3D PRINTING.

In addition, to evaluate the effect of the filament printing direction on the mechanical properties of the UV-3D printed structures, specimens were fabricated by UV-3D printing both along the longitudinal axis (90° in figure 7.6) and with a 45° mesh-type pattern (45° in figure 7.6). All UV-3D printed specimens were fabricated at the maximum filling density (100 % infill) and their mechanical response was compared with that obtained from OX50-20 and OX200-10 samples realized by mold casting. D43B-10 cast specimens could not be produced due to incomplete polymerization of such samples likely originating from the UV-shielding effect of the nanoclay based filler that partially hampers UV light from being absorbed by the DAR photoinitiator and prevents it from being efficiently used for the UV-curing reaction. Light scattering of D43B particles is likely to be the main cause for such limited polymerization. The UV-shielding effect is more pronounced for larger sample thicknesses as in the case of D43B-10 cast specimens (3 mm thick), while it is relatively negligible in the case of the thin wet filaments (0.2-0.84 mm nozzle diameter) characteristic of the UV-3D printing process. Representative stress-strain curves for the samples investigated here are presented in figure 7.6a, while the average values of elastic modulus, ultimate tensile strength, and deformation at break obtained from the tensile tests on such samples are plotted in figures 7.6b-d, respectively.

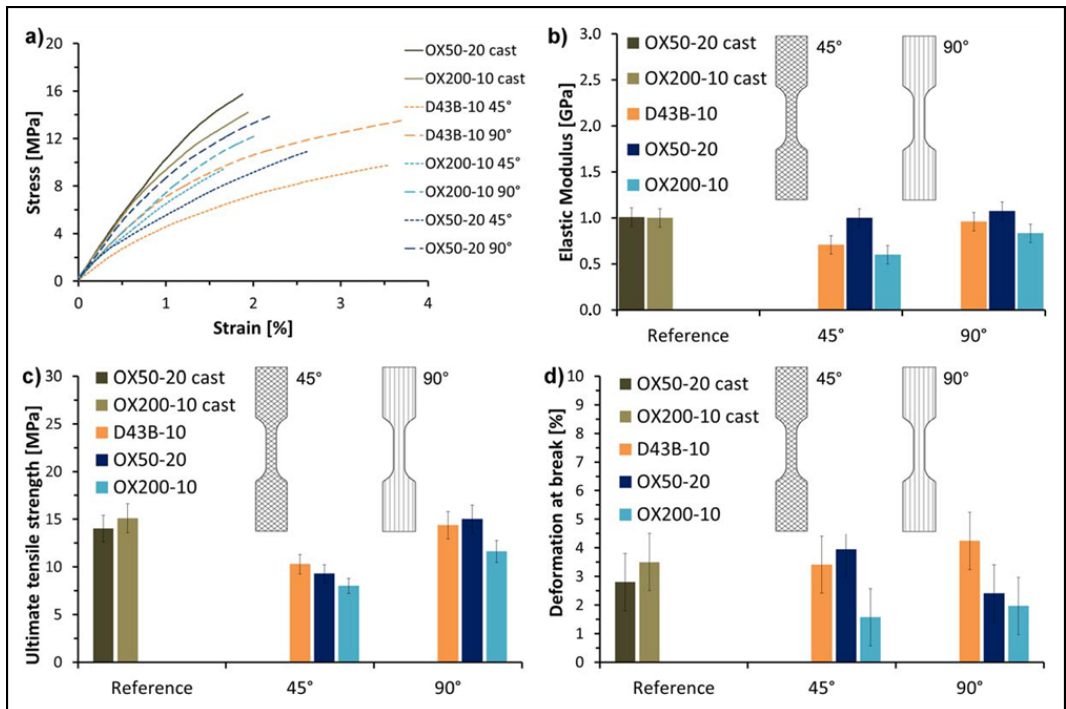


FIGURE 7.6 - A) REPRESENTATIVE STRESS–STRAIN CURVES OF UV-3D PRINTED AND CAST SAMPLES; AVERAGE VALUES OF B) ELASTIC MODULUS, C) ULTIMATE TENSILE STRENGTH, AND D) DEFORMATION AT BREAK.

As evident from figure 7.6b, the elastic modulus of the OX50-20UV-3D printed nanocomposite is comparable with that found for the corresponding cast sample and lies in the 1 GPa range, irrespective of the printing direction employed (45° and 90° printing pattern). As opposed to this, slightly lower values of elastic modulus are reported for OX200-10 UV-3D printed nanocomposites with respect to the homologous cast samples. In addition, D43B-10 materials exhibit elastic modulus values in line with those found in OX200-10 samples. As presented in figures 7.6b and c, the UV-3D printed samples with 90° printing pattern show a slight increase in elastic modulus and ultimate tensile strength compared to samples printed with a 45° printing pattern irrespective of the type of filler employed. In particular, values of ultimate tensile strength comparable to those found for cast samples are obtained in OX50-20, OX200-10, and D43B-10 samples printed with a 90° pattern (15 MPa range), while the corresponding samples printed with a 45° pattern are characterized by lower ultimate tensile strength values in the range between 7 and 10 MPa. These results suggest that the UV-3D printing process potentially allows for customized control of the mechanical properties of the UV-3D printed object by simple modification of the printing direction. Interestingly, all UV-3D printed samples show values of deformation at break in the 2-4 % range which are in close agreement with those obtained from the control cast samples, independently from the printing direction. Only OX200-10/90° nanocomposites seems to give lower deformation at break values, although this may not be statistically significant given the large standard deviations registered for these measurements. It is worth highlighting that the quality of the dispersion of the filler into the polymer matrix was also evaluated by means of SEM analysis on printed nanocomposites at varying filler type (see figure 7.7). By examination of the cryo-fractured surface of the printed nanocomposite samples, a good level of dispersion of the fillers into the UV curable polymer matrix is found even at high filler loading, thus suggesting the absence of any noticeable agglomerates that may affect the mechanical properties of the final printed samples. Thanks to the great design flexibility allowed by the UV-3D printing process, the fabrication of complex shapes with arbitrary patterns can be envisaged.

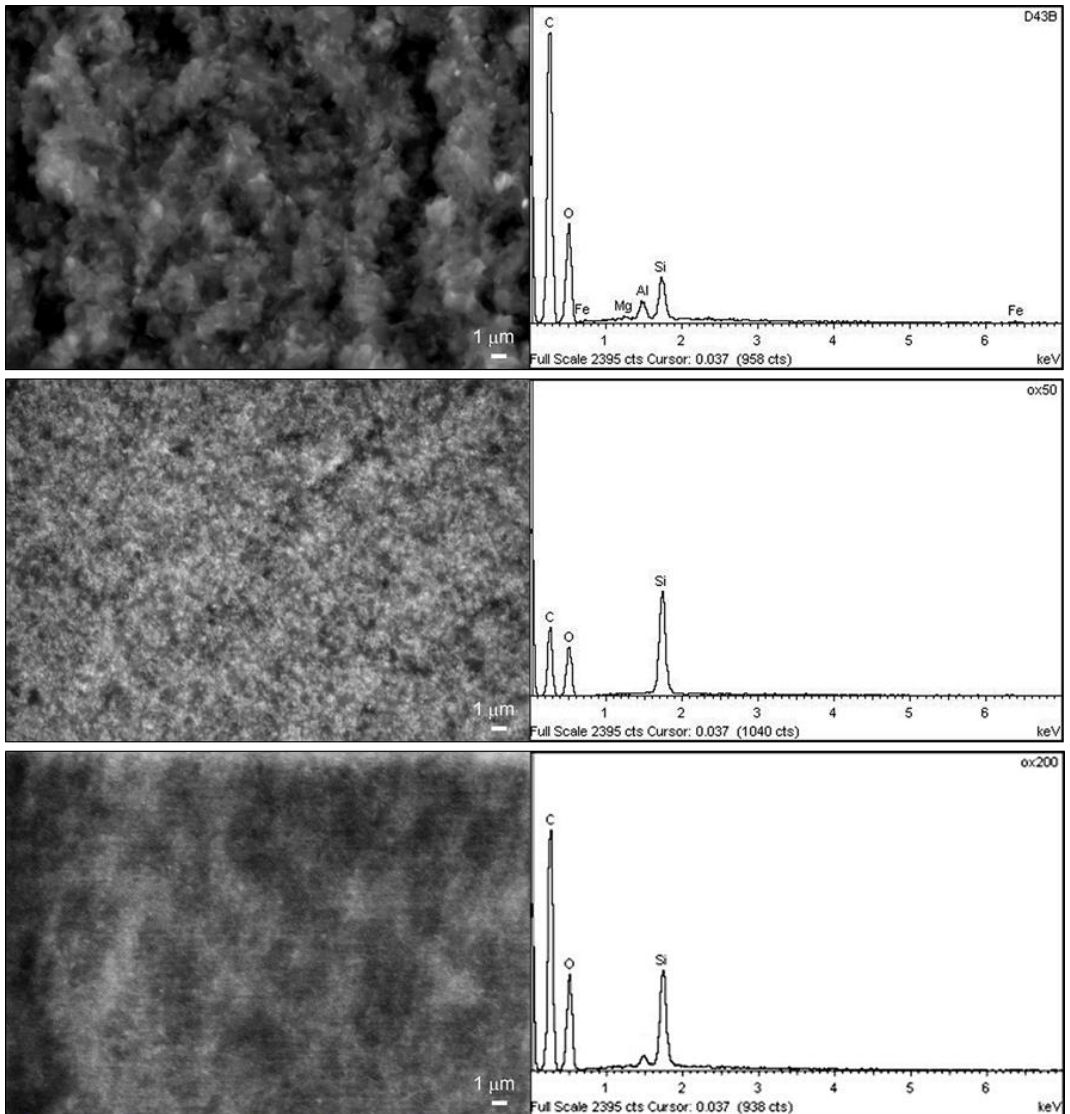


FIGURE 7.7 - SEM MICROGRAPHS OF CRYO-FRACTURED 3D-PRINTED NANOCOMPOSITE SAMPLES (15% D43B – TOP, 30% OX50 – MIDDLE, 15% OX200 – BOTTOM) WITH REPRESENTATIVE EDS ANALYSIS PERFORMED IN THE AREAS WHERE FILLER PARTICLES (WHITE DOTS IN THE IMAGE) ARE FOUND.

Taking inspiration from the natural world²³, cellular specimens with different unit cell geometry (infill pattern) and increasing infill density were realized by UV-3D printing, as shown in figures 7.8a-f where zoomed optical stereoscopic images of the UV-3D printed samples clearly highlight the excellent resolution and printing accuracy achievable with the UV-3D printing setup assembled in this work. In particular, samples with squared and hexagonal networks with three different relative densities (from 0.37 to 0.51) were UV-3D printed from OX200-10 nanocomposite formulation and mechanically characterized by means of uniaxial tensile tests.

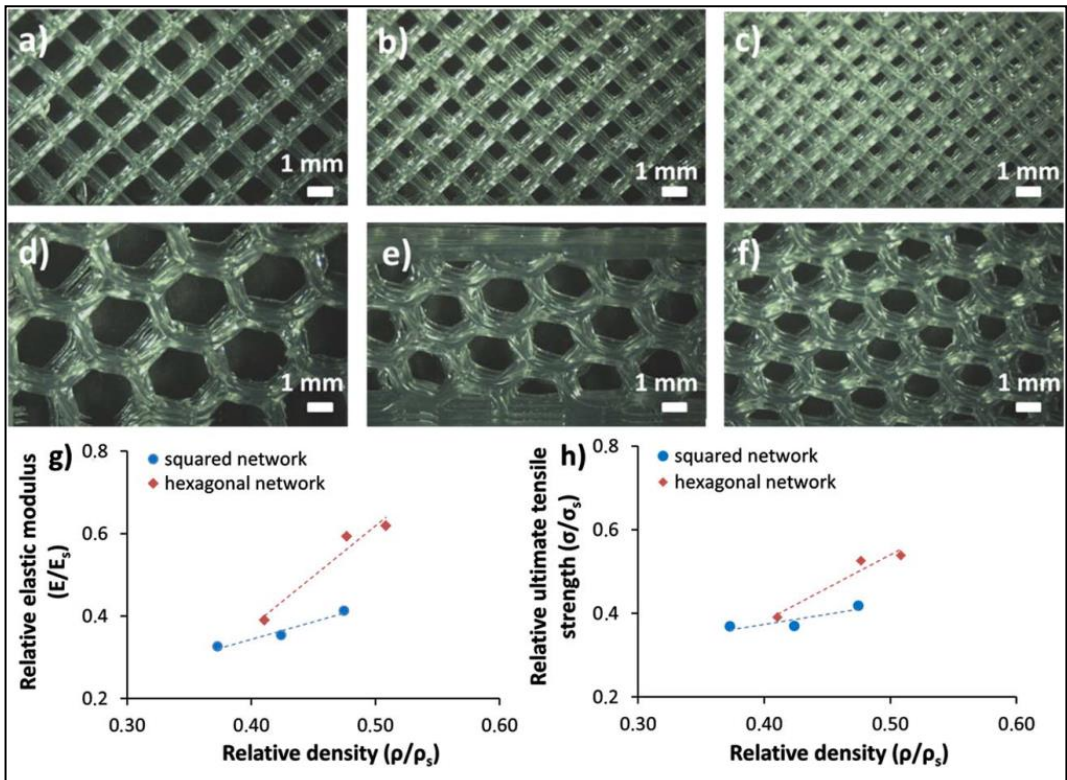


FIGURE 7.8 - A-C) OPTICAL STEREOSCOPIC IMAGES OF THE UV-3D PRINTED SPECIMENS WITH SQUARED UNIT CELL AT INCREASING INFILL DENSITY. D-F) ANALOGOUS IMAGES OF UV-3D PRINTED SPECIMENS WITH HEXAGONAL UNIT CELL. G) PLOTS OF THE RELATIVE ELASTIC MODULUS AND H) RELATIVE ULTIMATE TENSILE STRENGTH AS A FUNCTION OF THE RELATIVE DENSITY OF THE SPECIMENS. DOTTED LINES ARE A GUIDE FOR THE EYE.

Plots of the relative elastic modulus E/E_s and the relative ultimate tensile strength σ/σ_s as a function of the relative density ρ/ρ_s are presented in figures 7.8g and h, where E_s , σ_s , and ρ_s refer to the elastic modulus, tensile strength, and density of the OX200-10 solid material, while E , σ , and ρ are the elastic modulus, tensile strength, and density of the OX200-10 cellular specimen. Both the relative elastic modulus and the relative ultimate tensile strength are found to increase

at increasing relative density irrespective of the unit cell geometry. This trend is in line with the fact that for increasing relative densities, the mechanical behavior of the cellular specimen approaches that of the solid material ($\rho/\rho_s = 1$). Furthermore, the hexagonal unit cell is found to yield higher mechanical properties compared to the square unit cell for comparable values of relative densities, both in the case of the elastic modulus and the ultimate tensile strength. These results are in agreement with the typical mechanical behavior of cellular materials²⁴. These observations lead to the conclusion that the filling pattern takes on a fundamental role in determining the final mechanical properties of the UV-3D printed objects, further highlighting the ability of UV-3D printing to modulate the mechanical behavior of the printed material in a relatively simple, straightforward and versatile fashion. In order to demonstrate the potential of UV-3D printing in processing the nanocomposite dispersions developed in this work, different macrostructures and microstructures were fabricated using a low-cost benchtop 3D printer appropriately modified to accommodate a syringe dispenser feeding with the nanocomposite dispersions an extruding nozzle equipped with five low-power UV LEDs ($\lambda_{\text{emission}} = 365 \text{ nm}$) (figure 7.9a and section 7.2). First, a woven-like microstructure was obtained by UV-3D printing two layers of OX200-10 nanocomposite formulation on top of each other at a printing speed of 20 mm/s. As shown in the optical micrograph presented in figure 7.9b, the filament extrusion resulted in planar solid features of approximately 200 μm average width. The same printing process parameters (printing speed 20 mm/s, layer height 0.1 mm) and nanocomposite dispersion (OX200-10) were used to fabricate a UV-3D printed six layer matrix-like microstructure of approximately 600 mm height, 600 mm lateral size, and filament diameter of 200 μm (figure 7.9c). In addition, the UV-3D printing setup allowed to shift from the layer-by-layer deposition approach to obtain 3D freeform spanning features, as evident from figure 7.9d. In this case, OX200-10 system was employed at 3 mm/s, so as to be able to slow down the 3D printing process, induce rapid UV polymerization of the wet nanocomposite filament, and allow the formation of the spanning features that can cover a few millimeters in length without structural collapses. The fabrication of such 3D microstructures suggests the possibility to employ UV-3D printing to realize complex architectures and structural components at the microscale in a very versatile and straightforward fashion. As a further example of the high flexibility of the UV-3D printing approach combined with the nanocomposite materials presented in this work, macrostructures characterized by increasing levels of transparency/translucency were obtained using the OX200-10 nanocomposite formulation. As shown in figure 7.9e, by carefully controlling the UV-3D printing process parameters (layer height from 0.4 to 0.3 mm, printing speed 5 mm/s, infill density 100 %, and nozzle diameter 0.84 mm), it was possible to produce translucent planar structures with varying degrees of optical transparency, suggesting the potential use of such customizable 3D systems in fields such as optics and optofluidics where optical clarity may represent a requirement.

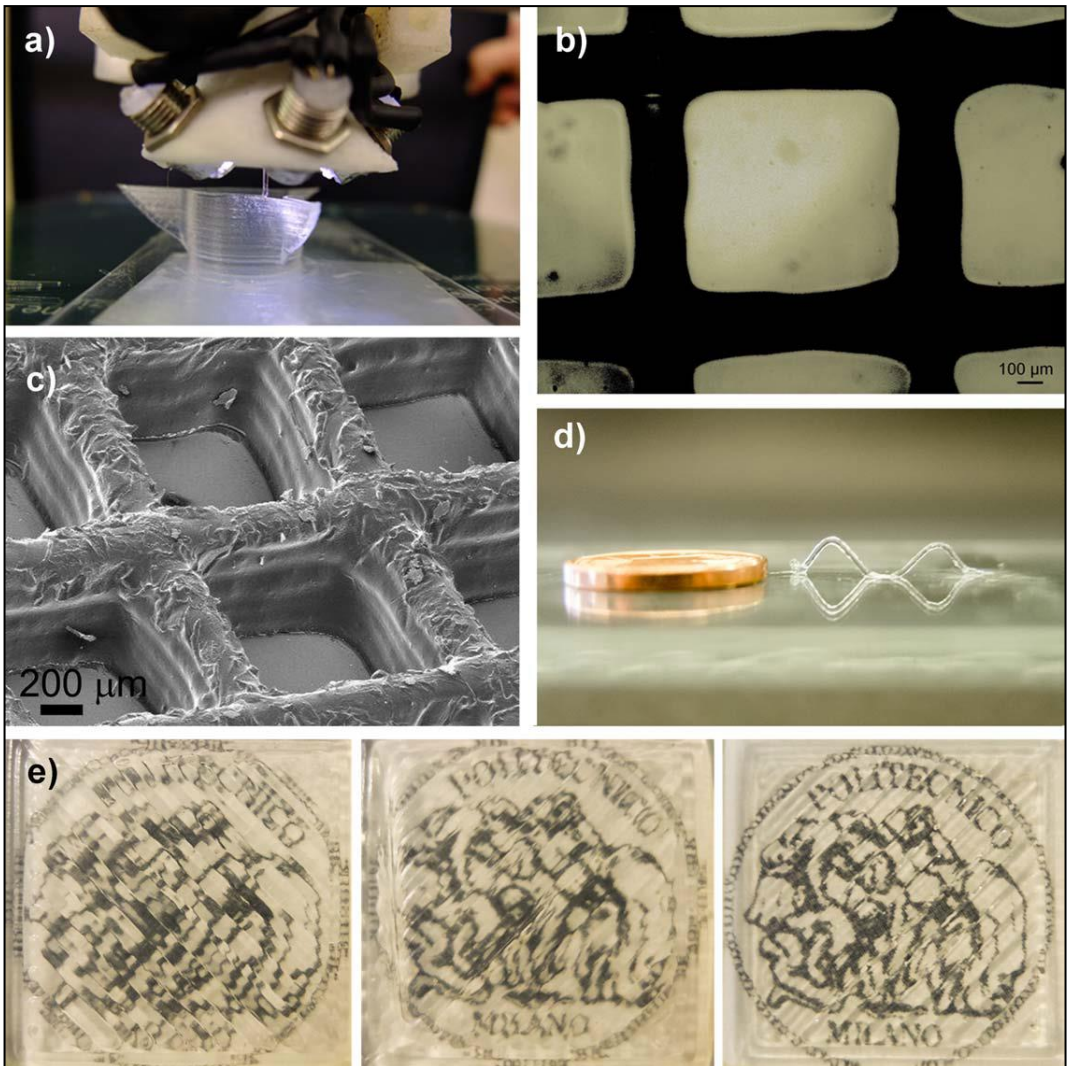


FIGURE 7.9 - A) OPTICAL IMAGE TAKEN DURING THE FABRICATION OF A UV-3D PRINTED MACROSCOPIC OBJECT; B) OPTICAL IMAGE OF A TWO-LAYER WOVEN-LIKE MICROSTRUCTURE; C) SEM IMAGE OF A MULTILAYER MATRIX-LIKE MICROSTRUCTURE; D) UV-3D PRINTED SPANNING FEATURES (A 1 CENT EURO COIN IS REPORTED IN THE IMAGE FOR DIMENSIONAL REFERENCE); AND E) TRANSLUCENT PLANAR STRUCTURES OF INCREASING TRANSPARENCY OBTAINED BY UV-3D PRINTING THE NANOCOMPOSITE DISPERSION WITH DIFFERENT LAYER-HEIGHT SETTINGS.

As a final demonstration of the potential of the nanocomposite dispersions developed in this work, examples of macroscopic UV-3D printed objects were also fabricated, with length scales in the cm range (see figure 7.10), thereby giving a further practical demonstration of the direct applicability of this approach in the field of advanced additive manufacturing.

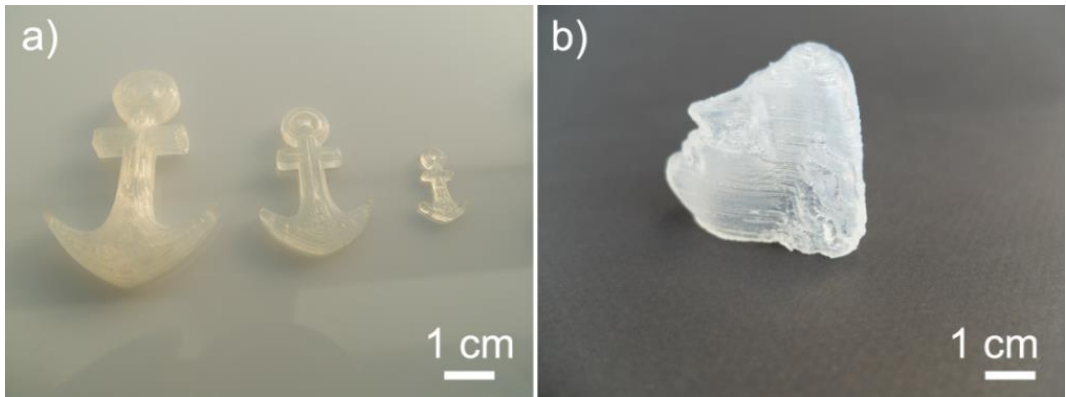


FIGURE 7.10 - EXAMPLES OF UV-3DP MACRO-OBJECTS. A) ANCHORS PRINTED WITH DIFFERENT NOZZLE SIZES; B) SCALED MODEL OF THE HEAD OF THE MILO'S VENUS OBTAINED BY UV-3DP USING A 0.51 MM NOZZLE SIZE.

7.4 CONCLUSIONS

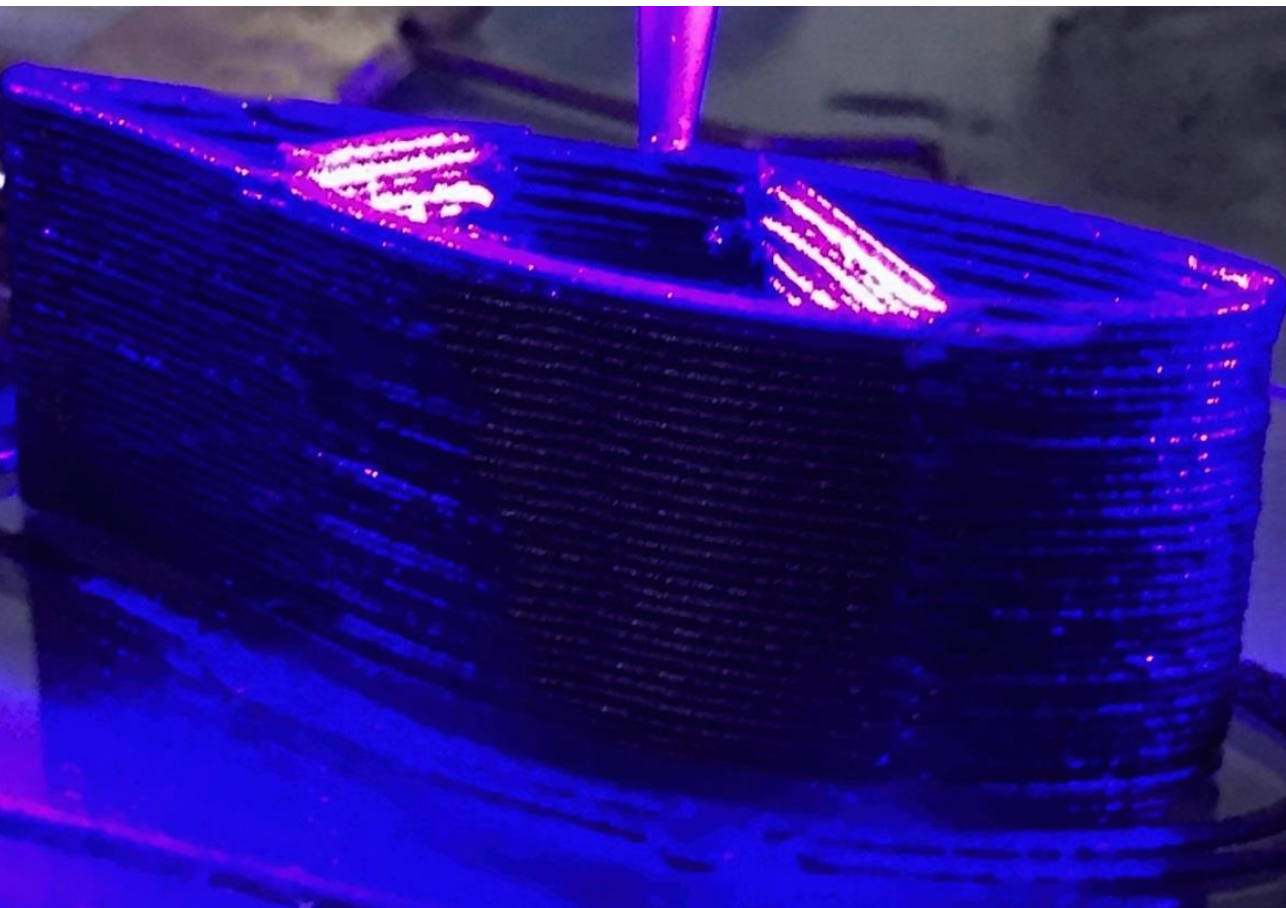
In conclusion, nanocomposites based on a UV-curable polymeric resin and different inorganic fillers were developed in this work for use in UV-3D printing applications. A rheological characterization of the nanocomposite dispersions at varying filler concentration was performed and optimal extrusion and printability parameters for these systems were identified based on the shear rate of the materials at the extrusion nozzle by applying classical power-law fluid relationships and the capillary flow model. Photocalorimetric measurements demonstrated that a very rapid (4 s) curing reaction could be achieved with these systems upon UV-light irradiation, and that the presence of the inorganic fillers did not affect the thermodynamics and kinetics of the UV-curing process of the polymeric matrix. The direct UV-3D printing of such homogeneous solvent-free polymer-based nanocomposite dispersions allowed to investigate the effect of printing direction, infill density, and fill pattern on the mechanical response of UV-3D printed specimens by uniaxial tensile tests. All samples exhibited excellent mechanical properties comparable to those found in the homologous casted materials. In addition, cellular nanocomposite materials were produced with hexagonal or squared unit cells that allowed to demonstrate the possibility to control the mechanical properties of the UV-3D printed materials by simply varying the infill design structure. Finally, examples of 3D macroarchitectures and microarchitectures, spanning features, and planar transparent structures directly formed upon UV-3D printing of such nanocomposite dispersions were reproducibly obtained and demonstrated, clearly highlighting the suitability of these polymeric materials for advanced UV-3D printing applications.

7.5 REFERENCES

1. P. M. Ajayan, L. S. Schadler & P. V. Braun (editors), *Nanocomposite Science and Technology*, Wiley-VCH, Weinheim; 2003.
2. S. Kaur, M. Gallei & E. Ionescu, Polymer-Ceramic Nanohybrid Materials, *Adv. Polym. Sci.* **267**, 143-185 (2015).
3. H. Althues, J. Henle & S. Kaskel, Functional inorganic nanofillers for transparent polymers, *Chem. Soc. Rev.* **36**, 1454-1465 (2007).
4. A. Di Gianni, E. Amerio, O. Monticelli & R. Bongiovanni, Preparation of polymer/clay mineral nanocomposites via dispersion of silylated montmorillonite in a UV curable epoxy matrix, *Appl. Clay. Sci.* **42**, 116-124 (2008).
5. S. Li, M. M. Lin, M.S. Toprak, D. K. Kim & M. Muhammed, Nanocomposites of polymer and inorganic nanoparticles for optical and magnetic applications, *Nano Rev.* **1**, 5214 (2010).
6. M. Vaezi, H. Seitz & S. Yang, A review on 3D micro-additive manufacturing technologies, *Int. J. Adv. Manuf. Technol.* **67**, 1721-1754 (2013).
7. I. Gibson, D. W. Rosen & B. Stucker, *Additive Manufacturing Technologies: Rapid Prototyping to Direct Digital Manufacturing*, Springer; 2010.
8. J. R. Tumbleston, D. Shirvanyants, N. Ermoshkin, R. Januszewicz, A. R. Johnson, D. Kelly, K. Chen, R. Pinschmidt, J. P. Rolland, A. Ermoshkin, E. T. Samulski & J. M. DeSimone, Continuous liquid interface production of 3D objects, *Science* **347**, 1349-1352 (2015).
9. V. Petrovic, J. V. Haro Gonzalez, O. Jordá Ferrando, J. Delgado Gordillo, J. R. Blasco Puchades & L. Portoles Griñan, Additive layered manufacturing: sectors of industrial application shown through case studies, *Int. J. Prod. Res.* **49**, 1061-1079 (2011).
10. B. C. Gross, J. L. Erkal, S. Y. Lockwood, C. Chen & D. M. Spence, Evaluation of 3D Printing and Its Potential Impact on Biotechnology and the Chemical Sciences, *Anal. Chem.* **86**, 3240-3253 (2014).
11. L. L. Lebel, B. Aïssa, M. A. El Khakani & D. Therriault, Ultraviolet-Assisted Direct-Write Fabrication of Carbon Nanotube/Polymer Nanocomposite Microcoils, *Adv. Mater.* **22**, 592-596 (2010).
12. R. D. Farahani, H. Dalir, V. Le Borgne, L. A. Gautier, M. A. El Khakani, M. Lévesque & D. Therriault, Direct-write fabrication of freestanding nanocomposite strain sensors, *Nanotechnology* **23**, 085502 (2012).

13. B. Aïssa, D. Therriault, R. D. Farahani, L. L. Lebel, and M. A. El Khakani, Electrical transport properties of single wall carbon nanotube/polyurethane composite based field effect transistors fabricated by UV-assisted direct-writing technology, *Nanotechnology* **23**, 115705 (2012).
14. L. L. Lebel, B. Aïssa, M. A. El Khakani & D. Therriault, Preparation and mechanical characterization of laser ablated single-walled carbon-nanotubes/polyurethane nanocomposite microbeams, *Compos. Sci. Technol.* **70**, 518-524 (2010).
15. G. Postiglione, G. Natale, G. Griffini, M. Levi & S. Turri, Conductive 3D microstructures by direct 3D printing of polymer/carbon nanotube nanocomposites via liquid deposition modeling, *Composites Part A* **76**, 110-114 (2015).
16. R. D. Farahani, H. Dalir, V. Le Borgne, L. A. Gautier, M. A. El Khakani, M. Lévesque & D. Therriault, Reinforcing epoxy nanocomposites with functionalized carbon nanotubes via biotin–streptavidin interactions, *Compos. Sci. Technol.* **72**, 1387 (2012).
17. R. D. Farahani, L. L. Lebel & D. Therriault, Processing parameters investigation for the fabrication of self-supported and freeform polymeric microstructures using ultraviolet-assisted three-dimensional printing, *J. Micromech. Microeng.* **24**, 055020 (2014).
18. S. Ahn, M. Montero, D. Odell, S. Roundy & P. K. Wright, Anisotropic material properties of fused deposition modeling ABS, *Rapid Prototyping J.* **8**, 248-257 (2002).
19. B. M. Tymraka, M. Kreigerb & J. M. Pearce, Mechanical properties of components fabricated with open-source 3-D printers under realistic environmental conditions, *Mater. Des* **58**, 242-246 (2014).
20. B. G. Compton & J. A. Lewis, 3D-Printing of Lightweight Cellular Composites, *Adv. Mater.* **26**, 5930-5935 (2014).
21. H. A. Barnes, J. F. Hutton & K. Walters, *An Introduction to Rheology*, Elsevier; 1997.
22. J. Bruneaux, D. Therriault & M. Heuzey, Micro-extrusion of organic inks for direct-write assembly, *J. Micromech. Microeng.* **18**, 115020 (2008).
23. X. Xu, L. Heng, X. Zhao, J. Ma, L. Lin, & L. Jiang, Multiscale bio-inspired honeycomb structure material with high mechanical strength and low density, *J. Mater. Chem.* **22**, 10883-10888 (2012).
24. M. F. Ashby, The Mechanical Properties of Cellular Solids, *Metall. Trans.* **14A**, 1755-1769 (1983).

8.
3D-Printable
carbon fiber reinforced polymer
composites
with dual-cure
sequential interpenetrated polymer
networks



Published in: *Polymer* 91 (2016) 174-179.

"3D-printable CFR polymer composites with dual-cure sequential IPNs".

Authors: Gianmarco Griffini, Marta Invernizzi, Marinella Levi, Gabriele Natale, Giovanni Postiglione, Stefano Turri.

8.1 INTRODUCTION

The interest in 3D printing from the manufacturing industry has risen considerably in the last few years due to the many appealing features of this technology, such as its ability to realize complex geometries, the ease of personalization of the manufactured product, and the potential logistical advantages offered by the diffuse manufacturing paradigm. As a consequence, the demand for tailored 3D-printable materials with improved structural and functional properties is continuously growing, with polymers still playing a dominant role¹⁻⁵. In many fields, 3D-printing by fused deposition modeling (FDM) is widely used as rapid prototyping technology, in which thermoplastic polymer filaments (ABS, PLA, and a few others) are employed as structural inks. In order to shift away from the mere production of prototypes, more performing materials, especially in terms of mechanical and thermal properties, are required. Some attempts were made to reinforce thermoplastics with fillers, short fibers or post processing techniques. Despite some observed increase in materials performance, these strategies still rely on the FDM technology^{6,7} and on the consequent need to process pre-extruded filaments. Along with FDM technology, ultraviolet-assisted 3D (UV-3D) printing has been more recently proposed and developed for the fabrication of a variety of 3D microstructures with peculiar properties^{8,9}. This technology consists in the additive deposition of layers of a photocurable liquid polymer, which is crosslinked by an external UV light source as soon as it flows out of the nozzle during the printing process. The photocurable liquid precursor can be easily modified by formulation according to the desired final material properties. To this end, the use of embedded nano- and micro-particles has been demonstrated, leading to the production of reinforced components, conductive microstructures and microcoils⁸⁻¹¹. However, this technology has not yet been exploited for the fabrication of fiber-reinforced composites to date. This is partially due to the fact that UV-3D printing strictly requires materials with fast curing kinetics and loading with non-transparent particles or fibers may influence the UV light transmission through the sample, causing the inhibition of the polymerization or drastically slowing down its rate^{12,13}. Moreover, UV curable resins often do not offer sufficiently high mechanical properties to be used for the fabrication of high performance fiber-reinforced composites. In the light of the above considerations, the development of engineered polymeric systems capable to form sequential interpenetrating polymer networks (IPN) by dual-cure mechanisms can mechanical properties can be achieved when multifunctional polymers are entangled at the nanometric scale as in IPNs. Indeed, their peculiar chemical structure and morphology has favored their widespread diffusion in a variety of applications¹⁴⁻¹⁹. In this communication, we report on an easily 3D-printable carbon fiber reinforced (CFR) polymer composite formulation based on a new photo-thermocurable IPN

system. The material is successfully processed to form stable 3D structures by using a low cost, home-modified UV-3DP apparatus. A subsequent thermal treatment of the UV-3D printed object is performed to complete the crosslinking process and achieve full mechanical properties. Dual-cure resins have already been used for rapid prototyping, including the manufacturing of carbon fiber materials via photolithography²⁰ and stereolithography²¹. However, to the best of our knowledge, this is the first report on the direct UV-3D printing of CFR polymer composites with an IPN-based dual-cure ink.

8.2 EXPERIMENTAL SECTION

8.2.1 MATERIALS

Bisphenol A diglycidyl ether (DGEBA), 1,1-dimethyl, 3-(3',4'-dichlorophenyl) urea (Diuron™), dicyandiamide (DICY), and fumed silica (200m²/g, primary particle size distribution 8-20 nm, OX200 throughout the manuscript) were purchased from Sigma-Aldrich and used as received. Bisphenol A ethoxylate diacrylate (SR349) was kindly provided by Arkema, whilst the photoinitiator 2,4,6-trimethylbenzoylphenyl phosphinate (Irgacure TPO-L, TPO-L throughout the manuscript) was obtained from BASF. Carbon fibers were kindly provided by Zoltek (Panex™ 30 milled Carbon Fibers, 99% carbon, density 1.8 g/mL, fiber diameter 7.2 μm, fiber length 100-150 mm).

8.2.2 RESIN AND COMPOSITE FORMULATION AND CURING

Formulations were obtained by liquid blending the photocurable acrylic resin and the thermocurable epoxy resin with suspended hardener (DICY) and accelerator (Diuron™). The photocurable acrylic resin was a stock solution of SR349 doped with 3 wt% TPO-L mixed under magnetic stirring at room temperature for 30 min (indicated as p-A resin in the following). For the epoxy resin formulation (t-E resin in the following), 20 g of liquid DGEBA, 1.36 g (6.19% w/w) of DICY and 0.66 g (3% w/w) of Diuron™ were poured into a beaker, stirred at 100 °C for 1 h and then mixed with an ultrasonicator tip (Sonic & Materials VCX130, power 130 W, frequency 20 kHz) to form a finely dispersed suspension. The epoxy system behaves as a monocomponent since no reaction occurs until the insoluble DICY remains phase separated (that is for T < 150 °C). The final dual-cure formulation was obtained by mixing the p-A resin and the t-E resin under magnetic stirring at 70 °C for 30 min at a 1:1 weight ratio (M50 sample). Characterizations concerning IPN systems were mostly performed on M50 formulation. For 3D printing tests, four other formulations were developed with increasing weight concentrations of p-A component, namely 5 %, 10 %, 15 % and 20 % by weight (indicated as M5, M10, M15, M20 in the following). Since the two starting resins and their blends are essentially low viscosity Newtonian liquids, depositing them from the syringe dispenser of the 3D printer resulted into a significant lateral spreading with poor control of 3D geometries. In order to solve this issue, a fixed amount of fumed silica (7% w/w) as thixotropic additive was added to all the formulations, making them suitable for 3D printing. The CFR composites for 3D printing were based on M50 formulation and were obtained by adding 5 % and 30 % w/w of carbon fibers (CF5 and CF30 samples, respectively). The thermal curing cycle after 3D-printing was carried out at 220 °C for 20 min in a ventilated oven.

8.2.3 CHARACTERIZATION TECHNIQUES

The thermal characterization of the IPN system and its precursors was performed using a differential scanning calorimeter (DSC). DSC scans were carried out on a Mettler-Toledo DSC/823e instrument, indium and n-hexane calibrated, heating from 20 °C to 250 °C with a rate of 20 °C/min in N₂ environment. Photocalorimetric tests were carried out at ambient temperature on 10-50 mg samples by coupling the DSC instrument with a UVA light source (Lightningcure LC8 by Hamamatsu, 98 mW/cm², 300-450 nm wavelength range) under N₂ atmosphere. The heat of reaction was obtained by integration of the resulting exotherms. Dynamic mechanical analyses (DMA) in three-point bending mode were carried out on a Mettler Toledo DMA/SDTA861 instrument at ambient temperature in strain sweep, and in dynamic scans from 20 °C to 250 °C at a heating rate of 3 °C/min. The frequency was kept constant at 1 Hz. Scanning electron microscopy (SEM) was performed on fractured M50 surfaces with a Carl Zeiss EVO 50 Extended Pressure scanning electron microscope (acceleration voltage of 15.00e17.50 kV) to evaluate the IPN morphology. Samples were subjected to an alkaline etching (10 % KOH in methanol for 1 h at 60 °C) to selectively remove or damage the acrylic phase.

8.2.4 3D-PRINTING EXPERIMENTS

A low-cost, home-assembled 3Drag 1.2 benchtop printer (Futura Elettronica, Italy) incorporating a syringe dispenser equipped with two 3W UV-A torches (WF-501B by Ultrafire Ltd, China) with light emission peaked at 405 nm was used for UV-3D printing the IPN composites (M5-M50, CF5, CF30). Print speed ranged between 1 and 10 mm/s and a 0.84 mm nozzle diameter was used. An image of the set-up used is shown in figure 8.1. The image of the 3D-object to be fabricated is shown in figure 8.2a. It was designed using “SolidWorks” software (Dassault Systèmes, France) to test the ability to print cantilevered geometries with different inclinations. In order to process the 3D model, the open source slicing software “Cura” (Ultimaker B.V., Holland) was used, and the printing test was carried out using spiral slicing option and a single wall thickness.

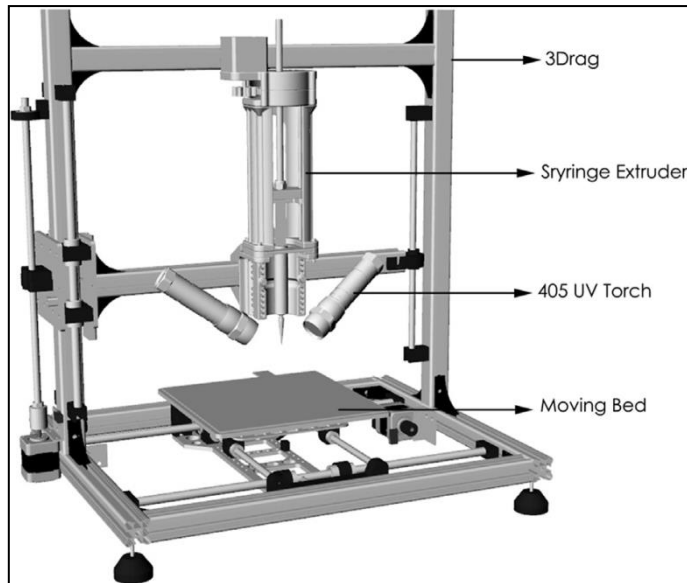


FIGURE 8.1 - SCHEMATIC REPRESENTATION OF THE UV-3D PRINTING EQUIPMENT EMPLOYED IN THIS WORK.

8.3 RESULTS AND DISCUSSION

The 3D-printing processability of the acrylic-epoxy IPN formulations and corresponding composites was assessed. All the formulations from M5 to M50 were loaded into the syringe, and printed in the attempt to reproduce the target 3D model whose frontal projection is presented in figure 8.2a. Such 3D model is constituted by a vertical column with overhanging features with angles ranging from 50° at the bottom to 20° at the top. The smaller the inclination angle the more challenging it is to print the material via layer-by-layer deposition without incurring into resin sagging or spreading. Therefore, this 3D model represents a convenient test designed to verify the ink processability while printing complex parts. During the printing process, it was found that all formulations were able to flow out of the nozzle and harden upon exposure to the UV sources embedded into the 3D printer (figure 8.1). The results of the printing tests on samples M5-M20 and CF5 are presented in figure 8.2b-e. The sample M5, containing only 5 % w/w of photocurable p-A resin, remained too soft after the photocuring process. Therefore, this ink did not allow to obtain a complete UV-3D print of the 3D target model, as already the first 45° overhang was found to show some visible structural imperfections (figure 8.2b). By increasing the p-A concentration to 10 % w/w (M10, figure 8.2c) and 15% w/w (M15, figure 8.2d) the printing quality was found to improve considerably as the material showed a solid-like behavior after UV exposure. The UV-3D printed model objects obtained with these formulations were very similar and only showed some visible structural defects during the top 20° overhang which could thus not be completely printed. On the other hand, the M20 ink allowed for a successful 3D printed reproduction of the target 3D model (figure 8.2e), thus demonstrating that a 1:5 weight ratio between p-A and t-E constitutes the minimum photopolymer concentration needed to reach optimal printing performance even in the presence of steeply overhanging parts. When considering carbon-fiber reinforced (CFR) composites, it was found that a higher fraction of photocurable resin was needed for correct ink processing, likely due to the presence of the black carbon fibers that are responsible for a lower photopolymerization efficiency. For this reason, all the experiments with CFR composites were performed based on M50 as resin matrix. As shown in figure 8.2f, UV-3D printing of CFR composites based on CF5 formulation could be successfully demonstrated up to an overhang of 30°. Optical microscopy analysis on the deposited CF5 liquid filament (before curing) showed that a portion of the carbon fibers embedded in the polymeric matrix maintains their structural integrity upon 3D printing without breaking apart, in addition to appearing partially oriented in the direction of the extrusion (figure 8.2g). This observation is also confirmed by optical microscopy image of the fractured surface that shows clear alignment of the carbon fibers in the proximity of the fracture (figure 8.2h). In the case of CF30 material, the viscosity was found to be too high to allow for an easy 3D deposition from the printer nozzle, and only simpler flat specimens suitable for further mechanical testing were realized.

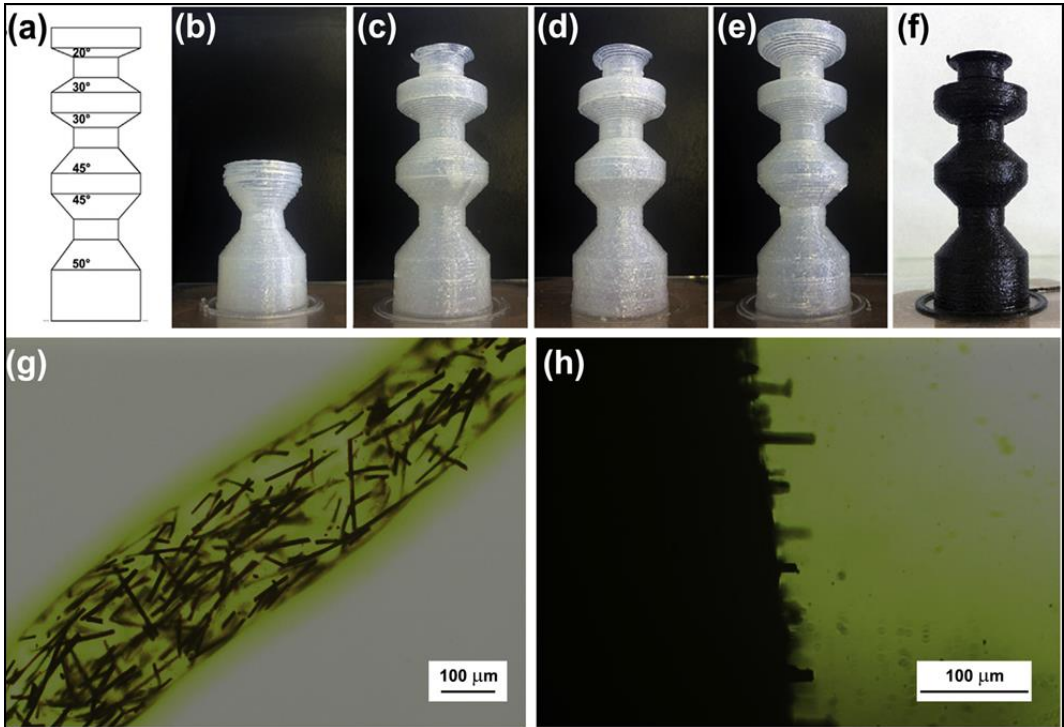


FIGURE 8.2 - (A) LAYOUT OF THE TARGET 3D MODEL USED TO ASSESS THE PRINTABILITY OF THE INKS DEVELOPED IN THIS WORK; UV-3D PRINTED REPRODUCTION OF THE TARGET MODEL USING (B) M5, (C) M10, (D) M15, (E) M20, AND (F) CF5; OPTICAL MICROSCOPY IMAGE OF (G) CF5 LIQUID FILAMENT AND (H) CRYO-FRACTURED UV-3D PRINTED CF5 SURFACE.

Furthermore, printed specimens from this ink only showed a semisolid behavior immediately after printing, calling for the need of a subsequent exposure to UV-A to dry them completely before the final thermal treatment. The photocuring process and the photopolymerization conversions were investigated by photocalorimetric measurements, and the results are shown in figures 8.3a-d. The enthalpy of polymerization of CF5 system was found to be about 111 J/g (figure 8.3b), which accounts for 92.5% of the enthalpy of polymerization reported for the unfilled M50 resin (figure 8.3a). This difference could be likely attributed to the presence of carbon fibers in the CF5 system that may partially prevent full access of the UV radiation to the photocurable resin, thus lowering the total heat of reaction. The same CF5 material after the 3D-printing cycle showed a residual enthalpy of 16 J/g (figure 8.3c), that corresponds to an apparent photocuring conversion after the UV-3D printing process of about 85 %. The photocuring conversion after UV-3D printing found for the 30CF composite system was significantly lower (51 % after normalization by the effective fraction of UV-curable component). This behavior can be very likely ascribed to a strong UV-absorbing action of the highly concentrated carbon fibers present in this formulation.

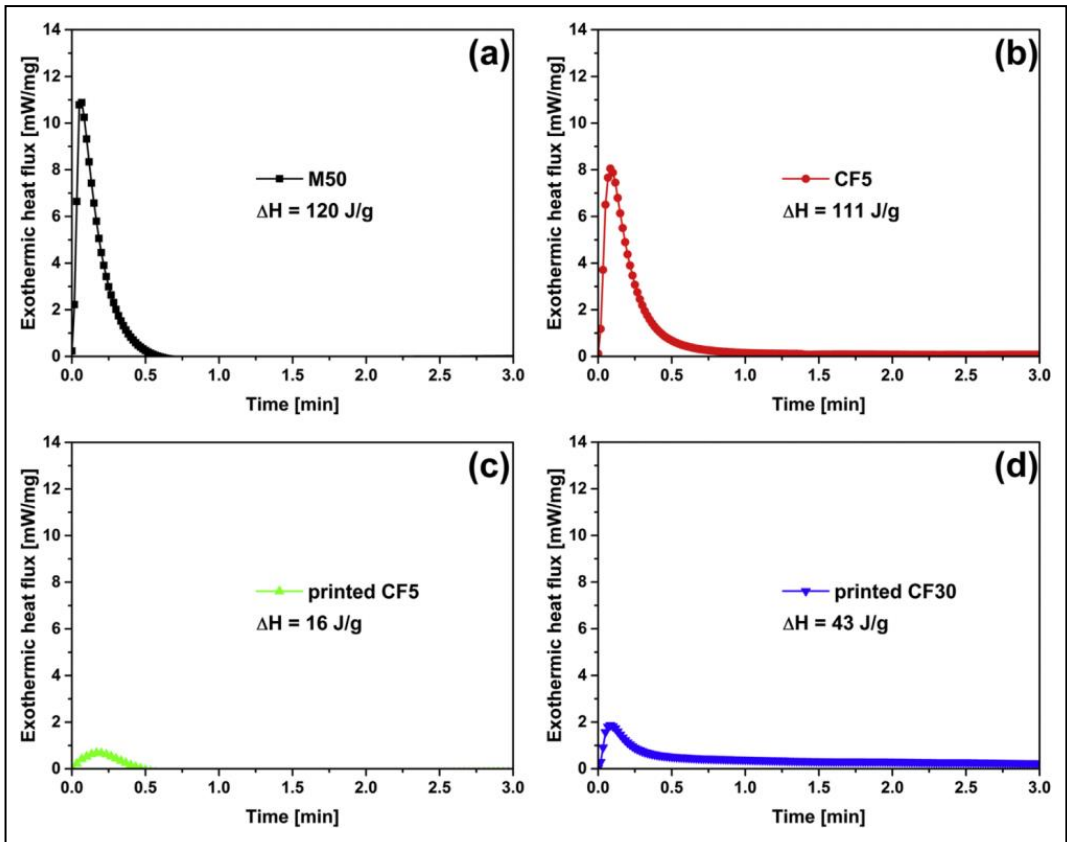


FIGURE 8.3 - PHOTOCALORIMETRIC (PHOTO-DSC) SCANS. A) M50 FORMULATION BEFORE PRINTING. B) CF5 FORMULATION BEFORE PRINTING. C) PRINTED CF5 FORMULATION. D) PRINTED CF30 FORMULATION.

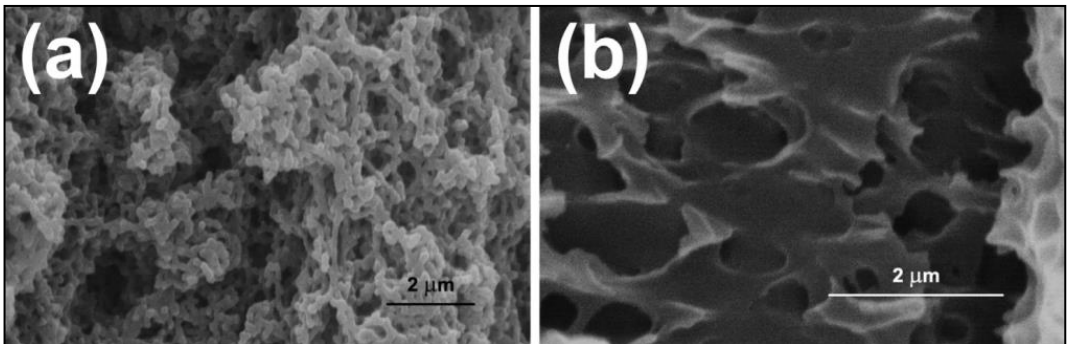


FIGURE 8.4 - SEM IMAGES OF FRACTURED SURFACE OF UV-3D PRINTED M50 SAMPLES AFTER ALKALINE ETCHING.

In order to investigate the morphology of the obtained dual-cure resins and 3D printed parts, SEM images were taken on the M50 sample after fracture and subsequent exposure to a 10 % w/w solution of KOH in methanol for 1 h at 60 °C to selectively etch the acrylic phase (figure 8.4). Clearly, a highly interconnected IPN structure is formed upon full dual-curing with typical sizes ranging from 10^1 to 10^2 nm.

The mechanical behavior and thermal transitions of the developed dual-cure inks were preliminarily investigated by means of DMA and DSC analyses. Results are summarized in table 8.1, where the experimental values for the storage modulus E' at room temperature and the temperature at the $\tan\delta$ peak as obtained from DMA as well as the glass transition temperature (T_g) as measured via DSC are presented. As it appears from table 8.1, a significant increase of both T_g (from 73 °C to 115 °C) and storage modulus (from 2.5 GPa to 3.0 GPa) can be obtained by re-formulating the UV curable resin in the form of an IPN dual-cure system. In addition, one single T_g was observed in the IPN system, as a further demonstration of the excellent structural homogeneity of the materials¹⁸.

	p-A resin	M50	CF5	CF30
E' (25 °C, GPa)	2.5 ± 0.2	3.0 ± 0.4	3.8 ± 0.2	7.7 ± 0.2
Max $\tan\delta$ (°C)	73	115	139	76
T_{gDSC} (°C)	37	103	n.d.	n.d.

TABLE 8.1 - STORAGE MODULUS E_0 AND TEMPERATURE AT THE $\tan\delta$ PEAK AS OBTAINED FROM DMA, AND T_g VALUE OBTAINED FROM DSC MEASUREMENTS OF CROSSLINKED RESINS AND CFR COMPOSITES.

High storage moduli were measured also for the CFR composites (3.8 GPa and 7.7 GPa for the CF5 and CF30 composite formulations, respectively). The measured data were compared with those predicted by the Halpin-Tsai model for random, discontinuous fiber reinforced composites²².

$$E = E_m \frac{1 + \eta\zeta v_f}{1 - \eta v_f} \quad (8.1)$$

$$\eta = \frac{E_f/E_m - 1}{E_f/E_m + \zeta} \quad (8.2)$$

with E , E_m , ζ , v_f and E_f being the modulus of the composite material, the modulus of the matrix, the fiber aspect ratio, the volume fraction of the fibers and the modulus of the fiber, respectively. Eq. (8.1) was fitted using the storage modulus of the carbon fibers $E_f = 200$ GPa and $\zeta = 2 l/d = 13.8$, where l and d are the length and the diameter of the reinforcing fiber, respectively. Measured moduli for composites were found to be systematically lower than the limiting theoretical values obtained from the Halpin-Tsai model. In particular, a theoretical value of storage modulus of 5.6 GPa was calculated for the CF5 composite systems, as opposed to a

measured value of 3.8 GPa. Larger differences were observed for the CF30 system that showed a theoretically predicted storage modulus of 19.8 GPa compared to an experimentally measured value of 7.7 GPa. A possible explanation for such discrepancies may lie in the likely and unavoidable overestimation of fiber aspect ratio l/d in the actual samples (some fibers are clearly broken during the printing process as shown in figure 8.2). In addition, in the case of the CF30 composite system, the unusually low value of T_g measured for this material may also play a role as this may be related to non-complete crosslinking and thus lower storage modulus. Nevertheless, the values found experimentally on the systems investigated in this work are in good agreement with experimental results reported in the literature on composites systems with the same type of reinforcing fibers²³⁻²⁵.

8.4 CONCLUSION

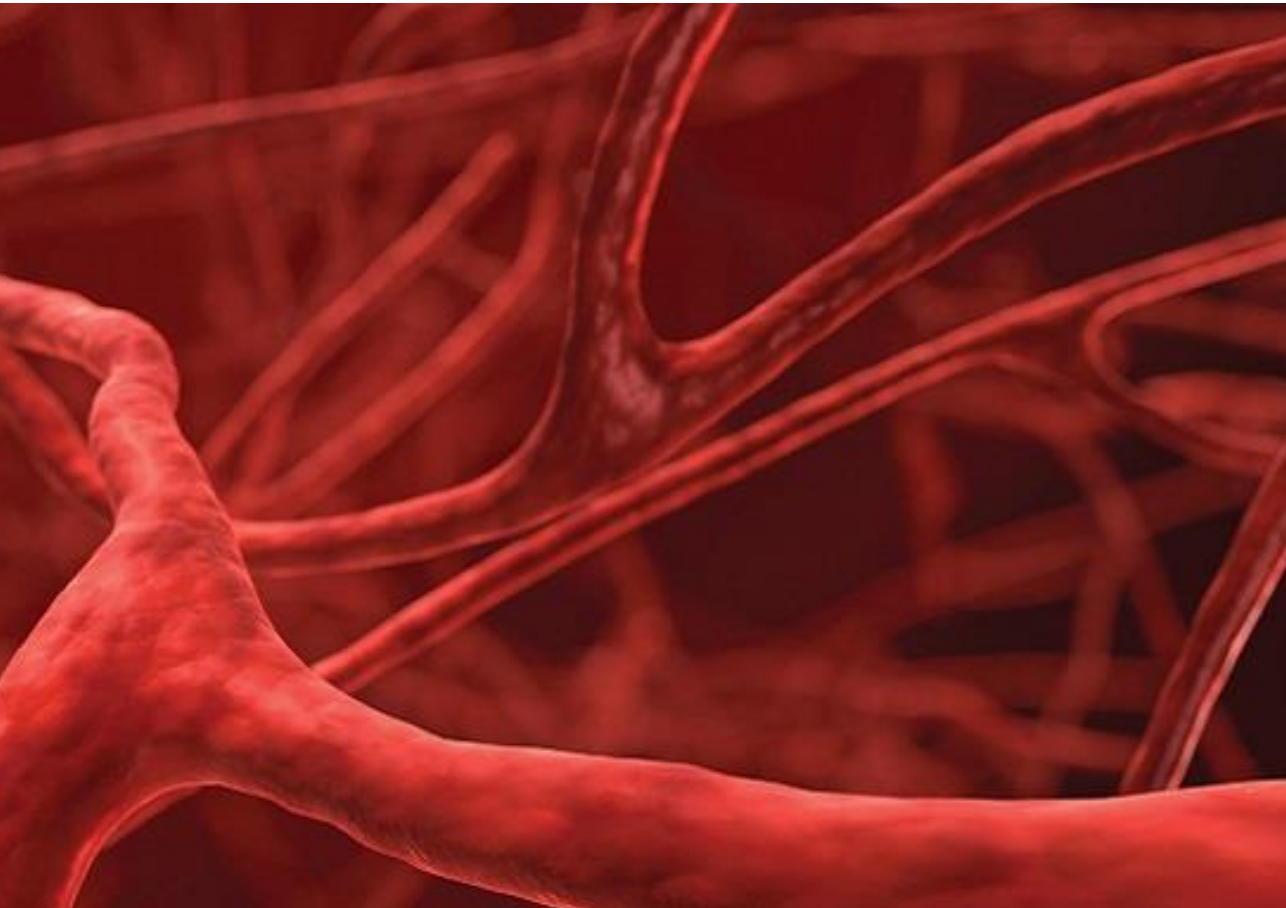
In conclusion, a new dual-cure IPN system was presented in this work obtained by blending a photocurable acrylic resin and a thermally reactive epoxy resin. The very fast UV-curing kinetics of the photocurable resin makes the IPN system very suitable for a rapid UV-assisted 3D printing, whilst the following thermal curing of the epoxy component confers enhanced thermo-mechanical properties to the printed part. The 3D-printing tests suggested that the weight ratio between the photocurable and the thermally curable components in the IPN system strongly influences the behavior of the dual-cure ink upon printing in such a way that its fine-tuned control is essential to achieve desirable final printing features. For the first time, UV-assisted 3D printing was also employed to successfully process CFR polymer composites based on an optimized dual-cure formulation. The concentration of carbon fibers in the composite ink was found to significantly affect the efficiency of the UV-curing process, thus indicating that successful UV-3D printing of high-fiber-content composites needs sufficiently high power UV sources to be accomplished. The results of this study open the way towards the digital fabrication of high performance composite materials through 3D printing technology.

8.5 REFERENCES

1. B. Y. Ahn, S. B. Walker, S. C. Slimmer, A. Russo, A. Gupta, S. Kranz, E. B. Duoss, T. F. Malkowski & J. A. Lewis, Planar and three-dimensional printing of conductive inks, *J. Vis. Exp.* **58**, 3189 (2011).
2. S. J. Leigh, R. J. Bradley, C. P. Purcell, D. R. Billson & D. A. Hutchins, A simple, lowcost conductive composite material for 3D printing of electronic sensors, *Plos One* **7**, (2012) 11.
3. S. J. Leigh, R. J. Bradley, C. P. Purcell, D. R. Billson & D.A. Hutchins, Using a magnetite/thermoplastic composite in 3D printing of direct replacements for commercially available flow sensors, *Smart Mater. Struct.* **23**, 095039 (2014).
4. A. Ian, I. A. Barker, M. P. Ablett, H. T. J. Gilbert, S. J. Leigh, J. A. Covington, J. A. Hoyland, S. M. Richardson & A. P. Dove, A microstereolithography resin based on thiol-ene chemistry: towards biocompatible 3D extracellular constructs for tissue engineering, *Biomater. Sci.* **2**, 472 (2014).
5. G. Postiglione, G. Natale, G. Griffini, M. Levi & S. Turri, Conductive 3D microstructures by direct 3D printing of polymer/carbon nanotube nanocomposites via liquid deposition modeling, *Compos. A* **76**, 110-114 (2015).
6. J. T. Belter & A. M. Dollar, Strengthening of 3D printed fused deposition manufactured parts using the fill compositing technique, *Plos One* **10**, 4 (2015).
7. F. Ning, W. Cong, J. Qiu, J. Wei & S. Wang, Additive manufacturing of carbon fiber reinforced thermoplastic composites using fused deposition modeling, *Compos. B* **80**, 369 (2015).
8. L. L. Lebel, B. Aissa, M. A. El Khakani & D. Therriault, Ultraviolet-assisted direct-write fabrication of carbon nanotube/polymer nanocomposite microcoils, *Adv. Mater.* **22**, 592 (2010).
9. G. Postiglione, G. Natale, G. Griffini, M. Levi & S. Turri, UV-assisted threedimensional printing of polymer nanocomposites based on inorganic fillers, *Polym. Compos.* <http://dx.doi.org/10.1002/pc.23735> (2015).
10. R. D. Farahani, H. Dalir, V. Le Borgne, L. A. Gautier, M. A. El Khakani, M. Lévesque & D. Therriault, Direct-write fabrication of freestanding nanocomposite strain sensors, *Nanotechnol.* **23**, 085502 (2012).
11. R. D. Farahani, L. L. Lebel & D. Therriault, Processing parameters investigation for the fabrication of self-supported and freeform polymeric microstructures using ultraviolet-assisted three-dimensional printing, *J. Micromech. Microeng.* **24**, 055020 (2014).

12. A. Endruweit, M. S. Johnson & A. C. Long, Curing of composite components by ultraviolet radiation: a review, *Polym. Compos.* **27**, 119 (2006).
13. A. Endruweit, W. Ruijter, M. S. Johnson & A. C. Long, Transmission of ultraviolet light through reinforcement fabrics and its effect on ultraviolet curing of composite laminates, *Polym. Compos.* **29**, 818 (2008).
14. L. H. Sperling, Interpenetrating polymer networks: an overview, *Adv. Chem.* **239**, 3 (1994).
15. L. H. Sperling & V. Mishra, The current status of interpenetrating polymer networks, *Polym. Adv. Technol.* **7**, 197 (1996).
16. L. K. Kostanski, R. Huang, C. D. M. Filipe & R. Ghosh, Interpenetrating polymer networks as a route to tunable multi-responsive biomaterials: development of novel concepts, *J. Biomater. Sci.* **20**, 271 (2009).
17. S. Simic, B. Dunjic, S. Tasic, B. Bozic, D. Jovanovic & I. Popovic, Synthesis and characterization of interpenetrated polymer networks with hyperbranched polymers through thermal-UV dual curing, *Prog. Org. Coat.* **63**, 43 (2008).
18. S. Marinovic, I. Popovic, B. Dunjic, S. Tasic, B. Bozic & D. Jovanovic, The influence of different components on interpenetrating polymer network's (IPNs) characteristics as automotive top coats, *Prog. Org. Coat.* **68**, 293 (2010).
19. M. Sangermano, W. Carbonaro, G. Malucelli & A. Priola, UV-cured interpenetrating acrylic-epoxy polymer networks: preparation and characterization, *Macromol. Mat. Eng.* **293**, 515 (2008).
20. A. Gupta & A. A. Ogle, Dual curing of carbon fiber reinforced photoresins for rapid prototyping, *Polym. Compos.* **23**, 1162-1170 (2002).
21. P. J. Bartolo & G. Mitchell, Stereo-thermal-lithography: a new principle for rapid prototyping, *Rapid Prototyp. J.* **9**, 150 (2003).
22. J. C. Halpin & J. L. Kardos, The HalpineTsai equations: a review, *Polym. Eng. Sci.* **16**, 344 (1976).
23. P. Tsotra & K. Friedrich, Electrical and mechanical properties of functionally graded epoxy-resin/carbon fibre composites, *Compos. A* **34**, 75 (2003).
24. H. Zhang, Z. Zhang & C. Breidt, Comparison of short carbon fibre surface treatments on epoxy composites I. Enhancement of the mechanical properties, *Compos. Sci. Technol.* **64**, 2021 (2004).
25. B. G. Compton, J. A. Lewis, 3D-printing of lightweight cellular composites, *Adv. Mater.* **26**, 5930 (2014).

9.
Self-healing materials
based on
microvascular networks
via additive manufacturing



Based on the manuscript submitted to: ACS Applied Materials & Interfaces.

"Effect of 3D-printed microvascular network design on the self-healing behaviour of crosslinked polymers".

Authors: Giovanni Postiglione, Mirco Alberini, Simon Leigh, Marinella Levi, Stefano Turri.

9.1 INTRODUCTION

In centuries of evolution nature has developed biological systems able to execute several complex functions. Microvascular networks are among the most diffused ones in living species for their ability to transport energy, regulate the temperature and repair tissues. This latter function has been a source of inspiration for researchers in the fabrication of self-healing materials, a class of smart materials able to autonomously recover damages at a micro- or macroscopic scale. Although biological features are highly complex and nearly impossible to replicate, due to the presence of a hierarchical circulatory pathway and sophisticated healing fluids, remarkable results have been achieved in the realization of microvascular networks¹⁻⁴ and the production of functional self-healing materials and coatings in recent years^{5,6}. Such materials try to mimic the ability of biological systems to deliver one or more healing agents to a damaged zone through a microvascular network. Previous attempts in self-healing material design had been made using microcapsules or nanofibers able to deliver healing agents upon rupture⁷⁻⁹. The fabrication of those systems, however, can be challenging because parameters such as the shell permeability, chemical resistance and fracture mechanics all need to be accurately controlled in order to achieve optimum final performances^{10,11}. Furthermore capsules limited processability in term of resistance to elevated temperature and mechanical mixing made many polymers difficult to functionalize. Microvascular channels, on the other hand, represent a promising new approach in materials functionalization. Even if their presence within a given material reduces its mechanical performance, their implementation have a valuable effect in improving material service lifetime. Many of the existent fabrication strategies such as placing hollow fibers or tubes, micromachining, electrical discharge and direct writing, were developed for structural healing applications¹². Particularly direct writing has emerged as one of the most predominant method because it combines the 3D printing finely controlled material deposition and the versatility of the lost-wax technique¹³. Generally a sacrificial positive structure is printed and embedded within a matrix; after the matrix has cured, the fugitive material is removed thus producing the microchannels. In the first generation design a microvascular network was placed underneath an epoxy coating, which could be repaired by a healing agent when a crack occurred⁵. Multiple healing cycle are possible when the healing agent flows through microchannels, a substantial advantage compared to other techniques⁶. Such functionality is limited, however, by the amount of healing agent stored. The healing time depends on the healing agent reaction kinetics. A significant advance was achieved when different regions of the embedded microvascular networks were isolated so as to selectively fill the channels with different chemicals¹⁴. Therefore two-part healing chemistry could easily be exploited, thus giving a wider choice when designing

self-healing formulations. Further improvements in the healing performance were achieved when the embedded microvascular network were three-dimensional interpenetrated. This feature allowed the two-part epoxy healing agents to diffuse on shorter distance reacting more efficiently. However, the fabrication of these materials relies on advancement such as dual direct writing and vertical printing¹⁵. The employment of dual direct writing requires the use of two syringe dispensers mounted side by side and adequately controlled by dedicated softwares able to handle multiple materials deposition. In addition the realization of stable vertical features of certain heights needs a thorough control of the ink elasticity for a given nozzle diameter.

The present work proposes and analyzes polymeric materials with multiple independent microvascular networks in which the self-healing ability is based on their proximity rather than on their interpenetration. This study offers a simple and versatile solution to exploit bicomponent healing chemistry avoiding the implementation of dual direct writing and vertical printing. The procedure for manufacturing samples with embedded independent microvascular networks, adapted from tissue engineering scaffolds fabrication¹⁶, was based on 3D printing *via* fused deposition modeling (FDM). Samples with different microchannels architecture and densities were designed to evaluate their effect on the release of the two components healing agents and consequently on the final self-healing ability. The fabrication method consists in 3D printing water soluble poly vinyl alcohol (PVA) molds containing various multilayer scaffolds. After resin casting and PVA dissolution, samples provided with different microvascular systems could be obtained. Different two-components polymeric materials, namely an elastomer and two epoxy resins, were used for the fabrication of samples and thermally characterized. Since the samples were provided with independent networks, the same two components constituting the matrix could be stored within the microchannels, without coming into contact until the sample were broken. A thorough X-rays microCT characterization was performed to observe the microvascular networks and to measure microchannels sizes, the amount of healing agents stored and their volume ratio at varying infill densities. Finally, the mechanical healing performance was evaluated through uniaxial tensile tests onto dumbbell shape samples before and after being broken, thus revealing the matrix ability to recover from a severe damage as a function of the microvascular density and the network design.

To the best of our knowledge this is the first time that the preparation of microvascular channels is based on a technology that is low-cost and diffused on a large-scale such as FDM. Since the versatility of our approach allows to use any water resistant and castable polymeric resin for samples fabrication, the potentiality of the proposed manufacturing method is not limited to mechanical self-healing but could also be adopted in applications such as damage detection and electrical self-healing^{17,18}.

9.2 EXPERIMENTAL SECTION

9.2.1 MATERIALS AND METHODS

The 3D printer used was a Dual Extrusion Flashforge Dreamer produced by FlashforgeUSA. Transparent poly vinyl alcohol (PVA) printing filament (1.75 mm) was purchased from Formfutura and used as received. The polydimethylsiloxane (PDMS) and the corresponding hardener used in this work were purchased from Premier Farnell UK under the commercial name Sylgard® 184 whilst bisphenol A diglycidyl ether (DGEBA), hexamethylenediamine (HMDA), O,O'-bis(2-aminopropyl)polypropylene glycol (JD400) and benzyl alcohol (BA) were purchased from Sigma Aldrich and used without further modification. Samples with embedded microchannels were fabricated by resin casting using three different polymeric materials: PDMS and two epoxy resins. PDMS samples were fabricated by reacting the hardener with the resin using the recommended volumetric proportions: 1 to 10. One epoxy formulation was obtained by reacting JD400 with DGEBA at 1 to 1.47 volume ratio. Samples prepared with this formulation are referred to as Epoxy-J. The other epoxy formulation was prepared using the following procedure. An excess of HMDA was reacted to DGEBA (5:1 molar ratio) to form a liquid prepolymer that was diluted with 32.5 % w/w of BA. The resulting liquid prepolymer (PREP-BA10 from now on in the text) could be used as hardener for DGEBA. PREP-BA10 was formulated so that it reacted stoichiometrically with DGEBA at 1 to 1.9 volume ratio. Samples prepared with this formulation are referred to as Epoxy-H. Samples were analyzed with computerized X-ray microtomography whose details are reported in section 9.2.2. Tensile tests were performed on five dumbbell specimens per type (narrow section 10 mm X 6 mm X 10 mm) on a Zwick-Roell Z010 with a 10 kN load cell. Sample made of PDMS and Epoxy-J were characterized using 5 mm/min testing speed whilst 0.5 mm/min was used for Epoxy-H. Differential scanning calorimetry (DSC) was carried out with a Mettler-Toledo TA3000 instrument, indium and n-hexane calibrated, heating with a rate of 20 °C/min in a N₂ environment.

9.2.2 SAMPLES DESIGN AND FABRICATION

As a first step in the sample fabrication sacrificial molds were manufactured *via* 3D printing using the water soluble PVA filament. A dumbbell shape perimeter with embedded four cylinders and two parallelepipeds was designed using a computer aided design (CAD) software package (SolidWorks 2014). The 3D CAD design was exported as .STL mesh file format for processing using Simplify3D. This software allowed to configure different settings for each of the objects composing the part. For instance the parallelepipeds were printed with only the infill pattern and without perimeter, thus generating independent scaffold structures centered within the sample gauge section, each one being connected to the outer perimeter with cylinders. Two mold types, named type 'A' and type 'B', were realized. A schematic representation of the type 'A' mold top

view is reported in figure 9.1a. The type 'A' mold side view, shown in figure 9.1b, allows to visualize that its full composition consists in three parts printed separately and then overlapped: a two layers thick dumbbell shape perimeter and two identical parts each one with four cylinders and two scaffolds (the one described above).

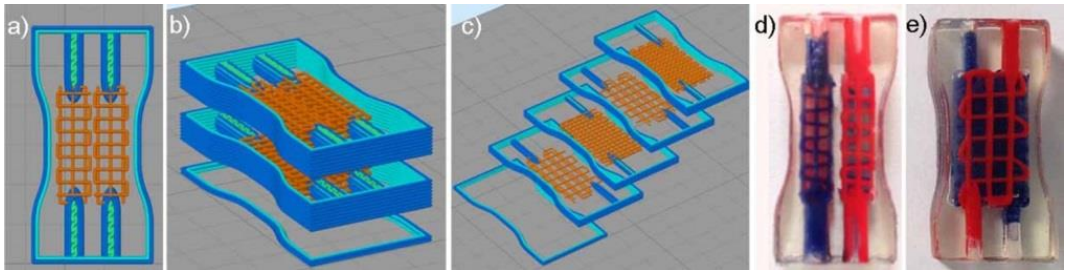


FIGURE 9.1 – A-B) SCHEMATIC REPRESENTATIONS OF TYPE 'A' PVA MOLD, TOP VIEW AND SIDE VIEW. C) REPRESENTATION OF TYPE 'B' PVA MOLD, SIDE VIEW. D-E) REPRESENTATIVE IMAGES OF TYPE 'A' AND 'B' CAST EPOXY-H SAMPLES AFTER CURING WITH DIFFERENTLY COLOURED HEALING AGENTS.

The two bottom perimeter layers were necessary so that during the casting stage the liquid resin could totally surround the scaffold structures. For the same reason the perimeter of the main parts is two layers higher than the scaffolds and the cylinders. The three parts could be easily glued together by wetting the PVA adhering edges and applying a gentle pressure. Therefore the final mold was composed by four independent and equal scaffold structures which would result into four microchannels networks having the same volume at the end of all fabrication stages. The cylinders guaranteed that the PVA internal scaffolds could be exposed to water and that in the final sample each network could be easily filled with the liquid healing agents. An analogous strategy was used in the production of samples with independent microchannels networks having different volumes. In this case the PVA type 'B' mold was composed by five overlapping 3D printed parts, as shown in figure 9.1c. The difference with the previous mold is that each part has only one larger scaffold structure within the gauge section and two cylinders. The mold was designed so that scaffold structures with different infill densities were overlapped in an alternate fashion. Note that the perimeter of each part is one layer higher than the scaffold and the cylinders thus avoiding contact between different scaffolds. In both type 'A' and type 'B' molds the infill settings were changed in order to tune the scaffold density which resulted in a more or less dense micro-channels network.

Before proceeding with the resin casting, the chosen resin (PDMS, for instance) was mixed with its curing agent at the proper volume ratio and the mixture was degassed in vacuum. The resin, slowly poured into the 3D printed mold, filled the scaffolds pores through capillary action. This operation was followed by another vacuum treatment for 1 h to ensure complete filling of the pores. PDMS was left to cure at room temperature for 48 h. Once cured, the entire mold was immersed in water so that the external PVA structure could be dissolved. With only the internal

PVA scaffold to dissolve, samples were placed in an ultrasonic water bath at 90 °C for 6 h to accelerate the PVA dissolution and therefore the microchannels network formation. A similar procedure was followed for Epoxy-J and Epoxy-H. The samples microchannels were subsequently filled with liquid healing agents. The independent networks of a cured sample were separately filled with its two components. Two images of type 'A' and type 'B' Epoxy-H sample obtained with this procedure are shown in figures 9.1d-e. The microchannels architecture was enlightened by coloring in blue and red the liquid healing agents. Once all networks were completely filled, PDMS samples were cut diagonally in half with a razor blade at the gauge section. The samples were cut diagonally to enhance the cross section surface area thus facilitating the healing process. As the liquids slowly began wetting the cross section surfaces the two parts were held back together and put in the oven at 60 °C for 4 h. For Epoxy-J and Epoxy-H a fragile fracture was induced using common mechanical workshop utensils. Damaged Epoxy-J and Epoxy-H samples were thermally treated at 150 °C for 3 h to promote the healing process.

9.2.3 COMPUTERIZED X-RAY MICROTOMOGRAPHY

Samples internal structure was reconstructed and analyzed using the Compact X-ray micro-CT SkyScan 1174v2 manufactured by Bruker microCT. The instrument relies on the use of high quality X-ray microfocus source operating at 20-50kV / 0-800 μ A, combined with high-resolution CCD-camera based on a 1.3 Megapixel CCD-sensor. The object manipulator rotated scanned samples to acquire angular shadow projections for tomographic reconstruction. The X-ray shadow projections were digitized as 1304x1024 pixel images with 16384 brightness gradations (14-bit). The control program acquired several images at each angular position converting them into a single image read by the reconstruction program NRecon with algorithms based on the filtered backprojection procedure for cone-beam geometry. After reconstruction, it was possible to display the sample cross sections on-screen and calculate the internal three-dimensional morphometric parameters based on binary segmentation of the given cross section images. Furthermore realistic 3D-images of scanned samples were constructed with the possibility to rotate the object model.

9.3 RESULTS AND DISCUSSION

9.3.1 SAMPLE FABRICATION AND MICRO-CT CHARACTERIZATION

This work focused on the design and realization of various smart polymers with embedded independent microvascular networks and on the investigation of their ability to self-heal in response to an extensive fracture. Samples were fabricated by casting PDMS, Epoxy-J and Epoxy-H (see section 9.2) around sacrificial PVA molds assembled using two different configurations: type 'A' and type 'B', correspondent to the representations reported in figures 9.1b-c respectively. Table 9.1 contains a resume of the five sample typologies manufactured. The first letter of the sample acronym (A or B) refers to the PVA mold configuration type described in 9.2.1. The number refers to the infill density used in Simplify3D to generate the original PVA scaffold. Samples A20, A25 and A30, therefore obtained from type 'A' molds, were characterized by the presence of 4 equivolumetric microchannels networks resulting from scaffolds with infill densities being 20 %, 25 % and 30 % respectively. The two last samples, on the other hand, presented two couples of independent microchannels networks having different volumes. Sample B20-45, for instance, was characterized by two microvascular networks obtained from scaffolds with 20 % infill density and two more from scaffolds with 45 % infill density. Similarly, sample B16-50 presented two couples of microvascular networks resulting from scaffolds having 16 % and 50 % infill density.

Samples Acronym	Independent Microchannel Networks	Infill Density [%]	Single Network Volume [mm³]	Networks Total Volume [mm³]	Curing agent/Resin Volume Ratio
A20	4	20	24	96	1 : 1
A25	4	25	30	120	1 : 1
A30	4	30	40	160	1 : 1
B20-45	2+2	20 - 45	21 - 40	122	1 : 1.9
B16-50	2+2	16 - 50	14 - 50	128	1 : 3.6

TABLE 9.1 - LIST OF FABRICATED SAMPLES WITH CORRESPONDING DATA ON MICROCHANNEL NETWORKS NUMBER, INFILL DENSITY AND NETWORK VOLUMES. SINGLE NETWORK VOLUMES WERE MEASURED FROM MICRO-CT SCANS THROUGH CT-AN SOFTWARE.

Table 9.1 also contains data on the networks volumes obtained thanks to the micro-CT characterization. Microtomographic scanners enabled 3D characterization of the salient features of manufactured samples. A micro-CT scan followed by 3D reconstruction of serial image sections was used to clearly visualize the internal sample microarchitecture and to determine the microchannels size and their volume in single networks and in the whole sample ('Networks Total Volume' column in table 9.1). CTscan images of the fabricated samples are shown in figure 9.2.

For type 'A' samples (A20, A25 and A30), the top views of their three-dimensional reconstructions, shown in figures 9.2a-c, emphasize their different network infill densities. Figures 9.2d-e, on the other hand, show a side view of B20-45 and B16-50 samples from which it is possible to detect all the four networks placed in an alternate fashion within the matrix. This characterization demonstrated that samples possessed well-defined microchannels structures and that the microchannel networks were effectively independent using both configurations. Finally, for each of the samples illustrated in figures 9.2a-e, the corresponding cross section is reported in figures 9.2a*-e*. For sake of clarity the empty microchannels were colored in red and the matrix was colored in blue. The channels cross section shape was observed to be generally rounded and uniform in all samples, with the exception of those correspondent to the scaffold first layer deposited, which tends to be elliptical. This happened because the distance of the nozzle from the printing bed is generally slightly inferior to the nozzle size to guarantee a good adhesion of the printed material onto the plate. The channel diameters measured approximately 400 μm , as expected having used an extruder with a nominal 0.4 mm nozzle size. Microvascular channels, produced with the direct-writing technology, displayed diameters within the range 200-330 μm for which the infiltration with highly viscous fluids may be problematic^{6,14,15}. The microchannel diameters of our samples allowed to easily flow through differently viscous healing components. The liquid delivery, during the healing process, is also favored. In figures 9.2a* and 9.2d* the separation among independent networks is also highlighted by enclosing each network in a dotted rectangle. Particularly in figure 9.2a*, top left and bottom right rectangles are colored in yellow differently from top right and bottom left ones (white) to indicate the criteria according to which the networks were subsequently filled with the two healing components. The dotted rectangles of figure 9.2d* show that microchannel networks of sample B20-45 are disposed in a stack, thus emphasizing the diverse network configuration of type 'B' samples compared to type 'A' ones. Analogously to those of figure 9.2a* the different colors (yellow and white) of rectangles in figure 9.2d* serve to remind that the networks were filled with the two healing components, in this specific case according to the appropriate volume ratio.

The microchannel network volumes were measured within the 10 mm of the gauge length. As already mentioned, measures of the volume of a single network and that of the total volume are reported in table 9.1. Note that the volume of a single network depended not only on the infill density but also on the number of layers of the original scaffold. Keeping in mind figures 9.1b-c, it is clear that the scaffolds used in type 'A' molds had a higher number of layers than those in type B molds. This explains why the volume of one network of sample A20 (24 mm^3) was higher than that of the 20 % infill network of sample B20-45 (21 mm^3) even though the two networks had the same infill density. Obviously, as the infill density of type A samples increases from 20 % to 30 %, the correspondent total volume also increases from 96 mm^3 to 160 mm^3 . The microchannel network total volumes of samples B20-45 and B16-50 were similar (122 mm^3 and 128 mm^3 respectively) and were comparable to the 120 mm^3 of sample A25 networks. These measures allowed to define the volume ratio between networks filled with the resin and those

filled with the hardener. In samples A20, A25 and A30 this ratio did not change because for each sample all networks had the same infill density. Samples B20-45 and B16-50 were specifically designed to alter the resin to hardener volume ratio: as a result, the volume ratios of networks with higher infill to those with lower infill were 1.9 and 3.6 respectively. The PDMS components normally reacts at the recommended volume ratio of 1:10, thus deviating considerably from the networks volume ratios found in all samples. DGEBA and J400, the components of Epoxy-J formulation, on the other hand, react stoichiometrically at the volume ratio 1:1.47, approaching the 1:1 volume ratio found in 'A' type samples. Finally, Epoxy-H formulation was specifically designed to have DGEBA and PREP-BA10 reacting stoichiometrically at the volume ratio 1:1.9, exactly the volume ratio of samples B20-45.

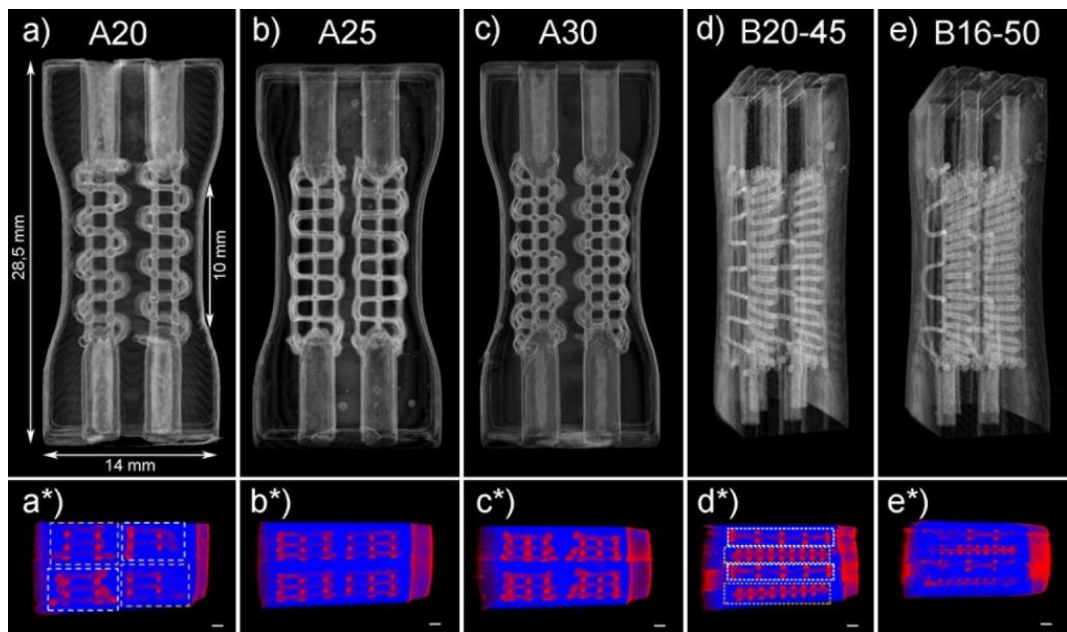


FIGURE 9.2 - CT SCANS OF DUMBELL SHAPE SAMPLES WITH EMPTY MICROCHANNELS. A-C) TOP VIEW OF TYPE A SAMPLES WITH MICROCHANNEL NETWORKS INFILL DENSITIES RANGING FROM 20% TO 30%. A*-C*) CORRESPONDENT CROSS-SECTION, SCALE BARS 1 MM. D-E) SIDE VIEW OF TYPE B SAMPLES WITH VARIABLE NETWORK DENSITIES. D*-E*) CORRESPONDENT CROSS SECTION, SCALE BARS 1 MM.

It is worth noting that the reacting volume ratio is not the only aspect influencing the healing process but the network architecture is also crucial. The different network configurations in type 'A' and 'B' samples have the effect, during the healing process, to alter the fluids interface proportions, which can in turn influence the mixing efficiency. Since the healing fluids in situ mixing relied primarily on molecular diffusion between chemical species, the components mixing capability can be limited and therefore lead to polymerization under non-stoichiometric conditions¹⁹. In this perspective the fabrication of samples having different network infill density

and architectures with adjacent networks (type 'A') or piled up (type 'B') can enlighten the predominant factor in determining the best healing performance.

9.3.2 HEALING TESTS AND MECHANICAL CHARACTERIZATION

After being damaged, samples were manually reconnected and thermally treated to promote the healing process. As a first step, the material self-healing capability was evaluated visually. Figures 9.3a-i show pictures of PDMS, Epoxy-J and Epoxy-H samples before being damaged, cut in two halves, and after being healed.

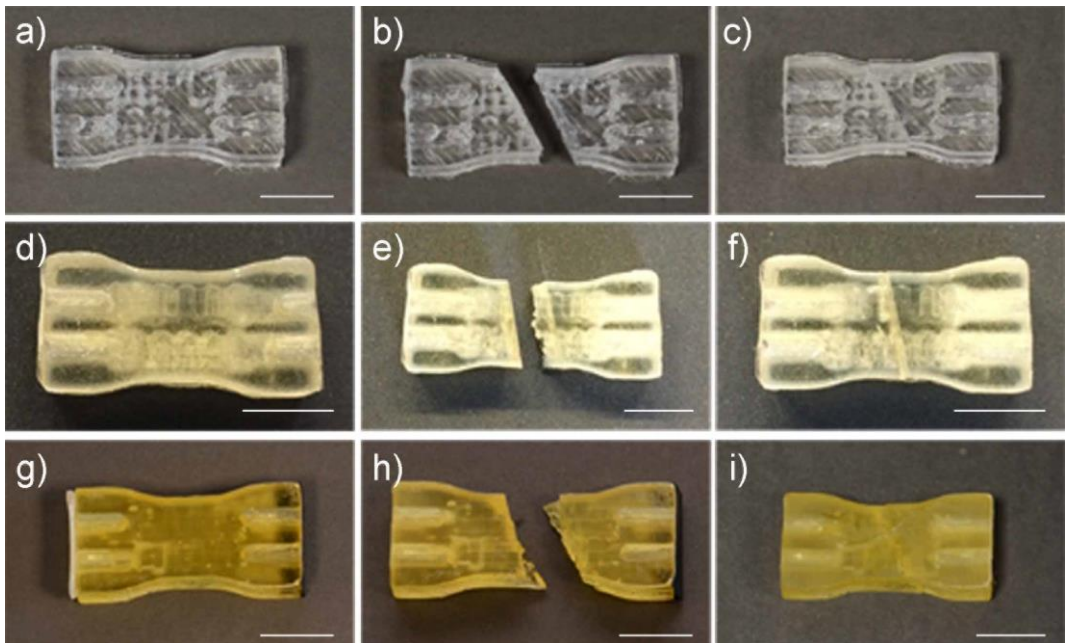


FIGURE 9.3 - IMAGES ILLUSTRATING THE DAMAGE-HEALING CYCLE OPERATED ON SAMPLES MADE OF DIFFERENT POLYMERIC RESINS. IN THE LEFT COLUMN INTEGER SAMPLES ARE DISPLAYED, IN THE CENTRAL COLUMN THE SAME SAMLES ARE CUT IN TWO HALVES AND FINALLY IN THE RIGHT COLUMN THEY ARE SHOWN AFETER THE HEALING TREATMENT. A-C) PDMS, D-F) EPOXY-J, G-I) EPOXY H. SCALES BAR 10 MM.

All pictures depict A30 samples, chosen as representative model in the evaluation of the aesthetical recovery. In all cases the severe damage executed could be recovered easily thanks to the prompt leakage of the healing agents. Aesthetically, the aspect of the samples after the healing cycle closely resemble that of the undamaged one. The fragile fracture of Epoxy-J and Epoxy-H samples led to the formation of irregular but perfectly corresponding surfaces. For Epoxy-H samples, in particular, the residual fracture plane was merely visible.

The self-healing ability of the various polymeric resins was also assessed by uniaxial tensile tests performed on integer reference samples (before being broken, as those displayed in figures 9.3a,

9.3d and 9.3g) and on samples after one damage-healing cycle (figures 9.3d, 9.3f and 9.3i). In order to investigate how network infill density and architecture influenced the healing performance, the mechanical response, in term of ultimate tensile strength (UTS), of all samples types (A20, A25, A30, B20-45 and B16-50) was evaluated. Figures 9.4a-c illustrate the results of the uniaxial tensile tests for PDMS, Epoxy-J and Epoxy-H respectively, whereas, representative stress-strain curves of one reference sample for each of the materials used are reported in figures 9.4d-f. Firstly, histograms of figures 9.4a-c show that, for each type of polymer, reference samples all had very similar UTS values with the exception of sample PDMS A20, having slightly higher UTS (0.42 MPa) compared to other PDMS reference samples and of sample Epoxy-H B16-50, that displayed slightly lower UTS (15 MPa) compared to other Epoxy-H reference samples.

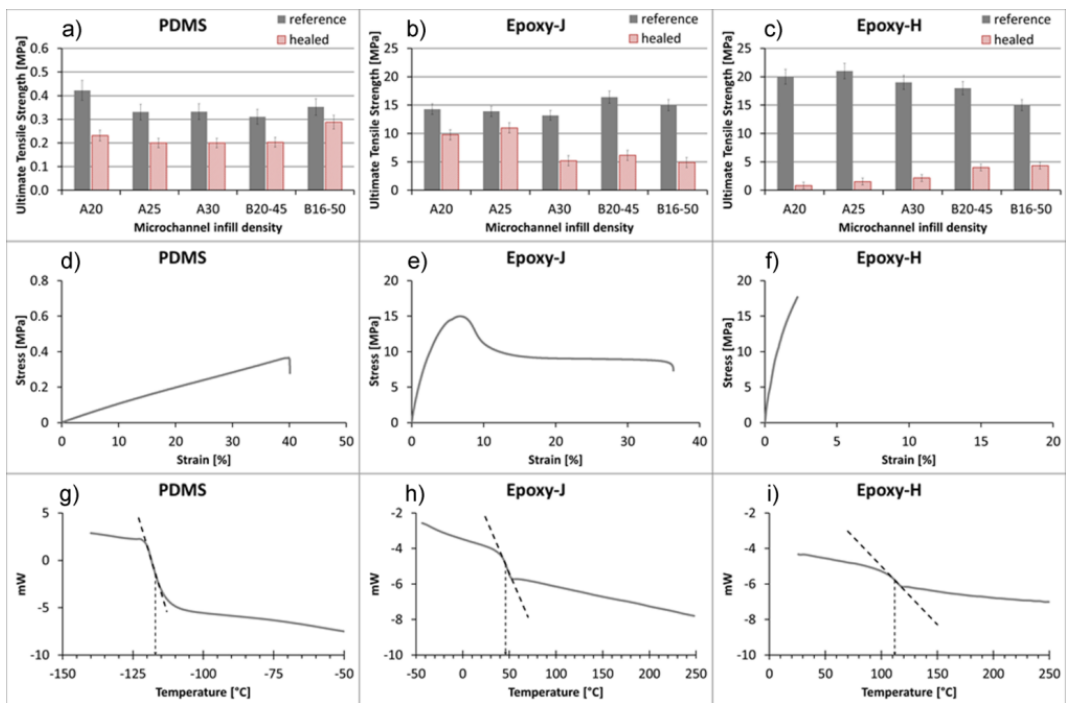


FIGURE 9.4 - A-C) HISTOGRAMS SHOWING THE ULTIMATE TENSILE STRENGTH OF HEALED SAMPLES HAVING DIFFERENT INFILL DENSITY COMPARED TO A REFERENCE: A) PDMS, B) EPOXY-J AND C) EPOXY-H RESPECTIVELY. D-F) REPRESENTATIVE STRESS-STRAIN CURVES OF A REFERENCE SAMPLE MADE OF D) PDMS, E) EPOXY-J AND F) EPOXY-H. G-I) DSC SCANS OF CROSSLINKED SAMPLES SHOWING THE TG OF G) PDMS, H) EPOXY-J AND I) EPOXY-H.

Therefore, the different types of microchannel networks had little or no influence on the resulting UTS, regardless of the kind of polymer used. Healed samples, on the other hand, showed UTS values generally dependent upon the microvascular network design and inferior to the correspondent reference. Commonly in a repaired material, the healing efficiency is defined

as the percentage recovery of a certain mechanical property. Accordingly, in our case, the healing efficiency, η , was defined as the ratio of the healed to the reference UTS:

$$\eta = \frac{UTS^{healed}}{UTS^{ref}} * 100 \quad (9.1)$$

A complete resume of the calculated healing efficiencies for the three different materials is reported in table 9.2.

Samples	PDMS	Epoxy-J	Epoxy-H
A20	55 %	68 %	4 %
A25	60 %	79 %	7 %
A30	60 %	39 %	11 %
B20-45	65 %	38 %	22 %
B16-50	82 %	33 %	29 %

TABLE 9.2 - HEALING EFFICIENCY OF PDMS, EPOXY-J AND EPOXY-H SAMPLES IN UNIAXIAL TENSILE TESTS

Regarding PDMS, the reference UTS values fell within the range 0.31-0.42 MPa whilst healed samples showed UTS ranging between 0.20 and 0.29 MPa. All 'A' type configuration and B20-45 PDMS samples performed similarly achieving a good healing efficiency (within the interval 55-65 %). Therefore no effect of the infill density on the healing efficiency was observed. B16-50 sample, being the sample in which the healing components reacted at the closest to the ideal volume ratio, reached an outstanding 82 % healing efficiency. A20 and A25 samples made of Epoxy-J displayed relatively high value of UTS: 9.8 and 11 MPa respectively, that compared to the 14.3 and 13.9 MPa of the corresponding reference samples resulted in 68 % and 79 % healing efficiency. A30, B20-45 and B16-50 samples presented slightly inferior healing recovery, falling within the interval 33-39 %. It is clear, in the case of Epoxy-J formulation, that the mixing efficiency of healing components was more favored in type A configuration samples, and that the increase of networks volume (A30 sample) and variations of healing components volume ratio (B20-45 and B16-50) had a detrimental effect on the healing efficiency. The overall positive performance of Epoxy-J samples, in term of healing efficiency, can be correlated with the fact that, during the healing process, its components reacted at a volume ratio approaching the 1:1.47 stoichiometric ratio. Finally all Epoxy-H samples showed a limited healing recovery with UTS values falling within the range 0.8-4.3 MPa, relatively low strength values compared to those of reference samples (15-21 MPa). For type 'A' configuration samples an increasing trend of UTS at increasing infill density is appreciable, but the healing efficiency did not exceed 11 %. Even sample B20-45, that possessed microchannel networks with a volume ratio corresponding to the stoichiometric volume ratio of Epoxy-H healing components, only showed 22 % healing efficiency. A only slightly higher value of healing efficiency (29 %) was observed for sample B16-50. It is plausible that the moderate healing recovery of Epoxy-H samples was caused by a reduced mixing efficiency of the healing components, DGEBA and PREP-BA10 (see section 9.2).

Related to this problem there is their reaction kinetics: since chain aliphatic polyamines reacts rapidly with epoxy groups the interdiffusion phenomena of the healing liquids in this case was probably obstructed.

From a wider perspective that takes into account the chemical nature of the polymers used, samples self-healing capability can be correlated to the material thermo-mechanical behaviour. To this end DSC scans of PDMS, Epoxy-J and Epoxy-H were performed and the resulting curves are reported in figures 9.4g-i. Glass transition temperatures (taken at the inflection point; tangents were indicated by straight dotted lines) revealed, predictably, significantly different thermal behaviors. PDMS presented a low T_g , at $-117\text{ }^\circ\text{C}$ whilst Epoxy-J and Epoxy-H both displayed T_g above room temperature, at $46\text{ }^\circ\text{C}$ and $111\text{ }^\circ\text{C}$ respectively. Due to its high T_g , Epoxy-H molecular chains possessed an extremely reduced mobility that resulted in a fragile mechanical behaviour. This is also shown by the stress-strain curve in figure 9.4f. It is reasonable to assume that the healing process of Epoxy-H samples was largely affected by its extreme fragility. Although upon reconnection of the two broken parts the fracture surfaces were apparently well recovered, the healing fluids probably produced at the interface a polymeric layer with a low degree of crosslinking. In addition, the reduced healing performance could have been caused by the blockage of the microchannels due to the fast reaction kinetics of Epoxy-H components²⁰. Such circumstances are likely the major factors impeding Epoxy-H healed samples to hold significantly higher loads. In Epoxy-J formulation, on the other hand, these factors are absent. Its lower T_g ($46\text{ }^\circ\text{C}$) compared to Epoxy-H, in fact, conferred an higher molecular mobility to the material which, in turn, resulted in an higher toughness. Epoxy-J ductile behaviour is also clearly evident from figure 9.4e where a wide plastic deformation was observed. The fact that such material characteristics could enhance the healing performance was not completely surprising. In self-healing polymers and composites, in fact, epoxy blends are often combined with toughening particles and reactive diluents to increase the overall material toughness that generally prevents further damage in the healed region²¹. Finally, PDMS samples presented the highest healing efficiency percentages regardless of the large discrepancy between the recommended volume ratio of the healing components (1:10) and the networks volume ratio (1:1 in type 'A' samples and 1:1.9 and 1:3.6 in type 'B' samples). Such behaviour can be associated to the PDMS extremely low T_g ($-117\text{ }^\circ\text{C}$) and consequent high molecular mobility that allow the healing agents to freely diffuse on longer distances thus reacting more efficiently.

The possibility to achieve consecutive self-healing events was not investigated but it is possible, in principle, as long as a continuous delivery of healing agents to the fracture plane is guaranteed. For instance, a pumping system, connected to the self-healing device, could supply after a damage-heal cycle, new healing fluids through the main channels. Modifications to the microchannel architecture and assembly of the network could also be implemented to adapt the proposed fabrication method to polymer coatings or to one-component healing systems. Thanks to the method versatility, in fact, any castable and water resistant resin could be converted into a full functional self-healing polymer.

9.4 CONCLUSIONS

FDM 3D printing and resin casting were successfully combined to manufacture samples with four independent microvascular networks enclosing healing components ready to be released upon damage. Since multiple independent microvascular networks allowed to use two-component healing chemistry different polymeric systems could be enabled with self-healing ability thus extending their service lifetime.

The self-healing tests performed on severely damaged samples demonstrate a promising behaviour in both aesthetical and mechanical recovery. The uniaxial tensile tests revealed that healing efficiencies up to 82 % and 79 % can be achieved for PDMS and Epoxy-J respectively. Being the healing agents exactly the same chemicals used for the matrix, they possessed the ideal chemical compatibility, a key requirements, together with a low viscosity, for an appropriate autonomic curing within the crack plane. For Epoxy-H samples, the inability of the two healing components to sufficiently mix after damage and its extreme fragile behaviour were probably the limiting factors in obtaining an higher healing efficiency.

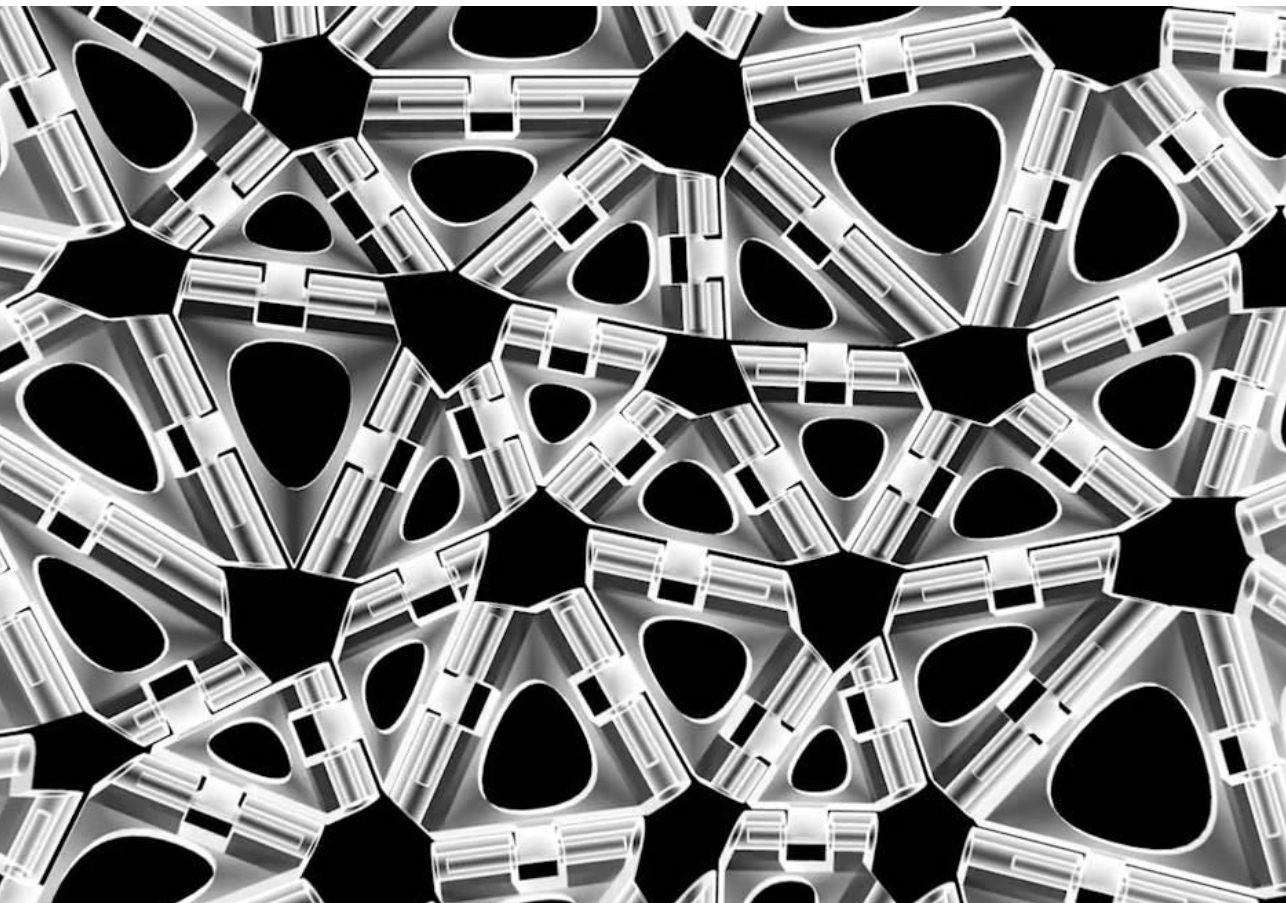
The possibility offered by 3D printing in term of placing salient features exactly where needed allow to imagine structural printed parts provided with microvascular networks only in areas with high risk of failure. In term of materials used, the versatility of the manufacturing process proposed allows to conceive materials with a dual self-healing mechanism by integrating the microvascular networks approach with a matrix material that already possesses the intrinsic self-healing functionality at a molecular level. Following the example of natural species, microchannel networks could also be employed to fulfill fundamental functions other than mechanical recovery. Proper healing fluids could be used, for instance, to restore conductivity in electrical self-healing polymers or to display cracks in damage sensing materials.

9.5 REFERENCES

1. S. C. Olugebefola *et al.* Polymer Microvascular Network Composites, *J. Compos. Mater.* **44**, 2587–2603 (2010).
2. W. Wu, A. Deconinck & J. A. Lewis, Omnidirectional printing of 3D microvascular networks, *Adv. Mater.* **23**, 178–183 (2011).
3. D. Therriault, S. R. White, & J. A. Lewis, Chaotic mixing in three-dimensional microvascular networks fabricated by direct-write assembly, *Nat. Mater.* **2**, 265–271 (2003).
4. A. P. Esser-Kahn *et al.* Three-dimensional microvascular fiber-reinforced composites, *Adv. Mater.* **23**, 3654–3658 (2011).
5. K. S. Toohey, N. R. Sottos, J. A. Lewis, J. S. Moore & S. R. White, Self-healing materials with microvascular networks, *Nat. Mater.* **6**, 581–585 (2007).
6. K. S. Toohey, N. R. Sottos & S. R. White, Characterization of microvascular-based self-healing coatings, *Exp. Mech.* **49**, 707–717 (2009).
7. S. R. White *et al.* Autonomic healing of polymer composites, *Nature* **409**, 794–797 (2001).
8. M. W. Lee *et al.* Self-healing transparent core–shell nanofiber coatings for anti-corrosive protection, *J. Mater. Chem. A* **2**, 7045–7053 (2014).
9. M. Huang & J. Yang Facile microencapsulation of HDI for self-healing anticorrosion coatings, *J. Mater. Chem.* **21**, 11123 (2011).
10. R. Wang, Honglin Hu, Xiaodong He, Wenbo Liu, Haiyan Li & L. Y. Qiong Guo, Synthesis and Characterization of Chitosan/Urea-Formaldehyde Shell Microcapsules Containing Dicyclopentadiene, *J. Appl. Polym. Sci.* **121**, 2202–2212 (2011).
11. M. M. Caruso *et al.* Robust, double-walled microcapsules for self-healing polymeric materials, *ACS Appl. Mater. Interfaces* **2**, 1195–1199 (2010).
12. M. U. Saeed, Z. Chen, & B. Li, Manufacturing strategies for microvascular polymeric composites: A review, *Compos. Part A Appl. Sci. Manuf.* **78**, 327–340 (2015).
13. J. A. Lewis, Direct ink writing of 3D functional materials, *Adv. Funct. Mater.* **16**, 2193–2204 (2006).
14. K. S. Toohey, C. J. Hansen, J. A. Lewis, S. R. White & N. R. Sottos, Delivery of two-part self-healing chemistry via microvascular networks, *Adv. Funct. Mater.* **19**, 1399–1405 (2009).

15. C. J. Hansen *et al.* Self-healing materials with interpenetrating microvascular networks, *Adv. Mater.* **21**, 4143–4147 (2009).
16. S. Mohanty *et al.* Fabrication of scalable and structured tissue engineering scaffolds using water dissolvable sacrificial 3D printed moulds, *Mater. Sci. Eng. C* **55**, 569–578 (2015).
17. B. J. Blaiszik *et al.* Autonomic restoration of electrical conductivity, *Adv. Mater.* **24**, 398–401 (2012).
18. J. W. C. Pang & I. P. Bond, ‘Bleeding composites’ - Damage detection and self-repair using a biomimetic approach, *Compos. Part A Appl. Sci. Manuf.* **36**, 183–188 (2005).
19. J. F. Patrick *et al.* Continuous self-healing life cycle in vascularized structural composites, *Adv. Mater.* **26**, 4302–4308 (2014).
20. A. R. Hamilton, N. R. Sottos & S. R. White, Self-healing of internal damage in synthetic vascular materials, *Adv. Mater.* **22**, 5159–5163 (2010).
21. D. T. Everitt *et al.* Optimisation of epoxy blends for use in extrinsic self-healing fibre-reinforced composites, *Polym. (United Kingdom)* **69**, 283–292 (2015).

10. Towards 4D Printing



10.1 CONCLUSIVE REMARKS

The main focus of this PhD work was the implementation of smart functionalities within polymeric materials exploiting the possibilities offered by additive manufacturing technologies. It has been shown that smart materials and additive manufacturing are two intensely investigated research topics. Damage sensing and self-healing materials attracted our attention for their potentially disruptive impact on maintenance operations of industrial components. The development of specific formulations displaying stimuli-responsiveness required a great effort in designing efficient chemo-physical mechanisms driving the smart behaviour. Analogously, the exploration of advanced nanocomposites suitable for additive manufacturing was carried out by rigorous analyses on process related properties. Thus, the deep knowledge on the chemical formulation of innovative materials on one hand, combined with the expertise on 3D printing processing on the other, has allowed to conceive new pathways in material designing.

In the field of smart materials, the design of damage sensing and self-healing polymers has emerged as a promising strategy whose main goal is to provide a generic structure with the ability of displaying or self-repairing damages otherwise difficult to detect or treat. The fundamental findings of this part of the work can be summarized in the realization of two concrete examples of damage-responsive polymeric materials: a microcapsules based polymer composite emitting a fluorescent signal upon mechanical damage and a thermoreversible self-healing polymeric coating. The work on microcapsules led to the following main achievements:

- a fluorescent core was encapsulated thanks to the interfacial polymerization between an isocyanate prepolymer and a difunctional benzophenone amine forming a UV-screening shell;
- microcapsules were thermal resistant and chemically stable to different solvents;
- the damage visualization ability of this new fluorescent probe was demonstrated by embedding the fluorescent-core/UV-screening microcapsules into a polymer coating.

As for the thermoreversible self-healing polymer the main results are listed below:

- the thermoreversibility within the interval 120-130 °C of a polymer based on Diels–Alder and retro-Diels-Alder reaction was proved by FTIR spectroscopy, DSC and DMA analyses;

- the smart behaviour of the polymer was significantly improved by the addition of benzyl alcohol, a plasticizer stable in the reversibility temperature range;
- the healing ability was assessed by uniaxial tensile tests giving a 48 % mechanical healing efficiency;
- the excellent aesthetical recovery of the surface appearance was demonstrated by gloss tests showing an efficiency of 95 %.

When focusing on additive manufacturing, the efforts were directed towards the realization of suitable polymeric formulation with advanced properties. A key requirement for such materials was their rheological behaviour at ambient temperature because it influenced their processability by newly conceived LDM and UV-assisted 3D printing methods. The technological potential of the studies conducted is demonstrated by the following results on conductive polymers, photopolymers with inorganic fillers and IPN carbon fibers reinforced:

- conductive 3D microstructures of a PLA/CNT nanocomposite with dimensions down to 100 μm could be reproducibly obtained by means of a LDM 3D printing method based on the solvent-assisted additive deposition;
- characterization of the nanocomposite electrical properties at increasing MWCNT concentrations allowed to identify the percolation threshold concentration of 0.67 wt%;
- at a fixed amount of MWCNT, the rheological properties of the nanocomposite dispersions at varying PLA content were investigated and printability windows for these systems were identified based on the estimation of the shear-rate of the dispersion at the extrusion nozzle;
- 3D macroarchitectures and microarchitectures, spanning features, and planar transparent structures directly formed upon UV-3D printing nanocomposite dispersions containing inorganic fillers were successfully obtained;
- the optimal extrusion and printability parameters for these systems were determined by applying classical power-law fluid relationships and the capillary flow model to a cone-plate rheological characterization;
- UV assisted 3D printing could be used thanks to the rapid curing reaction of these systems (4 s time to peak in photocalorimetric measurements). Furthermore the presence of inorganic fillers did not affect the thermodynamics and kinetics of the UV-curing process of the polymeric matrix;
- the possibility to influence the final mechanical properties of UV-3D printed materials by controlling printing direction, infill density and pattern was proved;

- UV-assisted 3D printing was also employed to successfully process CFR polymer composites based on an optimized dual-cure formulation;
- the dual-cure IPN system was obtained by blending a photocurable acrylic resin and a thermally reactive epoxy resin. The rapid polymerization upon UV exposure was fundamental to be processable via UV-assisted 3D printing;
- the thermal curing of the epoxy component and the addition of carbon fibers conferred enhanced thermo-mechanical properties to the printed part;
- a 1:5 weight ratio between the photocurable and the thermally curable components in the IPN system was established to achieve the best quality prints;
- the concentration of carbon fibers in the composite ink was found to significantly affect the efficiency of the UV-curing process, thus indicating that successful UV-3D printing of high-fiber-content composites needs sufficiently high power UV sources to be accomplished.

The final objective of the present research was exploiting the freedom given by additive manufacturing in designing complex geometries for the realization of a self-healing material. The following list highlights the most remarkable results of this last part:

- Different polymeric systems were enabled with self-healing thanks to their microstructure composed by multiple independent microvascular networks enclosing bicomponent healing agents;
- independent systems of microchannels were realized combining FDM 3D printing of water soluble PVA with resin casting;
- a thorough X-rays microCT characterization was performed to observe the microvascular networks and determine cross-section and volume of microchannels;
- the uniaxial tensile tests performed on severely damaged samples demonstrate a promising behaviour in both aesthetical and mechanical recovery, with PDMS and an high toughness epoxy polymer achieving up to 82 % and 79 % healing efficiencies respectively.

Exciting innovative ideas made possible thanks to additive manufacturing, obviously not only limited to microchannel networks and self-healing, are currently being developed to enable future materials with unconventional functions and fascinating smart properties.

10.2 FUTURE DEVELOPMENTS

Commercially available 3D printers can, at present, produce parts using a quite wide range of polymers: from thermoplastics, such as PLA, acrylonitrile butadiene styrene (ABS) and TPU with FDM technology, to photopolymers processed with stereolithography and similar vat technologies. A step-change in the range of available materials for 3D printing was one of the objective of this PhD thesis. Shifting away from the simple processing of engineering plastics, we explored the world of polymers and composites with advanced functionalities and tried to integrate their superior properties with the advantages offered by 3D printing. At first the attention was focused on the study of smart materials, independently from the manufacturing process used. Efforts made on the research of programmable materials lead to the realization of working samples of a damage sensing polymeric composite with embedded microcapsules (chapter 4) and of a full functional self-healing polymer based on the thermoreversible Diels-Alder reaction (chapter 5). Thereafter, to gain a clear insight on how to exploit the versatility of 3D printing processes, a study on viscoelastic polymeric materials and on their possible compatibility with methods based on extrusion and three-dimensional deposition was carried out. To this end Liquid Deposition Modeling (LDM, often referred to as direct ink writing in literature) and UV-assisted 3D printing were implemented for the controlled deposition of different formulations: an electrically conductive thermoplastic based on solvent and CNT (chapter 6), photopolymers loaded with inorganic nanofillers working as rheological modifiers and mechanical reinforce (chapter 7), and an IPN composite formed by blending a thermocurable epoxy and a photocurable acrylic resin and reinforced with carbon fibers (chapter 8). Finally, the knowledge on smart materials and the gained expertise on 3D printing processing were combined for the production of self-healing crosslinked polymers provided with microvascular networks enclosing healing agents to deliver in case of damage (chapter 9). In recent years, the final integration of 3D printing technologies with smart materials has become an extremely challenging but attracting issue for the scientific community. The main efforts are being concentrated on the direct processing of materials able to perform advanced functions after being printed. In term of applications, 3D-printed functional materials could be employed for drug delivery platforms, tissue scaffolds, energy storage devices, and force-sensors. Electrically conductive materials, such as the PLA/CNT system described in chapter 6, can also be considered valuable examples because they allow rapid customization of practical devices. The same material and

technique were in fact used to fabricate a helical liquid sensor in which the driving mechanism was polymer matrix swelling¹. With the solvent molecule penetrating the matrix, the conductive CNT network was disconnected causing a reduction in the resulting electrical conductivity. In an effort to expand the functions of 3D-printed devices beyond electrical properties, an interesting study has proposed a simple composite carrying magnetite nanoparticles in a thermoplastic matrix for the production of flow-sensing device able to reproduce the action of a commercially available flow sensor. The possibility to combine magnetic properties with multi-material printing was highlighted since it allowed to place the functional material only where it is specifically required thus reducing its amount and, in turn, the cost of the device². Multi-material printing is a common recourse in advanced systems since it provides additional means to customize the mechanical, chemical and physical properties of printed structures. It was also employed for the integration of 3D printing technologies with materials able to display mechano-chemical signals. In this way printed objects can be designed to possess specific areas designated to the responsive function. For instance, systems capable of coupling macroscopic mechanical forces with specific chemical reactivity have been proposed for the fabrication of prototype force sensors in which an applied load can be identified by a visual assessment of the mechanochromism. This was achieved by incorporating different spiropyran moieties into poly(ϵ -caprolactone) filament to 3D print *via* traditional FDM printers³. The isomerization of the spiropyran to its highly colored purple merocyanine isomer, induced by the application of an external force, allowed to immediately detect a macroscopic color change. In figure 10.1a-b, a CAD representation and an image of a dumbbell shape test specimen, fabricated using dual deposition, are shown. The mechanoresponsive material was identified by two red stripes that spanned the length of the printed specimen. Figure 10.1c illustrates that, as soon as the sample was elongated, only the regions containing the spiropyran moieties turned from red to purple, thus highlighting the potential offered by 3D printing to quickly fabricate mechanoresponsive devices with optimized design for a given application.

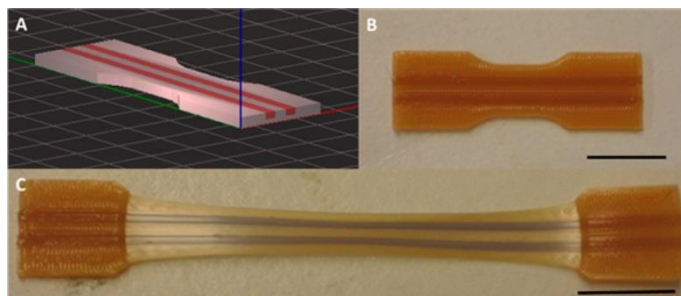


FIGURE 10.1 - A) CAD REPRESENTATION OF A DUMBELL SHAPE SPECIMEN, WITH RED STRIPES INDICATING THE LOCATION OF THE MECHANORESPONSIVE MATERIAL, B) TEST SPECIMEN PRE-ELONGATION AND C) TEST SPECIMEN POSTELONGATION SHOWING THE ACTIVATION OF THE MECHANOCROMIC RESPONSE. SCALE BARS = 20 MM³.

Among 3D printing techniques, direct-write assembly is finding an increasing attention for the realization of sensing devices, thanks to the possibility of processing polymers at low temperatures⁴. As partly shown in this thesis work, it exploits the viscoelastic properties of fluid materials, that can contain ceramic particles, metal particles, polyelectrolytes, hydrogels, filled epoxy resins, and even cell-laden extracellular matrices⁵. Recently this technique has been proposed for the fabrication of high-quality optical waveguides, exploiting the deposition of a soft functional material through a modified print head⁶. Specifically, a hybrid organic-inorganic core fluid, presenting low optical loss in the visible and NIR wavelengths and low shrinkage upon curing, was coextruded within a viscoelastic polymeric shell serving as a sacrificial support. Figure 10.2a shows the print head consisting of two cylindrical nozzles aligned coaxially whereas figure 10.2b shows the photocurable liquid core-fugitive shell printing of the optical waveguide. The outer shell was needed to contain the liquid core fluid, whose sole deposition would have resulted in lateral spreading due to its low viscosity. The core fluid and viscoelastic fugitive shell are loaded into separate reservoirs and printed simultaneously. The presence of the polymeric shell, being highly transparent to ultraviolet light, also allowed for UV-curing of the waveguide core. The image of a six-waveguide network coupled to three different colors of LED light, shown in figure 10.2c, well represents the potential of this approach in creating out-of-plane waveguides. The presence of the fugitive shells guaranteed the physical separation at each crossover point. The direct filamentary patterning, achieved using 3D printing methods could be employed for the realization of future optical systems and optical sensors.

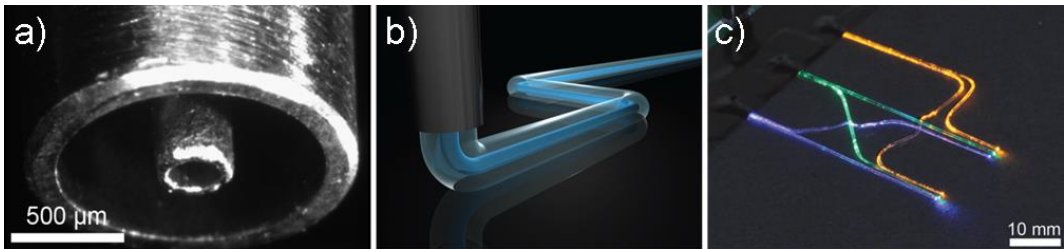


FIGURE 10.2 - A) OPTICAL IMAGES OF THE PRINTHEAD PRINT HEAD COMPOSED BY TWO COAXIAL CYLINDRICAL NOZZLES. B) SCHEMATIC REPRESENTATION OF THE 3D PRINTING OF PHOTOCURABLE LIQUID CORE-FUGITIVE SHELL INKS. C) IMAGE OF POLYMERIC OPTICAL WAVEGUIDES NETWORK COMPOSED OF SIX WAVEGUIDES COUPLED WITH THREE LEDs⁶.

The idea of co-extruding multiple materials at once was furtherly developed to create new wearable electronic devices. Particularly, capacitive sensors consisting of a dielectric layer sandwiched between two conductive layers, were coextruded in the desired configuration using a custom-designed printhead composed of four cylindrical nozzles aligned coaxially⁷. A viscoelastic silicone elastomer was used for the dielectric layer and for the outer encapsulating layer whereas the ionically conductive ink was composed of glycerol, sodium chloride, and polyethylene glycol. The working principle of the capacitive sensor lies on the thickness changes of the various layers in response to an applied deformation. Capacitive soft strain sensors were successfully integrated onto textiles to demonstrate the capacity to capture the gate cycle of a wearer in real time. Beyond wearable electronics, these devices may find application in, human/machine interfaces, soft exosuits, and soft robotics. Linked to sensing devices, another typology of smart materials processable through additive manufacturing that deserve a special mention are shape memory polymers, materials with the ability to return from a deformed state to their original shape. The transformation of the object following the three-dimensional fabrication means that a new “dimension”, namely the time domain, is added to the process. For this reason the name 4D printing is being given to those processes involving the use of shape changing materials. Researchers consider 4D printing the ultimate frontier that, once consolidated, will definitely shift the application range of additive manufacturing technologies from prototyping to the production of finite objects with form and function thoroughly integrated. The most promising recourses, currently found in literature, for the implementation of 4D printing are direct ink writing and shape deformation induced by swelling. A first strategy to produce 4D printed material consists in exploiting the relatively fast and reversible muscle-like linear actuation of some hydrogels. Particularly an alginate/poly(*N*-isopropyl acrylamide) ionic

covalent entanglement gel, with a structure similar to that of double network hydrogels, was demonstrated to display simultaneously mechanical robustness and a thermally-actuating behaviour. It was used to fabricate a smart valve that controlled the flow of water by automatically closing upon exposure to hot water and opening in cold water⁸. Magnetic particles were instead employed in another innovative multimaterial additive manufacturing technology in which the orientation of magnetized stiff platelets contained within a fluid ink was controlled by applying magnetic fields during the process⁹. In details, inks consisting of magnetically responsive anisotropic stiff particles suspended in a light-sensitive liquid resin were deposited using a direct-writing approach. The 3D printer, modified to enable particle alignment with a low-cost neodymium magnet, was also equipped with four syringes to be charged with differently formulated inks. Besides the traditional 3D shaping capabilities, this approach allowed to control the local composition and the particle orientation. With the proposed multimaterial magnetically assisted 3D printing system, heterogeneous composites with unparalleled microstructural features and multifunctional shape-changing soft devices for adhesive-free mechanical fastening could be produced. Figures 10.3a-b, for instance, show a CAD image and the actual print of an intricate heterogeneous helix microstructure. Since the platelets of the spiral staircase ink was brown, its structure was visible within the optical transparent surrounding ink. The surprising aspect is that the local orientation of platelets in each of the staircase steps of the helix was designed to display tangential or radial orientations in an alternating manner from the bottom to the top, thus demonstrating the refined level of control over the local composition of the object. Additional functionality could be achieved in devices undergoing programmed shape changes in 3D when triggered by an external stimulus that causes expansion or contraction of the composite polymer phase. With the same technique a mechanical interlocking was experimentally realized by printing cuboid elements with bilayer walls consisting of crosslinked polymers with different swelling behaviour. Figure 10.3c shows a printed hollow cuboid before the swelling in ethyl acetate. After the treatment (figure 10.3d), the expected shape change was observed with concave and convex surfaces generated by inwards and outwards bending of opposing walls of the cuboid. In figure 10.3d the simulated cross-section of the cuboid, superimposed on the actual part, is also displayed, demonstrating the good agreement between experimental and predicted curvatures.

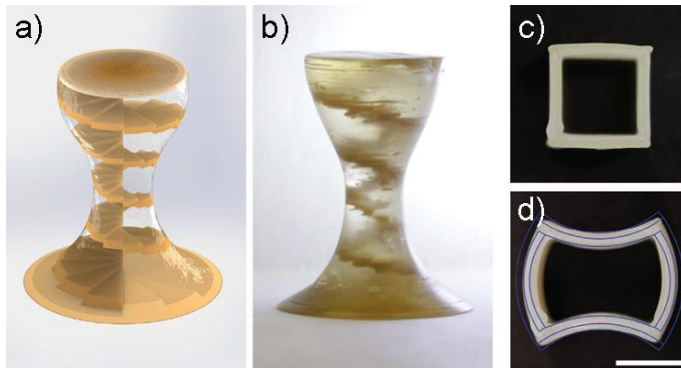


FIGURE 10.3 - A) CAD IMAGE OF A HETEROGENEOUS HELIX MICROSTRUCTURE. B) ACTUAL PRINT COMPOSED BY A PLATELETS LOADED INK (BROWN) AND A TRANSPARENT SURROUNDING INK. C) TOP VIEW OF A PRINTED HOLLOW CUBOID BEFORE SWELLING. D) TOP VIEW OF THE SAME PART AFTER THE INDUCED SHAPE CHANGE⁹.

In the near future, shape-changing parts, as this one, will easily be implemented for manufacturing reconfigurable key-lock connectors, flexible joints and pick-and-place systems in soft robotics. Exploring a wider range of chemistries and adopting biological design guidelines can enable the fabrication of smart composite materials provided with the unique microstructural features exhibited by natural materials. Using a similar strategy based on the alignment of cellulose fibrils at the exit of the nozzle, a shape-morphing system inspired by plant motion has been realized¹⁰. Just as the organs of botanical system respond to environmental stimuli, the printed composite hydrogel architectures proposed in this study showed a controlled anisotropic swelling behaviour when immersed in water. Differently from the magnetically assisted 3D printing, the shape change is induced using a single material patterned in a one-step process. The hydrogel composite material was composed of a soft acrylamide matrix with embedded stiff cellulose fibrils that could be aligned by the shear stress induced during the extrusion, as clearly shown in figure 10.4a. The material swelling behaviour in the longitudinal direction could be consequently associated to the anisotropic stiffness.

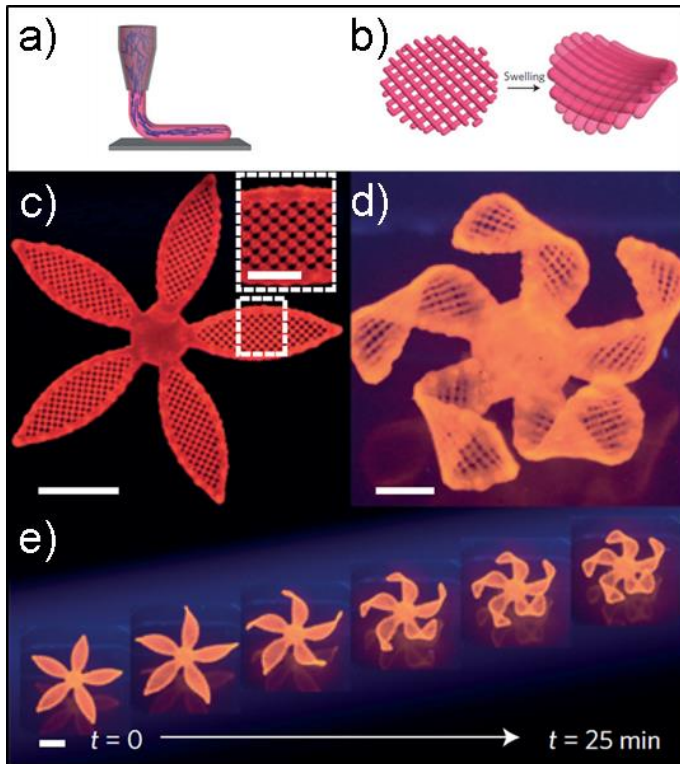


FIGURE 10.4 - A) SHEAR-INDUCED ALIGNMENT OF CELLULOSE FIBRILS DURING HYDROGEL COMPOSITE MATERIAL EXTRUSION. B) EXAMPLE OF THE SWELLING EFFECT ON A PRINT. C) 4D PRINTED FLOWER COMPOSED OF BILAYERS ORIENTED AT 45° WITH RESPECT TO THE LONG AXIS OF EACH PETAL. D) 4D PRINTED FLOWER TWISTED AFTER SWELLING. E) TIME-LAPSE SEQUENCES OF THE FLOWERS MORPHOLOGIES DURING THE SWELLING PROCESS (SCALE BARS, 5 MM, INSET IN C) 2.5 MM)¹⁰.

Figure 10.4b illustrates a bilayer system in which the curvature was induced by the differential swelling between the top and bottom layers, forced to remain in contact along the entire midplane. Exploiting this principle and fitting the experimental behaviour with mathematical models it was possible to 4D print functional folding flower architectures. The floral form, shown in figure 10.4c, comprised of a bilayer lattice with a 45° configuration with respect to the longitudinal axis of each petal. The structure yielded a twisted configuration upon swelling (figure 10.4d). In figure 10.5e the time-lapse sequence of flower morphologies during the swelling process is also shown. Such shape-morphing systems could find applications in many areas, including smart textiles, autonomous robotics, biomedical devices, drug delivery and tissue engineering.

Many of the examples presented so far demonstrate that the fabrication of functional devices often involves the incorporation of multiple materials. Sometimes multimaterial processing consists in the sequential printing of individual materials using multiple nozzles, as in the cases of the mechanoresponsive device and of the magnetically assisted printing process previously illustrated. The drawbacks of printing one material at a time include the need to carefully align each nozzle as well as start-and-stop ink flow on demand without introducing defects. A brilliant solution to avoid such problems consists in a microfluidic printhead that allows to simultaneously print multiple viscoelastic inks through a single nozzle without interrupting the material flow¹¹. The ability to switch between two materials during fabrication in a programmable manner opens new opportunities for creating functional equipment properties defined by the distribution of the different materials. Extrusion-based printing methods have been used to fabricate numerous functional devices, from wearable sensors to structural composites and vascularized 3D tissue. However, one of the fields that is pushing the boundaries towards more innovative shape-shifting systems is soft robotics. The versatility and maneuverability of traditional robotic systems is significantly limited by their intrinsic rigidity. Rigid elements cannot be simply replaced with more compliant ones because robotic systems still need to apply considerable forces and pressure on their surroundings. A valuable option to satisfy these opposing requirements consists in using continuously deformable structures based on smart materials capable of transitioning between hard and soft states. An illustrative example is represented by a flexible cellular solid coated in wax, designed to achieve tunable stiffness, strength, and volume in response to thermal changes¹². The cellular solid could either be a disordered random skeleton like an open-cell polyurethane foam or an ordered lattice structure like a 3D-printed flexible acrylic scaffold. In figure 10.5a two 3D-printed scaffold structures are presented. When uncoated the flexible acrylic scaffold was deformable under applied load whereas the wax-coated scaffold maintained a rigid configuration. Figures 10.5b-c illustrate how to exploit the thermally tunable properties of such composite material. A wax-coated polyurethane foam was connected to an heating element and used as an articulated joint with an applied tip load: at room temperature the composite behaved like a rigid beam and was able to hold the tip load positioned on its edge (figure 10.5b). When an heating element was activated, the wax locally melted causing the beam to bend under the applied load (figure 10.5c). Remarkably, in addition to thermally tunable stiffness, such novel composites, were reported to also exhibit self-healing properties. The wax-coated outer structure, in fact, could lose its structural

stiffness if cracking occurred. However these damages were restored to their original states via reheating, allowing the wax to soften and self-heal.

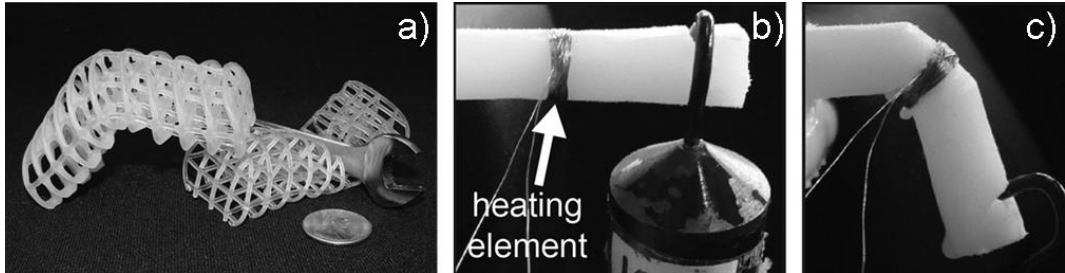


FIGURE 10.5 - A) TWO 3D-PRINTED SOFT, FLEXIBLE SCAFFOLDS; THE ONE ON THE LEFT IS MAINTAINED IN A RIGID, BENT POSITION AFTER BEING COATED IN LIQUID WAX AND COOLED TO RIGIDIFY; THE SAMPLE ON THE RIGHT IS UNCOATED AND REMAINS COMPLIANT, COLLAPSING UNDER A WRENCH. B) A WAX-FILLED, OPEN-CELL POLYURETHANE FOAM BEAM USED AS A RIGID ARTICULATED JOINT. C) AFTER BEGIN LOCALLY HEATED, THE SAME BEAM BENT DUE TO APPLIED TIP LOAD¹².

To conclude, the research on programmable printed materials can potentially revolutionize the future vision of products and processes. For instance, smart wearable materials will sense and adapt to signals given by body temperature, sweat and internal pressure. Finished products will also respond to external stimuli such as moisture content, environmental temperature, pressure, altitude or sound. The impact on traditional industrial manufacturing will be similarly disruptive with easily transformable materials able to self-assemble and reconfigure upon low activation energy. Their tendency to be shape-changing will be exploited during their transportation. Having materials that possess a low volume configuration will cause, as a consequence, drastic reductions in the total volume of shipped objects. Their advanced functionality could probably allow to better resist external force and optimize load distribution during their service life-time. Finally, completely new way of recycling will be available thanks to self-healing or self-disassemble devices. All of these future smart materials will meet the increasing demand of new products by mimicking closer and closer lifelike capabilities^{13,14}.

10.3 REFERENCES

1. Guo, S.-Z., Yang, X., Heuzey, M.-C. & Therriault, D. 3D printing of a multifunctional nanocomposite helical liquid sensor. *Nanoscale* **7**, 6451–6 (2015).
2. Leigh, S. J., Purssell, C. P., Billson, D. R. & Hutchins, D. A. Using a magnetite/thermoplastic composite in 3D printing of direct replacements for commercially available flow sensors - Abstract - Smart Materials and Structures - IOPscience. *Smart Mater. Struct.* **23**, 95039 (2014).
3. Peterson, G. I., Larsen, M. B., Ganter, M. A., Storti, D. W. & Boydston, A. J. 3D-Printed Mechanochromic Materials. (2015). doi:10.1021/am506745m
4. Lewis, J. A. Direct ink writing of 3D functional materials. *Adv. Funct. Mater.* **16**, 2193–2204 (2006).
5. Rutz, A. L., Hyland, K. E., Jakus, A. E., Burghardt, W. R. & Shah, R. N. A multimaterial bioink method for 3D printing tunable, cell-compatible hydrogels. *Adv. Mater.* **27**, 1607–1614 (2015).
6. Lorang, D. J. *et al.* Photocurable liquid core-fugitive shell printing of optical waveguides. *Adv. Mater.* **23**, 5055–5058 (2011).
7. Frutiger, A. *et al.* Capacitive soft strain sensors via multicore-shell fiber printing. *Adv. Mater.* **27**, 2440–2446 (2015).
8. Bakarich, S. E., Gorkin, R., in het Panhuis, M. & Spinks, G. M. 4D Printing with Mechanically Robust, Thermally Actuating Hydrogels. *Macromol. Rapid Commun.* **36**, 1211–7 (2015).
9. Kokkinis, D., Schaffner, M. & Studart, A. R. Multimaterial magnetically assisted 3D printing of composite materials. *Nat. Commun.* **6**, 8643 (2015).
10. Sydney Gladman, A., Matsumoto, E. A., Nuzzo, R. G., Mahadevan, L. & Lewis, J. A. Biomimetic 4D printing. *Nat. Mater.* **15**, 413–8 (2016).
11. Hardin, J. O., Ober, T. J., Valentine, A. D. & Lewis, J. A. Microfluidic Printheads for Multimaterial 3D Printing of Viscoelastic Inks. *Adv. Mater.* 1–6 (2015). doi:10.1002/adma.201500222
12. Cheng, N. G., Gopinath, A., Wang, L., Iagnemma, K. & Hosoi, A. E. Thermally tunable, self-healing composites for soft robotic applications. *Macromol. Mater. Eng.* **299**, 1279–1284 (2014).

13. Tibbits, S. 4D Printing. *Archit. Des.* **84**, 116–121 (2014).
14. Wang, Z., Abdulla, R. & Parker, B. 4D bioprinting : the next-generation technology for biofabrication enabled by stimuli-responsive materials. *Biofabrication* **9**, 12001 (2017).

>>

Appendix A:
list of symbols
and abbreviations

%DA	Conversion of Diels-Alder reaction
2F	Bifuran compound
2M	1,1 ¹ -(methylenedi-4,1-phenylene)bismaleimide
3D	Three-Dimensional
3DP	Three-Dimensional Printing
3F	Trifuran compound
4D	Four-Dimensional
ABS	Acrylonitrile Butadiene Styrene
ACBP	2-amino-5-chlorobenzophenone
AFM	Atomic Force Microscopy
ASTM	American Society for Testing and Materials
α	Critical exponent in the equation of the electrical percolation threshold
BA	Benzyl Alcohol
BF	Bright-field
BuOAc	Butyl Acetate
CAD	Computer-Aided Design
CB	Chlorobenzene
CCD	Charge-coupled Device
CFR	Carbon-fiber Reinforced
CLIP	Continuous Liquid Interface Production
CT	Computed Tomography
D43B	Dellite VR 43B
DA	Diels-Alder
DABP	4,4'-Diaminobenzophenone
DAR	2-hydroxy-2-methyl-1-phenyl-propan-1-one
DCF	2',7'-dichlorofluorescein
DCM	Dichloromethane
DF	Dark-field
DGEBA	Bisphenol A Diglycidyl Ether
DGGO	N,N-diglycidyl-4-glycidylloxylaniline
DICY	Dicyandiamide
DMA	Dynamic Mechanical Analysis
DMF	Dimethylformamide
DMLS	Direct Metal Laser Sintering
DSC	Differential Scanning Calorimetry
DMLS	Direct Metal Laser Sintering
E	Modulus of the composite material
EDM	Electric Discharge Machining
EDS	Energy-dispersive X-ray Spectroscopy

E_f	Modulus of the fiber
E_m	Modulus of the matrix
η	Viscosity
η (chapter 8)	Healing efficiency
FA	Furfurylamine
FDM	Fused Deposition Modeling
FTIR	Fourier-Transform Infrared
φ	MWCNT volume concentration
φ_c	Critical MWCNT volume concentration at electrical percolation
GA	Gum Arabic
$\dot{\gamma}$	Process-related wall shear-rate
$\dot{\gamma}_{app}$	Apparent shear rate
HMDA	Hexamethylenediamine
I_c^x	Carbonyl peak intensity after x hours of curing time
I_m^x	Maleimide peak intensity after x hours of curing time
I_c^{ref}	Carbonyl peak intensity of the reference sample
I_m^{ref}	Maleimide peak intensity of the reference sample
IPN	Interpenetrating Polymer Network
JD400	O,O'-bis(2-aminopropyl)polypropylene glycol
K	Consistency index
L	Length of the capillary
LDM	Liquid Deposition Modeling
LED(s)	Light Emitting Diode(s)
m_c	Mass of the extracted core
MeOH	Methanol
m_i	Initial mass of microcapsules
MRI	Magnetic Resonance Imaging
MWCNT(s)	Multi-Walled Carbon Nanotube(s)
n	Power-law index
NMR	Nuclear Magnetic Resonance
OX200	Fumed silica, specific surface area 200 m ² /g
OX50	Fumed silica, specific surface area 50 m ² /g
P2VP	Poly(2-vinyl pyridine)
P_a	Atmospheric pressure
PCL	Poly(caprolactone)
PDMS	Polydimethylsiloxane
PLA	Poly(lactic acid)
P_{max}	Maximum applicable pressure
PVA	Poly Vinyl Alcohol

Q	Volumetric flow rate
R	Inner radius of the capillary
SEM	Scanning Electron Microscope
SHS	Selective Heat Sintering
SLA	Stereolithography
SLM	Selective Laser Melting
SLS	Selective Laser Sintering
SP	1',3'-dihydro-1',3',3'-trimethyl-6-nitrospiro[2H-1-benzopyran-2,2'-(2H)-indole]
SR349	Bisphenol A Ethoxylate Diacrylate
σ	Electrical conductivity
TDI	Toluene-diisocyanate
TGA	Thermogravimetric Analysis
THF	Tetrahydrofuran
TMPETA	Trimethylolpropane Ethoxylate Triacrylate
TPO-L	2,4,6-trimethylbenzoylphenyl phosphinate
TPU	Thermoplastic Polyurethane
τ	Process-related wall shear-stress
UTS	Ultimate Tensile Strength
UTS^{healed}	Ultimate Tensile Strength of healed samples
UTS^{ref}	Ultimate Tensile Strength of reference samples
UV-3DP	Ultra Violet assisted Three-Dimensional Printing
v_f	Volume fraction of the fibers
VPy	1-Vinyl-Pyrene
X_c	Microcapsules core fraction
ζ	Fiber aspect ratio

>>

Appendix B:
list of publications
and communications

Articles in international journals with referee:

- ❖ **G. Postiglione**, S. Turri, M. Levi.
“Effect of the plasticizer on the self-healing properties of a polymer coating based on the thermoreversible Diels–Alder reaction”.
Progress in Organic Coatings. Volume: 78. Pages: 526-531. 2015
- ❖ **G. Postiglione**, G. Natale, G. Griffini, M. Levi, S. Turri.
“Conductive 3D microstructures by direct 3D printing of polymer/carbon nanotube nanocomposites via liquid deposition modeling”.
Composites Part A-Applied Science and Manufacturing. Volume: 76 Pages: 110-114. 2015
- ❖ **G. Postiglione**, G. Natale, G. Griffini, M. Levi, S. Turri.
“UV-Assisted Three-Dimensional Printing of Polymer Nanocomposites Based on Inorganic Fillers”.
Polymer Composites. DOI: 10.1002/pc.23735. 2015
- ❖ G. Griffini, M. Invernizzi, M. Levi, G. Natale, **G. Postiglione**, S. Turri.
“3D-printable CFR polymer composites with dual-cure sequential IPNs”.
Polymer. Volume: 91. Pages: 174-179. 2016

Communications at national and international conferences:

- ❖ **G. Postiglione**, S. Turri, M. Levi, B. Di Credico.
European Conference. Smart & Functional Coatings. Turin 2013.
Oral presentation:
“A self-healing polymer network based on thermoreversible Diels-Alder reaction”
- ❖ **G. Postiglione**, B. Di Credico, M. Levi, S. Turri.
NanotechItaly 2013. Venice.
Poster presentation:
“A new thermoreversible polymer with self-healing ability”
- ❖ **G. Postiglione**, S. J. Leigh, M. Levi, S. Turri.
Bruker Micro-CT User Meeting 2016. Luxembourg.
Oral presentation:
“Self-healing polymers based on microvascular networks”

The following articles were published on international journals:



Effect of the plasticizer on the self-healing properties of a polymer coating based on the thermoreversible Diels–Alder reaction



Giovanni Postiglione*, Stefano Turri, Marinella Levi

Department of Chemistry, Materials and Chemical Engineering "Giulio Natta" Politecnico di Milano, Piazza Leonardo da Vinci 32, 20133 Milan, Italy

ARTICLE INFO

Article history:
Available online 16 June 2014

Keywords:
Self-healing polymer
Diels–Alder reaction
Thermoreversible polymer network
Scratch recovery

ABSTRACT

A self-healing polymer for coating application was developed based on thermoreversible Diels–Alder (DA) reactions. The polymer network is formed by reacting a mixture of trifunctional and difunctional furanized resins (3F and 2F) with a bismaleimide (2M). The DA reaction occurs at temperature above 50 °C whilst retro-DA reaction occurs at about 120 °C. FTIR spectra were taken in order to monitor the reaction progress, and the thermal reversibility of the reaction was proved by DSC and DMA tests. A significant improvement of both the mechanical properties and the self-healing behaviour was achieved by introduction of small amount of a suitable plasticizer like benzyl alcohol. Self-healing properties of the plasticized polymer resulted in complete scratch recovery after retro-DA and DA reaction, whilst tensile testing reveals a 48% restoring of the pristine mechanical strength.

© 2014 Elsevier B.V. All rights reserved.

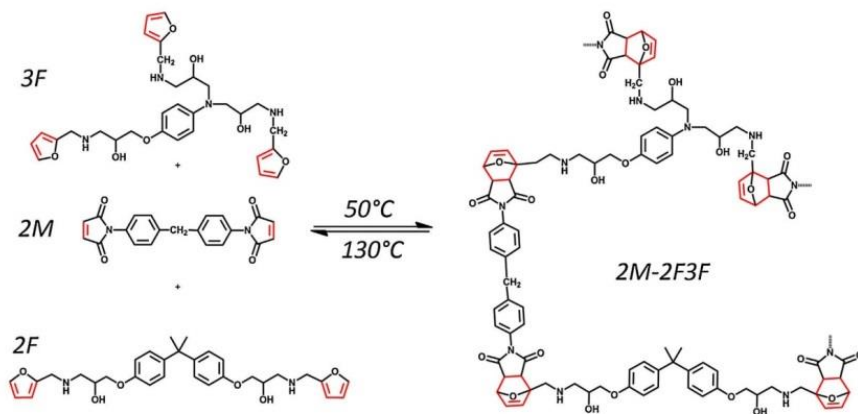
1. Introduction

Smart polymers are materials able to respond to changes in external environments by developing readable signals and/or corrective actuation mechanisms; among them, self-healing polymers are gaining an increasing interest for their ability to heal cracks or mechanical damages thus extending their lifetime [1]. Different approaches have been followed to design and realize a self-healing mechanism: namely autonomous and heteronomous healing. The first approach is achieved introducing microcapsules [2–5], hollow fibres [6] or microvascular networks [7] inside the material, so that, in response to a mechanical damage, a healing agent can be released, and repairs the structure by spontaneous polymerization. With this approach the healing efficiency is granted only once, thus limiting their applications. Externally stimulated or heteronomous healing systems, on the contrary, exploit physical or chemical changes occurring in the material in response to stimuli such as heat, light, electricity or magnetic field [8]. In Urban et al. works some examples of polymers self-repairing in response to UV-light radiation and magnetic field oscillation are reported [9–11]. The well-known Diels–Alder reaction, which is thermally reversible, can be used for designing thermosetting self-healing

polymers [12–14]. In that case, multiple cycles of heating treatment for activating the healing reaction are possible. Frequently used Diels–Alder functional groups are furans and maleimides as dienes and dienophiles, respectively, allowing the material to heal in a narrow temperature range [15–22]. In Tian et al. work [23,24], a new molecule with both epoxide and furan groups was synthesized and crosslinked with maleimides, and the final material showed both mending ability and high mechanical strength. In these polymer networks at temperature above 120 °C the chemical linkages disconnect (through retro-DA reaction) and then reconnect upon cooling. It was also possible to graft furan and maleimide pendant groups to polymeric chains; crosslinking, via DA reaction, gave the polymer self-repairing properties. This approach has been followed for polyamides, polyketones and copolymers [25–28]. In another study, a reversible crosslinked healing gel totally based on DA bonds was synthesized in dimethylformamide (DMF) as solvent. Subsequently, it was included as a secondary phase within the structure of a conventional epoxy-amine thermoset polymer [29]. Our study combines the idea of creating a network totally based on DA crosslinks with the use of thermosetting polymers for adhesives and coating application. Using an epoxy resins as precursors, a new thermosetting polymer network completely based on DA crosslinks has been realized. Benzyl alcohol was used as a plasticizer in order to improve the healing efficiency. During the curing process, DA adducts formation has been monitored by means of infrared spectroscopy. Thermal and mechanical characterization, together with optical microscopy observations and gloss measurements, demonstrated the ability to heal scratches and cracks several times

* Corresponding author. Tel.: +39 0223993249; fax: +39 0270638173.
E-mail addresses: giovanni.postiglione@polimi.it (G. Postiglione), stefano.turri@polimi.it (S. Turri), marinella.levi@polimi.it (M. Levi).

<http://dx.doi.org/10.1016/j.porgcoat.2014.05.022>
0300-9440/© 2014 Elsevier B.V. All rights reserved.



Scheme 1. DA and retro-DA reactions.

with controlled thermal treatments and quantified the healing efficiency.

2. Experimental

2.1. Materials and methods

Furfurylamine (FA), 1,1'-(methylene-4,4'-phenylene) bismaleimide (2M), N,N-diglycidyl-4-glycidylxyaniline (DGGO), bisphenol A diglycidyl ether (DGEBA), dichloromethane and methanol were all purchased by Sigma Aldrich and used as received. Fourier transform infrared spectra (FTIR) were acquired using a Thermo Nicolet Nexus FTIR spectrometer. Spectra were collected from 400 to 4000 cm^{-1} . Thermo gravimetric analyses (TGA) were performed on a TA Instrument Q500 in nitrogen and air at a heating rate of $3^{\circ}\text{C}/\text{min}$. Differential scanning calorimetry (DSC) was carried out with a Mettler–Toledo TA3000 instrument, indium and *n*-hexane calibrated, heating from 20°C to 140°C with a rate of $10^{\circ}\text{C}/\text{min}$ in a N_2 environment. Dynamic mechanical analysis (DMA) was conducted on a Mettler Toledo DMA/SDTA861 instrument from 20°C to 180°C at a $3^{\circ}\text{C}/\text{min}$ heating rate. Tensile properties were tested at room temperature by a Zwick/Roell Z010 under a constant crosshead rate of $25\text{ mm}/\text{min}$ (5 specimens, 18 mm gauge length, 5 mm width, 3 mm thickness). Gloss measurements were made on $100\text{ }\mu\text{m}$ thick coatings deposited on a white cementitious substrate at a reflective angle of 60° .

2.2. Synthesis of 3F and 2F compounds

First, 12 g of viscous resin DGGO were mixed with 12.6 g of liquid FA (in the stoichiometric ratio 1:3 molar) under stirring and left to react in methanol at 85°C for 3 h. At the end of the reaction, the product (trifuran, 3F) was obtained by drying the sample under vacuum until constant weight was reached. Similarly, 10 g of DGEBA were mixed and heated with 5.7 g of furfurylamine (in the stoichiometric ratio 1:2 molar) leading to the formation of bifuran, 2F following the same procedure. Yields were $>95\%$ in both cases. Chemical characterization of furan adducts was performed with FTIR spectroscopy, monitoring the progressive disappearance of peak of oxirane ring at 910 cm^{-1} .

2.3. Synthesis of 2M-3F2F polymer

The Diels-Alder based polymer was prepared by reacting a mixture of the two furan adducts (3F:2F = 1:1 molar ratio, $3\text{F} + 2\text{F} = 0.0106\text{ mol}$), pre-heated at 70°C for lowering their viscosity, with the bismaleimide powder (2M, 0.0132 mol) dissolved in dichloromethane. The reaction mixture was heated on a hot-plate at 50°C with a magnetic stirrer until most of the solvent was evaporated. The resultant highly viscous liquid was poured in a mould and cured at 80°C for 10 h in vacuum to remove the residual solvent. A highly crosslinked network (2M-2F3F) based on DA bonds was achieved as shown in Scheme 1.

An identical procedure was followed for plasticized formulations. Benzyl alcohol (10%, w/w) was added into the solution at the beginning of the crosslinking reaction leading to formation of 2M-3F2F/BA polymer.

3. Results and discussion

3.1. Synthesis and characterization of 2M-3F2F polymer

The monitoring of the 2M-2F3F polymer synthesis and its curing process was carried out by means of FTIR analysis. There are three significant peaks that have been considered: one at 700 cm^{-1} , representing the C–H bonds attached the C=C in the maleimide ring, which is involved in the DA reaction, the peak at 1774 cm^{-1} typical of the DA adducts of maleimides and the maleimide carbonyl peak at 1712 cm^{-1} (invariant during the reaction). The first two peaks give a measure of the DA adducts formation from maleimide pendant groups; the third has been taken as a reference. In Fig. 1, FTIR spectra of 2M, 2M-2F3F uncured and 2M-2F3F after curing at 80°C are presented. The presence of the peak at 1774 cm^{-1} in the 2M-2F3F polymer reveals the DA adducts generation within their structure after the reaction. As expected the intensity of the peak at 700 cm^{-1} is high in the 2M compound but its signal is reduced in the 2M-2F3F polymers; moreover after the curing process, the peak is even less intense but does not disappear.

Although the network is totally composed by DA bonds, not all pendant groups can react generating DA crosslinks. DA adducts conversion in the 2M-2F3F has been estimated by a spectroscopic quantitative analysis of absorbance spectra, comparing the

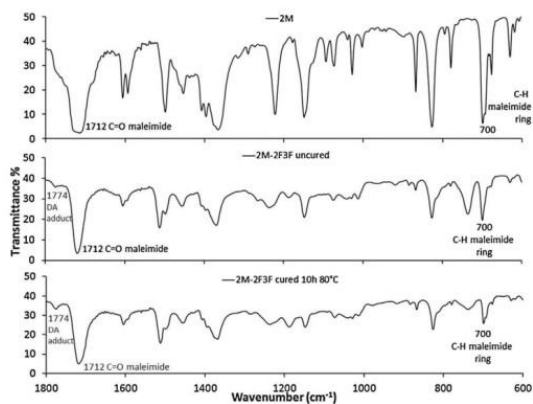


Fig. 1. FTIR spectra of 2M, 2M-2F3F not cured and 2M-2F3F cured for 10 h at 80 °C.

maleimide peak intensity at 700 cm^{-1} (I_m) to the carbonyl peak intensity at 1712 cm^{-1} (I_c) at different curing times.

In particular, the fraction of unreacted maleimide groups can be calculated using the following equation:

$$\%DA = \left(1 - \frac{I_m^x / I_c^x}{I_m^{ref} / I_c^{ref}}\right) \times 100$$

in which I_m^x and I_c^x are the maleimide peak intensity and the carbonyl peak intensity of the 2M-2F3F polymer after x hours of curing time, whilst I_m^{ref} and I_c^{ref} refer to the intensity of the 2M. The percentage of DA conversion has been calculated at different curing times. Results are shown in Fig. 2. It seems that after 10 h of curing at 80 °C about 60% of the maleimide groups has reacted.

The trend shown in Fig. 2, suggests that extending the curing time does not lead to a further progression of the reaction. This is due to the fact that the crosslinking process proceeds until the T_g of the material meets the cure temperature and vitrification occurs (see also Fig. 3). Being the polymer network thermoreversible at temperature exceeding 100 °C, it is not possible to further increase the process temperature because such a treatment would result

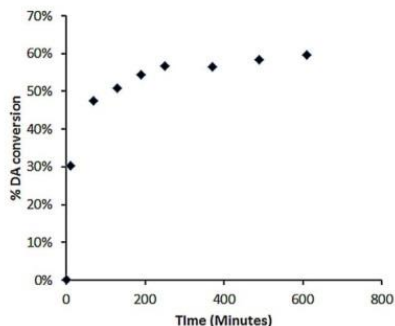


Fig. 2. isothermal (80 °C) conversion curve of the DA polymer.

into a partial debonding of DA adducts just formed. This could be therefore an intrinsic limitation of the particular formulation developed in this present work. DSC and DMA analyses help to better interpret the thermal behaviour of the 2M-2F3F polymer. Fig. 3 shows the heating DSC curve of the cured 2M-2F3F polymer. The curve has a first transition, corresponding to the T_g , at about 80 °C

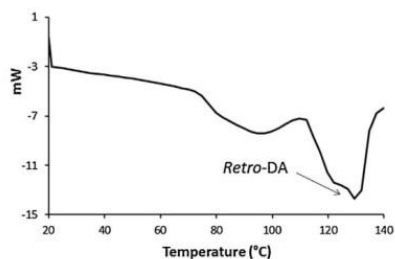


Fig. 3. DSC scan of 2M-2F3F polymer. Heating rate at 10 °C/min.

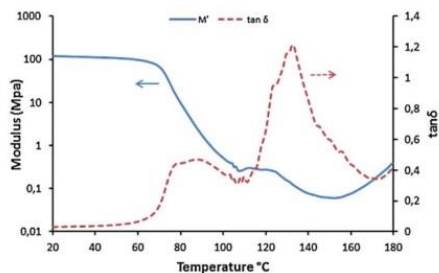


Fig. 4. DMA curves of 2M-2F3F polymer. Heating rate at 3 °C/min.

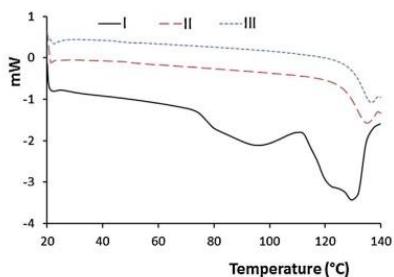


Fig. 5. DSC curves of 2M-2F3F polymer. Three heating cycle on the same sample at 10°C/min.

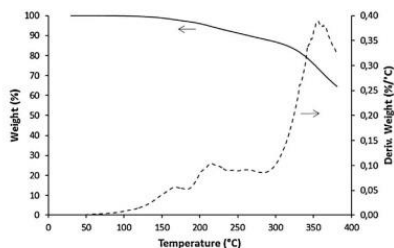


Fig. 6. TGA curve of 2M-2F3F/BA polymer.

and an evident endothermic peak at 130°C, the latter indicating the retro-Diels-Alder reaction occurring in the polymer.

Such behaviour is confirmed by also the DMA analysis in which the $\tan \delta$ curve also shows a peak around +130°C and a glass transition at +80°C (Fig. 4).

DSC was also used to study the effects of multiple heating cycles on the sampled polymer. Fig. 5 shows three subsequent DSC scans performed at a rate of 10°C/min on the same sample, letting it cooling down after every cycle at ambient temperature. A large endothermic peak is evident at about 130°C in the first heating curve; in following heating cycles the peaks, despite being slightly pushed towards higher temperatures, still confirm the presence of retro-DA reaction.

The repeatability of the process of disconnection and reconnection of DA bonds has interesting implication as it is possible to perform multiple healing cycles on a same damaged spot.

In spite of the evidences of thermal analysis, the 2M-3F2F neat polymer was very brittle and showed visually a quite poor efficiency in the healing process of scratches and cracks induced on the surface. Brittleness and unsatisfactory healing performances are likely due to the low conversion and early vitrification. Introduction of a plasticizer may increase the free volume and molecular mobility of the polymer network, allowing to obtain a higher conversion of the crosslinking process. Benzyl alcohol has been chosen as a plasticizer for its good compatibility, low toxicity and relatively low volatility. FTIR analyses demonstrated that DA and retro-DA reactions are not affected by the presence of the plasticizer, while a TGA was needed to assess the suitability of BA with the thermal cycles used for the thermally induced self-healing experiments.

As shown in Fig. 6, the 2M-3F2F/BA plasticized polymer shows a good thermal stability in the whole temperature range needed to activate DA and retro-DA reactions. At 140°C it only has <1% of weight loss. A significant weight loss which can be attributed to

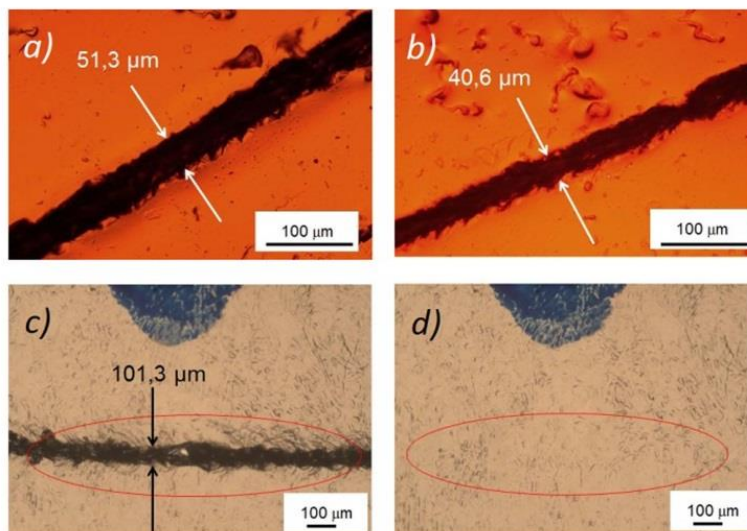


Fig. 7. Optical microscope images of (a) 2M-2F3F polymer scratched, (b) 2M-2F3F polymer after 10 min heating treatment at 120°C, (c) 2M-2F3F/BA polymer scratched, (d) 2M-2F3F/BA polymer after 10 min heating treatment at 120°C.

530

G. Postiglione et al. / Progress in Organic Coatings 78 (2015) 526–531

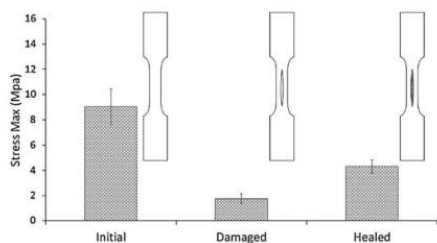


Fig. 8. Mechanical strength for virgin, mechanically damaged, and thermally healed DA polymers.

BA evaporation starts above 200 °C. The DA polymer network plasticized with 10% of benzyl alcohol showed macroscopically much better mechanical and self-healing properties, which are described in detail the Section 3.2.

3.2. Healing properties

The self-healing properties of the neat and plasticized DA polymers were first investigated through optical microscopy. The resulting images are shown in Fig. 7. A razor blade was used to make a scratch on the sample surface. The sample was then heated at 120 °C for 10 min. Fig. 7a and b shows the effect of the heating treatment on the 2M-3F2F neat polymer. The average width of the crack, being 51.3 μm before heating, became 40.6 μm, thus resulting in a minimal healing of the scratch. The low mobility of the high T_g chains does not allow the material to totally recover the damage. Fig. 7c and d shows the same experiment repeated for the 2M-3F2F/BA formulation. The same heating cycles allows for the total recovery of a 100 μm scratch. The same location on the surface has been scratched and re-healed two more times with the same effectiveness demonstrating that multiple healing cycles are feasible.

A more quantitative assessment of the healing performances was done through tensile tests carried out on virgin, mechanically damaged, and thermally healed samples. The results concerning maximum stress values are shown in Fig. 8. The mechanical strength of the 2M-3F2F/BA polymer is about 9 MPa. After causing a 15 mm lengthwise damage on the sample (images of a virgin, an artificially damaged and a healed sample are shown in the inset), the stress values drop significantly to less than 2 MPa. After the 120 °C/10 min healing cycle, the mechanical properties are partially restored leading to a maximum stress of 4.3 MPa. The significant 48% recovery in maximum stress reached by the 2M-3F2F/BA polymer indicates an efficient thermoreversibility of the DA network. In previous reports, the healing efficiency of DA based formulation has been investigated through different mechanical tests. In compact tension experiments the healing efficiency as a percentage of the load recovered stays within a 37–80% range [29,30]. On dumbbell-shaped samples a 55% tensile strength recovery has been reported [31], thus confirming the results of our formulation.

The healing behaviour of the 2M-3F2F/BA polymer was also assessed in term of gloss recovery after a mar test. The optical measurements were firstly taken on a virgin sample, then the surface was marred with a steel scrub to obtain a matt finish, and finally the gloss measurements were repeated after the thermal healing cycle. Results are shown in Fig. 9.

The virgin DA coating surface is very bright resulting in an average gloss value of 93.5 GU; the same surface, once marred, becomes opaque thus inducing a significant drop of the gloss values down

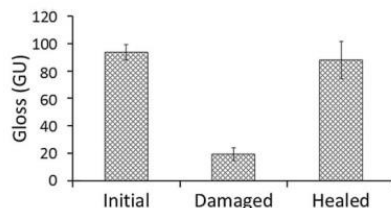


Fig. 9. Gloss values for virgin, marred and thermally healed DA polymers.

to 19.4 GU. The healing treatment allows the material to almost completely recover its original gloss (88.0 GU), corresponding to an aesthetic healing efficiency of about 95%. The procedure was repeated three times always observing an excellent gloss recovery.

4. Conclusive remarks

A new crosslinked polymer based on thermoreversible Diels–Alder reaction was presented. Thermoreversibility was proved by FTIR spectroscopy, DSC and DMA. It was however observed that thermoreversibility alone is not enough to provide an efficient thermally stimulated healing behaviour. The smart behaviour of the polymer was significantly improved by the addition of low amounts (10% w/w) of a proper plasticizer, benzyl alcohol in the specific instance, which is thermally stable in the temperature range needed to activate the retro Diels–Alder reaction. The plasticized formulation showed an excellent recovery of aesthetic appearance of the scratched surface. The use of benzyl alcohol as a plasticizer is intrinsically a limitation, however a good thermal stability and no exudation in practical use conditions were verified. The thermally stimulated healing behaviour was positively demonstrated more times in the same place. An evaluation of the healing efficiency was done through proper mechanical and gloss tests, showing an efficiency of around 48% and 95% respectively. Diels–Alder polymers are promising candidates for the development of heteronomous self-healing coatings with multiple healing efficiency, and excellent aesthetic recovery of the surface appearance.

References

- [1] S.J. Garcia, H.R. Fischer, S. van der Zwaag, *Prog. Org. Coat.* 72 (2011) 211–221.
- [2] S.R. White, N.R. Sottos, P.H. Geubelle, J.S. Moore, M.R. Kessler, S.R. Srimam, E.N. Brown, S. Viswanathan, *Nature* 409 (2001) 794–797.
- [3] B. Di Credico, M. Levi, S. Turri, *Eur. Polym. J.* 49 (2013) 2467–2476.
- [4] J.L. Yang, M.W. Keller, J.S. Moore, S.R. White, N.R. Sottos, *Macromolecules* 41 (2008) 9650–9655.
- [5] M. Koubi, A. Mohebbi, M. Mirzaei, M. Peikari, *Prog. Org. Coat.* 76 (2013) 1006–1015.
- [6] J.W.C. Pang, I.P. Bond, *Compos. Sci. Technol.* 65 (2005) 1791–1799.
- [7] K.S. Toohy, N.R. Sottos, J.A. Lewis, J.S. Moore, S.R. White, *Nat. Mater.* 6 (2007) 581–585.
- [8] E.B. Murphy, F. Wudl, *Prog. Polym. Sci.* 35 (2010) 223–251.
- [9] B. Ghosh, M.W. Urban, *Science* 323 (2009) 1458–1460.
- [10] C.C. Corien, M.W. Urban, *Adv. Mater.* 21 (2009) 5011–5015.
- [11] M.W. Urban, *Prog. Polym. Sci.* 34 (2009) 679–687.
- [12] X.X. Chen, M.A. Dam, K. Ono, A. Mal, H.B. Shen, S.R. Nutt, K. Sheran, F. Wudl, *Science* 295 (2002) 1698–1702.
- [13] M.A. Tasdelen, *Polym. Chem.* 2 (2011) 2133.
- [14] A. Gandini, *Prog. Polym. Sci.* 38 (2013) 1–29.
- [15] Y. Imai, H. Itoh, K. Naka, Y. Chujo, *Macromolecules* 33 (2000) 4343–4346.
- [16] T.A. Plaisted, S. Nemat-Nasser, *Acta Mater.* 55 (2007) 5684–5696.
- [17] Y.L. Liu, C.Y. Hsieh, *J. Polym. Sci. A: Polym. Chem.* 44 (2006) 905–913.
- [18] C. Zeng, H. Setino, J. Ren, K. Hatanaka, N. Yoshie, *Macromolecules* 46 (2013) 1794–1802.
- [19] N. Bai, K. Saito, G.P. Simon, *Polym. Chem.* 4 (2013) 724–730.
- [20] M. Wouters, E. Craemnehr, K. Tempelaars, H. Fischer, N. Stroeks, J. van Zanten, *Prog. Org. Coat.* 64 (2009) 156–162.

- [21] G. Scheltjens, M.M. Diaz, J. Brancart, G. Van Assche, B. Van Mele, *React. Funct. Polym.* 73 (2013) 413–420.
- [22] C. Vilela, L. Cruciani, A.J.D. Silvestre, A. Gandini, *Adv. RSC* 2 (2012) 2966.
- [23] Q. Tian, Y.C. Yuan, M.Z. Rong, M.Q. Zhang, *J. Mater. Chem.* 19 (2009) 1289.
- [24] Q. Tian, M.Z. Rong, M.Q. Zhang, Y.C. Yuan, *Polym. Int.* 59 (2010) 1339–1345.
- [25] Y.-L. Liu, Y.-W. Chen, *Macromol. Chem. Phys.* 208 (2007) 224–232.
- [26] C. Toncelli, D.C. De Reus, F. Picchioni, A.A. Broekhuis, *Macromol. Chem. Phys.* 213 (2012) 157–165.
- [27] M.J. Barthel, T. Rudolph, A. Teichler, R.M. Paulus, J. Vitz, S. Hoepfener, M.D. Hager, F.H. Schacher, U.S. Schubert, *Adv. Funct. Mater.* 23 (2013) 4921–4932.
- [28] A.A. Kavitha, N.K. Singha, *Macromolecules* 43 (2010) 3193–3205.
- [29] A.M. Peterson, R.E. Jensen, G.R. Palmese, *ACS Appl. Mater. Interfaces* 1 (2009) 992–995.
- [30] X.X. Chen, F. Wudl, A.K. Mal, H.B. Shen, S.R. Nutt, *Macromolecules* 36 (2003) 1802–1807.
- [31] N. Yoshie, S. Saito, N. Oya, *Polymer* 52 (2011) 6074–6079.



Contents lists available at ScienceDirect

Composites: Part A

journal homepage: www.elsevier.com/locate/compositesa

Short communication

Conductive 3D microstructures by direct 3D printing of polymer/carbon nanotube nanocomposites *via* liquid deposition modeling

Giovanni Postiglione, Gabriele Natale, Gianmarco Griffini*, Marinella Levi, Stefano Turri

Department of Chemistry, Materials and Chemical Engineering "Giulio Natta", Politecnico di Milano, Piazza Leonardo da Vinci 32, 20133 Milano, Italy

ARTICLE INFO

Article history:

Received 7 November 2014

Received in revised form 15 May 2015

Accepted 17 May 2015

Available online 27 May 2015

Keywords:

A. Polymer-matrix composites (PMCs)

B. Electrical properties

B. Rheological properties

3D printing

ABSTRACT

In this work, a new three-dimensional (3D) printing system based on liquid deposition modeling (LDM) is developed for the fabrication of conductive 3D nanocomposite-based microstructures with arbitrary shapes. This technology consists in the additive multilayer deposition of polymeric nanocomposite liquid dispersions based on poly(lactic acid) (PLA) and multi-walled carbon nanotubes (MWCNTs) by means of a home-modified low-cost commercial benchtop 3D printer. Electrical and rheological measurements on the nanocomposite at increasing MWCNT and PLA concentrations are used to find the optimal processing conditions and the printability windows for these systems. In addition, examples of conductive 3D microstructures directly formed upon 3D printing of such PLA/MWCNT-based nanocomposite dispersions are presented. The results of our study open the way to the direct deposition of intrinsically conductive polymer-based 3D microstructures by means of a low-cost LDM 3D printing technique.

© 2015 Elsevier Ltd. All rights reserved.

1. Introduction

Three-dimensional (3D) printing is a fabrication technology that consists in the creation of a 3D object starting from a digital model. 3D printing technologies have evolved very rapidly in recent years and have shifted apart from their traditional application field, namely rapid prototyping. Indeed, 3D printing is now being used routinely in a variety of manufacturing sectors ranging from aerospace and automotive to bioengineering [1,2]. At present, stereolithography, selective laser sintering, selective laser melting and fused deposition modeling (FDM) are among the most widely employed and investigated additive manufacturing methods both in academia and in industrial environments [3]. The various 3D printing technologies differ in terms of cost, maximum spatial resolution and type of materials used. In particular, for the first three methods, 3D features with a very high spatial resolution (in the order of a few μm at most) have been demonstrated but at the expense of relatively high equipment costs and the need of specialized personnel to operate them [3,4]. On the other hand, FDM has recently become fairly popular especially among non-specialized personnel as it represents a very cost effective approach to produce 3D objects with a relatively good resolution, which can approach 40 μm [5]. However, being a thermally-driven process that requires melting of a thermoplastic filament prior to the additive

deposition of the extruded feature, it exhibits some limitations related to the materials to deposit, as only relatively few polymers possess the right thermal and rheological properties to be easily processable with this technology (with poly(lactic acid) – PLA and acrylonitrile-butadiene-styrene – ABS being among the most widely employed) [6]. Recently, the FDM approach was shown to allow a high degree of orientation of short reinforcing fibers in polymer-based composites during filament extrusion, resulting in 3D printed components with unique structural properties that can significantly exceed those of traditional compression molded samples [7]. In addition, the potential of the FDM technology for the fabrication of electronic sensors was recently demonstrated by 3D-printing solid filaments obtained starting from a dispersion of conductive carbon black into a solution of a commercial formulation of poly(caprolactone) (PCL) in dichloromethane (DCM) followed by evaporation of the solvent to form the solid filament to be extruded in a table-top FDM 3D printer [8]. Even though the approach presented in this work clearly allows the possibility to 3D-print objects with embedded sensors and electronic functionalities in a relatively simple fashion, it still requires the additional step of the production of a solid (nano)composite filament to be heated and melted in order to be processed with a standard FDM 3D printer.

Very recently solvent-cast 3D printing has emerged as a versatile and cost-effective strategy to overcome some of the limits imposed by the FDM approach [9]. This relatively new technology consists in the additive deposition of material layers directly from a solution in

* Corresponding author. Tel.: +39 02 2399 3213.

E-mail address: gianmarco.griffini@polimil.it (G. Griffini).

a volatile solvent. By means of this technology, the production of freeform structures, scaffolds and other self-standing microstructures was recently demonstrated using a computer-controlled robot moving along the x, y and z axes a dispensing apparatus equipped with a 100 μm inner-diameter extruding nozzle, starting from a concentrated solution of PLA in DCM [9]. In addition, by sputtering a metallic layer a few tens of μm thick onto the 3D printed structure, electrically conducting objects could also be obtained. However, no examples of the fabrication of intrinsically conductive 3D microstructures via direct 3D printing of conductive polymer-based nanocomposite materials from liquid dispersion have so far been reported in the literature, notwithstanding their enormous technological potential for application in fields such as microelectronics and biomedical engineering, where this approach would allow the direct fabrication of conductive microstructures with tailored 3D architectures in a low-cost and highly versatile fashion.

In the effort to address this issue, a 3D printing technique is developed in this work for the fabrication of conductive 3D microstructures with arbitrary shapes via the deposition of a new conductive nanocomposite from liquid dispersion by means of a low-cost commercial benchtop 3D printer equipped with a syringe dispenser (see [Supplementary data](#)). This method, that will be called liquid deposition modeling (LDM) throughout the text in analogy to the FDM approach introduced earlier, is based on the direct deposition of a homogeneous dispersion of multiwall carbon nanotubes (MWCNTs) in PLA using a high volatility solvent (i.e., DCM) as dispersion medium to ensure fast evaporation during wet filament deposition and rapid formation of rigid 3D microstructures. A thorough electrical characterization of the nanocomposite at increasing MWCNT concentrations is performed to evaluate the percolation threshold to achieve electrical conductivity. In addition, the rheological behavior of the nanocomposite dispersion is experimentally investigated at varying solid (PLA) content and a printability window for this system is identified based on the shear-rate of the material at the extrusion nozzle. Finally, examples of conductive 3D microstructures directly formed upon LDM of such MWCNT-based nanocomposite dispersion are presented. Conductive features as small as 100 μm can be reproducibly obtained with this method, indicating the high reliability of our approach. LDM clearly lends itself to the possibility of incorporating different types of structural and functional (nano)fillers in the 3D printed extruded feature without the need of producing a solid (nano)composite filament, thus presenting clear benefits compared to the more common FDM approach.

2. Experimental

MWCNTs were purchased from Nanocyl, Belgium (Nanocyl NC 3100, purity >95%, 9.5 nm average diameter and 1.5 μm average length). PLA pellets were supplied by Futura Elettronica, Italy. DCM was purchased from Sigma–Aldrich, Italy. All products were used as received. For the preparation of the nanocomposite dispersions at increasing MWCNT concentration, a 3 wt% stock solution of PLA in DCM was prepared under magnetic stirring at room temperature for 3 h. After complete dissolution of PLA, the desired amount of MWCNTs (ranging from 0.5 wt% to 10 wt% in PLA) was dispersed in the PLA/DCM solution using the following procedure [10]: addition of the MWCNTs, 30 min magnetic stirring at 950 rpm, 1 h ultrasonic bath (Starsonic 90) at room temperature, 30 min ultrasonication with a Sonic & Materials VCX130 sonicator tip (20 kHz, 130 W, oscillation amplitude 80%). This last step was carried out in an ice bath in order to prevent DCM evaporation and to minimize undesired exothermic phenomena resulting from the ultrasonication process. A similar procedure was employed for

the preparation of nanocomposite dispersions at increasing PLA concentrations in DCM. In this case, a 1 wt% MWCNT concentration in PLA was employed and the PLA content in DCM was progressively varied (25 wt%, 30 wt% and 35 wt%). To perform electrical measurements, 25 mm \times 75 mm thin film samples with a thickness ranging between 40 and 100 μm were prepared by drop-casting each nanocomposite dispersion with a given MWCNT concentration on a glass substrate. Upon drying in a ventilated oven, a solid self-standing nanocomposite film was obtained. The electrical conductivity of the nanocomposite films was measured using a four-point probe apparatus connected to a Keithley 2612 digital source-measure unit. A current scan between 0.01 and 0.1 A was applied on each sample with 50 steps and a settling time of 1 s for each measured step. The electrical conductivity of the nanocomposites was then calculated from resistance measurements [11]. Characterization of the rheological properties of the nanocomposite dispersions at increasing PLA concentrations (1 wt% MWCNT in PLA) was performed using a Rheometrics DSR200 rheometer with a 25 mm plate–cone configuration at 25 $^{\circ}\text{C}$. Steady shear tests on the MWCNT/PLA/DCM dispersions were performed for 3 min in the 0–4500 Pa range. Optical microscopy was employed to evaluate the microstructural features of the 3D-printed architectures using an Olympus BX-60 reflected-light optical microscope with bright-field (BF) and dark-field (DF) imaging equipped with an Infinity 2 digital camera. Scanning electron microscopy (SEM) was performed on 3D-printed nanocomposite-based microstructures with a Carl Zeiss EVO 50 Extended Pressure scanning electron microscope (acceleration voltage of 15.00–17.50 kV) to evaluate their surface morphology and the 3D architecture (samples were sputtered with a gold coating prior to SEM analysis). A low-cost home-assembled 3D printer (Futura Elettronica, Italy) was used for LDM-based 3D printing of the conductive nanocomposite microstructures (see [Supplementary data](#) for details on the 3D printer setup).

3. Results and discussion

In this work, the high electrical conductivity of MWCNTs was exploited to impart conductive character to the final MWCNT/PLA nanocomposite. To determine the effect of the addition of MWCNTs to the PLA matrix, the volume electrical conductivity σ of MWCNT/PLA nanocomposites was evaluated from resistance measurements on solvent-cast nanocomposite films with increasing MWCNT content (0.5–10 wt%). As shown in [Fig. 1a](#), conductivity σ is found to increase substantially with respect to pristine PLA already upon addition of 0.5 wt% MWCNTs. Furthermore, a progressive increase in σ is observed for increasing MWCNT concentrations following a typical percolation behavior, until values in the range 10–100 S/m are reached for highly concentrated (5–10 wt%) MWCNT/PLA nanocomposites. Similar values of electrical conductivity were obtained on analogous nanocomposite systems based on MWCNTs and PLA matrix [12,13].

Achieving a uniform homogeneous dispersion of MWCNTs within a polymeric matrix is a key factor for the development of printable MWCNT-based nanocomposites because of the high tendency of MWCNTs to form bundles and aggregates [14] that may cause clogging of the printing nozzle and flux instability during the printing process. Therefore, an appropriate MWCNT concentration is required to obtain a nanocomposite material that is simultaneously conductive and 3D printable. The fracture surface of cryo-fractured 3D printed MWCNT/PLA nanocomposites containing 10 wt% of MWCNTs obtained from SEM analysis is shown in [Fig. 1b](#). As evident from the SEM micrograph, a good level of dispersion and distribution of MWCNTs (white dots in the image) is achieved in the PLA matrix without the formation of any noticeable

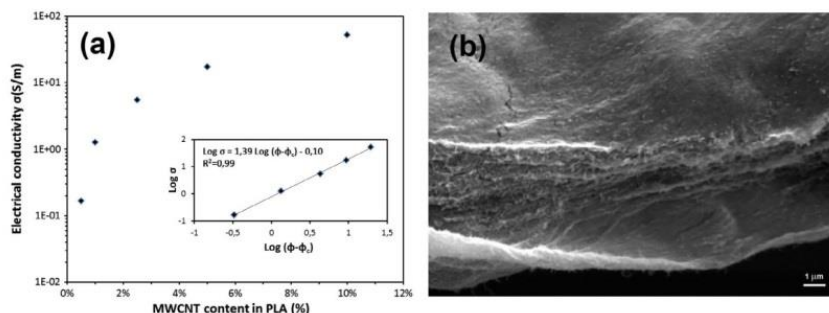


Fig. 1. (a) Volume electrical conductivity as a function of MWCNT concentration. The inset shows the log–log plot of the electrical conductivity versus the volume fraction of MWCNTs; (b) SEM micrograph of cryo-fractured 3D-printed MWCNT/PLA nanocomposites (10 wt% MWCNT in PLA). (For interpretation of the references to color in this figure legend, the reader is referred to the web version of this article.)

aggregates, even at high MWCNT content. With the aim of determining the minimum theoretical MWCNT concentration to achieve electrical conductivity in the nanocomposite system, the electrical percolation threshold for the MWCNT/PLA nanocomposite system was evaluated using the following power law [15]:

$$\sigma \propto (\varphi - \varphi_c)^\alpha \quad (1)$$

where σ is the electrical conductivity, φ is the MWCNT volume concentration in the nanocomposite, φ_c is the critical MWCNT volume concentration at electrical percolation and α is a critical exponent. An excellent fit to the experimental values of $\log(\sigma)$ versus $\log(\varphi - \varphi_c)$ was obtained by a MWCNT percolation threshold concentration of 0.67 wt% and $\alpha = 1.39$, as shown in the inset to Fig. 1a. These values are in agreement with recently reviewed data on polymer-based nanocomposites, in which α values between 1.3 and 4 and φ_c well below 1 wt% are commonly found for systems containing MWCNTs [16]. Despite electrical measurements in this work were conducted on cast nanocomposite films, it is worth pointing out that the percolation threshold values obtained herein should represent an underestimate of the actual electrical behavior found in 3D printed filaments. Indeed, it was shown that the percolation conductivity of the nanocomposite may also be affected by the shearing at the nozzle tip due to shear-induced alignment of the MWCNT [17]. In addition to optimizing the electrical properties of the MWCNT/PLA nanocomposites, their rheological behavior needs to be thoroughly analyzed. Indeed, in the LDM-based 3D printing process the rheological profile of the nanocomposite dispersion critically determines its ability to flow through the printing nozzle and thus influences its actual printability into stable 3D solid microstructures. To this end, the viscosity of nanocomposite dispersions with varying PLA/DCM weight ratio (25/75, 30/70, 35/65) and fixed MWCNT concentration (1 wt% in PLA) was determined by isothermal cone–plate rheological measurements and the results are presented in Fig. 2. All nanocomposite dispersions clearly exhibited a typical shear-thinning behavior characterized by decreasing viscosity with increasing shear rate. In addition, an increase in viscosity is found upon addition of MWCNT. This rheological response is highly desirable in the context of LDM-based 3D printing as it allows to enhance nanocomposite processability through the capillary nozzle under the high shear-rates typical of the extrusion process due to the decreased viscosity of the material.

In order to determine the correct printability window of the nanocomposite dispersions investigated, the process-related wall shear-rate and wall shear-stress were estimated using the capillary

flow model (see Supplementary data for details on the calculations) [18,19]. As a result, an allowable process-related shear-stress interval for a given material could also be estimated as a function of the printing-speed (*viz.*, shear-rate) settings. Accordingly, plots of the process-related shear-stress τ as a function of the process-related shear-rate $\dot{\gamma}$ for the different MWCNT/PLA nanocomposite dispersions investigated in this work were constructed and presented in Fig. 2b, where the corresponding above mentioned printability windows are also shown. As evident from Fig. 2b, the rheological curve of the highly concentrated C1-PLA35 system (35 wt% PLA in DCM, 1 wt% MWCNTs) is completely outside its printability window, indicating that a minimum extruding pressure (minimum applied shear-stress τ) higher than the maximum pressure attainable by the printing machine P_a (maximum allowable shear-stress τ_{max}) is required to process such system. This means that the viscosity of such nanocomposite dispersion is not compatible with our printing system. On the other hand, C1-PLA30 and C1-PLA25 dispersions (1 wt% MWCNTs – 30 wt% and 25 wt% PLA in DCM, respectively) showed a finite overlap between the process-related shear-stress curve of the material and its printability window, indicating that printing of these nanocomposite systems can be accomplished, provided that the appropriate combination of processing conditions (namely, shear-rate and shear-stress) are employed. In particular, it is evident from Fig. 2b that C1-PLA30 only allows for a very short range of useful shear-rates ($\dot{\gamma} = 5\text{--}11 \text{ s}^{-1}$, low printing speeds) while C1-PLA25 is characterized by a much broader $\dot{\gamma}$ printability range (higher printing speeds). These differences can be attributed to the different rheological response of these two systems at high shear-rates, as also evident from Fig. 2a. These results were confirmed by printing experiments of these nanocomposite systems directly performed with the 3D printing apparatus. Although the C1-PLA25 system offered a wider range of printing speeds, the best results in terms of resolution of 3D printed features at constant printing settings were obtained by processing the C1-PLA30 system at very low printing speeds (*i.e.*, 0.1 mm s^{-1} , $\dot{\gamma} = 10 \text{ s}^{-1}$), likely due to the lower amount of solvent present in this case.

In order to demonstrate the potential of LDM-based 3D printing of conductive MWCNT-based nanocomposite systems, different microstructures were fabricated using a low-cost benchtop 3D printer appropriately modified to accommodate a pressure-activated syringe (see Supplementary data) feeding the extruding nozzle with the MWCNT/PLA nanocomposite dispersions (Fig. 3). First, a woven-like microstructure was obtained by depositing two layers of materials on top of each other. In order

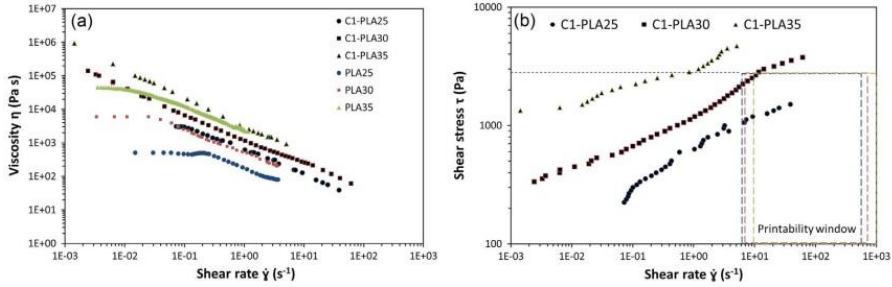


Fig. 2. (a) Viscosity and flow curves for neat PLA and MWCNT/PLA nanocomposite dispersions at increasing PLA concentration in DCM; (b) shear-stress as a function of shear-rate for the MWCNT/PLA nanocomposite dispersions at increasing PLA concentrations in DCM (25 wt% (C1-PLA25), 30 wt% (C1-PLA30) and 35 wt% (C1-PLA35) – the corresponding printability windows are also presented as the areas within the dashed lines). (For interpretation of the references to color in this figure legend, the reader is referred to the web version of this article.)

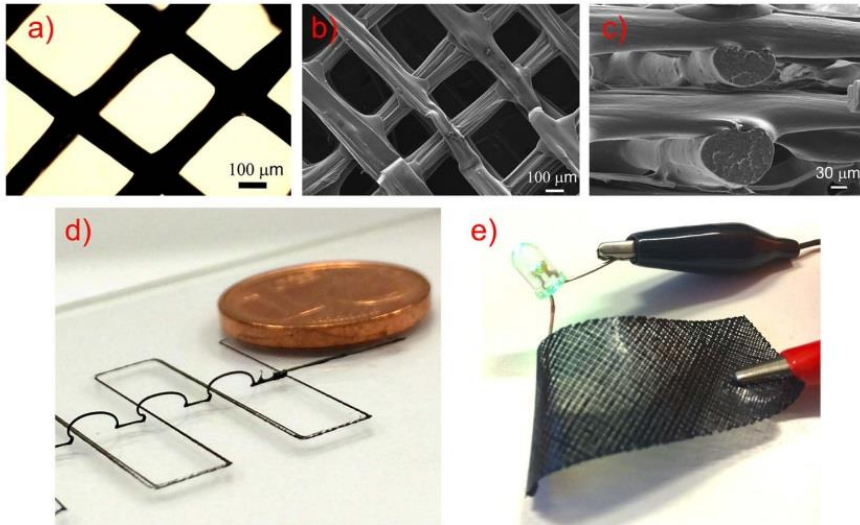


Fig. 3. (a) Top-view optical microscopy image of a LDM-based 3D printed two-layer woven-like microstructure; SEM (b) top and (c) side view images of a representative ten-layer scaffold; (d) optical photograph of a LDM-based 3D printed filament deposited in a freeform manner (a 1 cent euro coin is reported in the image for dimensional reference); (e) 3D printed MWCNT-based nanocomposite woven structure used as conductive element in a simple electrical circuit. (For interpretation of the references to color in this figure legend, the reader is referred to the web version of this article.)

to do so, the C1-PLA30 nanocomposite system was employed, at a printing speed of 0.1 mm s^{-1} ($\dot{\gamma} = 7 \text{ s}^{-1}$). As shown in the optical micrograph presented in Fig. 3a, the wet MWCNT/PLA nanocomposite filament extrusion resulted in planar solid features of $100 \mu m$ average width. The same printing process parameters (0.1 mm s^{-1} printing speed) and MWCNT-PLA nanocomposite system (C1-PLA30) were used to fabricate a 3D-printed ten-layer scaffold. As shown in Fig. 3b and c where the SEM images of different regions of a representative 3D-printed scaffold are presented, a

comparable feature resolution ($100 \mu m$) as that obtained in the 2D woven-like microstructure presented in Fig. 3a could be achieved. In addition, the stability of the as-formed solid nanocomposite filament allows to fabricate 3D features spanning over a few hundreds μm , as evident from Fig. 3b. Furthermore, the scaffold side-view reveals the characteristic circular cross-section of the extruded filament of approximately $100 \mu m$ (Fig. 3c) of diameter, which is maintained even in the presence of multiple overlying layers. Fig. 3d presents an example of a freeform 3D microstructure

in which a 100 μm diameter solid filament allows to achieve spanning self-standing features covering a few mm in length repetitively. In this case, C1-PLA25 system was employed at 5 mm s^{-1} ($\dot{\gamma} = 315 \text{ s}^{-1}$), so as to be able to speed-up the 3D printing process, induce rapid solvent evaporation and allow the formation of the spanning features. Such 3D microstructures suggest the possibility of employing these LDM-based 3D-printed architectures to fabricate conductive electronic components at the microscale in a very versatile fashion. To this end, a $75 \text{ mm} \times 25 \text{ mm}$ free-standing and flexible woven structure was fabricated by means of the proposed LDM technology (Fig. 3e) and it was employed to set up a simple electrical circuit to turn on a commercial green LED by means of a 3 V CR2032-type watch battery, thus giving a further practical demonstration of the potential applicability of these fully-functional conductive microstructured systems in the field of microelectronics.

4. Conclusions

In summary, the fabrication of conductive 3D microstructures with arbitrary shapes is demonstrated by means of a new LDM 3D printing method based on the solvent-assisted additive deposition of a conductive nanocomposite using a modified low-cost benchtop 3D printer. Characterization of the electrical properties of the materials at increasing MWCNT concentrations evidenced a significant increase in the electrical conductivity of the nanocomposite with respect to the pristine PLA matrix material. Values of electrical conductivity in the 10–100 S/m range were obtained for high (>5 wt%) MWCNT concentrations, with a percolation threshold concentration of 0.67 wt%. Characterization of the rheological properties of the nanocomposite dispersions at varying PLA content was performed and printability windows for these systems were identified based on the estimation of the shear-rate of the dispersion at the extrusion nozzle. Finally, examples of spanning and self-supported conductive 3D microstructures directly formed upon LDM-based 3D printing of such MWCNT-based nanocomposite dispersions were presented. Conductive features as small as 100 μm could be reproducibly obtained with our method, demonstrating the high reliability of our approach. To the best of our knowledge, this represents the first demonstration of direct additive layer deposition of intrinsically conductive 3D microstructures from polymeric nanocomposite materials by means of a low-cost 3D printing technique based on the LDM approach. The results of this study clearly demonstrate the technological potential of conductive nanocomposite LDM-based 3D printing that may enable the integration of electronic functionalities into complex 3D objects in a straightforward and versatile fashion.

Appendix A. Supplementary material

Supplementary data associated with this article can be found, in the online version, at <http://dx.doi.org/10.1016/j.compositesa.2015.05.014>.

References

- [1] Gross BC, Erkal JL, Lockwood SV, Chen C, Spence DM. Evaluation of 3D printing and its potential impact on biotechnology and the chemical sciences. *Anal Chem* 2014;86:3240–53.
- [2] Petrovic V, Haro Gonzalez JV, Jordá Ferrando O, Delgado Gordillo J, Blasco Puchades JR, Portoles Griñán L. Additive layered manufacturing: sectors of industrial application shown through case studies. *Int J Prod Res* 2011;49:1061–79.
- [3] Gibson I, Rosen DW, Stucker B. Additive manufacturing technologies – Rapid prototyping to direct digital manufacturing. Springer; 2010.
- [4] Farahani RD, Chizari K, Theriault D. Three-dimensional printing of freeform helical microstructures: a review. *Nanoscale* 2014;6:10470–85.
- [5] Yamada A, Nishikura F, Ikuta K. A three-dimensional microfabrication system for biodegradable polymers with high resolution and biocompatibility. *J Micromech Microeng* 2008;18:025035.
- [6] Monzón MD, Gibson I, Benítez AN, Lorenzo L, Hernández PM, Marrero MD. Process and material behavior modeling for a new design of micro-additive fused deposition. *Int J Adv Manuf Technol* 2013;67:2717–26.
- [7] Tekinalp HI, Kunc V, Velez-Garcia GM, Duty CE, Love IJ, Naskar AK, et al. Highly oriented carbon fiber-polymer composites via additive manufacturing. *Compos Sci Technol* 2014;105:144–50.
- [8] Leigh SJ, Bradley RJ, Purssell CF, Billson DR, Hutchins DA. A Simple, low-cost conductive composite material for 3D printing of electronic sensors. *PLoS ONE* 2012;7:e49365.
- [9] Guo S-Z, Gosselin F, Guerin N, Lanouette A-M, Heuzey M-C, Theriault D. Solvent-cast three-dimensional printing of multifunctional microsystems. *Small* 2013;9:4118–22.
- [10] Molina D, Griffini G, Levi M, Turri S. Novel conductive nanocomposites from perfluoropolyether waterborne polyurethanes and carbon nanotubes. *Polym Adv Technol* 2014;25:1082–8.
- [11] ASTM Designation: F84–99. Standard test method for measuring resistivity of silicon wafers with an in-line four-point probe.
- [12] Mai F, Habibi Y, Raquez J-M, Dubois P, Feller J-F, Peijs T, et al. Poly(lactic acid)/carbon nanotube nanocomposites with integrated degradation sensing. *Polymer* 2013;54:6818–23.
- [13] Moon S-I, Jin F, Lee C-J, Tsutsumi S, Hyon S-H. Novel carbon nanotube/poly(L-lactic acid) nanocomposites: their modulus, thermal stability, and electrical conductivity. *Macromol Symp* 2005;224:287–95.
- [14] Ma P-C, Siddiqui NA, Marom G, Kim J-K. Dispersion and functionalization of carbon nanotubes for polymer-based nanocomposites: a review. *Compos A* 2010;41:1345–67.
- [15] Balberg I. A comprehensive picture of the electrical phenomena in carbon black polymer composites. *Carbon* 2002;40:139–43.
- [16] Bauhofer W, Kovacs JZ. A review and analysis of electrical percolation in carbon nanotube polymer composites. *Compos Sci Technol* 2009;69:1486–98.
- [17] Du F, Fischer JE, Winey KI. Effect of nanotube alignment on percolation conductivity in carbon nanotube/polymer composites. *Phys Rev B* 2005;72:121404.
- [18] Barnes HA, Hutton JF, Walters K. An introduction to rheology. Elsevier; 1997.
- [19] Pidcock GC, in: het Parhuis M. Extrusion printing of flexible electrically conducting carbon nanotube networks. *Adv Mater* 2012;22:4790–800.

UV-Assisted Three-Dimensional Printing of Polymer Nanocomposites Based on Inorganic Fillers

Giovanni Postiglione, Gabriele Natale, Gianmarco Griffini, Marinella Levi, Stefano Turri

Department of Chemistry, Materials and Chemical Engineering "Giulio Natta", Politecnico di Milano, Milan, Italy

In this work, nanocomposites based on a UV-curable polymeric resin and different inorganic fillers were developed for use in UV-assisted three-dimensional (UV-3D) printing. This technology consists in the additive multilayer deposition of a UV-curable resin for the fabrication of 3D macro structures and microstructures of arbitrary shapes. A systematic investigation on the effect of filler concentration on the rheological properties of the polymer-based nanocomposites was performed. In particular, the rheological characterization of these nanocomposites allowed to identify the optimal printability parameters for these systems based on the shear rate of the materials at the extrusion nozzle. In addition, photocalorimetric measurements were used to assess the effect of the presence of the inorganic fillers on the thermodynamics and kinetics of the photocuring process of the resins. By direct deposition of homogeneous solvent-free nanocomposite dispersions of different fillers in a UV-curable polymeric resin, the effect of UV-3D printing direction, fill density, and fill pattern on the mechanical properties of UV-3D printed specimens was investigated by means of uniaxial tensile tests. Finally, examples of 3D macroarchitectures and microarchitectures, spanning features, and planar transparent structures directly formed upon UV-3D printing of such nanocomposite dispersions were reproducibly obtained and demonstrated, clearly highlighting the suitability of these nanocomposite formulations for advanced UV-3D printing applications. POLYM. COMPOS., 00:000-000, 2015. © 2015 Society of Plastics Engineers

INTRODUCTION

Polymer-based nanocomposites have been studied extensively in the last decades as a means to achieve improved thermal, mechanical, optical, magnetic, and barrier properties in the resulting material *via* the control of the interactions between the polymeric host and the nanostructured filler [1–5]. Currently, great efforts are being produced in the attempt to develop new nanocomposite

processing techniques that may allow the production of highly reliable and precise three-dimensional (3D) microdevices [6]. Stereolithography, two-photon polymerization, multijet modeling, and digital light processing represent some of the most explored techniques used for the fabrication of such microdevices that make use of photopolymerizable resins to achieve spatial resolutions that can approach 100 nm [7, 8].

Besides these relatively consolidated microfabrication technologies, a very promising and potentially cost-effective approach to manufacture such microdevices is represented by 3D printing, which consists in the direct fabrication of a 3D object starting from a digital model. 3D printing is now being used routinely in a variety of manufacturing sectors ranging from aerospace and automotive to bioengineering [9, 10]. An interesting evolution of the 3D printing technology is represented by ultraviolet-assisted 3D (UV-3D) printing, which allows the manufacturing of microdevices with 3D freeform or supported features starting from a photocurable polymeric material [11]. This technology consists of a computer-controlled microextrusion apparatus to which a source of UV light is applied. Upon UV light exposure, the extruded photocurable material undergoes a crosslinking process which gives instant rigidity to the extruded filament, thereby enabling the creation of multidirectional self-supported shapes along the trajectory of the extrusion point. In the last few years, the use of UV-3D printing has allowed the fabrication of polymer-based conductive microstructures, sensors, and electrical components by addition of conductive organic nanofillers such as carbon nanotubes into the polymeric matrix [12–16]. In addition, it has been recently demonstrated that by fine-tuning UV-3D printing processing parameters such as the extrusion nozzle speed, the material flow rate, and the intensity and position of the UV source according to the rheological properties of the photocurable resin, the fabrication of microcoils in a freeform manner can be made possible [17].

While most of the works on UV-3D printing have been mainly focused on the fabrication of free-standing or spanning micro-features embedding conductive

Correspondence to: Gianmarco Griffini; e-mail: gianmarco.griffini@polimi.it

DOI 10.1002/pc.23735

Published online in Wiley Online Library (wileyonlinelibrary.com).

© 2015 Society of Plastics Engineers

POLYMER COMPOSITES—2015

nanofillers to impart electrical functionalities [11–15], very little is known about the effect of the addition of inorganic fillers into the photocurable resin on the rheological and mechanical properties of the resulting UV-3D printed nanocomposite material. Clearly, this information would provide a greater insight into the UV-3D printing process, thus allowing to widen the material selection and potentially improve further the mechanical properties of the 3D printed microstructure. Moreover, the effect of 3D printing direction, fill density (infill), and fill pattern on the mechanical properties of UV-3D printed microstructures has not been thoroughly investigated in the literature to date, being the vast majority of the studies on this topic mainly focused on more traditional 3D printing techniques such as fused deposition modeling (FDM) based on thermoplastic materials [18, 19]. In particular, the fabrication of cellular nanocomposites *via* UV-3D printing and the evaluation of their mechanical properties for different printing patterns and different reinforcing fillers have not been demonstrated in the literature to date, notwithstanding the enormous potential of these systems as light-weight highly performing structural materials [20].

In the effort to address these issues, a systematic investigation on the effect of the addition of different inorganic fillers on the rheological and mechanical properties of polymer-based nanocomposites for UV-3D printing is presented in this work. In particular, the rheological response of nanocomposite dispersions based on a solvent-free UV-curable resin loaded with different types of inorganic fillers is experimentally investigated at varying filler content. The fillers employed in this work are two different types of silica characterized by different specific surface areas and a montmorillonite-based nanoclay. Following such rheological characterization, optimal printability parameters for these systems are identified based on the shear rate of the materials at the extrusion nozzle. In addition, photocalorimetric measurements are used to assess the effect of the presence of the inorganic fillers on the thermodynamics and kinetics of the photocuring process of the resins. Moreover, by direct deposition of homogeneous solvent-free nanocomposite dispersions of filler in the UV-curable matrix, the effect of UV-3D printing direction, infill density, and fill pattern on the mechanical properties of UV-3D printed specimens is investigated by means of uniaxial tensile tests. Finally, examples of 3D macrostructures and microstructures directly formed upon UV-3D printing of such dispersions are reproducibly obtained and demonstrated, with a maximum spatial resolution approaching 200 μm .

EXPERIMENTAL

Materials

Fumed silica (specific surface area 50 m^2/g , primary particle size distribution range 10–100 nm) was purchased

from Evonik Industries, Germany (Aerosil®OX50, OX50). Dichloromethane (DCM), fumed silica OX200 (200 m^2/g , primary particle size distribution 8–20 nm), and the photoinitiator 2-hydroxy-2-methyl-1-phenyl-propan-1-one (Darocur®1173, DAR) were purchased from Sigma-Aldrich, Italy. Trimethylolpropane ethoxylate triacrylate (TMPETA, average $M_n \sim 560$) was kindly provided by Arkema, while the nanoclay (Dellite® 43B, 6–8 μm characteristic length, D43B) was obtained from Laviosa Chimica Mineraria, Italy. All products were used as received.

Nanocomposite Dispersions

For the preparation of the nanocomposite dispersions at increasing filler concentration, a 3 wt% stock solution of DAR in TMPETA was prepared under magnetic stirring at room temperature for 30 min. Two different procedures were followed for dispersing fumed silica and dellite into the DAR/TMPETA stock solution. For silica compounds, the desired amount of OX200 or OX50 (ranging from 5 wt% to 15 wt% for OX200 and from 15 wt% to 30 wt% for OX50) was slowly added to the DAR/TMPETA solution, which was manually mixed until homogenization. The nanoclay dispersions were prepared by mixing the desired amount of D43B in DCM so as to obtain a 0.01 w/w dispersion. After 10 min magnetic stirring at 500 rpm, the solution was ultrasonicated for 45 min with a Sonic & Materials VCX130 sonicator tip. This last step was carried out in an ice bath to prevent DCM evaporation and to minimize undesired exothermic phenomena resulting from the ultrasonication process. Finally, the proper amount of DAR/TMPETA solution was added to the D43B dispersion and the solvent was evaporated under a fume hood. Four dispersions of D43B in DAR/TMPETA at D43B concentrations ranging from 3 wt% to 15 wt% were prepared.

Characterization Techniques

The rheological characterization of the nanocomposite dispersions at increasing filler concentration was performed using a Rheometrics DSR200 rheometer with a 25 mm plate-cone configuration at 25°C. Steady shear tests on the DAR/TMPETA dispersions were performed for 3 min in the 0–4500 Pa range.

Photocalorimetric measurements were performed on a DSC/823e (Mettler Toledo) coupled to a fiber-guided UV light source generated by a medium-pressure mercury lamp (Lightingcure LC8, Hamamatsu) in the 300–450 nm wavelength range at an intensity of 15 mW/cm^2 . Nanocomposite samples (5 mg, 500 μm thickness) were placed into an open aluminum crucible and exposed to such UV light at 25°C under nitrogen flow (50 mL/min). The heat of reaction was obtained by integration of the resulting exotherms.

Optical microscopy was employed to evaluate the microstructural features of the UV-3D printed architectures

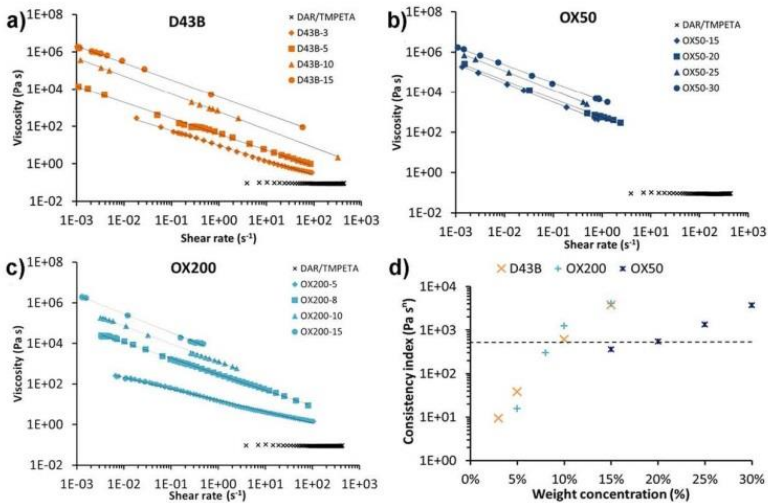


FIG. 1. Viscosity curves of (a) D43B, (b) OX50, (c) OX200 formulations at different filler concentrations. (d) Corresponding consistency indexes K as a function of filler concentration. [Color figure can be viewed in the online issue, which is available at [wileyonlinelibrary.com](http://www.wileyonlinelibrary.com).]

using an Olympus BX-60 reflected-light optical microscope with bright-field (BF) and dark-field (DF) imaging and a SZ-CTV Olympus stereoscopic microscope both equipped with an Infinity 2 digital camera.

Scanning electron microscopy (SEM) was performed on UV-3D printed nanocomposite-based microstructures with a Carl Zeiss EVO 50 Extended pressure scanning electron microscope (acceleration voltage of 15.00–17.50 kV) to evaluate their surface morphology and the 3D architecture. SEM analysis with energy-dispersive X-ray spectroscopy (EDS) on cryo-fractured samples was performed to evaluate the quality of filler dispersion into the polymer matrix.

A low-cost home-assembled 3Drag 1.2 benchtop printer (Futura Elettronica, Italy) incorporating a syringe dispenser equipped with five low-power UV light emitting diodes (LEDs) with light emission peaked at 365 nm and a viewing angle of 20–25° (Aftertech SAS, Italy) was used for UV-3D printing of the nanocomposite microstructures (see Supporting Information). Print speed and nozzle diameter ranged between 0.1–30 mm/s and 0.2–1.5 mm, respectively.

Tensile tests were performed on cast and UV-3D printed dumbbell specimens (narrow section 3 mm × 5 mm × 20 mm) at 1 mm/min testing speed on a Zwick-Roell Z010 with a 10 kN load cell and a longstroke extensometer following the American Society for Testing and Materials (ASTM) D638 standard. The specimens with reduced infill density had a 3 mm × 13 mm × 50 mm narrow section. UV-3D printed specimens were obtained

by operating the 3D printer at 7 mm/s with a 0.51 mm nozzle. At least three specimens of each type were tested.

RESULTS AND DISCUSSION

In order to ensure optimal printability of the liquid nanocomposite dispersions into stable 3D solid structures at the printing nozzle exit, their rheological behavior needs to be comprehensively investigated. To this end, the viscosity of nanocomposite dispersions based on DAR/TMPETA and increasing concentrations of D43B, OX50, and OX200 was determined by isothermal cone-plate rheological measurements. Figure 1a–c shows the plots of DAR/TMPETA viscosity as a function of shear rate at different filler concentrations (the name of the sample is identified by the acronym indicating the type of filler used, followed by a number indicating the filler concentration as wt%). Four different concentrations were selected for each filler type, so that the viscosity of the resulting polymer composite dispersion was suitable for processing in the UV-3DP apparatus presented in this work. In order to allow for comparisons, the plot of viscosity vs. shear rate for the unloaded DAR/TMPETA resin is also presented. As expected, the pristine resin shows a typical Newtonian behavior, characterized by a constant viscosity for increasing shear-rate values ($\eta \approx 0.09 \text{ Pa s}$ in the $3\text{--}5 \cdot 10^2 \text{ 1/s}$ shear-rate interval).

As opposed to this, all nanocomposite dispersions clearly exhibit a typical shear-thinning response characterized by decreasing viscosity with increasing shear rate, indicating

that both fumed silica and dellite strongly interact with the polymer matrix. Such rheological behavior is highly desirable as it allows to enhance the nanocomposite processability through the capillary extrusion nozzle due to the decreased viscosity of the material under the high shear-rate characteristics of the 3D printing process. As shown in the plots, the viscosity curves of all formulations can be very well fitted with a power-law fluid relationship according to the following equation:

$$\eta = K\dot{\gamma}^{n-1} \quad (1)$$

The values of the coefficients calculated by means of the power-law equation (consistency index K and power-law index n) were used to compare the rheological response of the different nanocomposite formulations (see Supporting Information). In particular, the power-law index n is related to the slope of the viscosity curve and can therefore provide an indication on the extent of shear-thinning character given to the UV-curable resin by the presence of the inorganic filler. Conversely, the consistency index K gives an indication of the viscosity of the specific formulation at shear rate of 1 1/s. Due to their shear-thinning behavior, all formulations present power-law indexes $n < 1$ with values slightly higher for the systems with filler concentration below 10 wt% (OX200-5, OX200-8, D43B-3, and D43B-5), likely ascribable to the weaker polymer-filler interactions arising in lightly loaded systems. Conversely, the consistency index K is found to be greatly affected by the concentration and type of inorganic filler. As shown in Fig. 1d where K values calculated for the different nanocomposite formulations by means of Eq. 1 are plotted as a function of filler concentration, a significantly lower increase in filler concentration gives rise to a much sharper increase of consistency index K in the case of OX200 as compared to OX50. In particular, while an over-two-order-of-magnitude increase in K is observed for OX200 when its concentration in the formulation is increased from 5 wt% to 15 wt%, the progressive addition of OX50 to the DAR/TMPETA system in the 15–30 wt% range only results in a tenfold increase in K . These trends can be explained by considering that OX200 fumed silica is characterized by a larger specific surface area than OX50 (200 g/m² vs. 50 g/m², respectively) that is responsible for stronger interactions between the inorganic filler and the polymer host matrix, leading to a more efficient viscosity increase on the UV-curable resin. As also evident from Fig. 1d, the addition of nanoclay filler D43B leads to a similar rheological response as that observed with OX200, likely indicating similar filler-polymer matrix interactions for D43B and OX200.

Based on the values of the consistency index K and the power-law index n for each formulation calculated from Eq. 1, it is possible to predict the rheological behavior of the nanocomposite dispersions within the 3D printer extruder using the capillary flow model [21, 22].

First, the apparent shear rate $\dot{\gamma}_{app}$ of the fluid inside a capillary is determined from the Hagen-Poiseuille equation:

$$\dot{\gamma}_{app} = \frac{4Q}{\pi R^3} \quad (2)$$

where Q is the volumetric flow rate and R is the radius of the capillary. The actual shear rate $\dot{\gamma}$ can be derived using the well-known Mooney-Rabinowitch correction for non-Newtonian fluids (with n being the power-law index calculated from the power-law equation):

$$\dot{\gamma} = \dot{\gamma}_{app} \frac{3n+1}{4n} \quad (3)$$

Since the volumetric flow rate through the 3D printer nozzle can easily be calculated from the printing speed and nozzle cross section, an allowable process related shear rate interval can be determined for a given material by simply varying the 3D printing speed settings and the nozzle size (see exemplary calculation in the Supporting Information).

Following the theoretical approach presented above, the printability of all dispersions was also practically tested with the 3D printer (see Supporting Information). Despite the fact the all formulations could be extruded through the various nozzles employed in this work in good agreement with the previous calculations, only some of them showed good printability properties (Supporting Information). Indeed, in order to guarantee optimal printing resolution and well defined printed features, the extruded wet filament must retain its integrity right after its deposition onto the printing plate and prior to UV irradiation. Considering this requirement, experimental 3D printing tests (Supporting Information) showed that only formulations with sufficiently high consistency indexes ($K > 550 \text{ Pa s}^n$) were found to exhibit optimal printability properties (this printability limit is represented in Fig. 1d as a dotted line).

In order to characterize the photopolymerization process of the UV-curable resin and the possible effect of the presence of the filler on the thermodynamics and the kinetics of the curing reaction, photocalorimetric measurements were performed on all nanocomposite formulations. The values of enthalpy of polymerization are shown in Fig. 2a as a function of filler type and concentration. In the plot, the measured heat (ΔH) of polymerization has been corrected considering the exact DAR/TMPETA weight fraction present in every formulations during the photocalorimetric scan. Clearly, the presence of the different inorganic fillers has no practical effect on the heat of polymerization of the nanocomposite, as in all cases a ΔH value of approximately 300 J/g is measured, similarly to what observed in unfilled DAR/TMPETA. Slightly lower ΔH values are found in OX200-8, OX200-10, OX200-15, and D43B-15 formulations, likely ascribable to the stronger filler-polymer matrix interactions

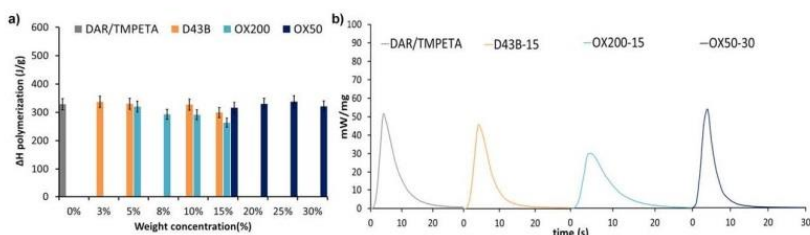


FIG. 2. (a) Enthalpy of photopolymerization of the UV-curable nanocomposites as a function of filler concentration and (b) photocalorimetric scans of the UV-curable resin: TMPETA/DAR and of the polymer-based UV-curable nanocomposites with different filler types. [Color figure can be viewed in the online issue, which is available at wileyonlinelibrary.com.]

occurring for these high specific surface area fillers at such high concentrations that may partially hinder polymer chain growth during the photopolymerization reaction. However, such counteracting effect is relatively limited, as even for the formulation exhibiting the lowest value of measured heat of polymerization (OX200-15), the conversion of the UV-curing reaction (calculated as the ratio between the enthalpy of reaction for the nanocomposite formulation and the enthalpy of reaction for the unfilled resin) is over 80%. As opposed to OX200-based and D43B-based nanocomposite systems, no effect on the UV-curing thermodynamics is observed for OX50 nanocomposites, irrespective of filler concentration.

In the attempt to investigate the effect of filler type and concentration on the photopolymerization kinetics of the DAR/TMPETA resin, the photocalorimetric scans of resin formulations based on different fillers (D43B, OX200, and OX50) were compared with the photocalorimetric scan of unfilled DAR/TMPETA. Figure 2b reports the results for the resin formulations based on the three different fillers at the highest filler concentration examined in this work (D43B-15, OX200-15, and OX50-30). As shown in the plot, all filled systems present similar polymerization kinetics, comparable to what found for the unfilled DAR/TMPETA resin, with the exothermic peak of polymerization found after 4 s from the beginning of the UV exposure. These results clearly indicate that the presence of the filler does not alter significantly the curing speed of the polymer-based nanocomposite at the filler concentrations investigated in this work (which are suitable for 3D printing purposes), thus enabling an effective UV-3D printing process *via* the rapid UV-induced polymerization of the extruded nanocomposite wet filament. This represents a very favorable feature in view of the UV-3D printing fabrication process of these polymer-based nanocomposite formulations. Indeed, the material flowing out from the extrusion nozzle can be polymerized rapidly enough to withstand the subsequent deposition of additional layers of materials without collapsing and to potentially allow for the production of spanning features. Additionally, the filler concentration in the UV-curable

resin may be tuned in such a way that desirable physical characteristics of the system such as the initial nanocomposite fluid viscosity or the mechanical properties of the final 3D printed material may be independently optimized without significantly affecting the UV-curing reaction.

In order to investigate the mechanical response of the nanocomposites with different filler types, dumbbell specimens were UV-3D printed and assessed by means of uniaxial tensile testing. According to the outcomes of the rheological characterization presented in Fig. 1, formulations containing the minimum allowable amount of filler to enable optimal UV-3D printing were selected for the mechanical tests, namely D43B-10, OX50-20, and OX200-10 (i.e., nanocomposite formulations with the lowest filler concentration giving consistency index values K above the printability threshold value represented by the dotted line in Fig. 1d). In addition, to evaluate the effect of the filament printing direction on the mechanical properties of the UV-3D printed structures, specimens were fabricated by UV-3D printing both along the longitudinal axis (90° in Fig. 3) and with a 45° mesh-type pattern (45° in Fig. 3). All UV-3D printed specimens were fabricated at the maximum filling density (100% *infill*) and their mechanical response was compared with that obtained from OX50-20 and OX200-10 samples realized by mold casting. It is worth noting that after UV-3D printing all samples achieved a nearly 100% crosslinking conversion, as evidenced by the negligible residual exothermic heat of reaction observed on UV-3D printed samples measured by photocalorimetric experiments (see Supporting Information).

D43B-10 cast specimens could not be produced due to incomplete polymerization of such samples likely originating from the UV-shielding effect of the nanoclay-based filler that partially hampers UV light from being absorbed by the DAR photoinitiator and prevents it from being efficiently used for the UV-curing reaction. Such UV-shielding effect is more pronounced for larger sample thicknesses as in the case of D43B-10 cast specimens (3 mm thick), while it is relatively negligible in the case of the thin wet filaments (0.2–0.84 mm nozzle diameter) characteristic of the UV-3D printing process.

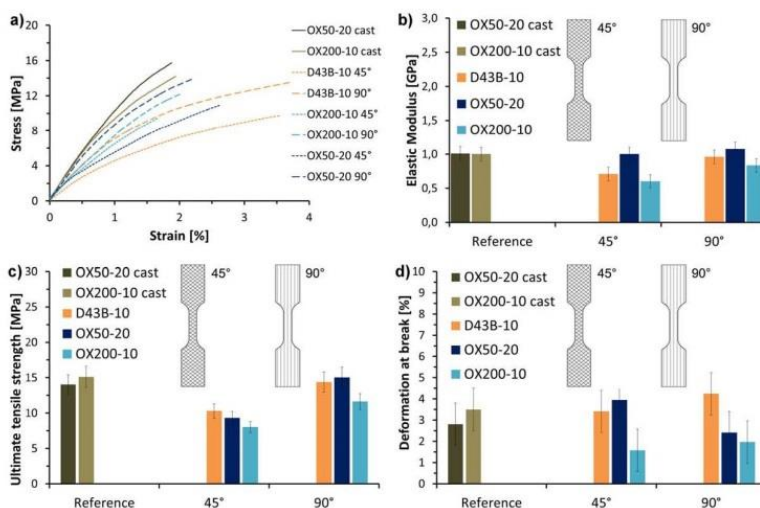


FIG. 3. (a) Representative stress–strain curves of UV-3D printed and cast samples; average values of (b) elastic modulus, (c) ultimate tensile strength, and (d) deformation at break. [Color figure can be viewed in the online issue, which is available at wileyonlinelibrary.com.]

Representative stress–strain curves for the samples investigated here are presented in Fig. 3a, while the average values of elastic modulus, ultimate tensile strength, and deformation at break obtained from the tensile tests on such samples are plotted in Fig. 3b–d, respectively. As evident from Fig. 3b, the elastic modulus of the OX50-20 UV-3D printed nanocomposite is comparable with that found for the corresponding cast sample and lies in the 1 GPa range, irrespective of the printing direction employed (45° and 90° printing pattern). As opposed to this, slightly lower values of elastic modulus are reported for OX200-10 UV-3D printed nanocomposites with respect to the homologous cast samples. In addition, D43B-10 materials exhibit elastic modulus values in line with those found in OX200-10 samples. As presented in Fig. 3b and c, the UV-3D printed samples with 90° printing pattern show a slight increase in elastic modulus and ultimate tensile strength compared to samples printed with a 45° printing pattern irrespective of the type of filler employed. In particular, values of ultimate tensile strength comparable to those found for cast samples are obtained in OX50-20, OX200-10, and D43B-10 samples printed with a 90° pattern (15 MPa range), while the corresponding samples printed with a 45° pattern are characterized by lower ultimate tensile strength values in the range between 7 and 10 MPa. These results suggest that the UV-3D printing process potentially allows for customized control of the mechanical properties of the UV-3D printed object by simple modification of the printing direction. Interestingly, all UV-3D printed samples show values of defor-

mation at break in the 2–4% range which are in close agreement with those obtained from the control cast samples, independently from the printing direction. Only OX200-10/90° nanocomposites seems to give lower deformation at break values, although this may not be statistically significant given the large standard deviations registered for these measurements. It is worth highlighting that the quality of the dispersion of the filler into the polymer matrix was also evaluated by means of SEM analysis on printed nanocomposites at varying filler type (see Supporting Information). By examination of the cryo-fractured surface of the printed nanocomposite samples, a good level of dispersion of the fillers into the UV-curable polymer matrix is found even at high filler loading, thus suggesting the absence of any noticeable agglomerates that may affect the mechanical properties of the final printed samples.

Thanks to the great design flexibility allowed by the UV-3D printing process, the fabrication of complex shapes with arbitrary patterns can be envisaged. Taking inspiration from the natural world [23], cellular specimens with different unit cell geometry (infill pattern) and increasing infill density were realized by UV-3D printing, as shown in Fig. 4a–f where zoomed optical stereoscopic images of the UV-3D printed samples clearly highlight the excellent resolution and printing accuracy achievable with the UV-3D printing setup assembled in this work. In particular, samples with squared and hexagonal networks with three different relative densities (from 0.37 to 0.51) were UV-3D printed from OX200-10 nanocomposite

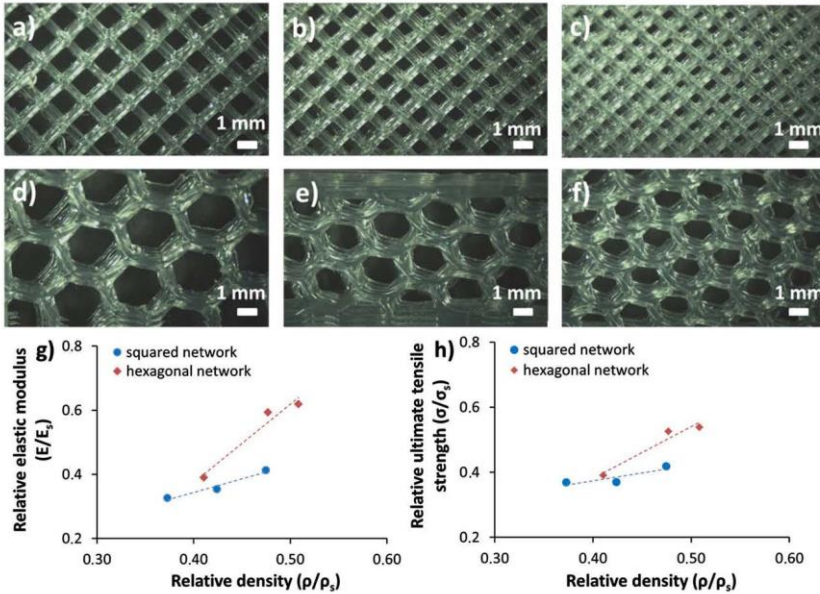


FIG. 4. Optical stereoscopic images of the UV-3D printed specimens with (a–c) squared unit cell and (d–f) hexagonal unit cell at increasing infill density. Plots of (g) the relative elastic modulus and (h) relative ultimate tensile strength as a function of the relative density of the specimens. Dotted lines are a guide for the eye. [Color figure can be viewed in the online issue, which is available at wileyonlinelibrary.com.]

formulation and mechanically characterized by means of uniaxial tensile tests. Plots of the relative elastic modulus E/E_s and the relative ultimate tensile strength σ/σ_s as a function of the relative density ρ/ρ_s are presented in Fig. 4g and h, where E_s , σ_s , and ρ_s refer to the elastic modulus, tensile strength, and density of the OX200-10 solid material, while E , σ , and ρ are the elastic modulus, tensile strength, and density of the cellular specimen. Both the relative elastic modulus and the relative ultimate tensile strength are found to increase at increasing relative density irrespective of the unit cell geometry. This trend is in line with the fact that for increasing relative densities, the mechanical behavior of the cellular specimen approaches that of the solid material ($\rho/\rho_s = 1$). Furthermore, the hexagonal unit cell is found to yield higher mechanical properties compared to the square unit cell for comparable values of relative densities, both in the case of the elastic modulus and the ultimate tensile strength. These results are in agreement with the typical mechanical behavior of cellular materials [24].

These observations lead to the conclusion that the filling pattern takes on a fundamental role in determining the final mechanical properties of the UV-3D printed

objects, further highlighting the ability of UV-3D printing to modulate the mechanical behavior of the printed material in a relatively simple, straightforward and versatile fashion.

In order to demonstrate the potential of UV-3D printing in processing the nanocomposite dispersions developed in this work, different macrostructures and microstructures were fabricated using a low-cost benchtop 3D printer appropriately modified to accommodate a syringe dispenser feeding with the nanocomposite dispersions an extruding nozzle equipped with five low-power UV LEDs ($\lambda_{\text{emission}} = 365 \text{ nm}$) (Fig. 5a and Supporting Information).

First, a woven-like microstructure was obtained by UV-3D printing two layers of OX200-10 nanocomposite formulation on top of each other at a printing speed of 20 mm/s. As shown in the optical micrograph presented in Fig. 5b, the filament extrusion resulted in planar solid features of approximately 200 μm average width. The same printing process parameters (printing speed 20 mm/s, layer height 0.1 mm) and nanocomposite dispersion (OX200-10) were used to fabricate a UV-3D printed six-layer matrix-like microstructure of approximately 600 μm

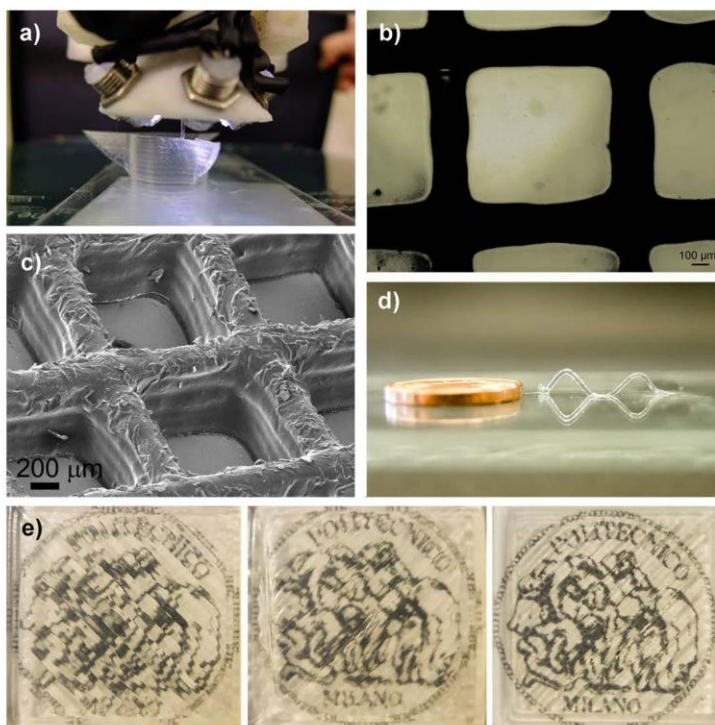


FIG. 5. (a) Optical image taken during the fabrication of a UV-3D printed macroscopic object; (b) optical image of a two-layer woven-like microstructure; (c) SEM image of a multilayer matrix-like microstructure; (d) UV-3D printed spanning features (a 1 cent euro coin is reported in the image for dimensional reference); and (e) translucent planar structures of increasing transparency obtained by UV-3D printing the nanocomposite dispersion with different layer-height settings. [Color figure can be viewed in the online issue, which is available at wileyonlinelibrary.com.]

height, 600 μm lateral size, and filament diameter of 200 μm (Fig. 5c). In addition, the UV-3D printing setup allowed to shift from the layer-by-layer deposition approach to obtain 3D freeform spanning features, as evident from Fig. 5d. In this case, OX200-10 system was employed at 3 mm/s, so as to be able to slow down the 3D printing process, induce rapid UV polymerization of the wet nanocomposite filament, and allow the formation of the spanning features that can cover a few millimeters in length without structural collapses. The fabrication of such 3D microstructures suggests the possibility to employ UV-3D printing to realize complex architectures and structural components at the microscale in a very versatile and straightforward fashion. As a further example of the high flexibility of the UV-3D printing approach combined with the nanocomposite materials presented in this work, macrostructures characterized by increasing

levels of transparency/translucency were obtained using the OX200-10 nanocomposite formulation. As shown in Fig. 5e, by carefully controlling the UV-3D printing process parameters (layer height from 0.4 to 0.3 mm, printing speed 5 mm/s, infill density 100%, and nozzle diameter 0.84 mm), it was possible to produce translucent planar structures with varying degrees of optical transparency, suggesting the potential use of such customizable 3D systems in fields such as optics and optofluidics where optical clarity may represent a requirement. As a final demonstration of the potential of the nanocomposite dispersions developed in this work, examples of macroscopic UV-3D printed objects were also fabricated, with length scales in the cm range (Supporting Information), thereby giving a further practical demonstration of the direct applicability of this approach in the field of advanced additive manufacturing.

CONCLUSIONS

In conclusion, nanocomposites based on a UV-curable polymeric resin and different inorganic fillers were developed in this work for use in UV-3D printing applications. A rheological characterization of the nanocomposite dispersions at varying filler concentration was performed and optimal extrusion and printability parameters for these systems were identified based on the shear rate of the materials at the extrusion nozzle by applying classical power-law fluid relationships and the capillary flow model. Photocalorimetric measurements demonstrated that a very rapid (4 s) curing reaction could be achieved with these systems upon UV-light irradiation, and that the presence of the inorganic fillers did not affect the thermodynamics and kinetics of the UV-curing process of the polymeric matrix. The direct UV-3D printing of such homogeneous solvent-free polymer-based nanocomposite dispersions allowed to investigate the effect of printing direction, infill density, and fill pattern on the mechanical response of UV-3D printed specimens by uniaxial tensile tests. All samples exhibited excellent mechanical properties comparable to those found in the homologous casted materials. In addition, cellular nanocomposite materials were produced with hexagonal or squared unit cells that allowed to demonstrate the possibility to control the mechanical properties of the UV-3D printed materials by simply varying the infill design structure. Finally, examples of 3D macroarchitectures and microarchitectures, spanning features, and planar transparent structures directly formed upon UV-3D printing of such nanocomposite dispersions were reproducibly obtained and demonstrated, clearly highlighting the suitability of these polymeric materials for advanced UV-3D printing applications.

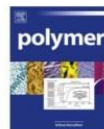
REFERENCES

1. P.M. Ajayan, L.S. Schadler, and P.V. Braun, *Nanocomposite Science and Technology*, Wiley-VCH, Weinheim (2003).
2. S. Kaur, M. Gallei, and E. Ionescu, *Adv. Polym. Sci.*, **267**, 143 (2015).
3. H. Althues, J. Henle, and S. Kaske, *Chem. Soc. Rev.*, **36**, 1454 (2007).
4. A. Di Gianni, E. Amerio, O. Monticelli, and R. Bongiovanni, *Appl. Clay Sci.*, **42**, 116 (2008).
5. S. Li, M.M. Lin, M.S. Toprak, D.K. Kim, and M. Muhammed, *Nano Rev.*, **1**, 5214 (2010).
6. M. Vaezi, H. Seitz, and S. Yang, *Int. J. Adv. Manuf. Technol.*, **67**, 1721 (2013).
7. I. Gibson, D.W. Rosen and B. Stucker, *Additive Manufacturing Technologies: Rapid Prototyping to Direct Digital Manufacturing*, Springer, New York (2010).
8. J.R. Tumbleston, D. Shirvanyants, N. Ermoshkin, R. Januszewicz, A.R. Johnson, D. Kelly, K. Chen, R. Pinschmidt, J.P. Rolland, A. Ermoshkin, E.T. Samulski, and J.M. DeSimone, *Science*, **347**, 1349 (2015).
9. V. Petrovic, J.V. Haro Gonzalez, O. Jordá Ferrando, J. Delgado Gordillo, J.R. Blasco Puchades, and L. Portoles Griñan, *Int. J. Prod. Res.*, **49**, 1061 (2011).
10. B.C. Gross, J.L. Erkal, S.Y. Lockwood, C. Chen, and D.M. Spence, *Anal. Chem.*, **86**, 3240 (2014).
11. L.L. Lebel, B. Aissa, M.A. El Khakani, and D. Theriault, *Adv. Mater.*, **22**, 592 (2010).
12. R.D. Farahani, H. Dalir, V. Le Borgne, L.A. Gautier, M.A. El Khakani, M. Lévesque, and D. Theriault, *Nanotechnology*, **23**, 085502 (2012).
13. B. Aissa, D. Theriault, R.D. Farahani, L.L. Lebel, and M.A. El Khakani, *Nanotechnology*, **23**, 115705 (2012).
14. L.L. Lebel, B. Aissa, M.A. El Khakani, and D. Theriault, *Compos. Sci. Technol.*, **70**, 518 (2010).
15. G. Postiglione, G. Natale, G. Griffini, M. Levi, and S. Turri, *Composites Part A*, **76**, 110 (2015).
16. R.D. Farahani, H. Dalir, V. Le Borgne, L.A. Gautier, M.A. El Khakani, M. Lévesque, and D. Theriault, *Compos. Sci. Technol.*, **72**, 1387 (2012).
17. R.D. Farahani, L.L. Lebel, and D. Theriault, *J. Micromech. Microeng.*, **24**, 055020 (2014).
18. S. Ahn, M. Montero, D. Odell, S. Roundy, and P.K. Wright, *Rapid Prototyping J.*, **8**, 248 (2002).
19. B.M. Tynraka, M. Kreigerb, and J.M. Pearce, *Mater. Des.*, **58**, 242 (2014).
20. B.G. Compton and J.A. Lewis, *Adv. Mater.*, **26**, 5930 (2014).
21. H.A. Barnes, J.F. Hutton, and K. Walters, *An Introduction to Rheology*, Elsevier, Amsterdam (1997).
22. J. Bruneaux, D. Theriault, and M. Heuzey, *J. Micromech. Microeng.*, **18**, 115020 (2008).
23. X. Xu, L. Heng, X. Zhao, J. Ma, L. Lin, and L. Jiang, *J. Mater. Chem.*, **22**, 10883 (2012).
24. M.F. Ashby, *Metall. Trans.*, **14A**, 1755 (1983).



Contents lists available at ScienceDirect

Polymer

journal homepage: www.elsevier.com/locate/polymer

Short communication

3D-printable CFR polymer composites with dual-cure sequential IPNs



Gianmarco Griffini, Marta Invernizzi, Marinella Levi, Gabriele Natale, Giovanni Postiglione, Stefano Turri*

Department of Chemistry, Materials and Chemical Engineering "Giulio Natta", Politecnico di Milano, Piazza Leonardo da Vinci 32, 20133 Milan, Italy

ARTICLE INFO

Article history:

Received 6 November 2015

Accepted 15 March 2016

Available online 17 March 2016

Keywords:

Interpenetrating polymer network

Composite

3D-printing

ABSTRACT

In this work a sequential interpenetrating polymer network (IPN) obtained by co-formulation of a photocurable acrylic resin with a thermocurable epoxy resin is presented and proposed as matrix for the fabrication of carbon-fiber reinforced (CFR) composite structures by means of 3D-printing technology. This approach combines the advantages of the easy free-form fabrication typical of the 3D-printing technology with the purposely customized features of the newly developed IPN material. Photo-calorimetric and dynamic-mechanical analyses were performed in order to investigate the photo- and thermal-crosslinking reactions and their effect on the development of the IPN system. The IPN resin was finally loaded with carbon fibers and successfully ultraviolet-assisted (UV)-3D printed, demonstrating the possibility of fabricating CFR composite materials in 3D with excellent mechanical properties. Being the first example of direct fabrication of IPN-based composites by 3D printing, this study clearly shows the great potential of this additive manufacturing technology for advanced industrial applications.

© 2016 Elsevier Ltd. All rights reserved.

1. Introduction

The interest in 3D printing from the manufacturing industry has risen considerably in the last few years due to the many appealing features of this technology, such as its ability to realize complex geometries, the ease of personalization of the manufactured product, and the potential logistical advantages offered by the diffuse manufacturing paradigm. As a consequence, the demand for tailored 3D-printable materials with improved structural and functional properties is continuously growing, with polymers still playing a dominant role [1–5].

In many fields, 3D-printing by fused deposition modeling (FDM) is widely used as rapid prototyping technology, in which thermoplastic polymer filaments (ABS, PLA, and a few others) are employed as structural inks. In order to shift away from the mere production of prototypes, more performing materials, especially in terms of mechanical and thermal properties, are required. Some attempts were made to reinforce thermoplastics with fillers, short fibers or post processing techniques. Despite some observed increase in materials performance, these strategies still rely on the FDM technology [6,7] and on the consequent need to process pre-extruded filaments.

Along with FDM technology, ultraviolet-assisted 3D (UV-3D) printing has been more recently proposed and developed for the fabrication of a variety of 3D microstructures with peculiar properties [8,9]. This technology consists in the additive deposition of layers of a photocurable liquid polymer, which is crosslinked by an external UV light source as soon as it flows out of the nozzle during the printing process. The photocurable liquid precursor can be easily modified by formulation according to the desired final material properties. To this end, the use of embedded nano- and micro-particles has been demonstrated, leading to the production of reinforced components, conductive microstructures and micro-coils [8–11]. However, this technology has not yet been exploited for the fabrication of fiber-reinforced composites to date. This is partially due to the fact that UV-3D printing strictly requires materials with fast curing kinetics and loading with non-transparent particles or fibers may influence the UV light transmission through the sample, causing the inhibition of the polymerization or drastically slowing down its rate [12,13]. Moreover, UV curable resins often do not offer sufficiently high mechanical properties to be used for the fabrication of high performance fiber-reinforced composites.

In the light of the above considerations, the development of engineered polymeric systems capable to form sequential interpenetrating polymer networks (IPN) by dual-cure mechanisms can offer significant advantages for this application. Specific

* Corresponding author.

E-mail address: stefano.turri@polimi.it (S. Turri).

mechanical properties can be achieved when multifunctional polymers are entangled at the nanometric scale as in IPNs. Indeed, their peculiar chemical structure and morphology has favored their widespread diffusion in a variety of applications [14–19].

In this communication, we report on an easily 3D-printable carbon fiber reinforced (CFR) polymer composite formulation based on a new photo-thermocurable IPN system. The material is successfully processed to form stable 3D structures by using a low cost, home-modified UV-3DP apparatus. A subsequent thermal treatment of the UV-3D printed object is performed to complete the crosslinking process and achieve full mechanical properties. Dual-cure resins have already been used for rapid prototyping, including the manufacturing of carbon fiber materials via photolithography [20] and stereolithography [21]. However, to the best of our knowledge, this is the first report on the direct UV-3D printing of CFR polymer composites with an IPN-based dual-cure ink.

2. Experimental

2.1. Raw materials

Bisphenol A diglycidyl ether (DGEBA), 1,1-dimethyl, 3-(3',4'-dichlorophenyl) urea (Diuron™), dicyandiamide (DICY), and fumed silica (200 m²/g, primary particle size distribution 8–20 nm, OX200 throughout the manuscript) were purchased from Sigma–Aldrich and used as received. Bisphenol A ethoxylate diacrylate (SR349) was kindly provided by Arkeam, whilst the photoinitiator 2,4,6-trimethylbenzoylphenyl phosphine oxide (Irgacure TPO-L, TPO-L throughout the manuscript) was obtained from BASF. Carbon fibers were kindly provided by Zoltek (Panex™ 30 milled Carbon Fibers, 99% carbon, density 1.8 g/mL, fiber diameter 7.2 μm, fiber length 100–150 μm).

2.2. Resin and composite formulation and curing

Formulations were obtained by liquid blending the photocurable acrylic resin and the thermocurable epoxy resin with suspended hardener (DICY) and accelerator (Diuron™). The photocurable acrylic resin was a stock solution of SR349 doped with 3 wt% TPO-L mixed under magnetic stirring at room temperature for 30 min (indicated as p-A resin in the following). For the epoxy resin formulation (t-E resin in the following), 20 g of liquid DGEBA, 1.36 g (6.19% w/w) of DICY and 0.66 g (3% w/w) of Diuron™ were poured into a beaker, stirred at 100 °C for 1 h and then mixed with an ultrasonicator tip (Sonic & Materials VCX130, power 130 W, frequency 20 kHz) to form a finely dispersed suspension. The epoxy system behaves as a monocomponent since no reaction occurs until the insoluble DICY remains phase separated (that is for T < 150 °C). The final dual-cure formulation was obtained by mixing the p-A resin and the t-E resin under magnetic stirring at 70 °C for 30 min at a 1:1 weight ratio (M50 sample). Characterizations concerning IPN systems were mostly performed on M50 formulation.

For 3D printing tests, four other formulations were developed with increasing weight concentrations of p-A component, namely 5%, 10%, 15% and 20% by weight (indicated as M5, M10, M15, M20 in the following). Since the two starting resins and their blends are essentially low viscosity Newtonian liquids, depositing them from the syringe dispenser of the 3D printer resulted into a significant lateral spreading with poor control of 3D geometries. In order to solve this issue, a fixed amount of fumed silica (7% w/w) as thixotropic additive was added to all the formulations, making them suitable for 3D printing. The CFR composites for 3D printing were based on M50 formulation and were obtained by adding 5% and 30% w/w of carbon fibers (CF5 and CF30 samples, respectively).

The thermal curing cycle after 3D-printing was carried out at

220 °C for 20 min in a ventilated oven.

2.3. Characterization techniques

The thermal characterization of the IPN system and its precursors was performed using a differential scanning calorimeter (DSC). DSC scans were carried out on a Mettler–Toledo DSC/823^e instrument, indium and n-hexane calibrated, heating from 20 °C to 250 °C with a rate of 20 °C/min in N₂ environment. Photocalorimetric tests were carried out at ambient temperature on 10–50 mg samples by coupling the DSC instrument with a UVA light source (Lightingcure LC8 by Hamamatsu, 98 mW/cm², 300–450 nm wavelength range) under N₂ atmosphere. The heat of reaction was obtained by integration of the resulting exotherms.

Dynamic mechanical analyses (DMA) in three-point bending mode were carried out on a Mettler Toledo DMA/SDTA861 instrument at ambient temperature in strain sweep, and in dynamic scans from 20 °C to 250 °C at a heating rate of 3 °C/min. The frequency was kept constant at 1 Hz.

Scanning electron microscopy (SEM) was performed on fractured M50 surfaces with a Carl Zeiss EVO 50 Extended Pressure scanning electron microscope (acceleration voltage of 15.00–17.50 kV) to evaluate the IPN morphology. Samples were subjected to an alkaline etching (10% KOH in methanol for 1 h at 60 °C) to selectively remove or damage the acrylic phase.

2.4. 3D-printing experiments

A low-cost, home-assembled 3Ddrag 1.2 benchtop printer (Futura Elettronica, Italy) incorporating a syringe dispenser equipped with two 3W UV-A torches (WF-501B by Ultrafire Ltd, China) with light emission peaked at 405 nm was used for UV-3D printing the IPN composites (M5–M50, CF5, CF30). Print speed ranged between 1 and 10 mm/s and a 0.84 mm nozzle diameter was used. An image of the set-up used is shown in Fig. 1. The image of the 3D-object to be fabricated is shown in Fig. 2a. It was designed using “Solidworks” software (Dassault Systèmes, France) to test the ability to print cantilevered geometries with different inclinations. In order to process the 3D model, the open source slicing software “Cura” (Ultimaker B.V., Holland) was used, and the printing test was carried out using spiral slicing option and a single wall thickness.

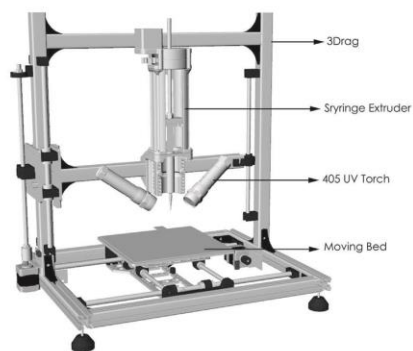


Fig. 1. Schematic representation of the UV-3D printing equipment employed in this work.

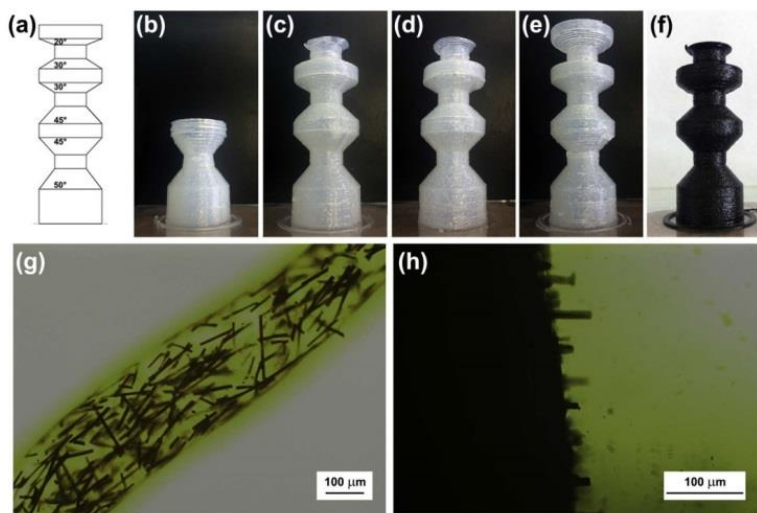


Fig. 2. (a) layout of the target 3D model used to assess the printability of the inks developed in this work; UV-3D printed reproduction of the target model using (b) M5, (c) M10, (d) M15, (e) M20, and (f) CF5; optical microscopy image of (g) CF5 liquid filament and (h) cryo-fractured UV-3D printed CF5 surface.

3. Results and discussion

The 3D-printing processability of the acrylic-epoxy IPN formulations and corresponding composites was assessed. All the formulations from M5 to M50 were loaded into the syringe, and printed in the attempt to reproduce the target 3D model whose frontal projection is presented in Fig. 2a. Such 3D model is constituted by a vertical column with overhanging features with angles ranging from 50° at the bottom to 20° at the top. The smaller the inclination angle the more challenging it is to print the material *via* layer-by-layer deposition without incurring into resin sagging or spreading. Therefore, this 3D model represents a convenient test designed to verify the ink processability while printing complex parts. During the printing process, it was found that all formulations were able to flow out of the nozzle and harden upon exposure to the UV sources embedded into the 3D printer (Fig. 1). The results of the printing tests on samples M5–M20 and CF5 are presented in Fig. 2b–e. The sample M5, containing only 5% w/w of photocurable p-A resin, remained too soft after the photocuring process. Therefore, this ink did not allow to obtain a complete UV-3D print of the 3D target model, as already the first 45° overhang was found to show some visible structural imperfections (Fig. 2b). By increasing the p-A concentration to 10% w/w (M10, Fig. 2c) and 15% w/w (M15, Fig. 2d) the printing quality was found to improve considerably as the material showed a solid-like behavior after UV exposure. The UV-3D printed model objects obtained with these formulations were very similar and only showed some visible structural defects during the top 20° overhang which could thus not be completely printed. On the other hand, the M20 ink allowed for a successful 3D printed reproduction of the target 3D model (Fig. 2e), thus demonstrating that a 1:5 weight ratio between p-A and t-E constitutes the minimum photopolymer concentration needed to reach optimal printing performance even in the presence of steeply

overhanging parts. When considering carbon-fiber reinforced (CFR) composites, it was found that a higher fraction of photocurable resin was needed for correct ink processing, likely due to the presence of the black carbon fibers that are responsible for a lower photopolymerization efficiency. For this reason, all the experiments with CFR composites were performed based on M50 as resin matrix. As shown in Fig. 2f, UV-3D printing of CFR composites based on CF5 formulation could be successfully demonstrated up to an overhang of 30°.

Optical microscopy analysis on the deposited CF5 liquid filament (before curing) showed that a portion of the carbon fibers embedded in the polymeric matrix maintains their structural integrity upon 3D printing without breaking apart, in addition to appearing partially oriented in the direction of the extrusion (Fig. 2g). This observation is also confirmed by optical microscopy image of the fractured surface that shows clear alignment of the carbon fibers in the proximity of the fracture (Fig. 2h). In the case of CF30 material, the viscosity was found to be too high to allow for an easy 3D deposition from the printer nozzle, and only simpler flat specimens suitable for further mechanical testing were realized. Furthermore, printed specimens from this ink only showed a semi-solid behavior immediately after printing, calling for the need of a subsequent exposure to UV-A to dry them completely before the final thermal treatment.

The photocuring process and the photopolymerization conversions were investigated by photocalorimetric measurements, and the results are shown in Fig. 3a–d. The enthalpy of polymerization of CF5 system was found to be about 111 J/g (Fig. 3b), which accounts for 92.5% of the enthalpy of polymerization reported for the unfilled M50 resin (Fig. 3a). This difference could be likely attributed to the presence of carbon fibers in the CF5 system that may partially prevent full access of the UV radiation to the photocurable resin, thus lowering the total heat of reaction. The same CF5

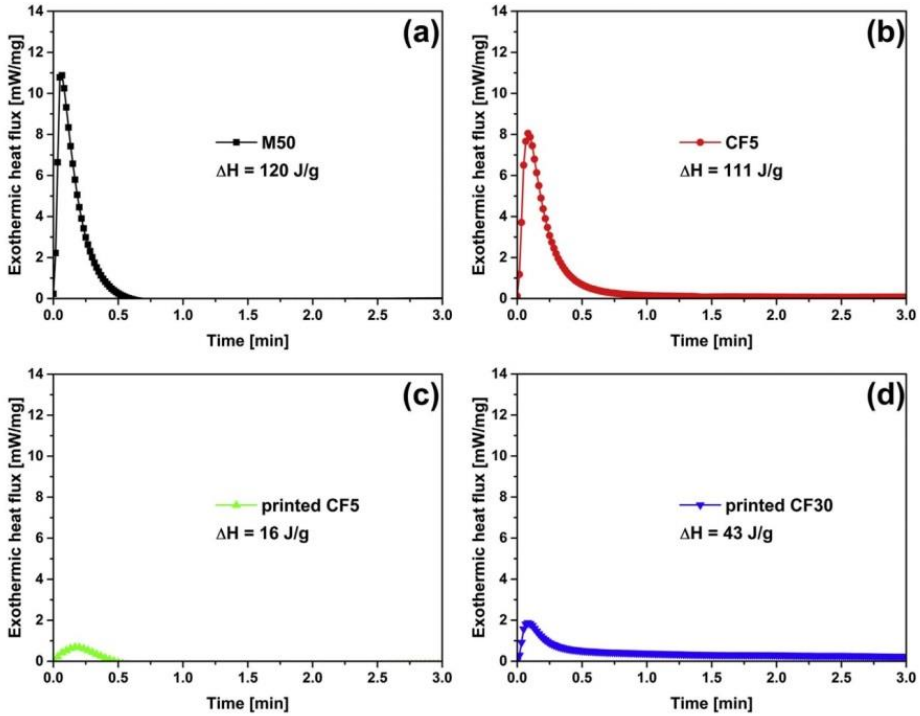


Fig. 3. Photocalorimetric (photo-DSC) scans of (a) M50 formulation before printing, (b) CF5 formulation before printing, (c) printed CF5 formulation, and (d) printed CF30 formulation.

material after the 3D-printing cycle showed a residual enthalpy of 16 J/g (Fig. 3c), that corresponds to an apparent photocuring conversion after the UV-3D printing process of about 85%. The photocuring conversion after UV-3D printing found for the 30CF composite system was significantly lower (51% after normalization by the effective fraction of UV-curable component). This behavior can be very likely ascribed to a strong UV-absorbing action of the highly concentrated carbon fibers present in this formulation.

In order to investigate the morphology of the obtained dual-cure resins and 3D printed parts, SEM images were taken on the M50 sample after fracture and subsequent exposure to a 10% w/w solution of KOH in methanol for 1 h at 60 °C to selectively etch the acrylic phase (Fig. 4). Clearly, a highly interconnected IPN structure is formed upon full dual-curing with typical sizes ranging from 10¹ to 10² nm.

The mechanical behavior and thermal transitions of the developed dual-cure inks were preliminarily investigated by means of DMA and DSC analyses. Results are summarized in Table 1, where the experimental values for the storage modulus E' at room temperature and the temperature at the tanδ peak as obtained from DMA as well as the glass transition temperature (T_g) as measured via DSC are presented.

As it appears from Table 1, a significant increase of both T_g (from 73 °C to 115 °C) and storage modulus (from 2.5 GPa to 3.0 GPa) can be obtained by re-formulating the UV curable resin in the form of an IPN dual-cure system. In addition, one single T_g was observed in the IPN system, as a further demonstration of the excellent structural homogeneity of the materials [18]. High storage moduli were measured also for the CFR composites (3.8 GPa and 7.7 GPa for the CF5 and CF30 composite formulations, respectively). The measured data were compared with those predicted by the Halpin-Tsai model for random, discontinuous fiber reinforced composites [22].

$$E = E_m \frac{1 + \eta \zeta \nu_f}{1 - \eta \nu_f} \quad (1)$$

$$\eta = \frac{E_f/E_m - 1}{E_f/E_m + \zeta} \quad (2)$$

with E, E_m, ζ, ν_f and E_f being the modulus of the composite material, the modulus of the matrix, the fiber aspect ratio, the volume fraction of the fibers and the modulus of the fiber, respectively.

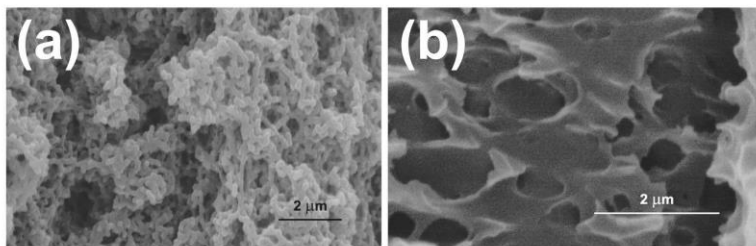


Fig. 4. SEM images of fractured surface of UV-3D printed M50 samples after alkaline etching.

Table 1

Storage modulus E' and temperature at the $\tan\delta$ peak as obtained from DMA, and T_g value obtained from DSC measurements of crosslinked resins and CFR composites.

	p-A resin	M50	CF5	CF30
E' (25 °C, GPa)	2.5 ± 0.2	3.0 ± 0.4	3.8 ± 0.2	7.7 ± 0.2
Max $\tan\delta$ (°C)	73	115	139	76
T_{DSC} (°C)	37	103	n.d.	n.d.

Eq. (1) was fitted using the storage modulus of the carbon fibers $E_f = 200$ GPa and $\zeta = 2$ $l/d = 13.8$, where l and d are the length and the diameter of the reinforcing fiber, respectively. Measured moduli for composites were found to be systematically lower than the limiting theoretical values obtained from the Halpin–Tsai model. In particular, a theoretical value of storage modulus of 5.6 GPa was calculated for the CF5 composite systems, as opposed to a measured value of 3.8 GPa. Larger differences were observed for the CF30 system that showed a theoretically predicted storage modulus of 19.8 GPa compared to an experimentally measured value of 7.7 GPa. A possible explanation for such discrepancies may lie in the likely and unavoidable overestimation of fiber aspect ratio l/d in the actual samples (some fibers are clearly broken during the printing process as shown in Fig. 2). In addition, in the case of the CF30 composite system, the unusually low value of T_g measured for this material may also play a role as this may be related to non-complete crosslinking and thus lower storage modulus. Nevertheless, the values found experimentally on the systems investigated in this work are in good agreement with experimental results reported in the literature on composites systems with the same type of reinforcing fibers [23,24,25].

4. Conclusion

In conclusion, a new dual-cure IPN system was presented in this work obtained by blending a photocurable acrylic resin and a thermally reactive epoxy resin. The very fast UV-curing kinetics of the photocurable resin makes the IPN system very suitable for a rapid UV-assisted 3D printing, whilst the following thermal curing of the epoxy component confers enhanced thermo-mechanical properties to the printed part. The 3D-printing tests suggested that the weight ratio between the photocurable and the thermally curable components in the IPN system strongly influences the behavior of the dual-cure ink upon printing in such a way that its fine-tuned control is essential to achieve desirable final printing features. For the first time, UV-assisted 3D printing was also employed to successfully process CFR polymer composites based on an optimized dual-cure formulation. The concentration of carbon fibers in the composite ink was found to significantly affect the

efficiency of the UV-curing process, thus indicating that successful UV-3D printing of high-fiber-content composites needs sufficiently high power UV sources to be accomplished. The results of this study open the way towards the digital fabrication of high performance composite materials through 3D printing technology.

References

- [1] B.Y. Ahn, S.B. Walker, S.C. Slimmer, A. Russo, A. Gupta, S. Kranz, E.B. Duoss, T.F. Malkowski, J.A. Lewis, Planar and three-dimensional printing of conductive inks, *J. Vis. Exp.* 58 (2011) 3189, <http://dx.doi.org/10.3791/3189>.
- [2] S.J. Leigh, R.J. Bradley, C.P. Pursell, D.R. Billson, D.A. Hutchins, A simple, low-cost conductive composite material for 3D printing of electronic sensors, *Plos One* 7 (2012) 11, <http://dx.doi.org/10.1371/journal.pone.0049365>.
- [3] S.J. Leigh, R.J. Bradley, C.P. Pursell, D.R. Billson, D.A. Hutchins, Using a magnetite/thermoplastic composite in 3D printing of direct replacements for commercially available flow sensors, *Smart Mater. Struct.* 23 (2014) 095039, <http://dx.doi.org/10.1088/0964-1726/23/9/095039>.
- [4] A. Ian, I.A. Barker, M.P. Ablett, H.T.J. Gilbert, S.J. Leigh, J.A. Covington, J.A. Hoyland, S.M. Richardson, A.P. Dove, A microstereolithography resin based on thiol-ene chemistry: towards biocompatible 3D extracellular constructs for tissue engineering, *Biomater. Sci.* 2 (2014) 472, <http://dx.doi.org/10.1039/c3bm60290g>.
- [5] G. Postiglione, G. Natale, G. Griffini, M. Levi, S. Turri, Conductive 3D microstructures by direct 3D printing of polymer/carbon nanotube nanocomposites via liquid deposition modeling, *Compos. A* 76 (2015) 110, <http://dx.doi.org/10.1016/j.compositesa.2015.05.014>.
- [6] J.T. Belter, A.M. Dollar, Strengthening of 3D printed fused deposition manufactured parts using the fill compositing technique, *Plos One* 10 (2015) 4, <http://dx.doi.org/10.1371/journal.pone.0122915>.
- [7] F. Ning, W. Cong, J. Qu, J. Wei, S. Wang, Additive manufacturing of carbon fiber reinforced thermoplastic composites using fused deposition modeling, *Compos. B* 80 (2015) 369, <http://dx.doi.org/10.1016/j.compositesb.2015.06.013>.
- [8] L.L. Lebel, B. Aissa, M.A. El Khakani, D. Theriault, Ultraviolet-assisted direct-write fabrication of carbon nanotube/polymer nanocomposite microcoils, *Adv. Mater.* 22 (2010) 592, <http://dx.doi.org/10.1002/adma.200902192>.
- [9] G. Postiglione, G. Natale, G. Griffini, M. Levi, S. Turri, UV-assisted three-dimensional printing of polymer nanocomposites based on inorganic fillers, *Polym. Compos.* (2015), <http://dx.doi.org/10.1002/pc.23735>.
- [10] R.D. Farahani, H. Dalir, V. Le Borgne, L.A. Gautier, M.A. El Khakani, M. Lévesque, D. Theriault, Direct-write fabrication of freestanding nanocomposite strain sensors, *Nanotechnol.* 23 (2012) 085502, <http://dx.doi.org/10.1088/0957-4484/23/8/085502>.
- [11] R.D. Farahani, L.L. Lebel, D. Theriault, Processing parameters investigation for the fabrication of self-supported and freeform polymeric microstructures using ultraviolet-assisted three-dimensional printing, *J. Micromech. Microeng.* 24 (2014) 055020, <http://dx.doi.org/10.1088/0960-1317/24/5/055020>.
- [12] A. Endruweit, M.S. Johnson, A.C. Long, Curing of composite components by ultraviolet radiation: a review, *Polym. Compos.* 27 (2006) 119, <http://dx.doi.org/10.1002/pc.20166>.
- [13] A. Endruweit, W. Ruijter, M.S. Johnson, A.C. Long, Transmission of ultraviolet light through reinforcement fabrics and its effect on ultraviolet curing of composite laminates, *Polym. Compos.* 29 (2008) 818, <http://dx.doi.org/10.1002/pc.20483>.
- [14] L.H. Sperling, Interpenetrating polymer networks: an overview, *Adv. Chem.* 239 (1994) 3, <http://dx.doi.org/10.1021/ba-1994-0239.ch001>.
- [15] L.H. Sperling, V. Mishra, The current status of interpenetrating polymer networks, *Polym. Adv. Technol.* 7 (1996) 197, [http://dx.doi.org/10.1002/\(SICI\)1099-1581\(199604\)7:4<197::AID-PAT514-3.0.CO;2-4](http://dx.doi.org/10.1002/(SICI)1099-1581(199604)7:4<197::AID-PAT514-3.0.CO;2-4).
- [16] L.K. Kostanski, R. Huang, C.D.M. Filipe, R. Ghosh, Interpenetrating polymer

- networks as a route to tunable multi-responsive biomaterials: development of novel concepts, *J. Biomater. Sci.* 20 (2009) 271, <http://dx.doi.org/10.1163/156856208X3999107>.
- [17] S. Simić, B. Dunjic, S. Tasic, B. Bozic, D. Jovanovic, I. Popovic, Synthesis and characterization of interpenetrated polymer networks with hyperbranched polymers through thermal-UV dual curing, *Prog. Org. Coat.* 63 (2008) 43, <http://dx.doi.org/10.1016/j.porgcoat.2008.04.006>.
- [18] S. Marinovic, I. Popovic, B. Dunjic, S. Tasic, B. Bozic, D. Jovanovic, The influence of different components on interpenetrating polymer networks (IPNs) characteristics as automotive top coats, *Prog. Org. Coat.* 68 (2010) 293, <http://dx.doi.org/10.1016/j.porgcoat.2010.03.010>.
- [19] M. Sangermano, W. Carbonaro, G. Malucelli, A. Priola, UV-cured interpenetrating acrylic-epoxy polymer networks: preparation and characterization, *Macromol. Mat. Eng.* 293 (2008) 515, <http://dx.doi.org/10.1002/mame.200800020>.
- [20] A. Gupta, A.A. Ogle, Dual curing of carbon fiber reinforced photoresins for rapid prototyping, *Polym. Compos.* 23 (2002) 1162–1170, <http://dx.doi.org/10.1002/pc.10509>.
- [21] P.J. Bartolo, G. Mitchell, Stereo-thermal-lithography: a new principle for rapid prototyping, *Rapid Prototyp. J.* 9 (2003) 150, <http://dx.doi.org/10.1108/13552540310477454>.
- [22] J.C. Halpin, J.L. Kardos, The Halpin–Tsai equations: a review, *Polym. Eng. Sci.* 16 (1976) 344, <http://dx.doi.org/10.1002/pen.760160512>.
- [23] P. Tsotra, K. Friedrich, Electrical and mechanical properties of functionally graded epoxy-resin/carbon fibre composites, *Compos. A* 34 (2003) 75, [http://dx.doi.org/10.1016/S1359-835X\(02\)00181-1](http://dx.doi.org/10.1016/S1359-835X(02)00181-1).
- [24] H. Zhang, Z. Zhang, C. Breidt, Comparison of short carbon fibre surface treatments on epoxy composites I. Enhancement of the mechanical properties, *Compos. Sci. Technol.* 64 (2004) 2021, <http://dx.doi.org/10.1016/j.compscitech.2004.02.009>.
- [25] B.G. Compton, J.A. Lewis, 3D-printing of lightweight cellular composites, *Adv. Mater.* 26 (2014) 5930, <http://dx.doi.org/10.1002/adma.201401804>.